Numerical Simulations of Lamb Waves in Plates Using a Semi-Analytical Finite Element Method

Dissertation

zur Erlangung des akademischen Grades

Doktoringenieur (Dr.-Ing.)

von M.Eng. Zair Asrar Bin Ahmad

geb. am 30. November 1980 in Alor Setar, Kedah

genehmigt durch die Fakultät für Maschinenbau

der Otto-von-Guericke-Universität Magdeburg

Gutachter: Prof. Dr.-Ing. habil. Dr. h. c. Ulrich Gabbert

Prof. Dr.-Ing. Rolf Lammering

Promotionskolloquium am 26. September 2011

Acknowledgements

All praises to Allah, who made this work possible. Firstly, I would like to use this opportunity to acknowledge and thank my supervisor, Prof. Dr.-Ing. habil. Dr. h.c. Ulrich Gabbert for his guidances and supports during my work and stay in Magdeburg. I have learned valuable lessons from him in many of our academic and non-academic discussions. Many thanks also to all colleagues which have helped me a lot during my work here in the Institut für Mechanik especially to my ex-roommate, Janko Kreikemeier, to my teachers Juan-Vivar Miguel-Perez, Christian Willberg, Seyed Muhammad Hossein Hosseini, Stefan Ringwelski, Sascha Duczek, Mathias Würkner and also many others who have generously lend me their knowledges and wisdoms. My thanks goes to Prof. Dr. Jürgen Pohl in Institut für Werkstoff-und Fügetechnik (IWF) and Daniel Schmidt in Deutsches Zentrum für Luft- und Raumfahrt (DLR) Braunschweig for the dispersion curves experimental data. I am indeed standing in the shoulders of giants.

Last but not least, my thanks goes to my whole family. To my wife, Nurul Sariyah Binti Md. Rajib for her company and for taking care of our kids. To my kids, Luqman Hakim and Naurah Mahfuzah for giving us joy and laughters. To my father, Ahmad Bin Said, my mother, Rokhiyah Binti Ahmad and my mother-in-law, Yahtimi Binti Sipin for all the prayers and encouragements. To all my siblings, in-laws and also to all my friends.

The financial supports from the Malaysian Ministry of High Education, from the Universiti Teknologi Malaysia and from the Institut für Mechanik, Otto-von-Guericke Universität Magdeburg are highly appreciated and fully acknowledged.

Abstract

The increase in structural safety and the reduction in structural maintenance cost can be achieved by the application of reliable monitoring systems of the structural "health". Such systems are called Structural Health Monitoring (SHM) systems. However, the application of such systems involved a lot of challenges. For thin structures, the applications of Lamb waves for SHM systems are highly desirable. Lamb waves are special types of ultrasonic waves having dispersive behaviors that propagate in plates and shell-like structures. The detection of damages comes from the interaction of Lamb waves with damages in the structures. These damages trigger and influence losses, reflections and conversions of the Lamb modes. The changes in the Lamb wave signals are measured to locate the position and size of the damages. These interactions are complex. Thus, an effective numerical method is required to understand these effects for the applications in SHM systems. A very fine time and space discretizations in the considered domain are required in the Lamb wave propagation simulations using standard Finite Element Method, thus in this work, an alternative numerical method is developed. The presented work focused on the study and development of the so-called Semi-Analytical Finite Element (SAFE) method. With the help of this method, three main characteristic of Lamb wave simulations are analyzed. Firstly, dispersion curves are calculated. These curves are made for homogeneous isotropic plates and composite plates with varied layer arrangements. Next, behavior of Lamb wave propagations due to obstacles are studied and followed by the study on displacement responses of the system due to different external force excitations. Based on these numerical studies, the advantages, disadvantages and limitations of SAFE method are presented. The main results of the work presented here are:

a. The effects of symmetric and unsymmetrical layer arrangements in the dispersion curves.
b. The effects of symmetric and unsymmetrical obstacles on the Lamb wave propagations.
c. Mode selection in thin piezoelectric actuator attached on composite plates.
d. Implementation of plate edges in the SAFE method.

Kurzfassung

Die Sicherheit von verschiedensten Konstruktionen könnte erheblich erhöht und Wartungskosten reduziert werden, wenn ein zuverlässiges System zur Überwachung der "Gesundheit" der Struktur realisiert werden kann. Solche Systeme tragen den englischen Namen Structural Health Monitoring (SHM) Systeme. Leider ergeben sich bei der Umsetzung dieser Idee weitreichende Probleme. Für dünnwandige Strukturen ist die Nutzung von Lambwellen für SHM-Systeme sehr beliebt. Lambwellen sind eine spezieller Typ von gerichteten Ultraschallwellen mit dispersiven Eigenschaften, die sich in platten- und schalenartigen Strukturen ausbilden. Die Erkennung von Fehlern beruht auf der Interaktion von Lambwellen mit den Schäden in Strukturen. Die Schäden können Reflexionen und Konversionen der Wellenmoden auslösen, wodurch das Ausbreitungsverhalten der Wellen beeinflusst wird. Diese Änderungen im Signal sollen gemessen werden, um Vorhersagen über die Position und Größe des Fehlers treffen zu können. Da die Interaktion sehr komplex ist, werden effektive numerisch Methoden benötigt, um die Lambwellenausbreitung zu verstehen und für SHM Systeme nutzen zu können. Da eine sehr feine zeitliche und räumliche Diskretisierung des betrachteten Gebietes nötig ist, um die Lambwellenausbreitung mit Standard-Finite-Elemente-Methoden zu analysiere, ist in dieser Arbeit ein alternatives numerisches Konzept entwickelt worden. Deshalb liegt der Fokus der vorliegenden Arbeit auf der Entwicklung und Untersuchung von sogenannten Semi-Analytischen-Finiten-Elementen (SAFE). Mit Hilfe dieser Methode wurden drei wichtige Eigenschaften von Lambwellen analysiert. In einem ersten Punkt sind Dispersionskurven berechnet worden. Das ist sowohl für homogen isotrope Materialien, als auch für Laminate mit unterschiedlichen Lagenaufbau geschehen. Des Weiteren ist das Verhalten von Lambwellen an Hindernissen in der Struktur untersucht worden, sowie die Verschiebungsantwort des Systems aufgrund unterschiedlicher äußerer Kraftanregungen. Basierend auf den numerischen Studien werden die Vorteile, Nachteile und Grenzen der SAFE Methode herausgearbeitet. Die wichtigsten Resultate der Arbeit, auf die hier verwiesen werden soll, sind:

a. Der Einfluss von symmetrischen und unsymmetrischen Lagenaufbauten auf die Dispersionskurven.
b. Der Einfluss von symmetrischen und unsymmetrischen Hindernissen auf die Ausbreitung von Lambwellen.
c. Die Ergebnisse zur selektiven Mode-Anregung durch dünne piezoelektrische Aktuatoren, appliziert auf Kompositplatten.
d. Die Ergebnisse zur Implementierung von Plattenrändern in der SAFE Methode.

Contents

List of Figures

List of Tables

List of Abbreviations

2D	**2** **D**imensional
3D	**3** **D**imensional
AFC	**A**ctive **F**ibre **C**omposite
BE/BEM	**B**oundary **E**lement / **B**oundary **E**lement **M**ethod
CPU	**C**entral **P**rocessing **U**nit
EMAT	**E**lectro-**M**agnetic **A**coustic **T**ransducer
FFT	**F**ast **F**ourier **T**ransform
FE/FEM	**F**inite **E**lement / **F**inite **E**lement **M**ethod
HBE	**H**ybrid **B**oundary **E**lement method
LISA	**L**ocal **I**nteraction **S**mulation **A**nalysis
MFC	**M**icro **F**ibre **C**omposite
SAFE	**S**emi-**A**nalytical **F**inite **E**lement method
SHM	**S**tructural **H**ealth **M**onitoring
P	**P**ressure wave
PWAS	**P**iezoelectric **W**afer **A**ctive **S**ensor
PZT	**P**ie**z**oelectric **T**ransducer
RAM	**R**andom **A**ccess **M**emory
SH	**S**hear **H**orizontal wave
SV	**S**hear **V**ertical wave
WFE	**W**ave **F**inite **E**lement method

List of Symbols

Chapter 3

$\mathbf{A}$,$\mathbf{B}$,$\mathbf{C}$	matrices in SAFE equation
$\mathbf{A}_x$,$\mathbf{A}_y$,$\mathbf{A}_z$,$\mathbf{B}_{xz}$,$\mathbf{C}_x$,$\mathbf{C}_y$,$\mathbf{C}_z$	components of matrices in SAFE equation
$\mathbf{B}_1$,$\mathbf{B}_2$	differential matrix
$\tilde{\mathbf{C}}$	stress-strain relationship matrix
d	differential
H	Hamiltonian
i	imaginary value, $i = \sqrt{-1}$
$\mathbf{I}$	identity matrix
$\mathbf{J}$	Jacobian matrix
k	wavenumber
$\mathbf{k}_1^{(e)}$,$\mathbf{k}_{12}^{(e)}$,$\mathbf{k}_2^{(e)}$,$\mathbf{k}_{21}^{(e)}$,$\mathbf{k}_3^{(e)}$	element stiffness matrices
$\mathbf{K}$	eigenvalue matrix
$\mathbf{K}_1$,$\mathbf{K}_2$,$\mathbf{K}_3$	global stiffness matrices
$\hat{\mathbf{K}}_2$	symmetrized $\mathbf{K}_2$ matrix
n_{el}	number of elements
n_{quad}	number of quadrature points
$\mathbf{m}^{(e)}$	element mass matrix
$\mathbf{M}$	global mass matrix
$\mathbf{N}$	shape function matrix
N_1,N_2,...,N_n	components of shape function matrix
$\mathbf{N}_{,x}$,$\mathbf{N}_{,y}$,$\mathbf{N}_{,z}$,$\mathbf{N}_{,\xi}$	derivatives of shape function matrix

q_e	element nodal displacement
$\mathbf{Q}$	eigenvector of SAFE equation
$\mathbf{R}$	factor for rotation matrix
t	time
T	kinetic energy
$\mathbf{T}$	transformation matrix
$\mathbf{T}(\theta)$	rotation matrix
$\mathbf{u}/\dot{\mathbf{u}}/\ddot{\mathbf{u}}$	displacement/velocity/acceleration vector
u_x,u_y,u_z	components of displacements vector
u_{xi},u_{yi},u_{zi}	components of displacements vector at ith node
U	strain energy
$\mathbf{U}$	eigenvector of SAFE equation
$\hat{\mathbf{U}}_x$,$\hat{\mathbf{U}}_y$,$\hat{\mathbf{U}}_z$	components of eigenvector
$\hat{\mathbf{U}}$	eigenvector of SAFE equation
V	volume
$\mathbf{W}_i$	weight at ith quadrature point
x,y,z	global Cartesian coordinate
x_L,y_L,z_L	local Cartesian coordinate
$\mathbf{Y}$	eigenvector of SAFE equation
$\mathbf{Z}$	eigenvector of SAFE equation
δ	partial differential
ω	angular frequency
Ω	domain
ρ	density
$\boldsymbol{\sigma}$	displacements vector
σ_x,σ_y,σ_z	components of stress vector
θ	angle between x axis and x_L axis
$\boldsymbol{\varepsilon}$	strain vector
ε_x,ε_y,ε_z	components of strain vector
ξ	natural coordinate

$(.)_e$	elemental values
$(.)^T$	matrix transpose
$(.)_{,x}/(.)_{,y}/(.)_{,z}/(.)_{,\xi}$	differentiation with respect to $x/y/z/\xi$
$(.)^*$	complex conjugate

Chapter 4

c_g	group velocity
c_p	phase velocity
d	differential
$\mathbf{E}$	Young's modulus
f	linear frequency
$\mathbf{G}$	Shear modulus
k	wavenumber
$\vec{k}$	wavenumber vector
$\vec{k}_\theta$	wavenumber vector along θ direction
$\mathbf{K}_1$,$\hat{\mathbf{K}}_2$,$\mathbf{K}_3$	global stiffness matrices
$\mathbf{K}(k)$	sum of global stiffness matrix
$\mathbf{K}'$	differentiation of the sum of global stiffness matrix with respect to k
$\mathbf{K}^{(0)}$	global stiffness matrix due to in-plane load
$\mathbf{M}$	global mass matrix
t	thickness
u_x,u_y,u_z	components of displacement vector
$\hat{\mathbf{U}}$	eigenvector of SAFE equation
$\hat{\mathbf{U}}^{(L)}$	left eigenvector of SAFE equation
$\tilde{\mathbf{V}}^{(e)}$	wavenumber vector along θ direction
x,y,z	global coordinate

δ	partial differential
$\boldsymbol{\varepsilon}$	linear strain vector
ε_{xx},ε_{xy},ε_{xz}, ε_{yx},ε_{yy},ε_{yz}, ε_{zx},ε_{zy},ε_{zz}	components of strain vector
$\mathfrak{E}$	non-linear strain vector
λ	wavelength
ν	Poisson's ratio
ψ	skew angle
ρ	density
$\boldsymbol{\sigma}$	stress vector
σ_{xx},σ_{xy},σ_{xz}, σ_{yx},σ_{yy},σ_{yz}, σ_{zx},σ_{zy},σ_{zz}	components of stress vector
$\boldsymbol{\sigma}^{(0)}$	initial stress vector
$\sigma_{xx}^{(0)}$	components of initial stress vector along x axis
ω	circular frequency
θ	wave propagation angle
$(.)^T$	matrix transpose
$(.)^*$	complex conjugate

Chapter 5

a^m	amplitude of the mth reflected mode (obstacles)
$\mathbf{A}$	reflected mode amplitude vector (obstacles)
A_p^{in}	incidence amplitude for pth mode
$\mathbf{A}$	matrix of reflected mode amplitude vector (obstacles)
b_i	amplitude of the ith reflected mode (plate edges)
$\mathbf{B}$	matrix of transmitted mode amplitude

	vector (obstacles)
$\mathbf{B}$	matrix of reflected mode amplitude
	vector (plate edges)
c_L	longitudinal wave velocity
c_T	transversal wave velocity
$\mathbf{F}$	force vector
$\mathbf{F}^{in}$	incidence wave force vector
$\mathbf{F}^{ref}$	reflected wave force vector
i	imaginary value, $i = \sqrt{-1}$
$\mathbf{I}_{pn}$	energy flux of nth reflected mode due to pth incidence mode
$\mathbf{I}_{p}^{in}$	energy flux of pth incidence mode
$\mathbf{I}_{pn}^{ref}$	energy flux of nth reflected mode due to pth incidence mode
$\mathbf{I}_{pn}^{trans}$	energy flux of nth transmitted mode due to pth incidence mode
k_p	wavenumber for pth mode
M	total number of modes
N_{pr}	total number of propagating modes
N_{tr}	total number of transmitted modes
$\mathbf{N}$	matrix of interpolation functions
P_m	average energy flux of mth mode
$\mathbf{q}$	displacement vector
$\mathbf{q}^{in}$	incidence wave displacement vector
$\mathbf{q}^{ref}$	reflected wave displacement vector
$\mathbf{R}_{pn}$	coefficient of nth reflected mode due to pth incidence mode
$\mathbf{S}$	dynamic stiffness matrix
$\mathbf{t}_m$	stress in plate due to mth mode
$\mathbf{U}$	displacement eigenvector
x,y,z	global coordinate

x_0,x_1,x_2	distance of finite element regions form origin
ϵ	error percentage in energy balance
ϕ	columns of displacement eigenvectors matrix
Φ	displacement eigenvectors matrix
Φ_p^-	displacement eigenvectors for pth in opposite direction
ψ	columns of force eigenvectors matrix
Ψ_p^-	force eigenvectors for pth in opposite direction
$(.)_B$	boundary nodes
$(.)^{in}$	incidence wave
$(.)^I$	incidence nodes
$(.)^{ref}$	reflected wave
$(.)^T$	matrix transpose
$(.)^*$	complex conjugate

Chapter 6

a	actuator half length
A_ϵ	modal strain amplitude
b	sensor width
$\mathbf{A}$,$\mathbf{B}$	matrices from SAFE equation
d	distance of monitored point from origin
$\mathbf{d}$	piezoelectric coefficient matrix
d_{31},d_{32}	components of piezoelectric coefficient matrix
$\mathbf{C}^E$	elastic stiffness matrix at zero electric field
C_{11}^E,C_{12}^E,C_{22}^E,C_{66}^E	components of elastic stiffness matrix
$\mathbf{D}$	charge density vector
$\mathbf{e}^{(\sigma)}$	dielectric permittivity matrix at zeros stress

$e_{33}^{(\sigma)}$	components of dielectric permittivity matrix
$\mathbf{E}$	electric field vector
E_3	component of electric field vector
$\mathbf{E}_r^{(2D)}$	2D excitability matrix for mode r
$\mathbf{E}_r^{(3D)}$	3D excitability matrix for mode r
$\mathbf{f}^{(2D)}$	2D force vector
$\mathbf{f}^{(3D)}$	3D force vector
$\overline{\mathbf{f}}^{(2D)}$	Fourier transform of 2D force vector
$\overline{\mathbf{f}}^{(3D)}$	Fourier transform of 3D force vector
$\mathbf{g}^{(2D)}$	2D Green's function
$\mathbf{g}^{(3D)}$	3D Green's function
$\mathbf{G}^{(2D)}$	Fourier transform of 2D Green's function
$\mathbf{G}^{(3D)}$	Fourier transform of 3D Green's function
h	plate thickness
$\hat{h}$	sensor thickness
i	imaginary value, $i = \sqrt{-1}$
k_r	wavenumber for rth mode
$\mathbf{k}$	wavenumber vector
l	sensor length
$\mathbf{P}_r$	average power flow for rth mode
$\mathbf{Q}$	eigenvector of SAFE equation
$\mathbf{u}^{(2D)}$	2D displacement vector
$\mathbf{u}^{(3D)}$	3D displacement vector
$\mathbf{U}_r$	displacement eigenvector for rth mode
x_m	x position of monitored point
n	number of wave cycles
N	number of nodes
t	time
T	half total time duration
$\mathbf{T}(\theta)$	transformation matrix
V	voltage

$\bar{V}$	voltage response amplitude
$\mathbf{V}^e$	energy velocity
x,y,z	global coordinate
x',y',z'	wave propagation coordinate
x_p	x position of actuated point
$Y^{(E)}$	Young's modulus
ν	Poisson's ratio
ϵ	strain vector
ϵ_{11},ϵ_{22},γ_{12}	components of strain vector
$\epsilon^{(a)}_{x'x'}$	strain along x'-axis at the point of entry into the sensor
λ_r	wavelength of rth mode
σ	stress vector
σ_r	stress tensor of rth mode
ω	circular frequency
ω_0	central circular frequency
ϕ	angle between wavenumber vector and energy velocity in x-y plane
Φ	phase
τ	shear stress
$\bar{\tau}$	Fourier transform of shear stress
θ	angle between x-axis and ξ-axis
$(.)^T$	matrix transpose
$(.)^*$	complex conjugate

Chapter 1

Introduction

1.1 Motivation

In structural designs, the trend is always to become more ambitious. For example, buildings get taller, bridges get longer and aircrafts get bigger. This lead to an increase in the requirement to provide both cost savings with regard to maintenances and safer environments by preventing structural failures. One of the possible means to achieve this goal is by the application of the Structural Health Monitoring (SHM) systems. By providing additional safety measures, the SHM systems enable the life of the structures to be maximized and reduce the structural life costs.

The SHM systems have been applied in many different applications ranging from rotating machineries, offshore platforms, space vehicles and aircrafts to bridges [9, 10]. It is highly desirable to have SHM systems in structures for which failures would result in a catastrophic loss of life, i.e in aircrafts. If the onset of the failures can be detected, actions can be taken to limit or prevent the use of these structures, while repairs can be carried out.

In current practices of the aircraft industries, the structural integrity of the aircrafts are ensured by using scheduled maintenances [11]. In these schedule maintenances, inspection on the component damages are made visually and by using the ultrasonic techniques to scan the component interiors for damages [10]. Such approaches are time consuming, require trained inspection personal as well as cost a lot to airline companies due to the aircraft down time as the inspected components need to be removed. Thus, alternative inspection approaches such as the on-line SHM system are highly demanded [12]. This includes the usage of optical fibers, electrical impedances, vibration analysis and guided structural waves.

The application of guided structural waves, i.e. Lamb waves in SHM applications for thin structures gain a high interest within the research communities due to its considerably long propagation ranges [13]. Thus, it can be used to interrogate the structures at relatively long distances. Lamb waves propagate at high frequencies giving it high resolutions from its small wavelengths. This makes Lamb waves sensitive to small damages in the structure i.e impact damages. However, Lamb waves are dispersive and multi-modal

causing complicated wave signals and data interpretations in damage detection processes. In general composite materials, these dispersive and multi-modal characteristics are also directionally dependent [14]. Furthermore, Lamb waves are also sensitive to environmental conditions and structural discontinuities such as borders which are typically available in the structures.

1.2 Objective

The behavior of the Lamb wave propagation in plates needs to be understood first before any meaningful utilization in the SHM applications either through analytical, numerical and experimental investigations can be performed. The most robust tool available for the Lamb wave numerical simulations is the Finite Element Method (FEM). However, high computational resources are needed to simulate the Lamb wave propagations due to the small wavelengths involved. High number of space and time discretizations are needed to correctly simulate these wavelengths. The present research is made to study an alternative numerical procedure for simulating the Lamb wave propagations by applying the Semi-Analytical Finite Element Method (SAFE). This method is attractive as it is not severely affected by the discretization problems found in the FEM and tailored to the needs of the Lamb wave simulations.

The first step in utilizing Lamb waves is to understand its multi-modal and dispersive behaviors. This can be proven by referring to the available literatures on Lamb waves [13]. Almost every author gives an indication about which Lamb modes and frequencies are being considered in his studies. These informations are obtained from the dispersion curves. Phase velocity dispersion curves show the velocity of Lamb waves while group velocity dispersion curves show the velocity of Lamb wave packets (or wave energy). From these curves, the velocity, the number and the type of modes involved at a particular frequency are obtained. By utilizing a specific mode or a frequency region, it is possible to reduce the complexity of interpreting Lamb wave signals. In this thesis, the SAFE method is applied for calculating the dispersion curves for isotropic and composite plates.

Damages or obstacles in plates are normally detected through scattering effects of Lamb waves. Thus, reflections and transmissions of the Lamb waves due to the obstacles need to be studied. In order to simulate arbitrary obstacle shapes in this thesis, the SAFE method is coupled with the FEM. The infinite plate regions are simulated using the SAFE method while the small and local plate regions containing these obstacles are simulated using the FEM. The reflection and transmission coefficients are obtained from these analysis. The effects of the obstacles on each Lamb mode can be shown as the coefficients are obtained separately for each mode.

Lamb waves are excited in plates either though occurring damages or by using actuators. These actuators exerted forces on the plates. Then, the propagating Lamb wave signals in the plates are sensed using sensors. Force response simulations are needed to simulate these actuators and sensors. By applying the SAFE method, force response analyses are made in this thesis for the 2D and the 3D cases. However, the SAFE method is based on

infinite plates. To overcome this, a novel approach is presented to simulate finite plates with edges in the force response simulations.

In summary, the objectives of this work are to study the applications of the SAFE method for:

- the calculations of Lamb wave dispersion curves,
- the Lamb wave reflection and transmission behaviors due to obstacles, and
- the force response simulations.

1.3 Scope

This thesis is organized as follows:

Chapter 2 This chapter contains the literature reviews on the application of the Lamb waves in the SHM systems. From this literature reviews, conclusions are made which lead to the presented thesis.

Chapter 3 The formulation of the SAFE method is given in this chapter. The available choices of the solution procedures and the mode separation techniques in the SAFE method are discussed.

Chapter 4 In this chapter, the dispersion curves for isotropic and composite plates are presented. Comparisons are made with available results in literatures and also with existing experimental results. Some examples on the application of the dispersion curves analysis are shown.

Chapter 5 In this chapter, the coupled SAFE-FE method is applied to simulate the Lamb wave reflection and transmission behaviors due to obstacles. The plate edges and obstacles located anywhere in the plate are considered. Some examples on the application of the reflection and transmission analysis on the effects of symmetrical and unsymmetrical obstacles, transducers and plate stiffeners are shown.

Chapter 6 The force response analysis using the SAFE method is described in this chapter. The forces from actuators can be decomposed into discrete point forces. Therefore, formulations for the 2D and the 3D point force response analysis using the SAFE method in infinite plates are given. An approach is shown to consider plate edges in the force response simulations. Some examples on the application of the force response analysis for mode tuning, point force response, rectangular sensor response and actuator/sensor coupled system simulation are given.

Chapter 7 The conclusions of this research work and the outlooks for future research work are presented in this chapter. Advantages, disadvantages and limitations of the SAFE method for Lamb wave simulations are given.

Chapter 2

Literature review

2.1 Brief history on Lamb wave

Travelling waves in structures are guided by the structural boundaries. These wave guiding structures are called waveguides. Common types of waveguide in technical applications are plates (i.e aircraft skin), rods (i.e cylindrical, square, rail), hollow cylinders (i.e pipe and tubing), multi-layer structures, curves or flat surfaces on a half spaces, and interfaces [15]. The waveguides influence the types of available waves. In general, Lamb waves belong to a family of guided waves, which is guided by the plate boundaries when it propagates. Thus, in literatures, it is also known as guided waves in plates.

Waves propagating on the surface of an infinite solid half space (known as Rayleigh wave) are firstly described by Lord Rayleigh in 1885 [16]. In 1917, Horace Lamb extended Rayleigh analysis to waves propagating within free isotropic plates with parallel surfaces [17]. To honour him, the plate waves are generally known as Lamb waves. Other than the Lamb waves, Love [18] showed mathematically that shear horizontal waves (also known as Love waves) are also solutions to the wave equation in plates. These waves have a shearing motion in the plane of the plates. Later, Stonely [19] described waves propagating at the interface between two solids. Conditions for the propagating and the leaky wave modes between two solids are given in [20, 21]. Leaky waves are the waves that loses its energy to the surrounding.

In true sense, only the waves in plates with parallel surfaces that are decoupled from the shear horizontal waves can be called Lamb waves, as originally described by Lamb. However in the available literatures, sometimes waves in anisotropic composite plates are also named as Lamb waves even with the coupling of the Lamb and the Love modes.

2.2 Characteristics of Lamb wave

In an infinite (bulk) solid, three types of bulk wave exist which are longitudinal (P) waves, shear vertical (SV) waves and shear horizontal (SH) waves as shown in Figure 2.1. When

the solid is constrained by the top and bottom surfaces in isotropic plates, the P and the SV waves are combined and create the Lamb waves [22].

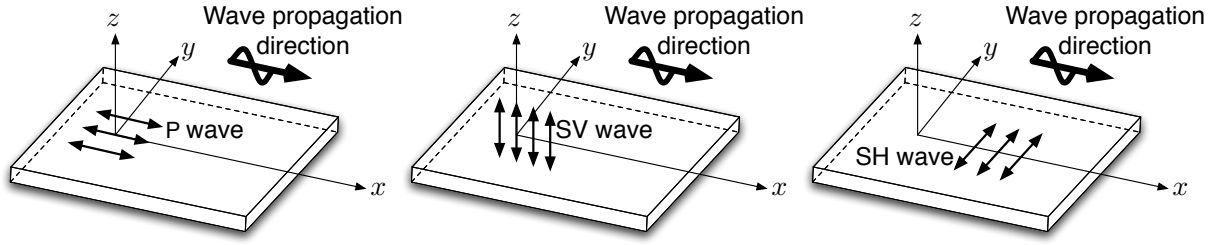

FIGURE 2.1: Bulk waves in solids.

The Lamb waves propagate in two types of modes; the symmetrical (S) and the anti-symmetrical (A) modes (see Figure 2.2). In the S modes, the plate displacements are symmetrical with respect to its center plane while in the A modes, it is anti-symmetrical. There are infinite number of modes (S and A) existing in a plate [23]. For a particular Lamb wave excitation, the available modes depend on the excitation frequencies and the thickness of the plate (see Figure 2.3). At a higher frequency and a larger plate thickness, more modes exist. The Lamb waves are dispersive as its velocities change with frequencies. From the dispersion curves for isotropic plates, a minimum of two Lamb modes exist at each frequency. The Lamb waves converge to the Rayleigh waves when the excitation frequency increases to a certain frequency limit. This physically means that the wave frequencies are too high causing the waves to travel only on the surface of the plates which correspond to the behavior of the Rayleigh (surface) wave.

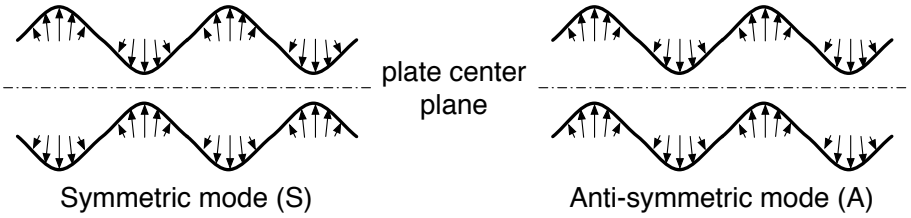

FIGURE 2.2: The symmetric and the anti-symmetric modes.

The Lamb waves are used to interrogate the whole thickness of the plates. Both the surfaces or the internal damages can be detected. However, due to the complexity of the multi-modal Lamb waves, only the symmetrical S_0 mode [24] and the anti-symmetrical A_0 mode [25] are normally considered in the literatures in order to simplify the wave signal interpretations. There is also some effort to utilize the shear horizontal SH_0 mode for damage detections as it has non dispersive behavior in the isotropic plates [26, 27].

Naturally, the Lamb wave propagations in non-homogeneous composite plates are more complex than in homogeneous isotropic plates due to the anisotropic material properties. In this case, the P waves, the SV waves and the SH waves are coupled together. Thus, the Lamb modes and the Love modes can not be solved separately. In a typical anisotropic composite plate, the material properties depend on the fiber and matrix properties, the fiber directions, the lamina thickness and arrangements in the plate thickness direction.

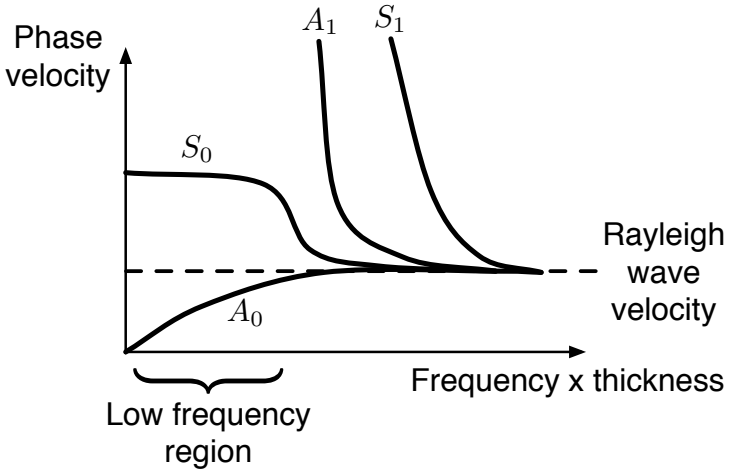

FIGURE 2.3: The typical dispersion curves for the isotropic materials.

2.3 Application of Lamb wave in SHM

Structural Health Monitoring (SHM) systems involving Lamb waves can be differentiated into two types, a passive system and an active system [28] (see Figure 2.4). In passive SHM systems, only sensors are required to detect the Lamb waves produced by occurring damages in the structures. However, in active SHM systems, the Lamb waves are excited into the structures using actuators and then sensed back by sensors with the damage informations embedded within the obtained signals.

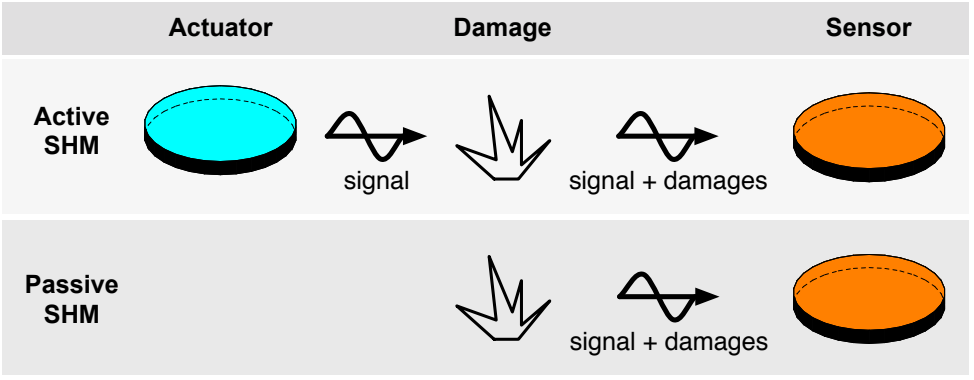

FIGURE 2.4: The damage detection in active and passive SHM systems.

A passive SHM system deals mainly with the problem of damage localizations. An active SHM system on the other hand gives the opportunity for utilizing certain mode types and frequency ranges, which can help to reduce the complexity in the signal processing for damage detections. The Lamb waves can be actuated and sensed by many types of transducers [13]. Among them are:

- Ultrasonic transducers,
- Laser transducers,
- Piezoelectric transducers,

- Interdigital/Comb transducers,
- Optical fiber transducers,
- Speckle Interferometry.

The ultrasonic transducers are used for actuating and sensing of single Lamb modes using angled wedge prism by applying the Snell's law [29–32]. However, the main problems for these ultrasonic transducers are (i) the required downtime of the inspected structures, and (ii) the inspected structures must be accessible from both sides. Furthermore, the non-negligible mass/volume of the transducers and limited access to the geometry reduces the practical applications especially for in-situ SHM systems.

The Lamb waves excitation using the laser-based ultrasonic waves and the Lamb wave sensing using the laser interferometers are high precision measurement techniques [33]. These Laser transducers are non-contact transducers. However, the main disadvantage is the high equipment cost.

By using the piezoelectric effects, an electrical potential can be converted into a mechanical displacement and vice versa in the piezoelectric transducers. Thus, the piezoelectric transducers can be used for both actuating and sensing of Lamb waves. The piezoelectric transducers made from piezoelectric lead zirconate titanate (PZT) have excellent performance in the Lamb wave actuation and sensing [34]. Advantages of these transducers include easy integration, negligible mass/volume, excellent mechanical strength, wide frequency responses, low power consumption, low acoustic impedance and low cost. However, these transducers generate multiple modes, exhibit nonlinear material behavior and hysteresis under large strains/voltages or under high temperature, have small force at high strain, measure strain instead of displacement, are brittle and have low fatigue life [35]. There are also composite versions of the PZT transducers i.e the micro fiber composites (MFC) and the active fiber composites (AFC) [36–38]. A mode selection approach for thin PZT ceramics fully coupled to the isotropic plates has been shown in [39, 40].

In interdigital transducers, the spacing between the interdigital elements is set according to the wavelength of the targeted modes in the actuation and sensing of Lamb waves [15, 41]. Thus, selective mode actuation and sensing can be made using this type of transducer [42–45]. The width of each interdigital element influences only the magnitude of the obtained signal, i.e the larger the width, the larger the signal amplitude [46]. The interdigital elements can be made by PZT ceramics or by polyvinylidene fluoride (PVDF) piezoelectric polymer films. The PVDF films are more flexible, have a higher dimensional stability, have a more stable piezoelectric coefficient over time and have a greater ease of handling compared to the PZT ceramics [42]. However, the PVDF transducers are mainly used as sensors due to the low actuating force.

The last two transducer types can be used only in the sensing of Lamb waves. In optical fiber transducers, the Fiber Bragg Grating (FBG) sensor is used to detect the Lamb waves. It is found that the embedded FBG sensors have more sensitivity to the Lamb waves than the surface mounted FBG sensor [13]. However, the surface mounted sensors are more practical as they are easier to repair and to replace. Furthermore, the embedded sensors may weaken the monitored plate structurally. In the speckle interferometry, phased map

obtained from the variations of interference light pattern (speckle) is used for the Lamb waves sensing and visualization [47].

The Lamb wave signals from the sensors are processed to indicate the presence of damages. Three types of signal processing techniques are available; (i) time domain analysis [48], (ii) frequency domain analysis [49, 50], and (iii) time-frequency domain analysis [13, 51–53]. The damages are detected in the wave signals by cross correlations with the baseline measurement data for pristine conditions [54, 55]. This baseline data is used to subtract the boundary effects from the wave signals. However, such baseline data are difficult to maintain and change with environmental conditions.

Damages can be located using the triangulation method [51, 54], the tomography techniques [56–60] and the time reversal method [61, 62]. Another approach which is computationally intensive is the neural network method [26, 63, 64]. Extensive FEM simulations are needed to 'teach' the neural network algorithm on how to locate the damages. However, the algorithm is not working if the teaching conditions change. Instead of using the time of flight, damage localizations can also be based on the energy propagation of the Lamb waves [65].

Many actuator/sensor location placements have been proposed. In [54], the actuators/sensors are located at the boundary of the plate. The actuators and sensors have been arranged in arrays to locate damages using phased reconstruction algorithm [66–68] and excite waves in particular directions applying phased array actuation-sensing concepts [6, 69–75]. MFC transducers have been arranged in a rosette arrangement as passive sensors for damage localisations in [76–78]. A damage localization algorithm based on the probabilistic correlation has been shown to be capable of detecting damages in complex aircraft structures [55].

2.4 Simulation of Lamb wave

Many examples in the literatures highlight the complexity of the Lamb waves in real world applications. Thus, numerical simulation is one of the best ways to understand the Lamb wave behaviors. Computations of dispersion curves and plate displacement profiles for isotropic plates have been made by Viktorov in 1967 [79] using Ural computer occupying 90-100 square metres of space [80]. Nowadays, with the advancements of computers, such computations can be made within minutes even for composite plates with normal personal and notebook computers [1] (with a 3.4GHz CPU and a 3.5GB RAM). The challenges now are to simulate not only the dispersion curves but also the Lamb wave propagations inside the plate itself. From these simulations, the induced Lamb wave signals from the actuators, the interactions of the Lamb waves with obstacles/damages and the signals obtained at the sensors can be calculated. The most robust numerical tool available is the FEM. However, such simulations in the FEM still requires a lot of computational resources even with todays computational power (minimum of ten elements per wavelength [81]). For example, a simulation of a vertical point force at the center frequency of 300kHz in a 1 mm thick aluminum plate with dimensions of 150mm×150mm, using hexagonal elements with a length of 0.25mm, requires the use of a Viglen CL2000 computer (having a 32GHz

CPU and a 8GB RAM) [82]. Symmetrical boundary conditions have also been used in this simulation to reduce the model size. Furthermore, special types of element are needed if infinite boundaries are required [83], especially for the modelling of actuators. Infinite boundaries are needed to remove the complexity induced by the wave reflections from the actuator simulations.

These facts have propel many researches to develop other types of numerical methods i.e the finite difference method [84–88], the spectral element method [72, 89–91], the hybrid boundary element (HBE) method [92–95], the wave finite element (WFE) method [96–101] and also the semi-analytical finite element (SAFE) method. It is worth noting that for research purposes, the FEM is still widely used to simulate Lamb wave propagations especially in complex structures and for comparison and verification purposes [102–105]. In general, the Lamb wave simulation problem in plates can be grouped into three main areas [13]; (i) the dispersion curves calculation, (ii) the Lamb wave scattering by damages/obstacles, and (iii) the actuator/sensor coupled system simulation.

2.4.1 Dispersion curves calculations

The Lamb wave dispersion curves show the relationships between wavenumber k and circular frequency ω (or linear frequency f from the equation $\omega = 2\pi f$). Phase velocity c_p is obtained from the wavenumber by applying the relationship $c_p = \omega/k$. For isotropic plates, an analytical expression for calculating the Lamb wave dispersion curves are available. These dispersion curves are obtained from the solution of the Rayleigh-Lamb equation [79] given by

$$\frac{\tan(\beta d)}{\tan(\alpha d)} = -\left[\frac{4k^2\alpha\beta}{(k^2-\beta^2)^2}\right]^{\pm 1} \tag{2.1}$$

with d as the half thickness of the plate. $\alpha^2 = (\omega^2/c_p^2) - k^2$ and $\beta^2 = (\omega^2/c_s^2) - k^2$. c_s denotes the shear wave velocity. The plus sign in (2.1) is for the symmetric mode and the minus sign is for the anti-symmetric mode. The plate curvatures have small effects on the Lamb wave dispersion curves, showing differences only at the very low frequency ranges [106].

There are two approaches to theoretically calculate the dispersion curves for composite plates; exact solution approaches and approximate solution approaches [107]. The exact solutions applying the 3D elasticity theory is solved using the matrix methods [108–110], i.e the transfer matrix method and the global matrix method. These formulations give a matrix description of the layered plates in terms of the stresses and the displacements at the free surface, and in terms of the incoming and the outgoing wave amplitudes. The transfer matrix method has an instability problem at higher frequencies and large thickness values. On the other hand, the global matrix method involves larger matrices and the solution process is relatively slow due to the slow convergence [13]. The global matrix method has been implemented in the software DISPERSE [111]. In a recent development, Green matrix approach has been used to calculate dispersion curves of composite plates [112]. However, this method requires high computational resources at high frequency ranges.

For the approximate solutions, the FEM has been used in obtaining the dispersion curves for general shaped waveguides. In anisotropic composite plates, homogenized material properties are used at each material layer within the plates. The available FEM modelling approaches are:

- **Time domain modelling** In this method, a length of a waveguide is modelled with an appropriate loading. From the obtained displacements, the dispersion curve data of each mode are extracted using the two dimensional Fast Fourier Transform (2D FFT) [113, 114] or the Wavelet transform [115, 116].
- **Mode shape of short waveguides** In this method, a relatively short length of a waveguide is modelled with the nodes at the ends constrained to move only in the plane perpendicular to the length of the waveguide. The mode shapes and resonance frequencies are then calculated. The number of periods along the length of the waveguide enables the calculation of the wavelength and the phase velocity of a guided wave mode [101]. Similar models with different lengths of waveguides are then used to obtain more points in the phase velocity-frequency space [4].
- **Semi-Analytical Finite Element (SAFE) method** In this method, only the cross section of the waveguide is modelled. Thus, reducing the dimensions of the simulation model to one (for plates) or two (for other general waveguides). The elements used have a prescribed displacement of complex exponential functions, that is associated with the wavelength. By applying this element in the equation of motion, an eigenvalue problem is obtained which is solved to give the dispersion curves.
- **Wave Finite Element (WFE) method** This method is based on the periodicity of the plates. Only a periodic section of the plates needs to be modelled using the FEM. From the dynamic stiffness matrix of the FEM model, a transfer matrix is obtained, which relates the forces and the displacements between the periodic boundaries. Applying the complex exponential functions in the displacement and force terms yield an eigenvalue problem which is solved to obtain the dispersion curves [96].

From these FEM approaches, the SAFE method is the most efficient [4]. However, a potential disadvantage of this method is that the necessary elements are not available as standard in commercial FEM packages and need to be developed by the user.

The SAFE method is pioneered by Waas for the calculation of surface waves in layered soils [117] under the name of thin layer method. He used it to create infinite boundaries in the FEM analysis. This method is then used by many researchers for layered soils analysis [118, 119]. For non-soil waveguides, the method was first proposed by Nelson and Dong[120] and Lagasse[121] for isotropic plates. Karunasena et al.[122] then extended the method for composite plates. This method has been used to calculate the wave propagation solutions for beams and other arbitrary shape waveguides [8, 123–128]. It is worth noting that this method is also known in the literatures as the stiffness method [122], higher order displacement based theory [129], strip element method [130] and spectral element method [131]. As the wave propagation is described analytically in the wave

propagation direction, this method is able to handle the high frequency wave propagation easily and is not severely affected by the small element size requirement in the FEM analysis. Apart from the FEM, approximate solutions of the dispersion curves are also obtained using the plate theory for composite plates as shown in [132–135].

The dispersion curves can be obtained experimentally using the amplitude spectrum method [136], the phase spectrum method [137] and the mechanical resonant response method [138, 139]. The 2D FFT method and the Wavelet transform method are also widely applied to obtain the dispersion curves from Lamb wave signals [2, 140–143]. Based on the dispersion curves from the Lamb wave signals, the material properties of an unidirectional composite plate have been obtained by applying an artificial neural network method in [144].

2.4.2 Lamb wave scattering simulations

The hybrid boundary element-normal mode expansion method has been used to study the mode reflection at plate edges [5, 92] and plate surface damages [93–95]. However, this approach is limited to isotropic plates as the plate edges/damages are modelled using the boundary element (BE) method. A combined FEM, modal decomposition and analytical propagation method has been applied to compute the interaction of the Lamb modes with micro-defects in an isotropic plate [145]. A coupled SAFE-FE method is used to obtain the mode participation coefficient for the wave scattering due to vertical plate edge reflections [146], plate edge cracks [147], angled plate edges [148], incline cracks and circular holes in unidirectional laminates [149], and delaminations in composite plates [150]. The coupled WFE-FE method has been used in [99] to simulate notches in isotropic plates. In all these simulations, the accuracy is ensured by checking the fulfilment of the reciprocity conditions and the energy errors between the incoming and the outgoing waves. The main idea of these simulations is to reduce the computational requirements by modelling infinite and undamaged plate regions using the normal-mode expansion/modal decomposition/WFE/SAFE method, and modelling the complex edge/obstacle/damage regions using the BE/FE method.

Another alternative for FEM simulations is the local interaction simulation approach (LISA). This method is based on the finite difference method and has been used to simulate Lamb wave propagations [85] and interactions with damages [86]. However, the computational requirement is still very large [88].

2.4.3 Actuator/sensor coupled system

The response of plates due to a surface load can be solved using an analytical approach as shown in [151]. Based on the 3D linear elasticity, the excitation of circular and rectangular shaped piezoelectric transducers [152] and anisotropic piezoceramic transducers (MFC and AFC) [153] are simulated. The forces from these actuators are assumed to be acting at the perimeter of the actuator (pin-force model). The SAFE method is used for 2D transient response analysis in infinite waveguides and plates [154–157]. For the 3D

transient response analysis, the stationary phase method is used to approximate the 3D force response solutions from the 2D force response solutions in isotropic and in composite plates [82]. In [158], the limitation of the stationary phase method applied in [82] is shown, which it is suitable only for isotropic plates and quasi-isotropic composite plates having a single stationary point. The SAFE method and the stationary phase method have been used to model phased array actuations in quasi-isotropic composite plates by including the directional dependence of the amplitude in the phased array algorithm [75].

2.5 Conclusions

It is clear that the behavior of the Lamb wave propagation needs to be understood first before any meaningful utilizations in the SHM applications either through numerical simulations or by performing experimental investigations are possible. The purpose of this thesis is to investigate the SAFE method for the numerical simulation of the Lamb waves. The SAFE method is chosen as it can be applied to all the three main areas of the Lamb wave simulations [13].

The first step in studying the Lamb waves propagation is to obtain the dispersion curves. This is required as one needs to know what are the available modes in the plates within a certain frequency range, and its relationship to the wave propagation direction. For this purpose, the SAFE method is suitable as it is much simpler and faster than the other methods as well as suitable for both isotropic and composite plates. As shown in the application examples, the effect of the symmetrical and unsymmetrical material arrangements and the in-plane load on the dispersion curves can be studied.

From the obtained dispersion curve data (wavenumbers and displacement profiles), the reflection and transmission behaviors of Lamb waves due to the obstacles are studied by the coupling of the SAFE method with the FEM. The FEM is chosen as it is effective in modelling complex geometries. In literatures, only simple plate edges and obstacles have been considered. Extensions are made here by considering more complex symmetrical and unsymmetrical obstacles. The effect of transducers and stiffeners attached on plates to the Lamb wave reflection and transmission coefficients are also calculated.

In Lamb wave transient response simulations, the solutions of interest are normally limited to certain regions in the plates. By applying the SAFE method, these regions can be selected without the need to model the whole plate. Only the actuator, the obstacle and the sensor regions need to be considered. For obtaining results at these small regions, the SAFE method is faster than the FEM. Furthermore, infinite boundaries are simulated naturally using the SAFE method. Here, the SAFE method is used for the 2D and the 3D force response analysis. From the 2D force response analysis, the mode tuning curves for composite plates are obtained. This enables the phased array actuation concept to be applied in composite plates. For the 3D force response analysis, an approach is presented which enables the point force locations to be shifted from the origin of the plate by considering additional phases in the solutions.

As the SAFE method is based on infinite plates, a special treatment is required for the simulation of plate edges. Here, a novel approach to simulate the effects of plate edge reflections is presented. Plate edge reflections are calculated as superposition of infinite plate solutions acting to the opposite direction of the incidence waves on the plate edges. As application examples, 2D and the 3D force response analyses for the infinite and the finite plates are performed.

Chapter 3

The Semi-Analytical Finite Element Method

3.1 Introduction

In this chapter, the formulation of the semi-analytical finite element (SAFE) method is given. The formulation ends with a construction of an eigenvalue problem. By solving this eigenvalue problem, Lamb wave dispersion relationships (from eigenvalues and eigenvectors) are obtained. Several solution approaches that need to be considered are discussed.

3.2 Theoretical background

Wave propagations in waveguides can be simulated using the finite element method (FEM). In the FEM, the waveguide discretization is made for every dimensions (i.e. length, width and depth/thickness). On the other hand, SAFE method combines the FEM with analytical expressions. Displacement fields in the waveguides cross-section are described using the FEM while displacement fields in the wave propagation direction are analytically described by a complex exponential. Thus, in comparison to the FEM, only the waveguides cross-section needs to be discretized.

Lamb waves are high frequency waves. In order to analyze the Lamb wave propagations with the FEM, small element sizes are required. This leads to a very high number of elements and subsequently high computational costs. However, the SAFE method is not severely affected to this requirement as no discretization is needed in the wave propagation directions. This requirement needs to be fulfilled only for the meshes of the waveguide cross-section.

The SAFE method can also be regarded as a method to obtain normal mode solutions of the plate at each frequency. By applying these normal mode solutions, The SAFE method can be used for force response analysis of waveguides which will be described in

more details in Chapter 6. In the following, the formulation of the SAFE method is given according to [1, 5, 8, 123, 159].

3.2.1 Problem definition

Consider an unloaded waveguide with a cross section as shown in Figure 3.1. Discritization is needed only in the waveguide cross section (here using 2D FE discretization). The wave propagates along x-axis with a wavenumber k and a frequency ω. The plate cross section lies on the y-z plane. The harmonic displacement, strain and stress field in the plate are given by

$$\begin{aligned}
\mathbf{u} &= \begin{bmatrix} u_x & u_y & u_z \end{bmatrix}^T, \\
\boldsymbol{\varepsilon} &= \begin{bmatrix} \varepsilon_x & \varepsilon_y & \varepsilon_z & \varepsilon_{yz} & \varepsilon_{xz} & \varepsilon_{xy} \end{bmatrix}^T, \\
\boldsymbol{\sigma} &= \begin{bmatrix} \sigma_x & \sigma_y & \sigma_z & \sigma_{yz} & \sigma_{xz} & \sigma_{xy} \end{bmatrix}^T.
\end{aligned}$$

Strain can be written in the form

$$\boldsymbol{\varepsilon} = \begin{bmatrix} \partial x & . & . \\ . & \partial y & . \\ . & . & \partial z \\ . & \partial z & \partial y \\ \partial z & . & \partial x \\ \partial y & \partial x & . \end{bmatrix} \mathbf{u} = \left[\mathbf{L}_x \frac{\partial}{\partial x} + \mathbf{L}_y \frac{\partial}{\partial y} + \mathbf{L}_z \frac{\partial}{\partial y} \right] \mathbf{u}$$

where

$$\mathbf{L}_x = \begin{bmatrix} 1 & . & . \\ . & . & . \\ . & . & . \\ . & . & . \\ . & . & 1 \\ . & 1 & . \end{bmatrix}; \quad \mathbf{L}_y = \begin{bmatrix} . & . & . \\ . & 1 & . \\ . & . & . \\ . & . & 1 \\ . & . & . \\ 1 & . & . \end{bmatrix}; \quad \mathbf{L}_z = \begin{bmatrix} . & . & . \\ . & . & . \\ . & . & 1 \\ . & 1 & . \\ 1 & . & . \\ . & . & . \end{bmatrix}.$$

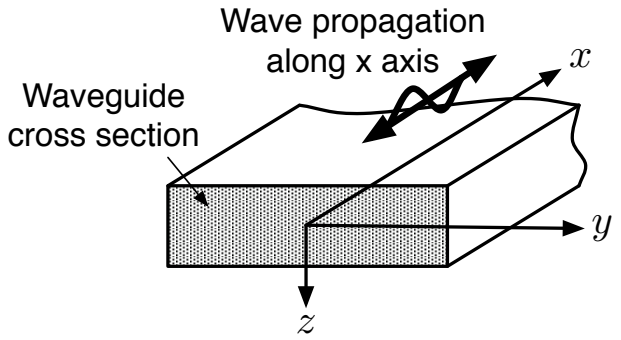

FIGURE 3.1: General waveguide cross section

3.2.2 Equations of motion

Equations of motion for the cross section are formulated by inserting the kinetic and the potential energies into the Hamilton equation. The variation of the Hamiltonian of the waveguide is given by

$$\delta H = \int_{t1}^{t2} \delta(U - T)\mathrm{d}t = 0 \tag{3.1}$$

where U is the strain energy and T is the kinetic energy. The strain energy is given by

$$U = \frac{1}{2}\int_V \boldsymbol{\varepsilon}^T \tilde{\mathbf{C}}\boldsymbol{\varepsilon}\mathrm{d}V.$$

Matrix $\tilde{\mathbf{C}}$ and V are the material stress-strain relationship matrix and the volume, respectively. Superscript T denotes matrix transpose. The kinetic energy is given by

$$T = \frac{1}{2}\int_V \dot{\mathbf{u}}^T \rho\dot{\mathbf{u}}\mathrm{d}V.$$

The vector $\mathbf{u}$ contains the displacements and ρ is the mass density. An upper point denotes derivative with respect to the time variable t. Performing the variation, eq.(3.1) can be written as

$$\int_{t1}^{t2}\left[\int_V \delta\left(\boldsymbol{\varepsilon}^T\right)\tilde{\mathbf{C}}\boldsymbol{\varepsilon}\mathrm{d}V + \int_V \delta\left(\mathbf{u}^T\right)\rho\ddot{\mathbf{u}}\mathrm{d}V\right]\mathrm{d}t = 0. \tag{3.2}$$

The displacement field is assumed to be harmonic along the x direction, and spatial functions are used to describe its amplitude in the cross sectional plane y-z; thus

$$\mathbf{u}(x,y,z,t) = \begin{bmatrix} u_x(x,y,z) \\ u_y(x,y,z) \\ u_z(x,y,z) \end{bmatrix} = \begin{bmatrix} u_x(y,z) \\ u_y(y,z) \\ u_z(y,z) \end{bmatrix} \exp^{-i(kx-\omega t)}. \tag{3.3}$$

Symbols k, ω, t and $i = \sqrt{-1}$ represent the wavenumber, circular frequency, time and imaginary unit, respectively.

It is worth noting that the exponential function $e^{-i(kx-wt)}$ in equation (3.3) can be replaced by the exponential function $e^{i(kx-wt)}$ as found is some literatures for example in [8]. For the same values of k, ω and t, both exponential functions are mathematically equal.

3.2.3 Finite element method

As stated before, the displacements are assumed to be harmonic along the wave propagation direction, x. Spatial functions are used to describe the wave amplitude in z. Therefore, the element displacements can be written as;

$$\mathbf{u}_e(x,y,z,t) = \begin{bmatrix} u_x(y,z) \\ u_y(y,z) \\ u_z(y,z) \end{bmatrix}_e \exp^{-i(kx-\omega t)} = \mathbf{N}(y,z)\mathbf{q}_e \exp^{-i(kx-\omega t)} \tag{3.4}$$

where $\mathbf{N}(y,z)$ is the matrix of shape function and the waveguide cross section is in y-z plane. This matrix and the nodal displacements are given by

$$\mathbf{N}(y,z) = \begin{bmatrix} N_1 & & N_2 & & \ddots & & N_n & \\ & N_1 & & N_2 & & \ddots & & N_n \\ & & N_1 & & N_2 & & \ddots & & N_n \end{bmatrix} \tag{3.5}$$

and

$$\mathbf{q}_e = \begin{bmatrix} u_{x1} & u_{y1} & u_{z1} & u_{x2} & u_{y2} & u_{z2} & \dots & \dots & \dots & u_{xn} & u_{yn} & u_{zn} \end{bmatrix}^T, \tag{3.6}$$

respectively. The number of nodes per element is denoted by n. The strain vector in the element is then written in terms of nodal displacements as;

$$\begin{aligned} \boldsymbol{\varepsilon}_e &= \left[\mathbf{L}_x\frac{\partial}{\partial x} + \mathbf{L}_y\frac{\partial}{\partial y} + \mathbf{L}_z\frac{\partial}{\partial z}\right]\mathbf{N}(y,z)\mathbf{q}_e \exp^{-i(kx-\omega t)} \\ &= \left(\mathbf{B}_1 - ik\mathbf{B}_2\right)\mathbf{q}_e \exp^{-i(kx-\omega t)} \end{aligned} \tag{3.7}$$

where $\mathbf{B}_1 = \mathbf{L}_y\mathbf{N}_{,y} + \mathbf{L}_z\mathbf{N}_{,z}$ and $\mathbf{B}_2 = \mathbf{L}_x\mathbf{N}$ with $\mathbf{N}_{,y}$ and $\mathbf{N}_{,z}$ as the derivatives of the shape functions with respect to the y and z axis, respectively. The discrete form of the Hamilton formulation in eq.(3.2) becomes

$$\int_{t1}^{t2}\left\{\bigcup_{e=1}^{n_{el}}\left[\int_{V_e}\delta\varepsilon_e^T\tilde{\mathbf{C}}_e\varepsilon_e \mathrm{d}V_e + \int_{V_e}\delta\mathbf{u}_e^T\rho_e\ddot{\mathbf{u}}_e \mathrm{d}V_e\right]\right\}\mathrm{d}t = 0 \tag{3.8}$$

where $\tilde{\mathbf{C}}_e$, ρ_e and n_{el} are the element stress-strain relationship matrix, the element mass density and the number of elements, respectively. For laminated or layered material structures, each material layer needs to be modeled by at least one element. Thus, the element stress-strain relationship matrix $(\tilde{\mathbf{C}}_e)_L$ needs to be converted from the local coordinates $x_L - y_L - z_L$ to the global coordinates $x - y - z$. Taking the z-axis to be the same for both references, the following transformation is applied [131]

$$\tilde{\mathbf{C}}_e = \mathbf{T}(\theta)^{-1}(\tilde{\mathbf{C}}_e)_L\mathbf{R}\mathbf{T}(\theta)\mathbf{R}^{-1} \tag{3.9}$$

with θ as the angle between the $x - y$ axis and the $x_L - y_L$ shown in Figure 3.2. The tensoral rotation matrix $\mathbf{T}(\theta)$ adapted to the Voigt form is given as

$$\mathbf{T}(\theta) = \begin{bmatrix} \cos^2(\theta) & \sin^2(\theta) & 0 & 0 & 0 & 2\sin(\theta)\cos(\theta) \\ \sin^2(\theta) & \cos^2(\theta) & 0 & 0 & 0 & -2\sin(\theta)\cos(\theta) \\ 0 & 0 & 1 & 0 & 0 & 0 \\ 0 & 0 & 0 & \cos(\theta) & -\sin(\theta) & 0 \\ 0 & 0 & 0 & \sin(\theta) & \cos(\theta) & 0 \\ -\sin(\theta)\cos(\theta) & \sin(\theta)\cos(\theta) & 0 & 0 & 0 & \cos^2(\theta) - \sin^2(\theta) \end{bmatrix} \tag{3.10}$$

while the coefficient matrix $\mathbf{R}$ due to engineering strain terms is given as

$$\mathbf{R} = \begin{bmatrix} 1 & 0 & 0 & 0 & 0 & 0 \\ 0 & 1 & 0 & 0 & 0 & 0 \\ 0 & 0 & 1 & 0 & 0 & 0 \\ 0 & 0 & 0 & 2 & 0 & 0 \\ 0 & 0 & 0 & 0 & 2 & 0 \\ 0 & 0 & 0 & 0 & 0 & 2 \end{bmatrix}. \tag{3.11}$$

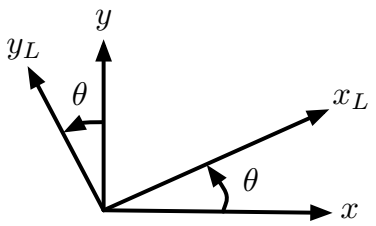

FIGURE 3.2: Reference transformation between local reference $x_L - y_L$ and global reference $x - y$.

Substituting the strain terms in eq.(3.7) to eq.(3.8) yields

$$\begin{aligned}
&\int_{V_e} \delta\left(\varepsilon_e^T\right) \tilde{\mathbf{C}}_e \varepsilon_e \mathrm{d}V_e \\
&\quad = \int_{\Omega_e}\int_x \delta\left(\varepsilon_e^T\right) \tilde{\mathbf{C}}_e \varepsilon_e \mathrm{d}x\mathrm{d}\Omega_e \\
&\quad = \int_{\Omega_e}\int_x \delta\left(\mathbf{q}_e^T(\mathbf{B}_1^T + ik\mathbf{B}_2^T)[e^{-i(kx-\omega t)}]^*\right) \tilde{\mathbf{C}}_e \left((\mathbf{B}_1 - ik\mathbf{B}_2)\mathbf{q}_e[e^{-i(kx-\omega t)}]\right) \mathrm{d}x\mathrm{d}\Omega_e \\
&\quad = x\delta\mathbf{q}_e^T \int_{\Omega_e} \left[\mathbf{B}_1^T\tilde{\mathbf{C}}_e\mathbf{B}_1 + ik\mathbf{B}_2^T\tilde{\mathbf{C}}_e\mathbf{B}_1 - ik\mathbf{B}_1^T\tilde{\mathbf{C}}_e\mathbf{B}_2 + k^2\mathbf{B}_2^T\tilde{\mathbf{C}}_e\mathbf{B}_2\right] \mathrm{d}\Omega_e\mathbf{q}_e.
\end{aligned} \tag{3.12}$$

Superscript $*$ indicates complex conjugate. The element kinetic energy contribution in eq.(3.8) is obtained by substituting for the displacement expression from eq.(3.4), giving

$$\begin{aligned}
&\int_{V_e} \delta\left(\mathbf{u}_e^T\right)\rho_e\ddot{\mathbf{u}}_e \mathrm{d}V_e \\
&\qquad = \int_{\Omega_e}\int_x \delta\left(\mathbf{u}_e^T\right) \rho_e\ddot{\mathbf{u}}_e \mathrm{d}x\mathrm{d}\Omega_e \\
&\qquad = \int_{\Omega_e}\int_x \delta\left(\mathbf{q}_e^T\mathbf{N}^T[e^{-i(kx-\omega t)}]^*\right) \rho_e(-\omega^2)\mathbf{N}\mathbf{q}_e[e^{-i(kx-\omega t)}]\mathrm{d}x\mathrm{d}\Omega_e \\
&\qquad = -\omega^2 x\delta\mathbf{q}_e^T \int_{\Omega_e} \mathbf{N}^T\rho_e\mathbf{N}\mathrm{d}\Omega_e\mathbf{q}_e.
\end{aligned} \tag{3.13}$$

Substituting eq.(3.12) and eq.(3.13) into eq.(3.8) gives

$$\int_{t1}^{t2} \left\{ \bigcup_{e=1}^{n_{el}} x\delta \mathbf{q}_e^T \left[\mathbf{k}_1^{(e)} + ik\mathbf{k}_2^{(e)} + k^2\mathbf{k}_3^{(e)} - \omega^2 \mathbf{m}^{(e)} \right] \mathbf{q}_e \right\} \mathrm{d}t = 0$$

where

$$\mathbf{k}_1^{(e)} = \int_{\Omega_e} [\mathbf{B}_1^T \tilde{\mathbf{C}}_e \mathbf{B}_1] \mathrm{d}\Omega_e \tag{3.14}$$

$$\mathbf{k}_2^{(e)} = \mathbf{k}_{21}^{(e)} - \mathbf{k}_{12}^{(e)} = \int_{\Omega_e} \mathbf{B}_2^T \tilde{\mathbf{C}}_e \mathbf{B}_1 \mathrm{d}\Omega_e - \int_{\Omega_e} \mathbf{B}_1^T \tilde{\mathbf{C}}_e \mathbf{B}_2 \mathrm{d}\Omega_e = (\mathbf{k}_{12}^{(e)})^T - \mathbf{k}_{12}^{(e)} \tag{3.15}$$

$$\mathbf{k}_3^{(e)} = \int_{\Omega_e} [\mathbf{B}_2^T \tilde{\mathbf{C}}_e \mathbf{B}_2] \mathrm{d}\Omega_e \tag{3.16}$$

$$\mathbf{m}^{(e)} = \int_{\Omega_e} [\mathbf{N}^T \rho_e \mathbf{N}] \mathrm{d}\Omega_e. \tag{3.17}$$

It is worth noting that if exponential function $e^{i(kx-wt)}$ is used, due to the sign of imaginary value i, the matrix $\mathbf{k}_2^{(e)}$ in equation (3.15) becomes

$$\mathbf{k}_2^{(e)} = \mathbf{k}_{12}^{(e)} - \mathbf{k}_{21}^{(e)} = \mathbf{k}_{12}^{(e)} - (\mathbf{k}_{12}^{(e)})^T. \tag{3.18}$$

By applying finite element assembling procedure to each element in the plate thickness yields;

$$\int_{t1}^{t2} \{x\delta \mathbf{U}^T \left[\mathbf{K}_1 + ik\mathbf{K}_2 + k^2\mathbf{K}_3 - \omega^2 \mathbf{M} \right] \mathbf{U}\} \mathrm{d}t = 0$$

where $\mathbf{U}$ is the global vector of unknown nodal displacement and global matrices are given by

$$\mathbf{K}_1 = \bigcup_{e=1}^{n_{el}} \mathbf{k}_1^{(e)} \qquad \mathbf{K}_2 = \bigcup_{e=1}^{n_{el}} \mathbf{k}_2^{(e)} \qquad \mathbf{K}_3 = \bigcup_{e=1}^{n_{el}} \mathbf{k}_3^{(e)} \qquad \mathbf{M} = \bigcup_{e=1}^{n_{el}} \mathbf{m}^{(e)}.$$

Value of $x\delta\mathbf{U}$ is arbitary, thus finally the SAFE eigenvalue equation is obtained as

$$\left[\mathbf{K}_1 + ik\mathbf{K}_2 + k^2\mathbf{K}_3 - \omega^2 \mathbf{M} \right] \mathbf{U} = 0. \tag{3.19}$$

3.3 Formulation for plate analysis

For a waveguide, such as an infinitely wide plate in the $\pm y$ axis direction as shown in Figure 3.3(a), the element displacement has no dependence on the y axis. Hence, the plate can be modelled using 1D finite elements. Here, the plate thickness is descretized using 1D three node elements with three degrees of freedom per node (Figure 3.3(b)). The nodes in each element are designated with number 1, 2 and 3. Therefore, by taking $n = 3$ in equations (3.5) and (3.6), the matrix of the shape functions and the vector of the element nodal displacements are obtained.

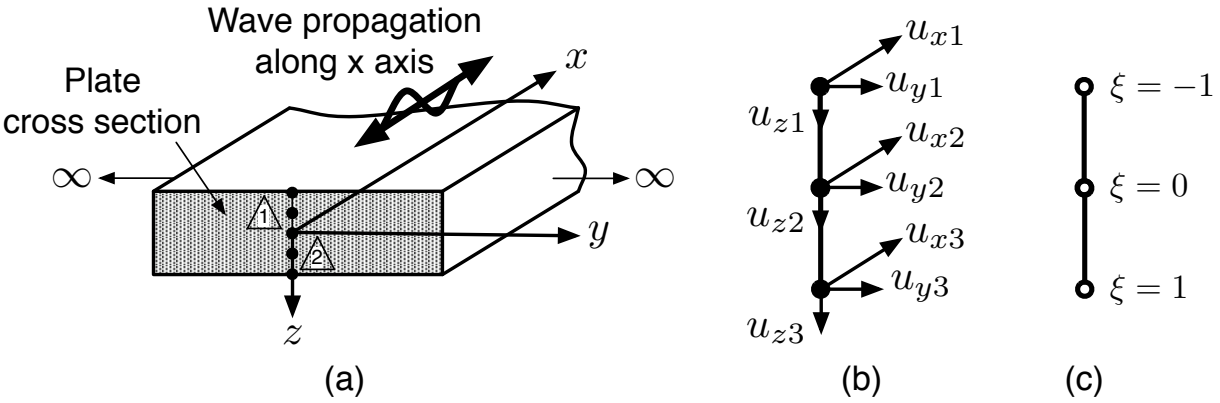

FIGURE 3.3: (a) Infinitely wide plate cross section (shown with two 1D elements along the plate thickness), (b) Degrees of freedom for a 1D three nodes element, (c) 1D three nodes isoparametric element.

As the plate is infinite in the y direction, the plane strain condition is used with $\mathbf{N}_{,y} = 0$. Hence, the element strain vector is obtained as

$$\boldsymbol{\varepsilon}_e = \left[\mathbf{L}_x \frac{\partial}{\partial x} + \mathbf{L}_z \frac{\partial}{\partial z}\right] \mathbf{N}(z)\mathbf{q}_e \exp^{-i(kx-\omega t)} = (\mathbf{B}_1 - ik\mathbf{B}_2)\,\mathbf{q}_e \exp^{-i(kx-\omega t)},$$

with $\mathbf{B}_1 = \mathbf{L}_z\mathbf{N}_{,z}$ and $\mathbf{B}_2 = \mathbf{L}_x\mathbf{N}$. In the plane strain analysis, the domain of integration reduced from $\mathrm{d}\Omega_e$ to $\mathrm{d}z$.

The integrals given in equations (3.14),(3.15),(3.16) and (3.17) are solved numerically using Gaussian quadrature with three sampling points. The integration limits need to be changed to -1 to +1. Thus, all the 1D elements are mapped to an isoparametric element as shown in Figure 3.3(c). The parameters $\xi = -1$, $\xi = 0$ and $\xi = 1$ are for the nodes 1, 2 and 3, respectively. Details on 1D isoparametric finite element can be found in [160]. The shape function can be written with the normalized coordinate ξ as

$$N_1(\xi) = \tfrac{1}{2}(\xi^2 - \xi), \qquad N_2(\xi) = (1 - \xi^2), \qquad N_3(\xi) = \tfrac{1}{2}(\xi^2 + \xi)\ .$$

The Jacobian function $\mathbf{J}$ is given by;

$$\mathbf{J} = \frac{\mathrm{d}z}{\mathrm{d}\xi} = \begin{bmatrix}\xi - \frac{1}{2} & -2\xi & \xi + \frac{1}{2}\end{bmatrix} \begin{bmatrix} u_{z1} \\ u_{z2} \\ u_{z3} \end{bmatrix}.$$

The derivative of the shape function in z direction $\mathbf{N}_{,z}$ is obtained as;

$$\mathbf{N}_{,z} = \frac{\mathrm{d}\xi}{\mathrm{d}z}\mathbf{N}_{,\xi} = \frac{1}{\mathbf{J}}\mathbf{N}_{,\xi}.$$

Therefore, the integration in equations (3.14),(3.15),(3.16) and (3.17) are calculated as

$$\Upsilon = \sum_{i=1}^{n_{\text{quad}}} \mathbf{W}_i \cdot \Xi^T \cdot \mathbf{C} \cdot \Xi \cdot \mathbf{J} \tag{3.20}$$

where n_{quad} and $\mathbf{W}_i$ are the number of sampling points and the weight of the Gaussian quadrature respectively. Matrix Υ represents element matrices $\mathbf{k}_1^{(e)}$, $\mathbf{k}_{12}^{(e)}$, $\mathbf{k}_{21}^{(e)}$, $\mathbf{k}_3^{(e)}$ or $\mathbf{m}^{(e)}$. Matrix Ξ can be replaced by either matrices $\mathbf{B}_1(\xi)$, $\mathbf{B}_2(\xi)$ or $\mathbf{N}(\xi)$. The variable ξ takes the values of the sampling points. Matrix $\mathbf{C}$ represents either the element material relationship matrix $\tilde{\mathbf{C}}_e$ or the element mass density ρ_e. After calculating the element matrices, the remaining procedures to construct equation (3.19) are the same as described in section 3.2.

3.4 Solution approaches

3.4.1 Symmetric matrices

From equation (3.19), the global matrices $\mathbf{K}_1$, $\mathbf{K}_3$ and $\mathbf{M}$ are symmetric. However, the global matrix $\mathbf{K}_2$ is skew symmetric. In order to have a better equation for numerical computation, $\mathbf{K}_2$ is changed into a symmetric form by pre-multiplying and post-multiplying equation (3.19) with transformation matrix $\mathbf{T}^T$ and $\mathbf{T}$ respectively. Matrix $\mathbf{T}$ has the properties $\mathbf{T}^T = \mathbf{T}^*$ and $\mathbf{T}^*\mathbf{T} = \mathbf{T}\mathbf{T}^* = \mathbf{I}$. The elements of $\mathbf{T}$ corresponding to u_y and u_z have the value 1 while those corresponding to u_x are equal to the imiginary unit. This multipication changes only $\mathbf{K}_2$ as the other matrices do not mix u_x with u_y and u_z [8]. Thus;

$$\mathbf{T}^T\mathbf{K}_1\mathbf{T} = \mathbf{K}_1; \quad \mathbf{T}^T\mathbf{K}_3\mathbf{T} = \mathbf{K}_3; \quad \mathbf{T}^T\mathbf{M}\mathbf{T} = \mathbf{M}. \tag{3.21}$$

The matrix $\mathbf{K}_2$ instead, mixes u_x with u_y and u_z but it does not mix u_y and u_z with each other. It follows that,

$$\mathbf{T}^T\mathbf{K}_2\mathbf{T} = -i\hat{\mathbf{K}}_2; \quad \hat{\mathbf{U}} = \mathbf{T}^T\mathbf{U}, \tag{3.22}$$

where $\hat{\mathbf{K}}_2$ and $\hat{\mathbf{U}}$ are the symmetrized $\mathbf{K}_2$ matrix and the new eigenvector, respectively. Thus, the symmetric SAFE eigenvalue equation is given as

$$\left[\mathbf{K}_1 + k\hat{\mathbf{K}}_2 + k^2\mathbf{K}_3 - \omega^2\mathbf{M}\right]\hat{\mathbf{U}} = 0. \tag{3.23}$$

3.4.2 Variable fixation and reformulation of equation

Equation (3.23) has two variables, the wavenumber k and the circular frequency ω. Thus, this equation can be solved by using two approaches:

(a) by first fixing the frequency, ω and solving for the wavenumber k, or

(b) by first fixing the wavenumber, k and solving for the frequency ω.

In approach (a), by taking $\mathbf{Q} = \begin{bmatrix} \hat{\mathbf{U}} \\ k\hat{\mathbf{U}} \end{bmatrix}$, equation (3.23) is changed into a linear form as

$$(\mathbf{A} - k\mathbf{B})\mathbf{Q} = 0. \tag{3.24}$$

Matrices $\mathbf{A}$ and $\mathbf{B}$ are given by

$$\mathbf{A} = \begin{bmatrix} . & \mathbf{K}_1 - \omega^2\mathbf{M} \\ \mathbf{K}_1 - \omega^2\mathbf{M} & \hat{\mathbf{K}}_2 \end{bmatrix}; \quad \mathbf{B} = \begin{bmatrix} \mathbf{K}_1 - \omega^2\mathbf{M} & . \\ . & -\mathbf{K}_3 \end{bmatrix}$$

or alternatively [155]

$$\mathbf{A} = \begin{bmatrix} \mathbf{K}_1 - \omega^2\mathbf{M} & . \\ . & -\mathbf{K}_3 \end{bmatrix}; \quad \mathbf{B} = -\begin{bmatrix} \hat{\mathbf{K}}_2 & \mathbf{K}_3 \\ \mathbf{K}_3 & . \end{bmatrix}.$$

On the other hand in approach (b), equation (3.23) is simplified as

$$\left[\mathbf{K}(k) - \omega^2\mathbf{M}\right]\hat{\mathbf{U}} = 0, \tag{3.25}$$

with $\mathbf{K}(k) = \mathbf{K}_1 + k\hat{\mathbf{K}}_2 + k^2\mathbf{K}_3$. In the approach (a), the Lamb mode wavenumbers can be calculated for required frequency values. However, the wavenumber k obtained would include real, pure imaginary and complex values. The real values of k represent the propagating modes while the imaginary and complex k represent the evanescent modes. In certain composite plate configurations, obtained wavenumbers can be all complex due to the numerical computation, with small imaginary values for the propagating waves. Thus, for some layer orientations and composite material properties, it is difficult to identify which of these modes are really the propagating modes. In the approach (b) however, the propagating modes can be considered exclusively by taking initially k as positive real numbers. Nevertheless, this approach is not so effective if one is interested in the dispersion curves within certain frequency range with only a couple of the modes involved. By fixing the k values and searching for the values of ω, N_{dof} number of propagating modes are obtained simultaneously. Furthermore, if the material attenuation is considered, then only the linear equation (3.24) is suitable ([8]). Equation (3.25) can be solved roughly 100 times faster than equation (3.24) [125]. This is due to the bigger problem size in equation (3.24). The eigenvector of this equation, $\mathbf{Q}$ is twice the size of the original eigenvector $\hat{\mathbf{U}}$.

We can also take advantage of the wave propagation behavior of the materials in solving equation (3.23). In isotropic plates, Lamb modes and shear horizontal (SH) modes are decoupled. Equation (3.23) is rewritten in the form of

$$\left[k^2\mathbf{A} + k\mathbf{B} + \mathbf{C}\right]\hat{\mathbf{U}} = 0 \tag{3.26}$$

with $\mathbf{A} = \mathbf{K}_3$, $\mathbf{B} = \hat{\mathbf{K}}_2$ and $\mathbf{C} = \mathbf{K}_1 - \omega^2\mathbf{M}$. Arranging equation (3.26) in terms of degrees of freedom [118, 119] yields;

$$\begin{bmatrix} k^2\mathbf{A}_x + \mathbf{C}_x & k\mathbf{B}_{xz} & . \\ k\mathbf{B}_{xz}^T & k^2\mathbf{A}_z + \mathbf{C}_z & . \\ . & . & k^2\mathbf{A}_y + \mathbf{C}_y \end{bmatrix} \begin{bmatrix} \hat{\mathbf{U}}_x \\ \hat{\mathbf{U}}_z \\ \hat{\mathbf{U}}_y \end{bmatrix} = \begin{bmatrix} 0 \\ 0 \\ 0 \end{bmatrix}. \tag{3.27}$$

For wave propagation direction along the x-axis, the displacements in the x and z direction ($\hat{\mathbf{U}}_x$ and $\hat{\mathbf{U}}_z$) correspond to Lamb modes, while the displacements in the y direction ($\hat{\mathbf{U}}_y$) correspond to SH modes. By separating the modes involved in equation (3.27), smaller

eigenvalue problems are obtained. Lamb mode solutions and SH mode solutions can be obtained separately. By considering only the Lamb modes, the size of the eigenvalue problem in equation (3.23) is reduced from $(6n_{el}+3)$ to $(4n_{el}+2)$ in equation (3.28) as

$$(\bar{\mathbf{A}}\mathbf{K}+\bar{\mathbf{C}})\mathbf{Z}=0 \tag{3.28}$$

where

$$\bar{\mathbf{A}}=\begin{bmatrix}\mathbf{A}_x & . \\ \mathbf{B}_{xz}^T & \mathbf{A}_z\end{bmatrix};\quad \bar{\mathbf{C}}=\begin{bmatrix}\mathbf{C}_x & \mathbf{B}_{xz} \\ . & \mathbf{C}_z\end{bmatrix};\quad \mathbf{K}=\text{diag}\left[k^2\right];\quad \mathbf{Z}=\begin{bmatrix}\hat{\mathbf{U}}_x \\ k\hat{\mathbf{U}}_z\end{bmatrix}.$$

Another form of this equation is obtained by transposing (3.28) giving;

$$\mathbf{Y}^T(\bar{\mathbf{A}}^T\mathbf{K}+\bar{\mathbf{C}}^T)=0 \tag{3.29}$$

with $\mathbf{Y}=\begin{bmatrix}k\hat{\mathbf{U}}_x \\ \hat{\mathbf{U}}_z\end{bmatrix}$ as the left eigenvector.

The wavenumber k can also be presented in terms of its component in x and y where $k_x=k\cos\theta$ and $k_y=k\sin\theta$. Angle θ represents the wave propagation angle with respect to the x axis in the x-y plane. Instead of having four matrices that need to be calculated ($\mathbf{K}_1,\mathbf{K}_2,\mathbf{K}_3$ and $\mathbf{M}$) there will be seven matrices by using this approach [130]. In this approach, the variation of plate material properties to the wave propagation angle is directly included in the formulation itself.

3.4.3 Separating symmetric and anti-symmetric Lamb modes

For isotropic and composite plates having symmetrical material properties with respect to the plate center plane (x-y plane at $z=0$ in Figure 3.3), the symmetric and anti-symmetric modes can be separated and calculated individually. This is done by modelling only half of the plate thickness and applying the following boundary conditions at the nodes on the plate center plane [122].

- Displacement $u_z=0$, stresses $\sigma_{zx}=0$ and $\sigma_{yz}=0$ for symmetric modes.
- Displacements $u_x=0$ and $u_y=0$, and stress $\sigma_{zz}=0$ for anti-symmetric modes.

If the whole plate is modelled, the symmetric (S) and the anti-symmetric modes (A) are differentiated by checking the displacement components obtained from the eigenvectors as shown in Figure 3.4. To illustrate how the mode is separated, the displacements of two points, (1) and (2) with distance $h_{(1)}=h_{(2)}$ from the plate center plane are compared for different modes. The relationship between the displacements and mode types are given in Table 3.1. Pure Lamb and SH modes exist in isotropic plates and certain configuration and direction of composite plates where Lamb and SH modes are decoupled, i.e wave propagation at 0° angle in an unidirectional composite plate with 0° fiber direction (see Figure 3.4(a)). In general composite plates at wave propagation angle θ coupled Lamb-SH modes exist (see Figure 3.4(b)). These coupled modes can be differentiated only as symmetric and anti-symmetric modes. It must be noted due to the

numerical computation, exact zero values as given in Table 3.1 are not obtained. Hence from the trials made, tolerance value of 1×10^{-7} is considered small enough to differentiate the modes.

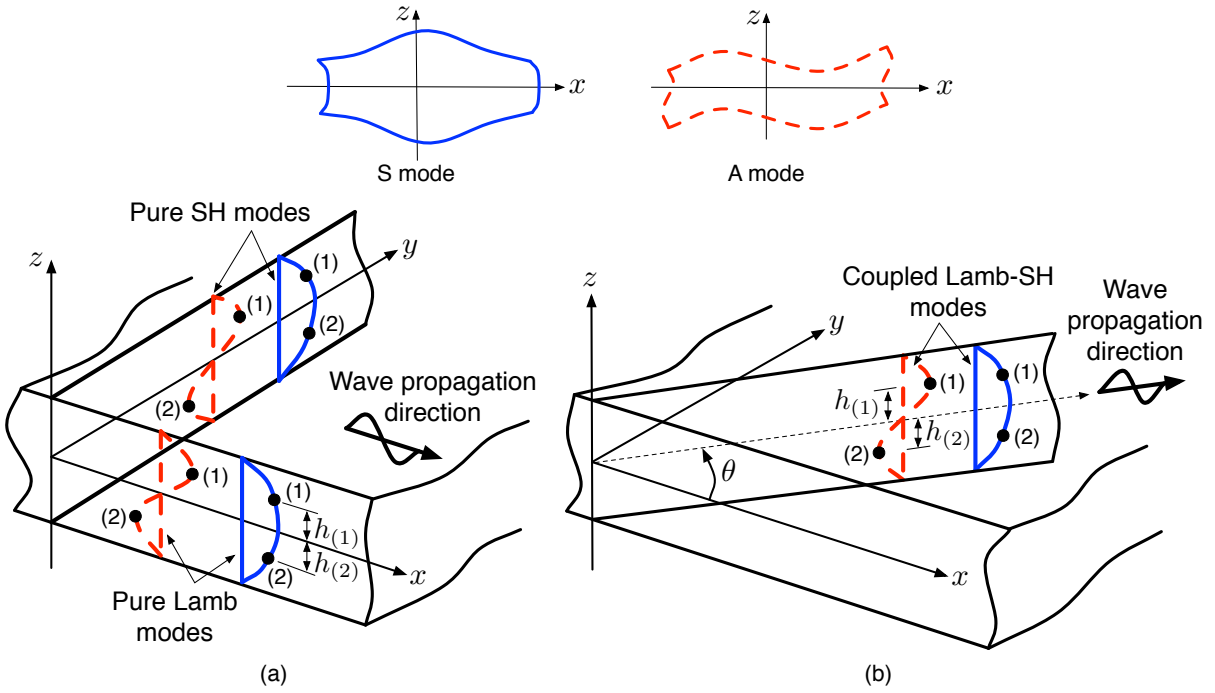

FIGURE 3.4: (a) Mode shapes for pure Lamb modes and pure SH modes, and (b) Mode shapes for coupled Lamb-SH modes. Straight lines are for the S modes and dotted lines are for the A modes.

TABLE 3.1: Relation between eigenvector displacements and mode types.

Pure Lamb modes		Pure SH modes		Lamb-SH modes	
S mode	A mode	S mode	A mode	S mode	A mode
$x_{(1)} = x_{(2)}$	$x_{(1)} = -x_{(2)}$	$x_{(1)} = x_{(2)} = 0$	$x_{(1)} = x_{(2)} = 0$	$x_{(1)} = x_{(2)}$	$x_{(1)} = -x_{(2)}$
$y_{(1)} = y_{(2)} = 0$	$y_{(1)} = y_{(2)} = 0$	$y_{(1)} = y_{(2)}$	$y_{(1)} = -y_{(2)}$	$y_{(1)} = y_{(2)}$	$y_{(1)} = -y_{(2)}$
$z_{(1)} = -z_{(2)}$	$z_{(1)} = z_{(2)}$	$z_{(1)} = z_{(2)} = 0$	$z_{(1)} = z_{(2)} = 0$	$z_{(1)} = -z_{(2)}$	$z_{(1)} = z_{(2)}$

The two approaches before are suitable only when the plates have symmetrical material properties with respect to the plate center plane. For general plates with unsymmetrical material properties, the orthogonality relationships of the eigenvectors is applied to differentiate the modes [155]. For example, from equation (3.24), the **B**-orthogonality relationships of eigenvectors are given as

$$\mathbf{Q}_a^T(\omega)\mathbf{B}\mathbf{Q}_b(\omega) = 0 \qquad \text{and} \qquad \mathbf{Q}_a^T(\omega)\mathbf{B}\mathbf{Q}_a(\omega) \neq 0. \tag{3.30}$$

The **B**-orthogonality of real eigenvectors at frequency step n to $n+1$ is computed as

$$\Theta = \mathbf{Q}_a^T(\omega_n)\mathbf{B}\mathbf{Q}_b(\omega_{n+1}). \tag{3.31}$$

From the relationships in (3.30), value of Θ is the largest when the eigenvectors are from the same mode, where $a = b$. Thus, by using this information, the obtained modes are separated.

The last option is the most robust as it can be applied even to anisotropic materials and unsymmetrical plates. However, it is more suitable for equation (3.25) (approach (b)) in comparison to equation (3.24) (approach (a)). In approach (b), for each real value of wavenumber k, a total of N_{dof} modes are obtained simultaneously. This makes mode numbering easier. N_{dof} is the number of total degrees of freedoms within the plate thickness. However in approach (a), for each value of circular frequency ω, only certain number of modes are obtained. Furthermore, there are also backward propagating modes (modes with negative group velocity), which have two solutions at a particular value of ω. These make the mode numbering in approach (a) more complicated.

Chapter 4

Lamb wave dispersion curves

4.1 Introduction

This chapter begins with an explanation on how group velocity curves are calculated in SAFE. Some verification results on the dispersion curve calculations are given next. Effects of varying the material properties along the plate thickness direction are presented for plates having layers of different isotropic materials. Skew angle calculations are made for an unidirectional composite plate. This chapter ends with the effect of in-plane load on the dispersion curves of isotropic plates.

4.2 Phase and group velocity curves

By solving the eigenvalue problem outlined in the previous chapter, the phase velocity curves can be obtained and plotted from the relationship $c_p = \frac{\omega}{k}$. The wavenumber k is obtained from the eigenvalue results. The group velocity, which is the velocity of a group of waves with a similar frequency (wave packet) is given by the equation $c_g = \frac{d\omega}{d\vec{k}}$ with $\vec{k}$ as the wave propagation direction. For guided wave propagating in x direction, the wave vector is $\vec{k} = k\vec{x}$, where $\vec{x}$ is the unit vector in the x direction. The group velocity is given by

$$c_g = \frac{d\omega}{d\vec{k}} = \frac{d\omega}{d(\frac{\omega}{c_p})} = \frac{c_p^2}{c_p - \omega\frac{dc_p}{d\omega}} = \frac{c_p^2}{c_p - f\frac{dc_p}{df}}.$$

In this formulation, the phase velocity curves need to be differentiated in order to obtain the group velocity curves. However in the SAFE method, the group velocity curves can be calculated directly from the results of the SAFE method [125]. The eigenvalue problem in eq.(3.25) can be rewritten as;

$$\hat{\mathbf{U}}^{(L)^T}\left[\mathbf{K}(k) - \omega^2\mathbf{M}\right] = 0, \tag{4.1}$$

where $\hat{\mathbf{U}}^{(L)}$ is the left eigenvector. The left eigenvector is the complex conjugate of the right eigenvector, thus;

$$\hat{\mathbf{U}}^{(L)} = \hat{\mathbf{U}}^{*},$$

where superscript $*$ represent complex conjugate and $\mathbf{K}(k) = \mathbf{K}_1 + k\hat{\mathbf{K}}_2 + k^2\mathbf{K}_3$. The matrix $\mathbf{K}(k)$ is Hermitian and the mass matrix $\mathbf{M}$ is real and symmetric for real values of k (propagating modes). The derivative of eq.(3.25) is then evaluated with respect to the wavenumber as

$$\frac{\partial}{\partial k}\{\left[\mathbf{K}(k) - \omega^2\mathbf{M}\right]\hat{\mathbf{U}}\} = \left[\frac{\partial \mathbf{K}(k)}{\partial k} - 2\omega\frac{\partial \omega}{\partial k}\mathbf{M}\right]\hat{\mathbf{U}} + \left[\mathbf{K}(k) - \omega^2\mathbf{M}\right]\frac{\partial \hat{\mathbf{U}}}{\partial k} = 0.$$

By premultipliying with the left eigenvector and using the relationship in eq.(4.1), the equation above becomes

$$\hat{\mathbf{U}}^{(L)^T}\left[\frac{\partial \mathbf{K}(k)}{\partial k} - 2\omega\frac{\partial \omega}{\partial k}\mathbf{M}\right]\hat{\mathbf{U}} = 0.$$

Knowning that $\frac{d\omega}{dk}$ is a scalar, the group velocity c_g is then written as

$$c_g = \frac{d\omega}{dk} = \frac{\hat{\mathbf{U}}^{(L)^T}\mathbf{K}'\hat{\mathbf{U}}}{2\omega\hat{\mathbf{U}}^{(L)^T}\mathbf{M}\hat{\mathbf{U}}}, \tag{4.2}$$

where $\mathbf{K}' = \frac{\partial \mathbf{K}(k)}{\partial k} = 2k\mathbf{K}_3 + \hat{\mathbf{K}}_2$.

For isotropic materials, directions of the phase velocity is equal to the group velocity. However, for general anisotropic composite plates, it is not the case. The relationship between slowness curve (inverse of the phase velocity curve) and wave energy direction (equal to the group velocity direction) is shown in Figure 4.1. The wave energy direction is normal to the slowness curve. The angle difference between the wave propagation direction $\vec{k}_\theta$ and the wave energy direction $\vec{\mathbf{V}}^e$ is denoted as skew angle ψ.

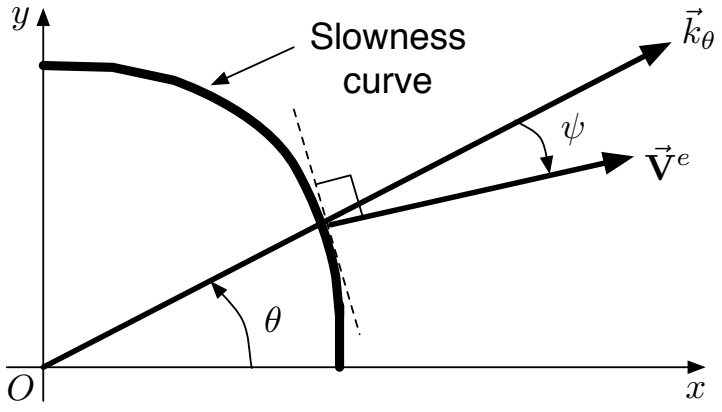

FIGURE 4.1: Skew angle ψ: angle between wave propagation direction $\vec{k}_\theta$ and wave energy direction $\vec{\mathbf{V}}^e$.

4.3 Dispersion curves verifications

Lamb wave dispersion curves for an aluminum plate with the Young's modulus of 70GPa, the Poisson's ratio of 0.33 and the density of 2700kg/m^{-3} is calculated using the SAFE method and the analytical solution [79]. Ten 1D quadratic elements are used to model the whole plate thickness in the SAFE method. The compared results are shown in Figure 4.2. A good agreement is obtained.

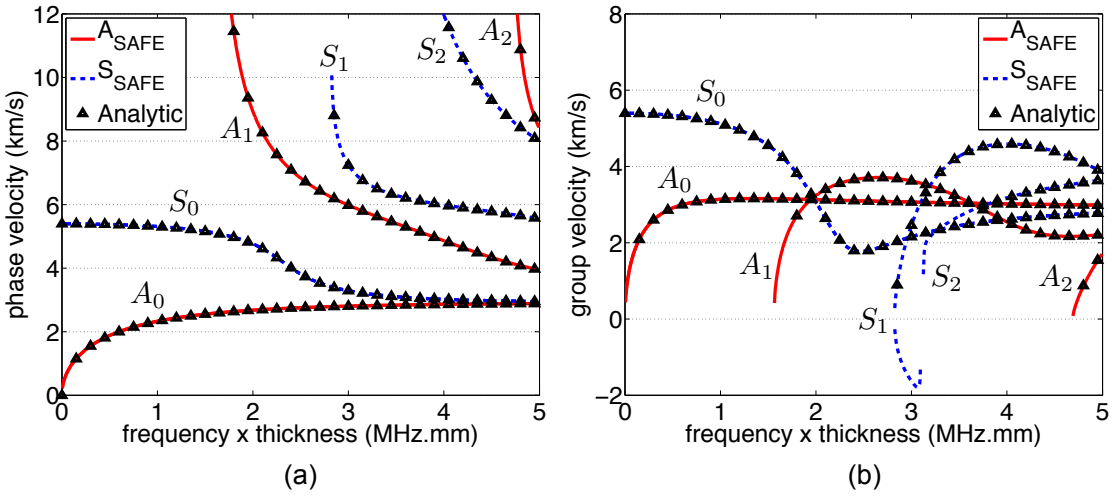

FIGURE 4.2: Dispersion curves comparison between SAFE and analytical solutions for aluminum plate: (a) phase velocity curves, and (b) group velocity curves.

The accuracy of the SAFE method depends on the used number of elements and the applied interpolation functions. As in the FEM, more elements used in the SAFE method means more accuracy. Here, only quadratic interpolation functions are used due to the interest in the lower frequency range, which have fewer modes and a low dispersive region. If higher accuracy is needed, one could increase the number of elements or could use higher order interpolation functions [161]. Figure 4.3 shows the effects on the phase velocity curves of an aluminum plate due to different numbers of elements per plate thickness. Comparisons are made only on the first four modes, A_0, S_0, A_1 and S_1. As shown in these figures, when the number of elements are more than three, the calculated dispersion curves match closely with the analytical solutions within these frequency ranges. The errors of the dispersion curves compared to the analytical solutions are given in 4.4. Higher number of elements per plate thickness in SAFE gives lesser errors. However, the errors increase as the frequency increases. Thus, higher number of elements are needed for better approximation at higher frequency ranges.

Another comparison is made with dispersion curves results presented in [1] for a 3.2 mm thick $[0°/45°/90°/-45°]_{s2}$ composite plate having 16 lamina layers. Material properties for a single lamina in 0° angle is given in Table 4.1. Each material layer is modelled by a single 1D quadratic element in SAFE. Here, a good aggreement is obtained as well, shown in Figure 4.5. In this composite plate, Lamb modes and SH modes are coupled and can not be differentiated. Thus, the dispersion curves can only be separated into symmetric or anti-symmetric modes.

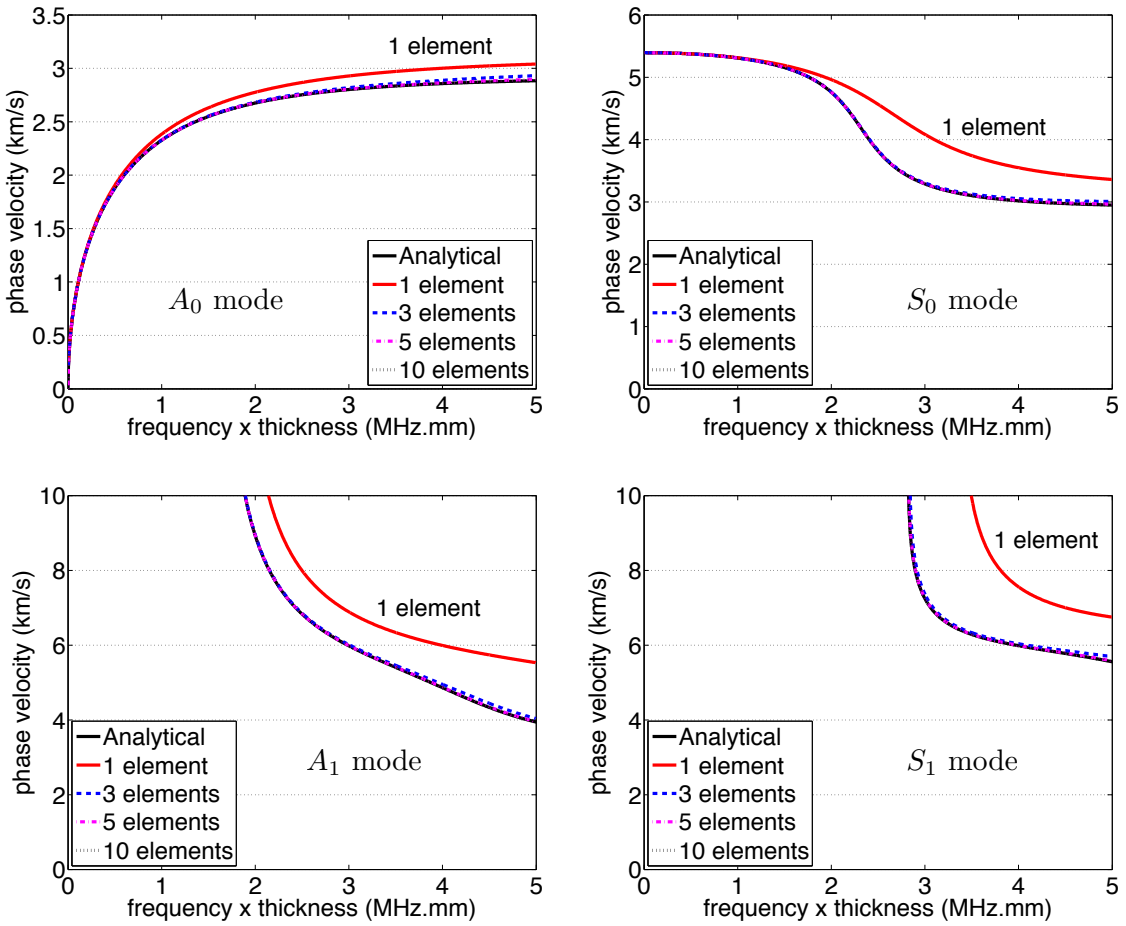

FIGURE 4.3: Aluminum plates phase velocity curve comparisons between analytical solutions and SAFE using different number of elements per thickness.

A software, based on the SAFE method presented here has been developed to calculate the dispersion curves. The software results have been compared with an independent experimental work by Pohl et al. [2] for determining the phase velocity curves of aluminum and polymethylmethacrylat (PMMA) plates. Material properties of these plates are measured by evaluating the ultrasonic longitudinal and transversal waves. The comparisons are shown in Figures 4.6 and 4.7. Good aggreements are obtained proving the suitability of the SAFE method. Details of the experimental work are given in [2]. The slight deviations for PMMA plate are explained by slight differences in the frequency dependent dynamic elastic properties common in plastics.

An independent experimental work to determine the dispersion curves of a composite plate has been done in Deutsches Zentrum für Luft- und Raumfahrt (DLR) by Schmidt

TABLE 4.1: Lamina material properties in 0° angle [1].

E_1(GPa)	E_2(GPa)	G_{12}(GPa)	G_{23}(GPa)	ν_{12}	ν_{23}	ρ (kg/m^3)
172	9.8	6.1	3.2	0.37	0.55	1608

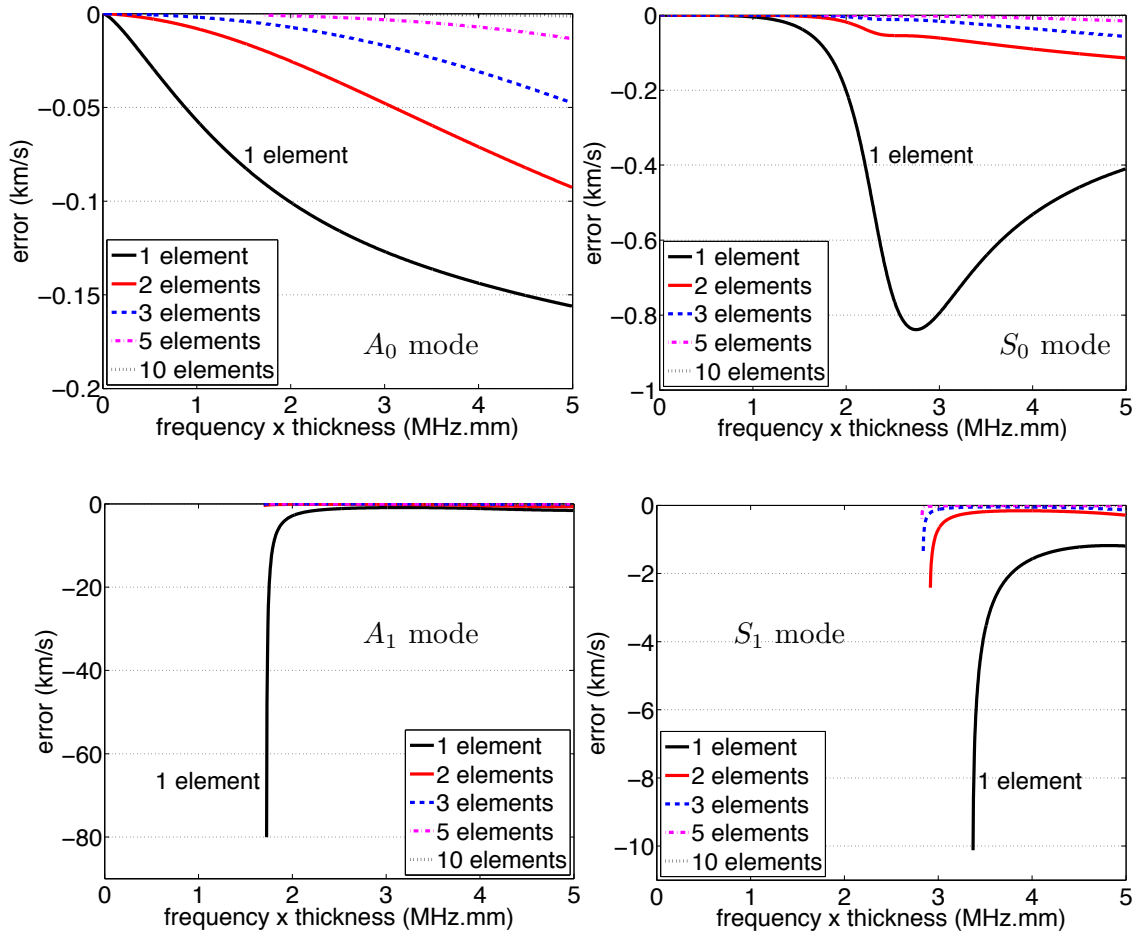

FIGURE 4.4: Errors between analytical solutions and SAFE using different number of quadratic elements per thickness.

[3] for a Deutsche Forschung Gesellschaft (DFG) project. The layer configurations and material properties are given in Tables 4.2 and 4.3 respectively. The composite plate is denoted as DFG09-08 plate. The phase velocity comparisons between the experimental results and SAFE are given in Figures 4.8 and 4.9 for S_0 and A_0 modes respectively. Four different wave propagation angles are considered, 0°, 45°, −45° and −90°. Good agreements are obtained. Details of the experimental work are published in [3].

Another comparison is made against an experimental data published in [2] for a different composite plate with a similar configuration as given in Tables 4.2 and 4.3. Figures 4.10(a)-(b) show the dispersion curves comparisons between the results in [2], [3] and the SAFE method for the wave propagation angle 0°. For the A_0 mode, a good agreement is obtained. However, for the S_0 mode, a good agreement is achieved only until the frequency of 0.45MHz. This disagreement is due to the homogenized material properties used in the SAFE method for the Köper and Leinwand layers (woven layers), which are assumed as orthotropic materials. Apparently, the homogenized material properties affect the S_0 mode more than the A_0 mode even when the S_0 mode has a larger wavelength λ (with higher c_p) than the A_0 mode (from the relationship $\lambda = 2\pi c_p/\omega$). Thus, for this plate, the SAFE method is applicable only until the frequency range of 0.45MHz.

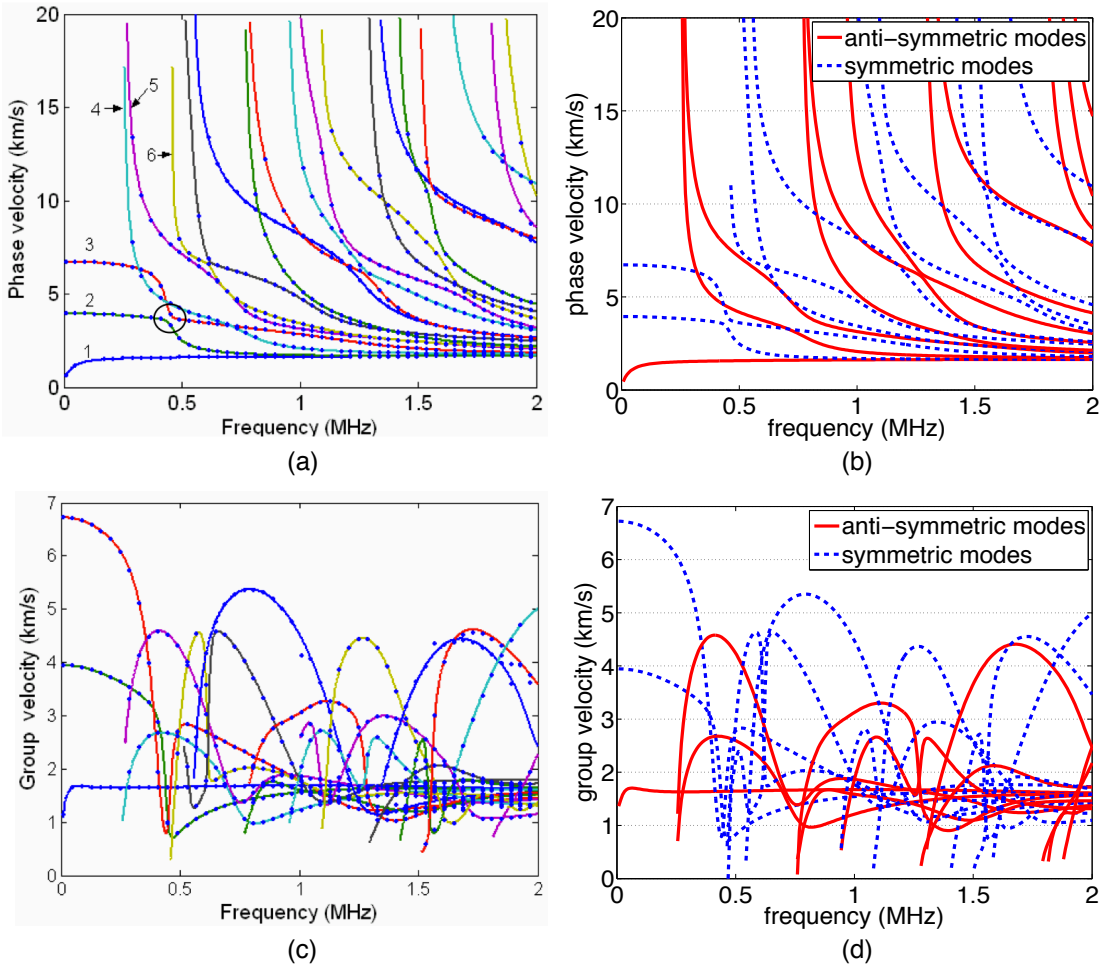

FIGURE 4.5: Dispersion curves comparison between SAFE and solutions in [1] for a 3.2 mm thick $[0°/45°/90°/-45°]_{s2}$ composite plate: (a) and (c) are solutions in [1], while (b) and (d) are SAFE results.

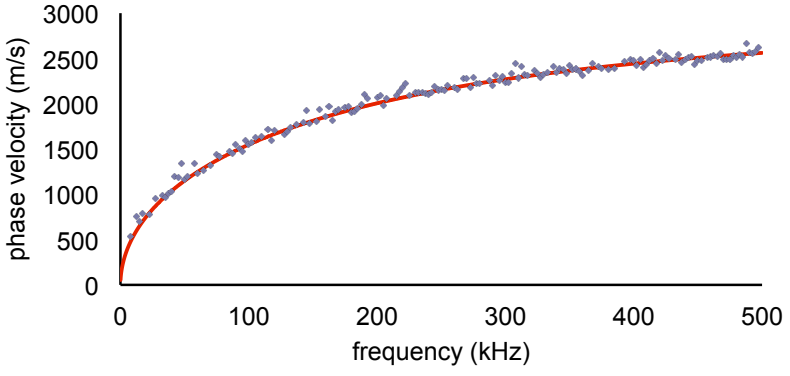

FIGURE 4.6: A_0 mode comparison between experimental results (.) presented in [2] and SAFE (−) for an aluminum plate.

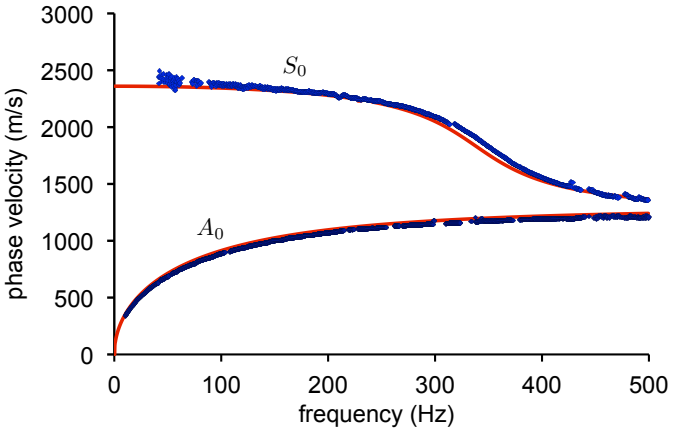

FIGURE 4.7: A_0 and S_0 modes comparisons between experimental resutls (.) presented in [2] and SAFE (−) for PMMA plate.

TABLE 4.2: Layer construction for DFG09-08 plate [3].

Layer	Fiber orientation (°)	Material/Fabric	Thickness (mm)
1	0°/90°	Köper (Twill) 2/2	0.4
2	45°	UD-Gelege (Unidirectional)	0.25
3	−45°	UD-Gelege (Unidirectional)	0.25
4	0°/90°	Leinwand (Plain)	0.22
5	−45°	UD-Gelege (Unidirectional)	0.25
6	45°	UD-Gelege (Unidirectional)	0.25
7	0°/90°	Twill (Köper) 2/2	0.4

TABLE 4.3: Layer material for DFG09-08 plate [3]. Layer thickness is in the 3 direction.

Material	Density (kg/m^3)	E_1 (GPa)	E_2 (GPa)	E_3 (GPa)	ν_{12}	ν_{13}	ν_{23}	G_{12} (GPa)	G_{13} (GPa)	G_{23} (GPa)
Köper 2/2	1520	49.6	49.6	6.1	0.03	0.034	0.322	3.56	2.67	2.67
Leinwand	1560	53.4	53.4	6.4	0.03	0.033	0.319	3.83	2.87	2.87
UD-Gelege	1550	127.5	7.9	-	0.273	-	-	5.58	-	2.93

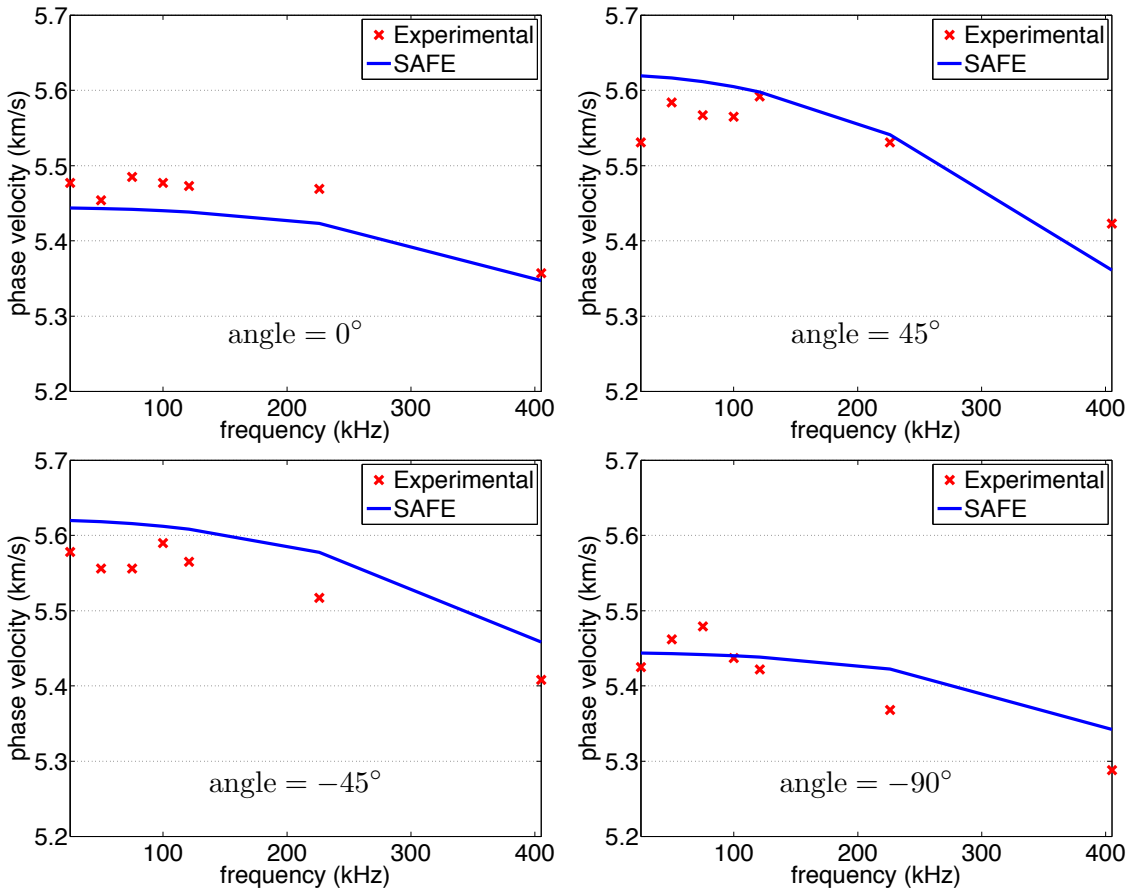

FIGURE 4.8: S_0 mode comparisons between experimental results presented in [3] and SAFE for DFG09-08 plate.

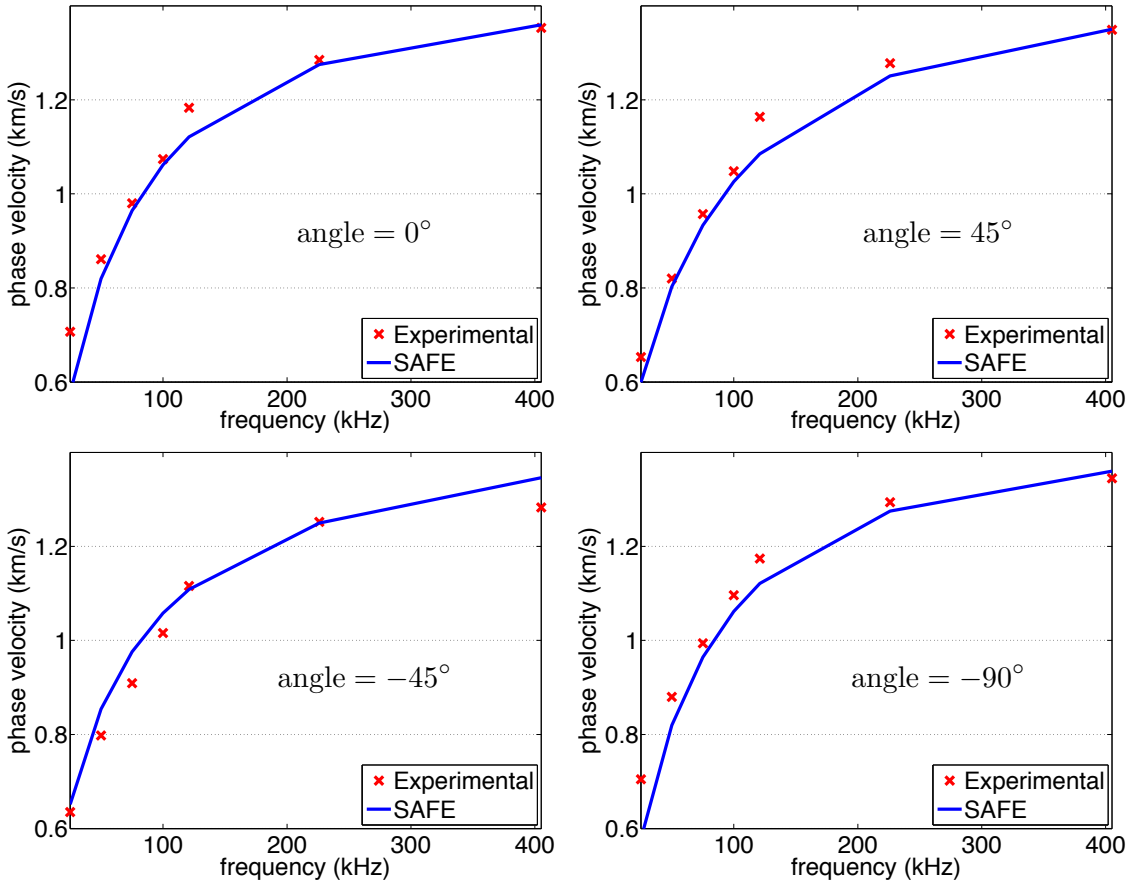

FIGURE 4.9: A_0 mode comparisons between experimental results presented in [3] and SAFE for DFG09-08 plate.

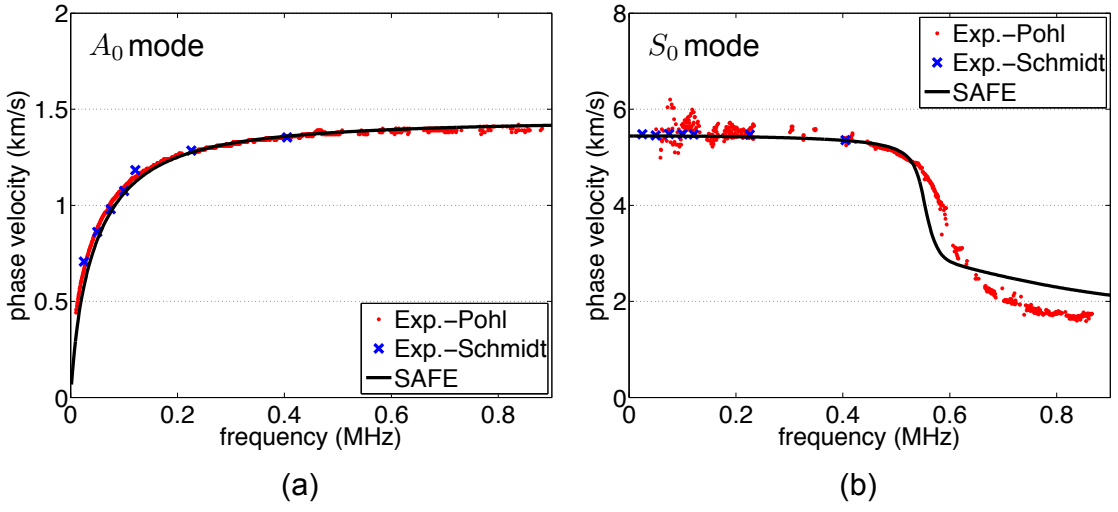

FIGURE 4.10: Comparisons between experimental results presented in [2], [3] and the SAFE method for DFG09 plate. (a) A_0 phase velocity curve, (b) S_0 phase velocity curve.

4.4 Application examples

4.4.1 Symmetrical and unsymmetrical material arrangements

In the following, the effects of symmetrical and unsymmetrical material arrangements are considered for plates with layers of isotropic materials. The thickness of the plates are 1mm. The different material properties are represented by two Young's modulus, E_1 and E_2, where $E_1 = E_{\text{aluminum}}$ and $E_2 = 0.5E_{\text{aluminum}}$. A Poisson's ratio of 0.33 and a density of 2700kg/m^{-3} are used for both materials. An unsymmetrical material arrangement is considered, as shown in Figure 4.11(a). The top layers of the plate have the lower Young's modulus of E_2 while the bottom layers have the higher Young's modulus of E_1. Having this unsymmetrical material arrangement in the plate layers causes the first and the second mode in the dispersion curves to be separated (marked by the circle). However, the effects on the dispersion curves are small if the layers with the lower Young's modulus of E_2 are less than 40% of the plate thickness. As the material properties of the plate is no longer symmetric, the Lamb modes are no longer differentiable into the symmetric and the anti-symmetric modes. Thus, these modes become quasi symmetrical and quasi anti-symmetrical modes.

A symmetrical material arrangement is considered next, as shown in Figure 4.11(b). The middle layers of the plate have the lower Young's modulus of E_2 while the top and bottom layers of the plate have the higher Young's modulus of E_1. In this case, the material arrangement is symmetrical. The A_0 and S_0 modes are always connected together and converge to the Rayleigh wave (marked by the circle). Due to the symmetrical material properties of the plate, the available Lamb modes can be differentiated into the anti-symmetric and symmetric modes. Applying this effect, the symmetricity of the plate material properties with respect to its center plane can be detected by looking at the dispersion curves. However, a limitation of this approach is that only the unsymmetrical or symmetrical material arrangements that span for the whole plate length (or the measured plate length) can be detected. Thus, if a stiffness reduction due to damages is being considered for detection from the dispersion curves, the damages must span for the whole plate length (or the measured plate length).

The effects on the fundamental modes (A_0 and S_0) are higher when the layers with the lower Young's modulus of E_2 are located near to the plate center plane compared to near the plate surface, as shown in Figure 4.12. The damages in the layered plates may cause degradation in the stiffness of certain layers within the plates. Thus, the obtained effect is convenient for the SHM purposes especially for the laminated composite plates as the damages near the plate center plane are more difficult to be detected visually than the damages at the plate surfaces. Stiffness reduction near the plate center plane reduces the quasi non-dispersion region of the S_0 mode. In both cases, the thickness of the layers with the Young's modulus of E_2 is 10% of the total plate thickness and the comparisons are made with the analytical solution for a 1mm thick aluminum plate (all layers with the Young's modulus of E_1).

The same effect as shown for plates with layers of isotropic material can also be seen in composite plates. Consider a laminated composite plate made of layers of unidirectional

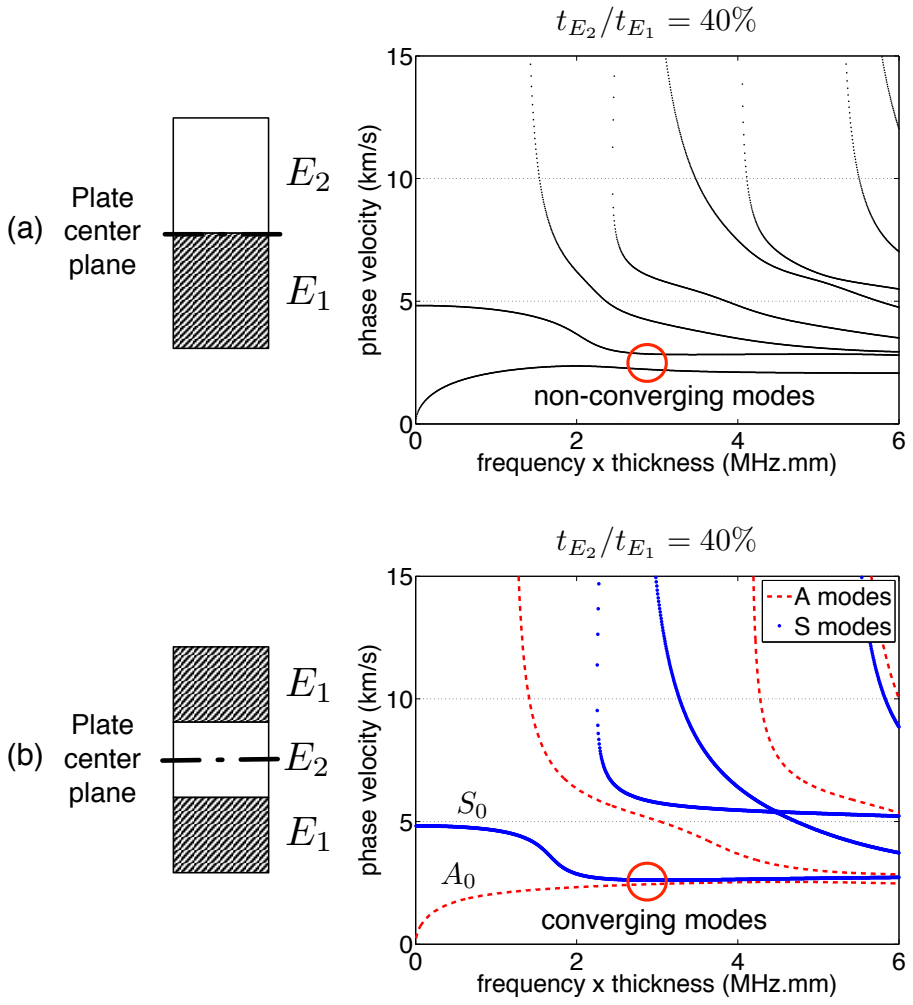

FIGURE 4.11: Effect of the material arrangements on the dispersion curves of a layered isotropic plate; (a) unsymmetrical material arrangement, (b) symmetrical material arrangement. The t_{E_2}/t_{E_1} ratio denotes the thickness ratio between the layers with the Young's modulus of E_2 and the layers with the Young's modulus of E_1.

lamina arranged in different angles. Even with the same material properties at each lamina, the effective lamina stiffness changes with respect to the wave propagation directions. For example, at the wave propagation angle of 0°, the lamina with the fibers arranged at angle 45° has 50% of the stiffness of the lamina with the fibers arranged at angle 0°. Thus, the effects shown here are also valid for the composite plates but depended on the wave propagation directions.

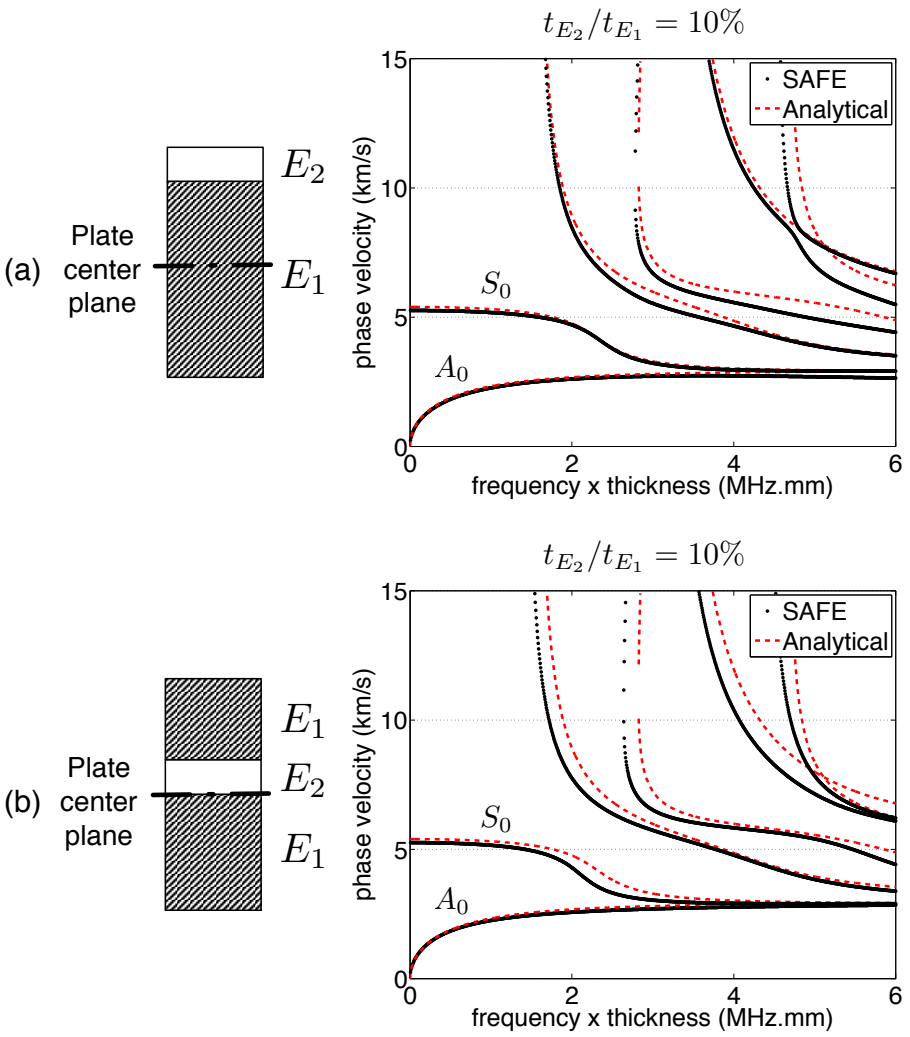

FIGURE 4.12: Effect of the E_2 layers location on the dispersion curves; (a) near the top plate surface (b) near the plate center plane. The analytical solution is for a 1mm thick aluminum plate.

4.4.2 Skew angles

The skew angle calculation is important for the anisotropic composite plates as it gives the differences between the wave propagation direction and the group velocity (wave energy) direction [162]. Consider a 1mm thick unidirectional composite plate with fibers oriented at angle 0°. The lamina material properties are given in Table 4.1. The wave energies travel mostly along the fiber directions. Thus, the wave propagation directions will coincide with the wave energy directions only at the angles 0°, 90°, 180° and 270°. At these angles, the Lamb modes are decoupled from the SH modes. The phase velocity curves at the angle 0° is shown in Figure 4.13(a). Here, for generality at all wave propagation directions, the four available modes are denoted as A_0, S_0, A_1, and S_1. However, as the Lamb modes can be differentiated from the SH modes at the angles 0°, 90°, 180° and 270°, we know that the S_0 mode is actually a SH_0 mode, and the S_1 mode is actually a S_0 mode. SH_0 mode is non dispersion and can be seen at a straight line in the phase velocity dispersion curves (marked in in Figure 4.13(a) as S_0).

For the other wave propagation angles, the Lamb modes are coupled with the SH modes. Therefore, they can be differentiated only as the symmetric and the anti-symmetric modes (S or A). One of the ways to display the variations of the phase velocities with the wave propagation directions is by plotting the slowness curves. The slowness curves are the inverse of the phase velocity curves showing the time taken by the wave to propagate per unit distance. A smaller value in the slowness curves means a faster wave propagation. Figure 4.13(b) shows the slowness curves for the different wave propagation angle θ at the frequency of 500kHz. Only three modes are available at this frequency namely the A_0, S_0, and S_1. From the slowness curves, it can be seen that the A_0 and S_1 modes are fastest along the 0° angle which correspond to the fiber direction.

The variation of the skew angle ψ with the frequency at the wave propagation angle $\theta = 45°$ is shown in Figure 4.13(c). This figure shows how the skew angle changes with frequency at a single wave propagation direction. The skew angle curve for the S_1 mode is straight indicating that the skew angle of this mode is non dispersive (independent from the frequency). This suggest that for the S_1 mode, only the variation of the skew angles with the wave propagation directions is important. However, this is only true when the wave propagation angle is less than 80°, as shown in Figure 4.14(d). At the wave propagation angles of 80° and above, the skew angle curves are no longer straight indicating dispersive behavior.

On the other hand, the skew angle curves of the other available modes are generally dispersive for any wave propagation angles as shown in Figures 4.14(a)-(c), except at the angles where the wave propagation directions coincide with the energy propagation directions. This fact can be seen in the Figure 4.13(d), that shows the variation of the skew angle for a different wave propagation angle at the frequency of 500kHz. The angles at the circumference of the polar plot denote the wave propagation angles while the angles at the radius of the polar plot denote the skew angles). At the wave propagation angles 0°, 90°, 180° and 270°, the values of the skew angle for all modes are zero. These mean that the wave propagation direction coincide with the energy propagation direction. At a frequency of 500kHz, only three modes are available namely the A_0, S_0, and S_1.

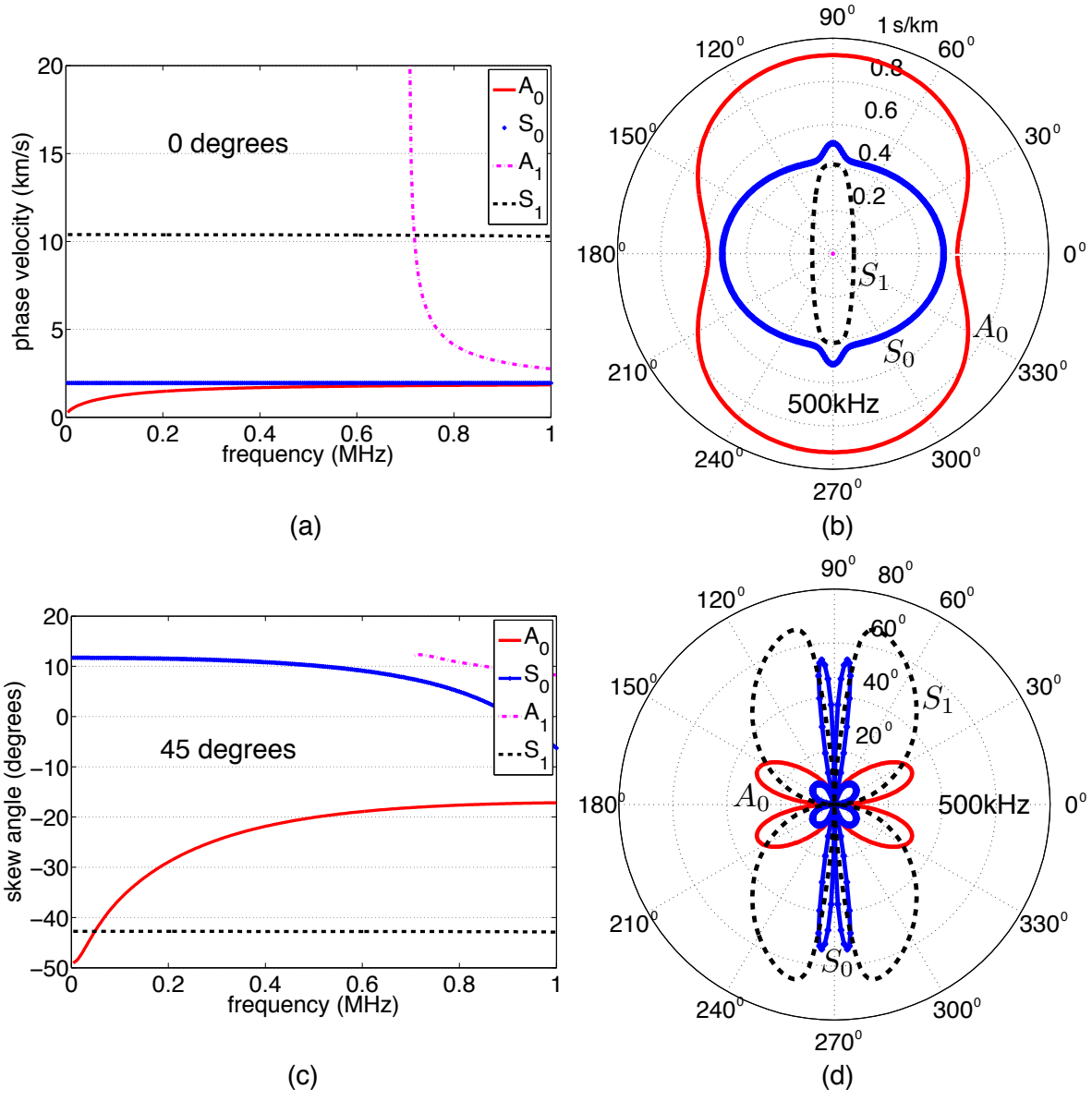

FIGURE 4.13: (a) Phase velocity curves at angle 0°, (b) Slowness curves at frequency 500kHz, (c) Skew angle curves at wave propagation direction angle $\theta = 45°$, and (d) Skew angle curves at frequency 500kHz.

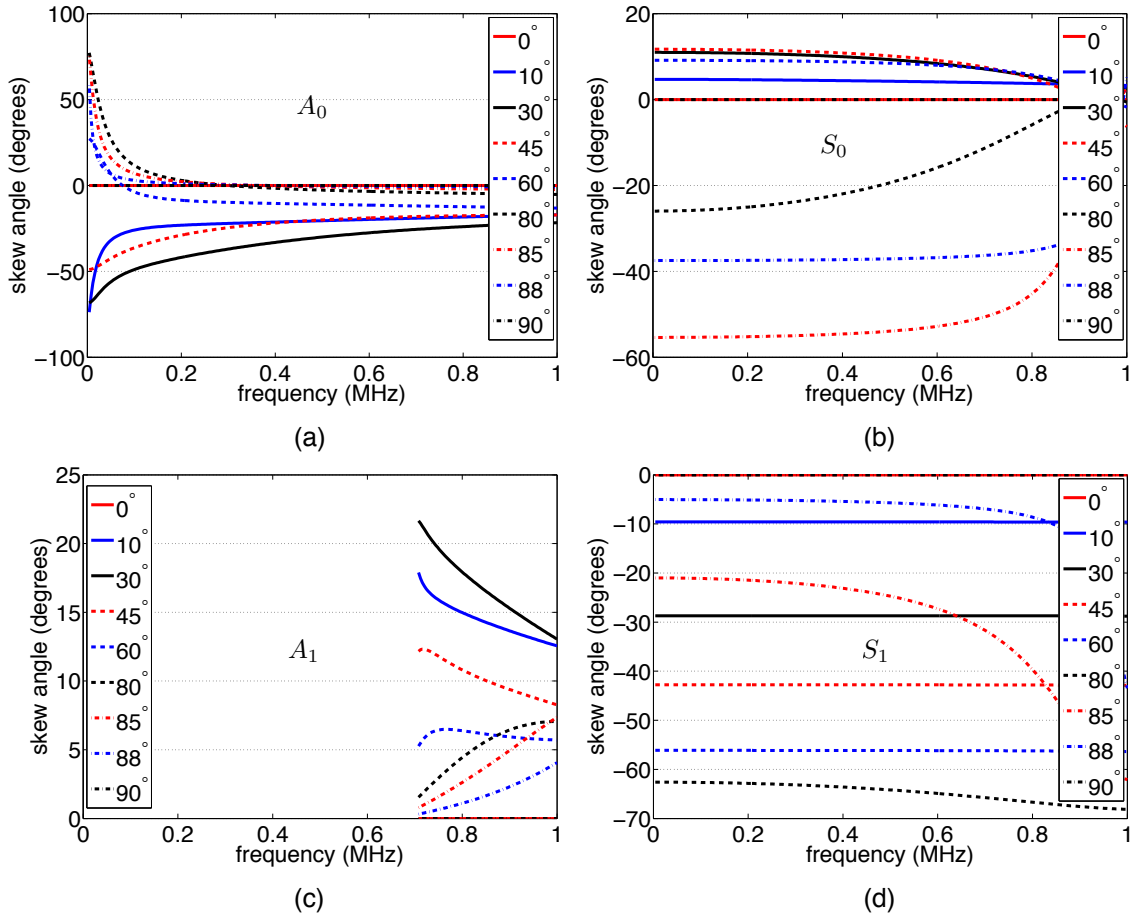

FIGURE 4.14: Skew angle at different wave propagation angles: (a) A_0 mode, (b) S_0 mode, A_1 mode, and S_1 mode. Each line represent a single wave propagation angle.

4.4.3 Plate with initial in-plane load

The effect of initial axial load has been included in the SAFE method for the analysis of rods and rails [163]. The same approach can be applied also to plates with an initial in-plane load. Previously, for analyzing small amplitude elastic waves, generally the infinitesimal strain-displacement relations are linear. However, for the cases where an initial load is present within the waveguide, it is necessary to apply the full strain-displacement relation [163]. The linear ($\boldsymbol{\varepsilon}$) and the full ($\mathfrak{E}$) strain-displacement relationships are given by

$$\boldsymbol{\varepsilon} = \begin{Bmatrix} \frac{\partial u_x}{\partial x} \\ \frac{\partial u_y}{\partial y} \\ \frac{\partial u_z}{\partial z} \\ \frac{\partial u_x}{\partial y} + \frac{\partial u_y}{\partial x} \\ \frac{\partial u_y}{\partial z} + \frac{\partial u_z}{\partial y} \\ \frac{\partial u_x}{\partial z} + \frac{\partial u_z}{\partial x} \end{Bmatrix}; \qquad \mathfrak{E} = \boldsymbol{\varepsilon} + \begin{Bmatrix} \frac{1}{2}\left[\left(\frac{\partial u_x}{\partial x}\right)^2 + \left(\frac{\partial u_y}{\partial x}\right)^2 + \left(\frac{\partial u_z}{\partial x}\right)^2\right] \\ \frac{1}{2}\left[\left(\frac{\partial u_x}{\partial y}\right)^2 + \left(\frac{\partial u_y}{\partial y}\right)^2 + \left(\frac{\partial u_z}{\partial y}\right)^2\right] \\ \frac{1}{2}\left[\left(\frac{\partial u_x}{\partial z}\right)^2 + \left(\frac{\partial u_y}{\partial z}\right)^2 + \left(\frac{\partial u_z}{\partial z}\right)^2\right] \\ \frac{\partial u_x}{\partial x}\cdot\frac{\partial u_x}{\partial y} + \frac{\partial u_y}{\partial x}\cdot\frac{\partial u_y}{\partial y} + \frac{\partial u_z}{\partial x}\cdot\frac{\partial u_z}{\partial y} \\ \frac{\partial u_x}{\partial y}\cdot\frac{\partial u_x}{\partial z} + \frac{\partial u_y}{\partial y}\cdot\frac{\partial u_y}{\partial z} + \frac{\partial u_z}{\partial y}\cdot\frac{\partial u_z}{\partial z} \\ \frac{\partial u_x}{\partial x}\cdot\frac{\partial u_x}{\partial z} + \frac{\partial u_y}{\partial x}\cdot\frac{\partial u_y}{\partial z} + \frac{\partial u_z}{\partial x}\cdot\frac{\partial u_z}{\partial z} \end{Bmatrix}, \tag{4.3}$$

where u_x, u_y and u_z are the displacements in the x, y and z directions, respectively. Potential energy per unit volume may be written as the sum of the strain energy associated with the small amplitude elastic wave (from $\boldsymbol{\sigma}$ term) and the work performed by the initial stress (from $\boldsymbol{\sigma}^{(0)}$ term) as

$$\mathbf{k} = \frac{1}{2}\boldsymbol{\sigma}^T \cdot \mathfrak{E} + \boldsymbol{\sigma}^{(0)^T} \cdot \mathfrak{E}. \tag{4.4}$$

In-plane load on the waveguide which extends in the x direction is considered. The initial stress due to this load is given by $\sigma_{xx}^{(0)}$. The stresses associated with the small amplitude elastic wave are assumed at least an order of magnitude smaller than the in-plane stress [163]. Thus, the product of these stresses and the non-linear strain terms are negligible. The strain energy can then be written as

$$\mathbf{k} = \frac{1}{2}\left[\sigma_{xx}\cdot\varepsilon_{xx} + \sigma_{yy}\cdot\varepsilon_{yy} + \sigma_{zz}\cdot\varepsilon_{zz} + \sigma_{xy}\cdot\varepsilon_{xy} + \sigma_{xz}\cdot\varepsilon_{xz} + \sigma_{yz}\cdot\varepsilon_{yz}\right] + \sigma_{xx}^{(0)}\cdot\mathfrak{E}_{xx}. \tag{4.5}$$

All of these terms except the term containing the initial in-plane load are already included in the linear strain energy used in the SAFE method. The term containing the initial in-plane load can be expanded as

$$\sigma_{xx}^{(0)}\cdot\mathfrak{E}_{xx} = \sigma_{xx}^{(0)}\cdot\frac{\partial u_x}{\partial x} + \sigma_{xx}^{(0)}\cdot\frac{1}{2}\left[\left(\frac{\partial u_x}{\partial x}\right)^2 + \left(\frac{\partial u_y}{\partial x}\right)^2 + \left(\frac{\partial u_z}{\partial x}\right)^2\right]. \tag{4.6}$$

The term $\sigma_{xx}^{(0)}\cdot\frac{\partial u_x}{\partial x}$ disappears when the variation of the Hamiltonian of the waveguide is taken as in [1] or alternatively when the Langrange equations are applied as in [154]. This term represents the interaction of the initial stress with the linear strain, which does not feature in the SAFE equation. Thus, the only term we need to add to the linear strain

energy expression, previously used in the SAFE method is

$$\mathbf{K}^{(0)} = \frac{1}{2}\sigma_{xx}^{(0)} \cdot \left[\left(\frac{\partial u_x}{\partial x} \right)^2 + \left(\frac{\partial u_y}{\partial x} \right)^2 + \left(\frac{\partial u_z}{\partial x} \right)^2 \right]. \tag{4.7}$$

Substituting the displacement interpolation functions used in equation (3.3) yield the additional strain energy term in the form of

$$\mathbf{K}^{(0)} = \frac{1}{2}\sigma_{xx}^{(0)} \cdot k^2 \left\{ -u_x \quad -u_y \quad -u_z \right\} \cdot \begin{Bmatrix} -u_x \\ -u_y \\ -u_z \end{Bmatrix}. \tag{4.8}$$

The form of this term is identical to that of the kinetic energy. Thus, the additional stiffness matrix is proportional to the mass matrix. The SAFE equation in (3.23) can be rewritten as

$$\left[k^2(\mathbf{K}_3 + \mathbf{K}^{(0)}) + k\hat{\mathbf{K}}_2 + \mathbf{K}_1 + \omega^2\mathbf{M} \right] \hat{\mathbf{U}} = 0, \tag{4.9}$$

where

$$\mathbf{K}^{(0)} = \frac{\sigma_{xx}^{(0)}}{\rho}\mathbf{M}. \tag{4.10}$$

The group velocity can be calculated using equation (4.2) with $\mathbf{K}' = 2k(\mathbf{K}_3 + \mathbf{K}^{(0)}) + \hat{\mathbf{K}}_2$.

In the following examples, the in-plane load is applied in terms of in-plain strain in a 1mm thick aluminum plate. The aluminum plate has a Young's modulus of 70.3 GPa, a Poisson's ratio of 0.3436 and a density of 2699 kg/m^3. The calculated phase velocity curves are normalized with the shear wave velocity of 3.158 km/s. Figure 4.15 shows the effect of the strain due to the in-plane load on the A_0 mode phase velocity curve, obtained using the SAFE method and the FEM [4], respectively. A good agreement is observed. The effect of the strain due to the in-plane load on the S_0 mode phase velocity curve, obtained using the SAFE method, is shown in Figure 4.16. By comparing Figures 4.15 and 4.16, effects of the in-plane load are more dramatic for the A_0 mode compared to the S_0 mode. In the A_0, the effect of the in-plane load is negligible for frequency $\times$ thickness value larger than 10 kHz·mm (or 10 Hz·m as shown in Figure 4.15). On the other hand, the effect of the in-plane load is still significant for the S_0 mode until about 500 kHz·mm. However, the magnitude differences in the phase velocity curves are smaller for the S_0 mode compared to the A_0 mode. This fact is in agreement with the statement made in [4], that the in-plane load affect mostly the anti-symmetric modes.

The actual frequency range for the low frequency region (region where only the fundamental symmetric and anti-symmetric modes exist) depends on the thickness of the plate in consideration. The more thicker the plate, the lower the frequency of the low frequency region. Thus, for such plates, the effects of the in-plane load may no longer be negligible. Similar analysis is not extended for anisotropic composite plates. However, the effect of the in-plane load is expected to be dependent on the wave propagation angles.

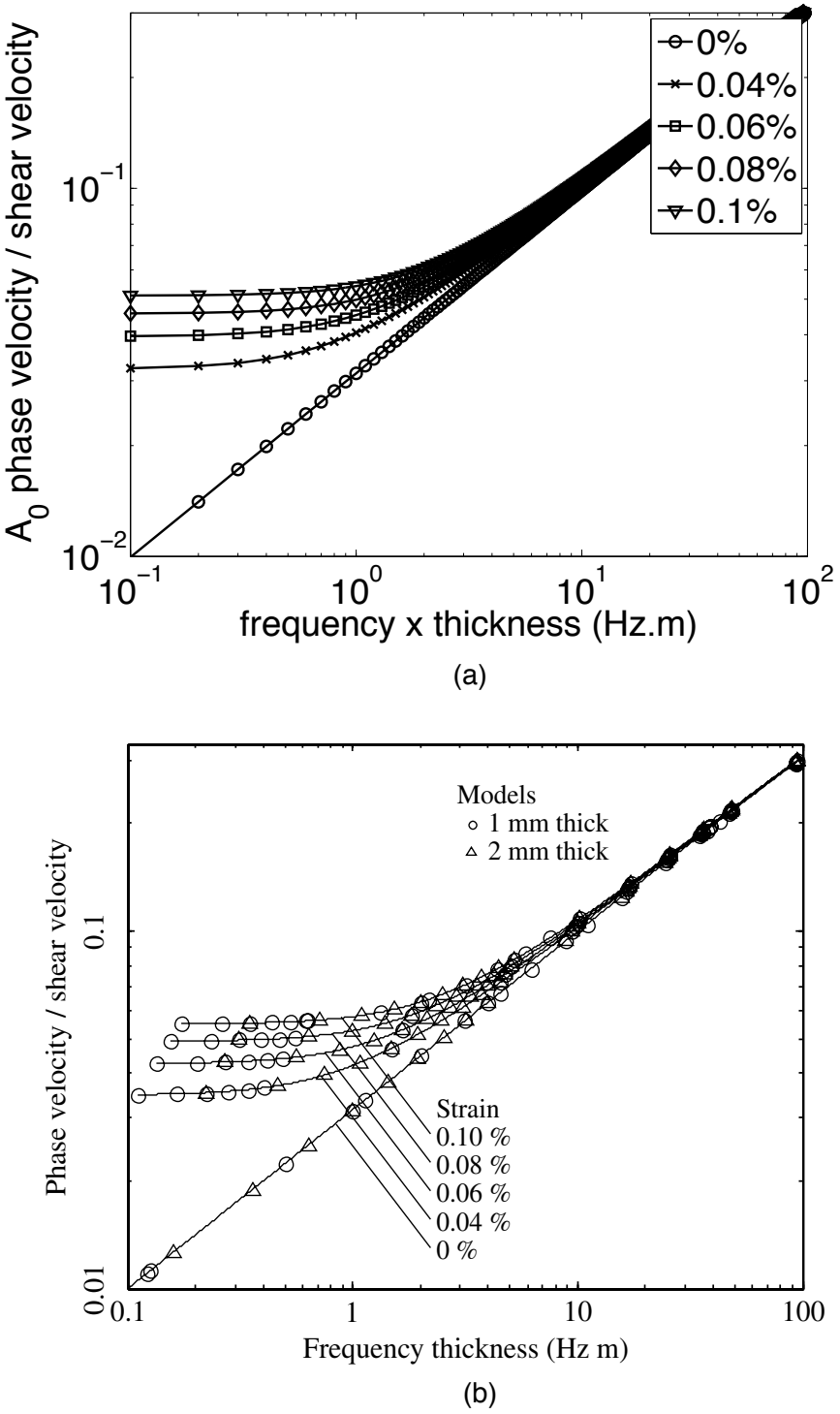

FIGURE 4.15: Effect of the in-plane strain on the A_0 phase velocity curve in a 1mm thick aluminium plate: (a) the SAFE method (b) Reference [4].

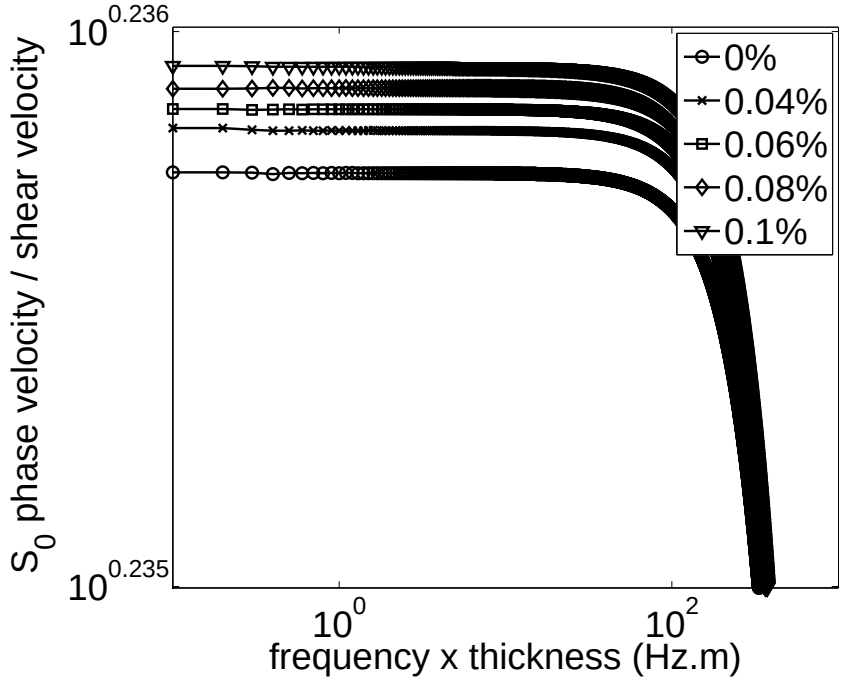

FIGURE 4.16: Effect of the in-plane strain on the S_0 phase velocity curve in a 1mm thick aluminium plate using the SAFE method.

Chapter 5

Lamb wave reflection

5.1 Introduction

In this chapter, Lamb wave reflection analysis are made for plate edges and general obstacles in isotropic plates. Complex symmetric and unsymmetric edges and obstacles are considered. Effects of transducers on the wave propagation are discussed. The analyses given covered only the plane waves where the Lamb modes are decoupled from the SH modes. Thus, the results have no dependence on the wave propagation directions.

5.2 Reflection by vertical plate edge

Consider the case of an incident wave from a pth propagating mode striking the edge at $x = 0$ as shown in Figure 5.1. The wavenumber of this propagating mode is k_p. The

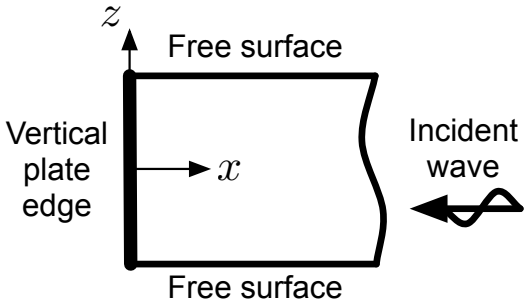

FIGURE 5.1: Vertical plate edge reflection.

displacement vector of the reflected wave $\mathbf{q}^{\text{ref}}$ at an arbitrary distance x is approximated by a modal sum of a finite number of modes M in the form of

$$\mathbf{q}^{\text{ref}} = \sum_{m=1}^{M} b_m \mathbf{U}_m \exp(-ik_m x); \quad x \geq 0. \tag{5.1}$$

The coefficient b_m is the amplitude of the mth reflected mode. The vector $\mathbf{U}_m$ is the eigenvector corresponding to the wavenumber k_m in equation (3.19). Thus, the reflected wave displacement vector at the edge ($x = 0$) is given as

$$\mathbf{q}^{\text{ref}} = \mathbf{\Phi}\mathbf{B}, \tag{5.2}$$

where $\mathbf{\Phi} = [\ \mathbf{U}_1 \quad \mathbf{U}_2 \quad \dots \quad \mathbf{U}_M\ ]$ and $\mathbf{B}^T = [\ b_1 \quad b_2 \quad \dots \quad b_M\ ]$. Superscript T denotes matrix transpose. The reflected wave force field at distance x can also be written as

$$\mathbf{F}^{\text{ref}} = \sum_{m=1}^{M} b_m \psi_m \exp(-ik_m x); \quad x \geq 0. \tag{5.3}$$

Thus, the force vector at the edge ($x = 0$) due to the reflected wave is given by

$$\mathbf{F}^{\text{ref}} = \mathbf{\Psi}\mathbf{B}. \tag{5.4}$$

The matrix $\mathbf{\Psi} = [\ \psi_1 \quad \psi_2 \quad \dots \quad \psi_M\ ]$ is the force eigenvector matrix which represents the nodal force components due to stresses σ_{xx} and σ_{xz} [146]. The force eigenvector for the whole elements in the plate corresponding to mode m can be written as [5]

$$\psi_m = (ik_m\mathbf{A} + \mathbf{P})\mathbf{U}_m, \tag{5.5}$$

with the matrices $\mathbf{A} = \mathbf{K}_3$ and $\mathbf{P} = \mathbf{K}_{12}$ as presented in section 3.2.3. The displacement and the force vector due to the incident wave are

$$\mathbf{q}^{\text{in}} = A_p^{\text{in}} \mathbf{\Phi}_p^-, \tag{5.6}$$

$$\mathbf{F}^{\text{in}} = A_p^{\text{in}} \mathbf{\Psi}_p^-. \tag{5.7}$$

with A_p^{in} as the amplitude of the incident mode p. The vector $\mathbf{\Phi}_p^-$ and $\mathbf{\Psi}_p^-$ are obtained from the pth column of $\mathbf{\Phi}$ and $\mathbf{\Psi}$, respectively, after replacing each x direction displacements and force components by its negative value. The total displacement and force vector at the edge are then given by

$$\mathbf{q} = \mathbf{q}^{\text{ref}} + \mathbf{q}^{\text{in}} = \mathbf{\Phi}\mathbf{B} + A_p^{\text{in}} \mathbf{\Phi}_p^-, \tag{5.8}$$

$$\mathbf{F} = \mathbf{F}^{\text{ref}} + \mathbf{F}^{\text{in}} = \mathbf{\Psi}\mathbf{B} + A_p^{\text{in}} \mathbf{\Psi}_p^-. \tag{5.9}$$

5.2.1 End plate boundary condition

The plate edge boundary conditions need to be included in the formulation. Two types of boundary conditions that can be prescribed are the fully free and fully fixed edges. The vector $\mathbf{B}$ for these boundary conditions are [5]:

- **Reflection by a free plate edge**
  At a free plate edge the traction is zero. Thus, the total consistent nodal forces are zero, $\mathbf{F}(x = 0, z) = 0$. Thus, this yields the prescribed forces on the plate edge as

$\mathbf{F}^{\text{ref}} = -\mathbf{F}^{\text{in}}$. From equation (5.9), the amplitudes of the reflected waves are obtained as

$$\mathbf{B} = -A_p^{\text{in}} \boldsymbol{\Psi}^{-1} \boldsymbol{\Psi}_p^{-}. \tag{5.10}$$

- **Reflection by a fixed plate edge**
  At a fixed plate edge the displacements are zero. Thus, the prescribed displacement on the plate edge is $\mathbf{q}^{\text{ref}} = -\mathbf{q}^{\text{in}}$. From equation (5.8), the amplitudes of the reflected waves are obtained as

$$\mathbf{B} = -A_p^{\text{in}} \boldsymbol{\Phi}^{-1} \boldsymbol{\Phi}_p^{-}. \tag{5.11}$$

  The fixed end condition of the plate can also be satisfied in a variational sense by applying the principle of virtual work [146].

After knowing the vector $\mathbf{B}$, the reflection coefficient $\mathbf{R}_{pn}$ of the nth reflected mode due to pth incident mode is obtained as

$$\mathbf{R}_{pn} = \mathbf{B}_n / A_p^{\text{in}}. \tag{5.12}$$

5.2.2 Energy conservation and reciprocity relation

The energy conservation and the reciprocity relation can be used to check the accuracy of the computed reflection coefficient. The reflected energy is carried only by the propagating modes through the plate cross section. This energy is calculated in terms of the time-average value of the energy flux (Poynting vector/power flow). The energy flux of mode m along the x axis across the plate thickness (in the z direction) is given by [164]

$$P_m = -\frac{1}{2}\text{Real}\left[i\omega \int_{-h/2}^{h/2} (\mathbf{t}_m^{*T} \cdot \mathbf{u}_m) \mathrm{d}z \right], \tag{5.13}$$

where $\mathbf{t}_m$ is the stress due to the mode m with $\mathbf{t}_m^T = \{\sigma_{xx} \quad \sigma_{xz}\}^T$ and h is the plate thickness. Vector $\mathbf{u}_m$ is the displacement eigenvector of the mode m with $\mathbf{u}_m = \mathbf{N}\mathbf{U}_m$, matrix $\mathbf{N}$ as the matrix of interpolation functions and $\mathbf{U}_m$ as the nodal displacement eigenvector. Superscript * denotes complex conjugate. From the FE discretization applied along the plate thickness, the force eigenvector of mode m is given by [5]

$$\psi_m = \int_{-h/2}^{h/2} (\mathbf{N}^T \cdot \mathbf{t}_m) \mathrm{d}z. \tag{5.14}$$

Therefore, the energy flux can be rewritten as

$$P_m = -\frac{1}{2}\text{Real}\Big[i\omega (\psi_m^{*T} \cdot \mathbf{U}_m) \Big]. \tag{5.15}$$

By considering the amplitude of the incidence and the reflected waves, the energy flux of the nth reflected mode due to the pth incident mode is obtained as [146]

$$\mathbf{I}_{pn} = -\frac{1}{2} |A_p^{\text{in}}|^2 |\mathbf{R}_{pn}|^2 \beta_n \tag{5.16}$$

with

$$\beta_n = \text{Real}\left[i\omega(\psi_n^{*T}\mathbf{U}_n)\right], \qquad 1 \leq n \leq N_{pr}.$$

N_{pr} is the number of propagating modes in the reflected field. ψ_n and $\mathbf{U}_n$ are the nth column of $\mathbf{\Psi}$ and $\mathbf{\Phi}$, respectively. The energy flux of the incident wave is written as [146]

$$\mathbf{I}_p^{\text{in}} = -\frac{1}{2}|A_p^{\text{in}}|^2\beta_p \tag{5.17}$$

with $\beta_p = \text{Real}\left[i\omega(\psi_p^{*T}\mathbf{U}_p)\right]$. The error percentage in energy balance ϵ is defined as

$$\epsilon = \left[\mathbf{I}_p^{\text{in}} - \sum_{n=1}^{N_{pr}}\mathbf{I}_{pn}\right]\frac{100}{\mathbf{I}_p^{\text{in}}}. \tag{5.18}$$

In the Figure 5.1, the closed plate edge region is bounded by $x = 0$, $x = x^+$(where $x > 0$) and the top and bottom plate surfaces. From the principle of the conservation of energy in this closed region, ϵ should be zero. Thus, a smaller ϵ value means a more accurate result. The proportion of incident energy transferred into the nth reflected mode is obtained as

$$\mathbf{E}_{pn} = \frac{\mathbf{I}_{pn}}{\mathbf{I}_p^{\text{in}}} = |\mathbf{R}_{pn}|^2\frac{\beta_n}{\beta_p}. \tag{5.19}$$

The reciprocity relation serves as another numerical check of the computations. The real elastodynamics reciprocity relation should satisfy

$$\mathbf{E}_{pn} = \mathbf{E}_{np}. \tag{5.20}$$

This reciprocity relation means that the amplitude of the pth mode reflected wave due to a nth mode incidence wave is equal with the amplitude of the nth mode reflected wave due to a pth mode incidence wave.

5.3 SAFE-FE coupling for reflection by general plate edges

In the previous vertical plate edge reflection problem, the boundary conditions can be defined easily as it is homogeneous for all points along the plate edge. However, for general boundary conditions and general plate edge geometries, the SAFE method needs to be coupled with other methods that can describe these boundary conditions and edge geometries. Here, the SAFE method is coupled with the FEM as shown in Figure 5.2. The FEM is chosen as it is suitable for modelling complex geometries and boundary conditions. The plate edge boundary conditions and geometries are defined in the FE region.

Continuity of displacements between the SAFE and the FE region is preserved by taking the same number of nodes and interpolation functions at the boundary between both regions. This boundary is located at x_0. In the SAFE method, the displacements and forces

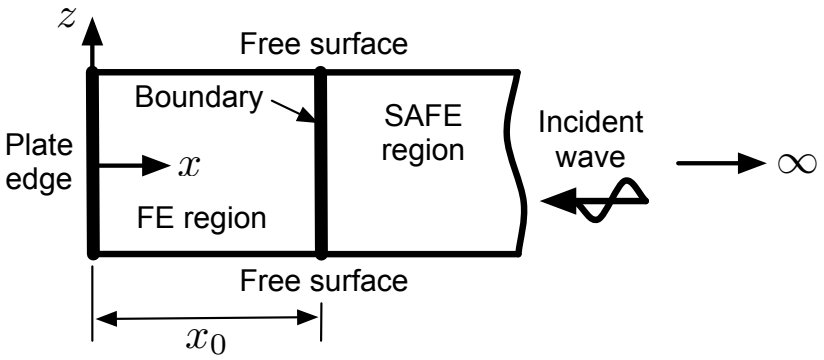

FIGURE 5.2: Coupling between SAFE-FE in the plate edge reflection.

are described by equations (5.1) and (5.3), respectively. Therefore, the displacements and forces at the boundary are obtained by multiplying the component of equations (5.8) and (5.9) with $\exp(-ikx_0)$ and $\exp(-ik_{(p)}x_0)$, respectively, giving

$$\mathbf{q}_B = \mathbf{q}_B^{\text{ref}} \exp(-ikx_0) + \mathbf{q}_B^{\text{in}} \exp(-ik_p x_0), \tag{5.21}$$

$$\mathbf{F}_B = \mathbf{F}_B^{\text{ref}} \exp(-ikx_0) + \mathbf{F}_B^{\text{in}} \exp(-ik_p x_0). \tag{5.22}$$

The subscript B and the superscripts 'in' and 'ref' represent the boundary, the incident wave and the reflected wave, respectively. In the FE region the total work must be zero, thus

$$\delta\mathbf{q}^{*T}\mathbf{S}\mathbf{q} - \delta\mathbf{q}_B^{*T}\mathbf{F}_B = 0. \tag{5.23}$$

The matrix $\mathbf{S}$ and the vector $\mathbf{q}$ are given by

$$\mathbf{S} = \mathbf{K}_{\text{FE}} - \omega^2\mathbf{M}_{\text{FE}} = \begin{bmatrix} \mathbf{S}_{II} & \mathbf{S}_{IB} \\ \mathbf{S}_{BI} & \mathbf{S}_{BB} \end{bmatrix},$$

$$\mathbf{q}^T = \begin{bmatrix} \mathbf{q}_I & \mathbf{q}_B \end{bmatrix}.$$

The matrices $\mathbf{K}_{\text{FE}}$ and $\mathbf{M}_{\text{FE}}$ are the global stiffness and mass matrices of the FE region. The subscript B is for the nodes at the boundary between the SAFE and the FE region. The subscript I is for the other nodes in the FE region. δ implies the first variation. By substituting equations (5.21) and (5.22) into equation (5.23) yields the amplitude of the reflected waves as

$$\begin{aligned} \mathbf{B}\exp(-ikx_0) = &\left[\bar{\mathbf{S}}_{BB}\mathbf{\Phi}\exp(-ikx_0) - \mathbf{\Psi}\exp(-ikx_0)\right]^{-1} \times \\ &\left[\mathbf{F}_B^{\text{in}}\exp(-ik_p x_0) - \bar{\mathbf{S}}_{BB}\mathbf{q}_B^{\text{in}}\exp(-ik_p x_0)\right] \end{aligned} \tag{5.24}$$

with

$$\bar{\mathbf{S}}_{BB} = \mathbf{S}_{BB} - \mathbf{S}_{BI}\mathbf{S}_{II}^{-1}\mathbf{S}_{IB}.$$

After solving the equation above for $\mathbf{B}$, the reflection coefficient can be obtained using equation (5.12). Vectors $\mathbf{q}_B^{\text{in}}$ and $\mathbf{F}_B^{\text{in}}$ are obtained using the equations 5.6 and 5.7, respectively.

5.3.1 Verification

A comparison is made with the result available in [5]. The reflection coefficients of the reflected modes at a vertical plate edge are calculated. The reference result in [5] is calculated by using the method outlined in section 5.2. The S_0 mode is used as the incident wave. The plate used is made of an isotropic material with a Poisson ratio of 0.25, a thickness of 2mm, a longitudinal wave velocity of $c_L = 1$km/s and a transversal wave velocity of $c_T = 1/\sqrt{3}$km/s. The vertical plate edge is fixed. A good agreement has been obtained, as shown in Figure A.1 in Appendix A.

5.3.2 Application examples

In the following examples, the stiffness and the mass matrices of the FE region are obtained from the Abaqus software. The quadratic plain strain rectangular element CPE8 and the triangle element CPE6 are used to model the plate edges. The number of degrees of freedom in the SAFE region is equal to the number of degrees of freedom at the boundary between the FE and the SAFE regions. The plate is made from aluminum with a thickness of 1mm, a Young's modulus of 70GPa, a density of 2700kg/m^3 and a Poisson's ratio of 0.33. Only frequencies until 4.5MHz are being considered. Within this frequency range, only five modes exist namely the S_0, S_1, S_2, A_0 and A_1 modes (refer to Figure 4.2).

5.3.2.1 Symmetric plate edges

A symmetric plate edge as given in Figure 5.3(a) is considered. The infinite plate region is modelled with the SAFE method and the plate edge is modelled with the FEM. The boundary conditions for the plate edges in the FE region, either free or fixed, are defined in the FEM [165]. S_0 mode is taken as the incident wave. A square mesh is used in the FE region with 10 elements per 1mm. The edge reflection coefficient E_{1n} for both symmetric and anti-symmetric modes are plotted as shown in Figure 5.3(b) and Figure 5.3(c), respectively. There is no reflection from the anti-symmetric modes. Thus, by having an incident symmetric mode and a symmetric plate edge, only the symmetric modes would be reflected back. The absolute value for the percentage of the energy error in Figure 5.3(d) is less than 2.5×10^{-7}. High errors are obtained at the frequencies where the phase velocity curves go to infinity. An opposite behavior is obtained when A_0 is taken as the incident wave as shown in Figure 5.4. Due to the symmetricity of plate edge only the anti-symmetric Lamb modes are reflected back (Figure 5.4(c)). There is no reflection from the symmetric Lamb modes (Figure 5.4(b)). The absolute value for the percentage of the energy errors is less than 8×10^{-11} (Figure 5.4(d)).

5.3.2.2 Unsymmetric plate edges

A free unsymmetric plate edge as shown in Figure 5.5(a) is considered. The plate edge is inclined at an angle of 45°. S_0 Lamb modes are used as the incidence wave. As the plate

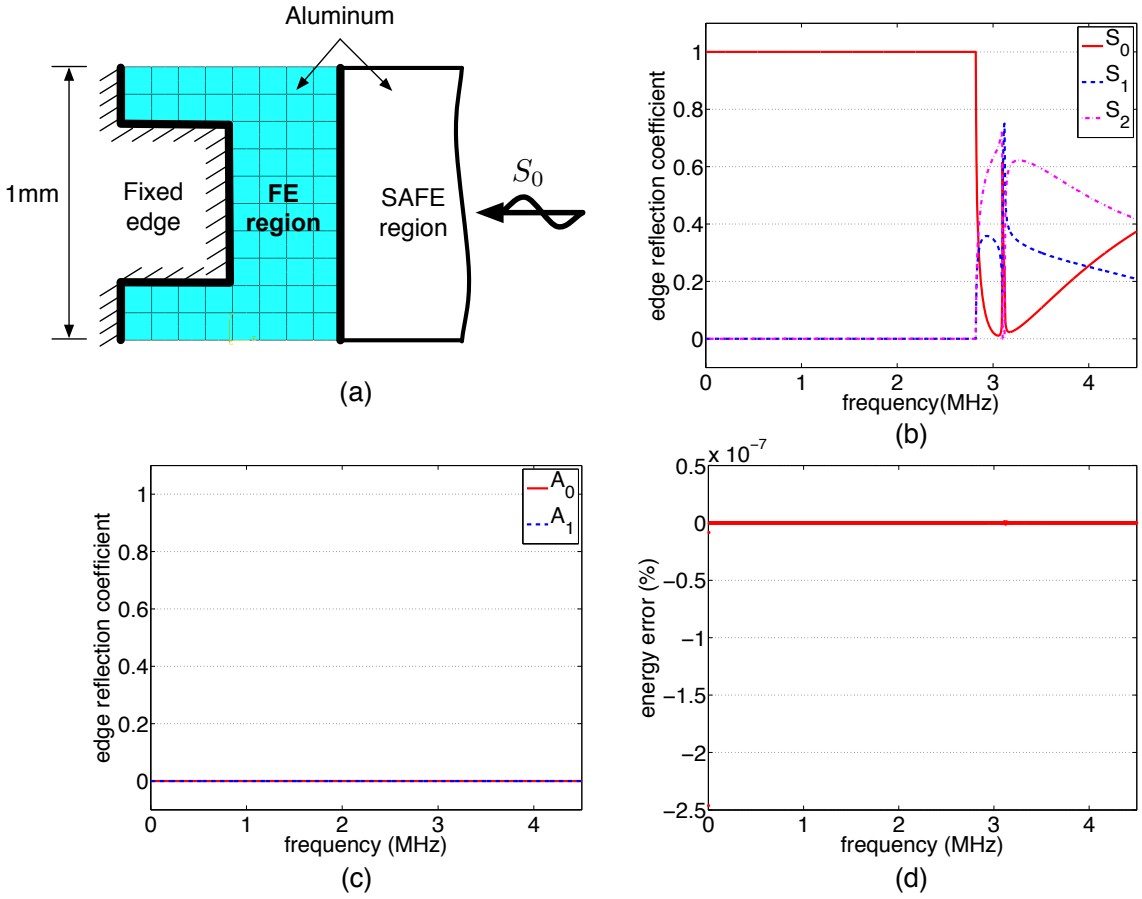

FIGURE 5.3: S_0 mode reflection by a fixed symmetric end plate; (a) SAFE-FE model, (b) Symmetric modes reflection, (c) Anti-symmetric modes reflection, (d) Percentage of energy error.

edge is unsymmetric, the S_0 incident waves produce symmetric and anti-symmetric Lamb mode reflections (see Figures 5.5(b) and 5.5(c)). The absolute value for the percentage of energy errors is less than 3×10^{-9}, shown in Figure 5.5(d). An equal behavior is obtained if the A_0 Lamb mode is taken as the incidence wave as shown in Figure A.2, Appendix A.

The reciprocity principle is also satisfied as shown in Figure 5.6(a). The edge reflection coefficient of the A_0 mode reflected by the S_0 incidence wave is the same as the edge reflection coefficient of the S_0 mode reflected by the A_0 incidence wave. This results is compared with the result presented in [5] which used the boundary element method to model the inclined plate edge. Slight disagreements in the higher frequency range are due to the differences in the method used to model the inclined plate edge.

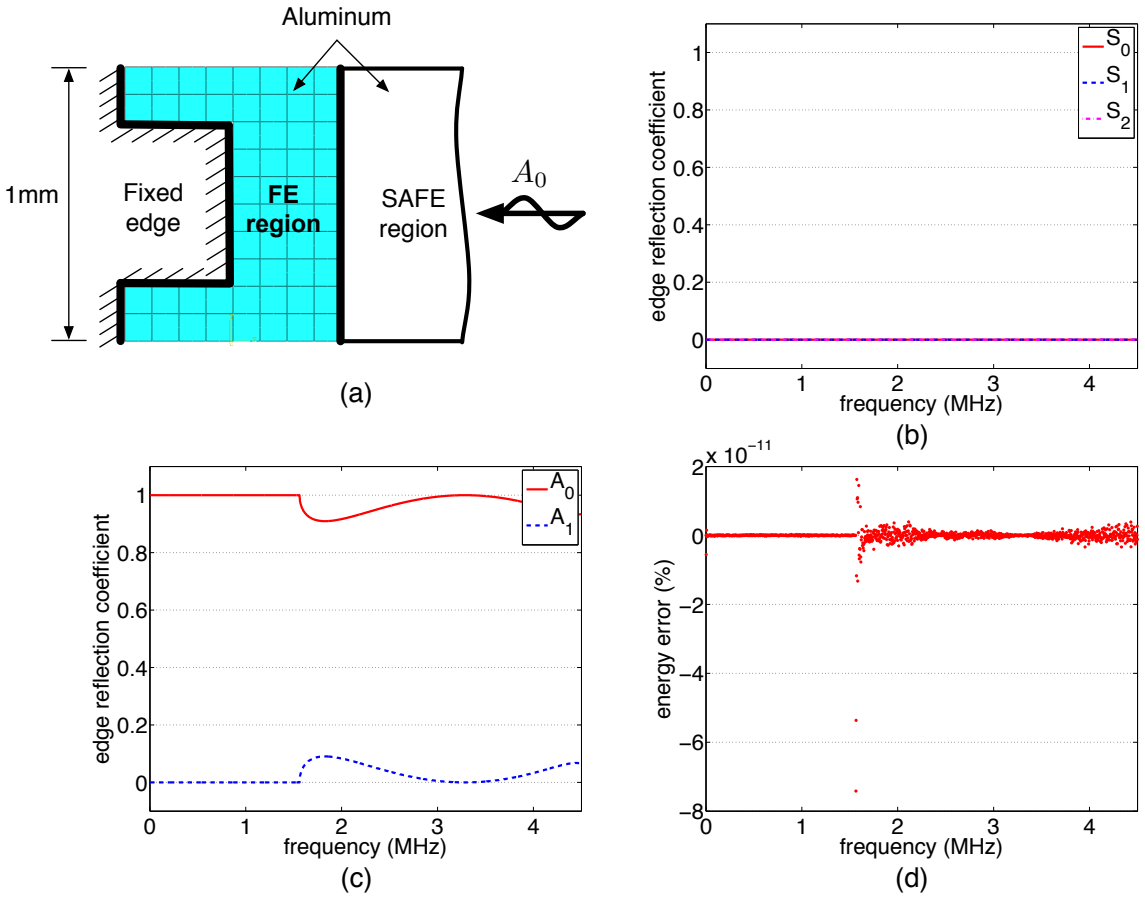

FIGURE 5.4: A_0 mode reflection by a fixed symmetric end plate; (a) SAFE-FE model, (b) Symmetric modes reflection, (c) Anti-symmetric modes reflection, (d) Percentage of energy error.

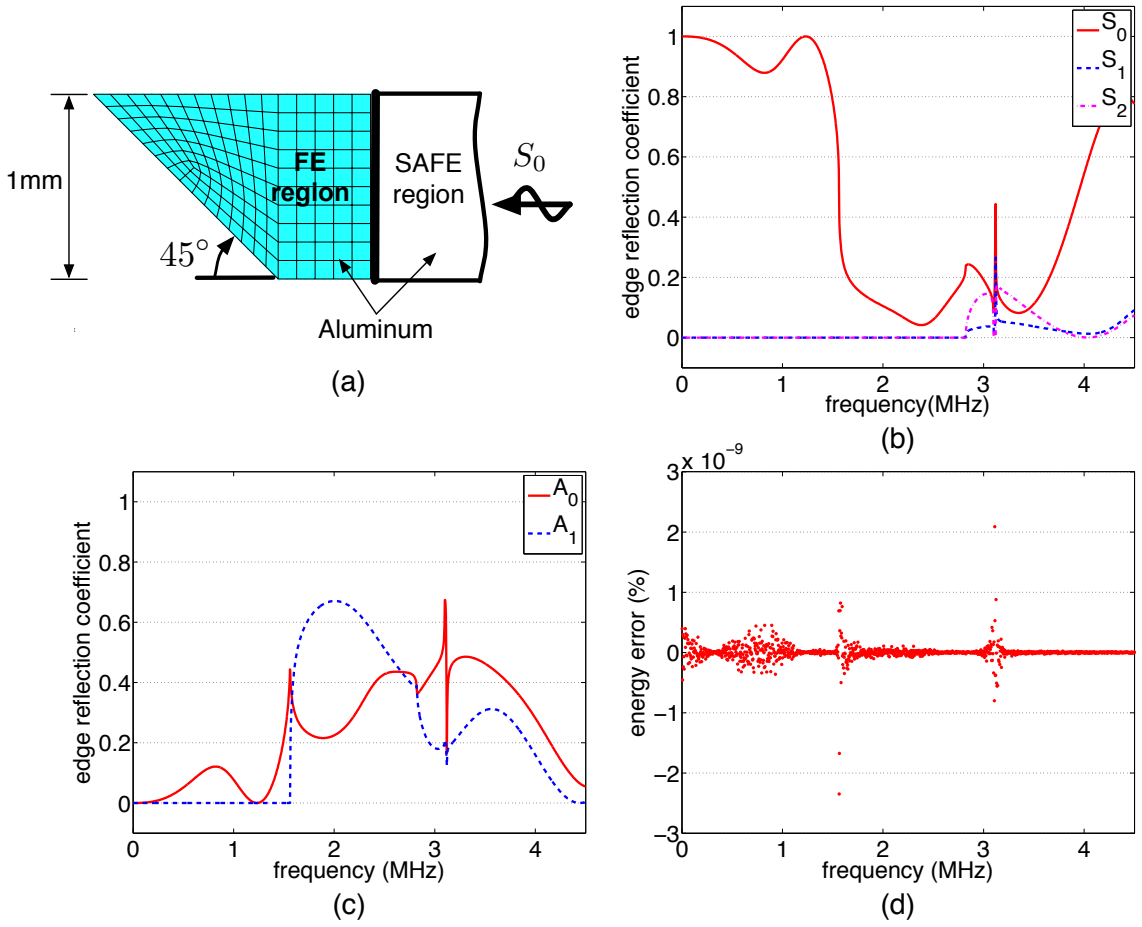

FIGURE 5.5: S_0 mode reflection by an inclined free edge (45°); (a) SAFE-FE model, (b) Symmetric modes reflection, (c) Anti-symmetric modes reflection, (d) Percentage of energy error.

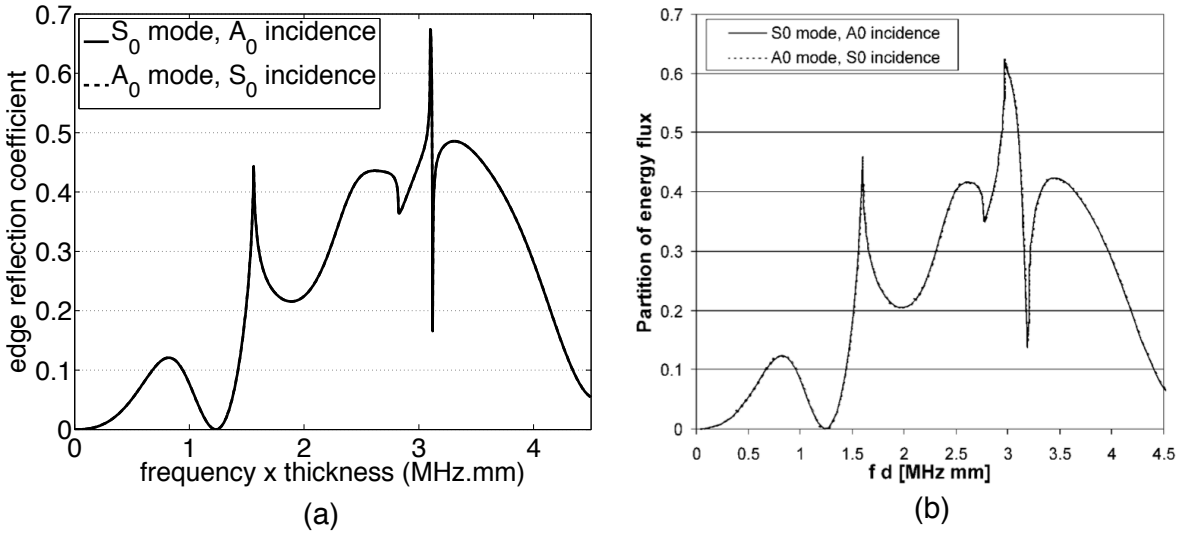

FIGURE 5.6: Check of the reciprocity principle for Lamb mode reflection at an inclined free edge (45°); (a) SAFE, (b) Reference [5].

5.4 Reflection by general obstacles

Lamb waves are not only being reflected by the plate edges but also by damages, actuators and even sensors. The coupled SAFE-FE method [150] is used to study the reflection and transmission behavior due to obstacles anywhere on the plate. The obstacle region is modelled using the FEM while the infinite plate regions before and after the obstacles are modelled with the SAFE method as shown in Figure 5.7.

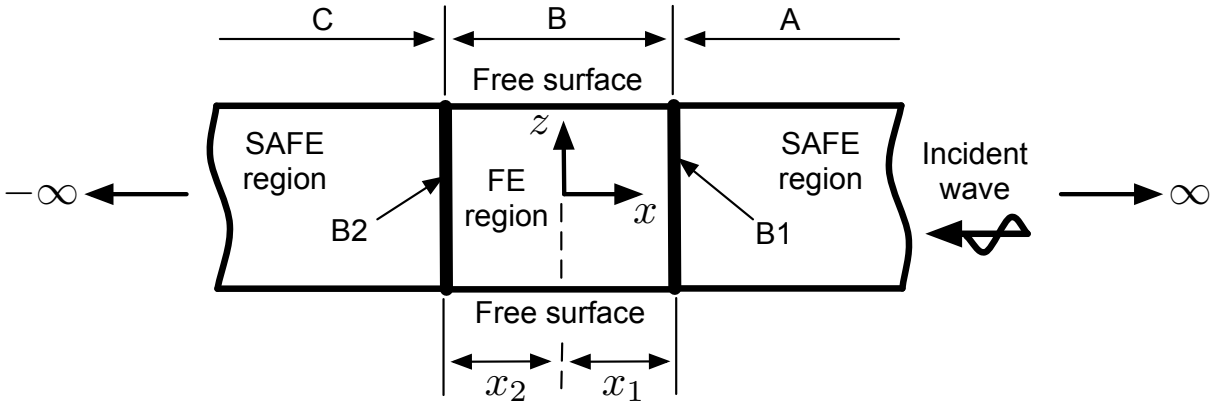

FIGURE 5.7: Coupling between SAFE-FE at any position on the plate.

The infinite plate region before the obstacle region, the obstacle region and the infinite plate after the obstacle region are denoted as regions A, B and C, respectively. The boundary B1 is between regions A and B, while boundary B2 is between regions B and C. In region A, where $x \geq x_1$, the waves are being reflected due to the obstacle. The reflected wave displacements are written in the same form as in equation (5.1), as

$$\mathbf{q}^{\text{ref}} = \sum_{m=1}^{M} a_m \mathbf{U}_m(k_m) \exp(-ik_m x); \quad x \geq x_1, \tag{5.25}$$

where a_m is the amplitude of the mth reflected mode. The reflective wave displacements at the boundary B1 at $x = x_1$ is given by

$$\mathbf{q}^{\text{ref}}(x_1) = \mathbf{\Phi}_1 \mathbf{A} \exp(-ik_m x_1) \tag{5.26}$$

with $\mathbf{\Phi}_1 = [\ \mathbf{U}_1(k_1) \quad \mathbf{U}_2(k_2) \quad \dots \quad \mathbf{U}_M(k_M)\ ]$ and $\mathbf{A}^T = [\ a_1 \quad a_2 \quad \dots \quad a_M\ ]$.
The reflected force field is written as in equation (5.3), as

$$\mathbf{F}^{\text{ref}} = \sum_{m=1}^{M} a_m \psi_m(k_m) \exp(-ik_m x); \quad x \geq x_1. \tag{5.27}$$

Thus, the force field at the boundary B1, at $x = x_1$ is given as

$$\mathbf{F}^{\text{ref}}(x_1) = \mathbf{\Psi}_1 \mathbf{A} \exp(-ik_m x_1), \tag{5.28}$$

where $\mathbf{\Psi}_1 = [\ \psi_1(k_1) \quad \psi_2(k_2) \quad \dots \quad \psi_M(k_M)\ ]$. By taking

$$\mathbf{D}_1 = \mathbf{A}\exp(-ik_m x_1), \tag{5.29}$$

the wave displacement and the force field at the boundary B1 are given by

$$\mathbf{q}^{\text{ref}}(x_1) = \mathbf{\Phi}_1\mathbf{D}_1, \tag{5.30}$$

$$\mathbf{F}^{\text{ref}}(x_1) = \mathbf{\Psi}_1\mathbf{D}_1. \tag{5.31}$$

The wave displacement and the force field at the boundary B1 for the pth incident wave are expressed as

$$\mathbf{q}^{in}(x_1) = a_p^{in}\mathbf{U}_p(-k_p)\exp(-ik_p x_1), \tag{5.32}$$

$$\mathbf{F}^{in}(x_1) = a_p^{in}\psi_p(-k_p)\exp(-ik_p x_1). \tag{5.33}$$

In region B, where $x \leq x_2$, the Lamb waves are being transmitted away. Therefore, following the same approach as the reflected wave displacements, the transmitted wave displacements are given by

$$\mathbf{q}^{\text{trans}} = \sum_{m=1}^{M} b_m\mathbf{U}_m(-k_m)\exp(-ik_m x); \quad x \leq x_2, \tag{5.34}$$

while the transmitted force fields are given as

$$\mathbf{F}^{\text{trans}} = \sum_{m=1}^{M} b_m\psi_m(-k_m)\exp(-ik_m x); \quad x \leq x_2. \tag{5.35}$$

At the boundary B2, where $x = x_2$, the wave displacements and the force fields are given by

$$\mathbf{q}^{\text{trans}}(x_2) = \mathbf{\Phi}_2\mathbf{B}\exp(-ik_m x_2), \tag{5.36}$$

$$\mathbf{f}^{\text{trans}}(x_2) = \mathbf{\Psi}_2\mathbf{B}\exp(-ik_m x_2), \tag{5.37}$$

where

$$\mathbf{\Phi}_2 = [\ \mathbf{U}_1(-k_1) \quad \mathbf{U}_2(-k_2) \quad \dots \quad \mathbf{U}_M(-k_M)\ ],$$

$$\mathbf{\Psi}_2 = [\ \psi_1(-k_1) \quad \psi_2(-k_2) \quad \dots \quad \psi_M(-k_M)\ ],$$

$$\mathbf{B}^T = [\ b_1 \quad b_2 \quad \dots \quad b_M\ ].$$

Then, by taking

$$\mathbf{D}_2 = \mathbf{B}\exp(-ik_m x_2), \tag{5.38}$$

the transmitted wave displacements and the force fields are given as

$$\mathbf{q}^{\text{trans}}(x_2) = \mathbf{\Phi}_2\mathbf{D}_2, \tag{5.39}$$

$$\mathbf{F}^{\text{trans}}(x_2) = \mathbf{\Psi}_2\mathbf{D}_2. \tag{5.40}$$

From the principle of virtual work, the total work in the FE region must be zero. Thus

$$\delta\mathbf{q}^{*T}\mathbf{S}\mathbf{q} - \delta\mathbf{q}_B^{*T}\mathbf{F}_B = 0.$$

The dynamic stiffness matrix $\mathbf{S}$ in this case is written as

$$\mathbf{S} = \mathbf{K} - \omega^2\mathbf{M} = \begin{bmatrix} \mathbf{S}_{II} & \mathbf{S}_{IB_1} & \mathbf{S}_{IB_2} \\ \mathbf{S}_{B_1I} & \mathbf{S}_{B_1B_1} & \mathbf{S}_{B_1B_2} \\ \mathbf{S}_{B_2I} & \mathbf{S}_{B_2B_1} & \mathbf{S}_{B_2B_2} \end{bmatrix} \tag{5.41}$$

where $\mathbf{K}$ and $\mathbf{M}$ are the global stiffness and mass matrix of the FE region, respectively. Substituting equation (5.41) into equation (5.23) gives

$$\mathbf{S}_{II}\mathbf{q}_I + \mathbf{S}_{IB_1}\mathbf{q}_{B_1} + \mathbf{S}_{IB_2}\mathbf{q}_{B_2} = 0, \tag{5.42}$$
$$\mathbf{S}_{IB_1}\mathbf{q}_I + \mathbf{S}_{B_1B_1}\mathbf{q}_{B_1} + \mathbf{S}_{B_1B_2}\mathbf{q}_{B_2} = \mathbf{F}_{B_1}, \tag{5.43}$$
$$\mathbf{S}_{IB_2}\mathbf{q}_I + \mathbf{S}_{B_2B_1}\mathbf{q}_{B_1} + \mathbf{S}_{B_1B_2}\mathbf{q}_{B_2} = \mathbf{F}_{B_2}. \tag{5.44}$$

The total nodal displacements and forces at boundaries B1 and B2 are given as

$$\mathbf{q}_{B_1} = \mathbf{q}^{\text{in}}(x_1) + \mathbf{q}^{\text{ref}}(x_1), \tag{5.45}$$
$$\mathbf{F}_{B_1} = \mathbf{F}^{\text{in}}(x_1) + \mathbf{F}^{\text{ref}}(x_1), \tag{5.46}$$
$$\mathbf{q}_{B_2} = \mathbf{q}^{\text{trans}}(x_2), \tag{5.47}$$
$$\mathbf{F}_{B_2} = -\mathbf{F}^{\text{trans}}(x_2). \tag{5.48}$$

Substituting equations (5.30)-(5.31), (5.32)-(5.33) and (5.39)-(5.40) into equations (5.45)-(5.48) yield

$$\mathbf{A}_{11}\mathbf{D}_1(x_1) + \mathbf{A}_{12}\mathbf{D}_2(x_2) = \mathbf{C}_1, \tag{5.49}$$
$$\mathbf{A}_{21}\mathbf{D}_1(x_1) + \mathbf{A}_{22}\mathbf{D}_2(x_2) = \mathbf{C}_2, \tag{5.50}$$

where

$$\begin{aligned}
\mathbf{A}_{11} &= \left[\mathbf{S}_{B_1B_1} - \mathbf{S}_{B_1I}(\mathbf{S}_{II})^{-1}\mathbf{S}_{IB_1}\right]\mathbf{\Phi}_1 - \mathbf{\Psi}_1, \\
\mathbf{A}_{12} &= \left[\mathbf{S}_{B_1B_2} - \mathbf{S}_{B_1I}(\mathbf{S}_{II})^{-1}\mathbf{S}_{IB_2}\right]\mathbf{\Phi}_2, \\
\mathbf{A}_{21} &= \left[\mathbf{S}_{B_2B_1} - \mathbf{S}_{B_2I}(\mathbf{S}_{II})^{-1}\mathbf{S}_{IB_1}\right]\mathbf{\Phi}_1, \\
\mathbf{A}_{22} &= \left[\mathbf{S}_{B_2B_2} - \mathbf{S}_{B_2I}(\mathbf{S}_{II})^{-1}\mathbf{S}_{IB_1}\right]\mathbf{\Phi}_2 + \mathbf{\Psi}_2, \\
\mathbf{C}_1 &= \mathbf{F}^{\text{in}}(x_1) - \left[\mathbf{S}_{B_1B_1} - \mathbf{S}_{B_1I}(\mathbf{S}_{II})^{-1}\mathbf{S}_{IB_1}\right]\mathbf{q}^{\text{in}}(x_1), \\
\mathbf{C}_2 &= -\left[\mathbf{S}_{B_2B_1} - \mathbf{S}_{B_2I}(\mathbf{S}_{II})^{-1}\mathbf{S}_{IB_1}\right]\mathbf{q}^{\text{in}}(x_1).
\end{aligned}$$

Rewritten in a short form gives

$$\mathbf{AD} = \mathbf{C}, \tag{5.51}$$

with

$$\begin{aligned}
\mathbf{A} &= \begin{bmatrix} \mathbf{A}_{11} & \mathbf{A}_{12} \\ \mathbf{A}_{21} & \mathbf{A}_{22} \end{bmatrix}, \\
\mathbf{D}^T &= \begin{bmatrix} \mathbf{D}_1^T(x_1) & \mathbf{D}_2^T(x_2) \end{bmatrix}^T, \\
\mathbf{C}^T &= \begin{bmatrix} \mathbf{C}_1^T & \mathbf{C}_2^T \end{bmatrix}^T.
\end{aligned}$$

The incident wave displacement and the force field are known. Therefore, by solving (5.51), the amplitudes A_m and B_m are calculated from $\mathbf{D}_1$ and $\mathbf{D}_2$ in equations (5.29)

and (5.38), respectively. The solutions should fullfill the energy conservation and the reciprocity relationships as in section 5.2.2. However, in the case of general obstacle on the plate, the energy conservation relationship becomes

$$\mathbf{I}_p^{\text{in}} = \mathbf{I}_{pn}^{\text{ref}} + \mathbf{I}_{pn}^{\text{trans}}. \tag{5.52}$$

The percentage of error in the energy balance is given by

$$\epsilon = \left[\mathbf{I}_p^{\text{in}} - \sum_{n=1}^{N_{pr}} \mathbf{I}_{pn}^{\text{ref}} - \sum_{n=1}^{N_{pt}} \mathbf{I}_{pn}^{\text{trans}} \right] \frac{100}{\mathbf{I}_p^{\text{in}}}, \tag{5.53}$$

where N_{pr} and N_{pt} are the number of reflected and transmitted propating modes, respectively.

5.4.1 Verifications

The easiest numerical check for the coupled SAFE-FE method is by modelling a plate free from an obstacle. The left and right infinite plate regions are modelled using the SAFE method while the FEM is used to model the middle plate region as shown in Figures A.4(a) and A.3(a) in Appendix A. A 1mm thick aluminum plate is used with a mesh density of 10 quadratic elements per mm. Both, the S_0 and the A_0 modes, are used as the incident wave. There is no feature that would reflect the incident Lamb waves. Thus, the obtained transmitted wave should be the same as the the incident wave. Good result are obtained as shown in Figures A.3 and A.4, respectively. The absolute value for the percentage of the energy error is around the computational error (in order of 10^{-12}).

5.4.2 Application examples

In the following examples, the type of plate, the element types and sizes, and the considered frequency ranges are the same as applied in the section 5.3.2. The obstacle region is modelled using the FEM while the infinite plate regions are modelled using the SAFE method. The mass and stiffness matrices of the obstacle region are obtained from the Abaqus software. The number of degrees of freedom at the boundaries between the FE and the SAFE regions are set to be equal.

5.4.2.1 Symmetric and unsymmetric obstacles

Symmetric and unsymmetric obstacles are considered as shown in Figures 5.8, 5.9 and 5.10. Until the frequency of 4.5MHz, only three symmetric modes and two anti-symmetric modes exist. It is shown, that the symmetric obstacles reflect and transmit the same type of modes as the incident mode for both the anti-symmetric A_0 mode and the symmetric S_0 mode incident waves in Figures 5.8 and 5.9, respectively. Although only shown here for the A_0 mode incident wave as in Figure 5.10, unsymmetrical obstacles reflect and

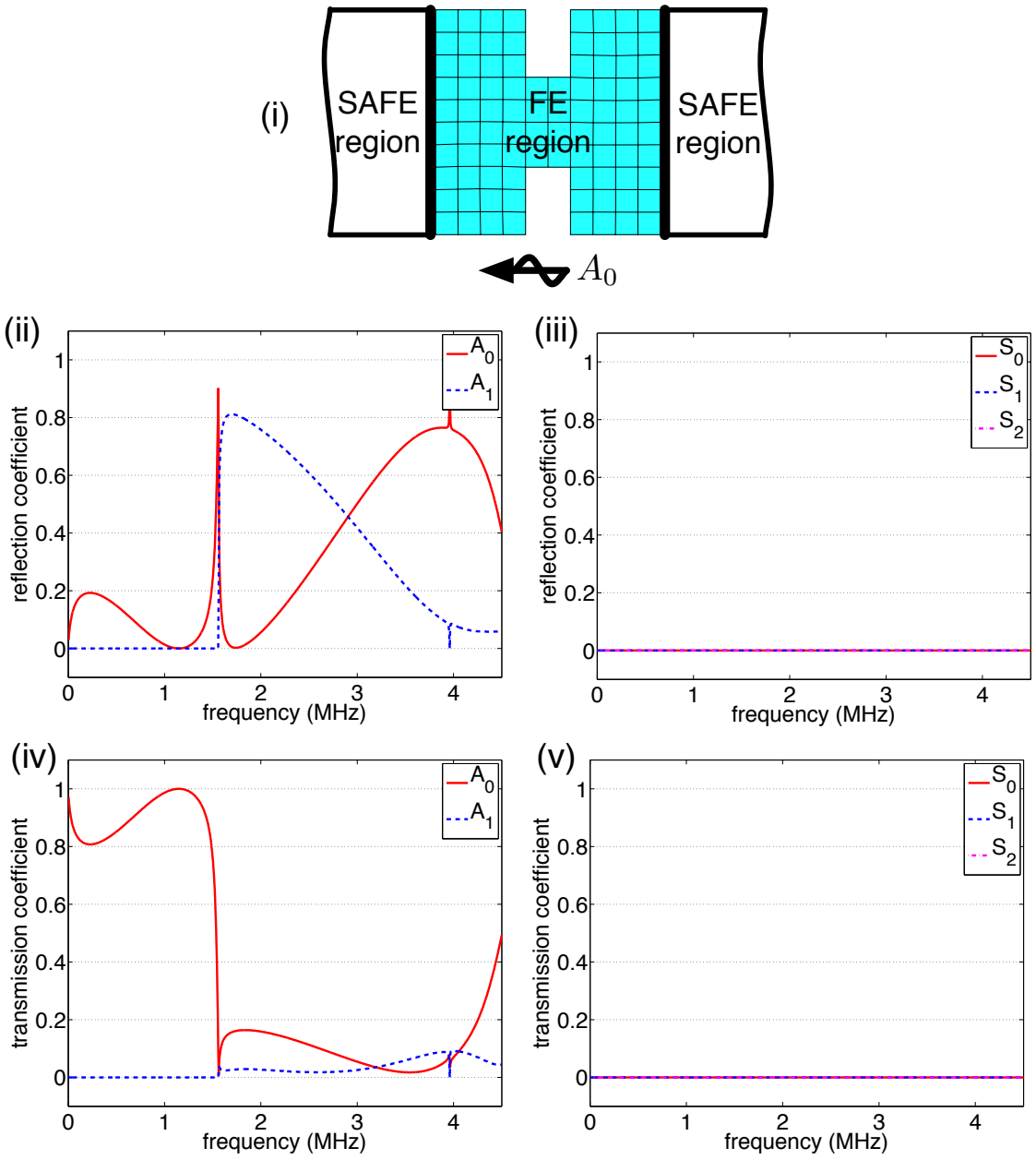

FIGURE 5.8: A_0 incident wave at a symmetric obstacle. Subfigures show (i) SAFE-FE model (ii) Anti-symmetric modes reflection, (iii) Symmetric modes reflection, (iv) Anti-symmetric modes transmission, and (v) Symmetric modes transmission.

transmit both symmetric and anti-symmetric modes for both types of incident modes. More obstacle examples are given in Appendix A. Therefore, it can be concluded that mode conversions only occur when the obstacles are unsymmetrical. This fact is in agreement with the FE simulations done in [166], on the effects of the local stiffness changes in the plates whereby the existence of the mode conversions is probed using a 2D FFT technique.

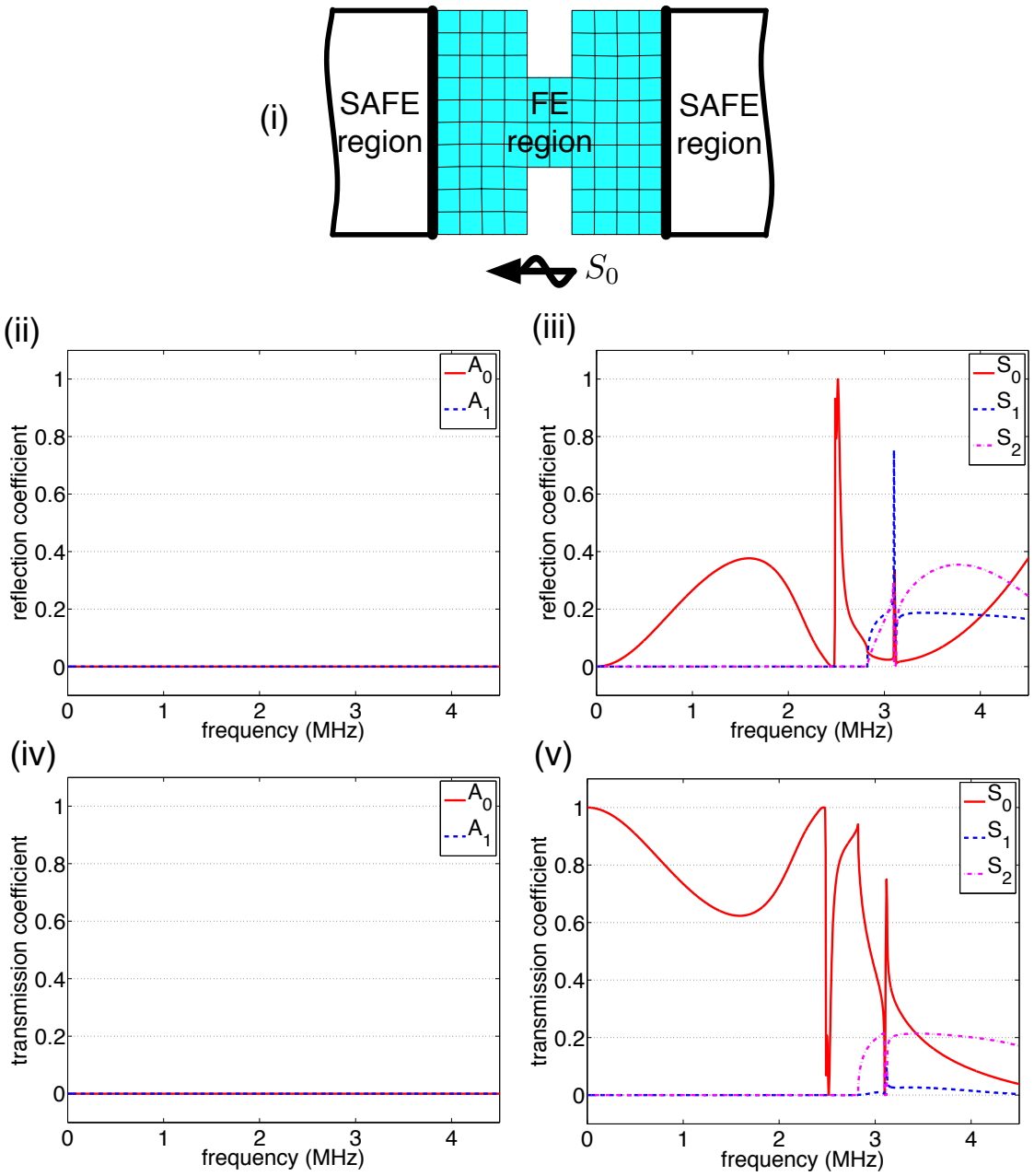

FIGURE 5.9: S_0 incident wave at a symmetric obstacle. Subfigures show (i) SAFE-FE model (ii) Anti-symmetric modes reflection, (iii) Symmetric modes reflection, (iv) Anti-symmetric modes transmission, and (v) Symmetric modes transmission.

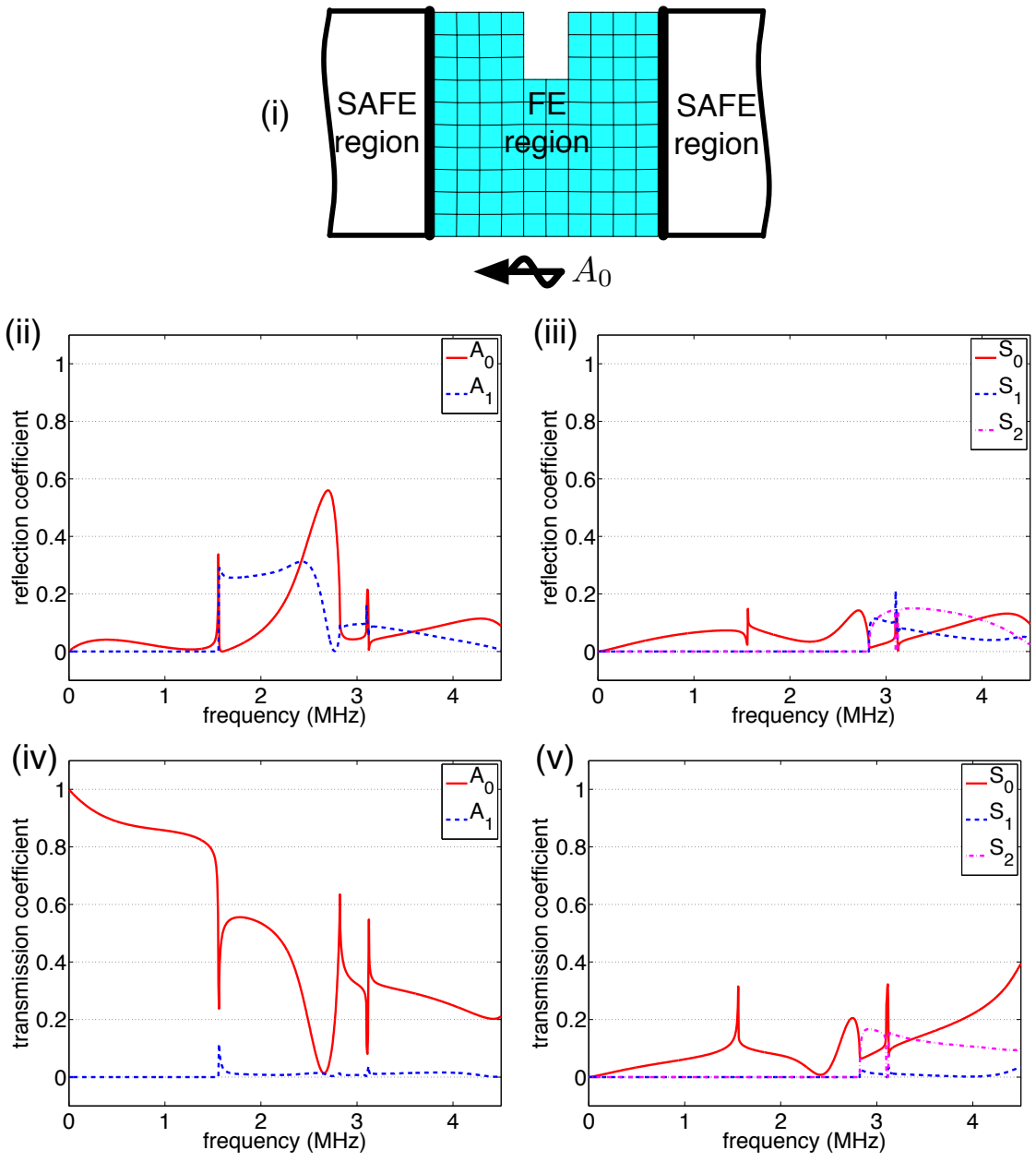

FIGURE 5.10: A_0 incident wave at an unsymmetrical obstacle. Subfigures show (i) SAFE-FE model (ii) Anti-symmetric modes reflection, (iii) Symmetric modes reflection, (iv) Anti-symmetric modes transmission, and (v) Symmetric modes transmission.

5.4.2.2 Transducers

Consider the case of a S_0 mode incident wave propagating to a transducer fully attached to the top surface of an aluminum plate with thickness $h = 1$mm as shown in Figure 5.11. This attachment is typical in SHM applications. Thus, the transducer becomes an unsymmetric obstacles to the Lamb wave propagation. The S_0 mode is selected as it has

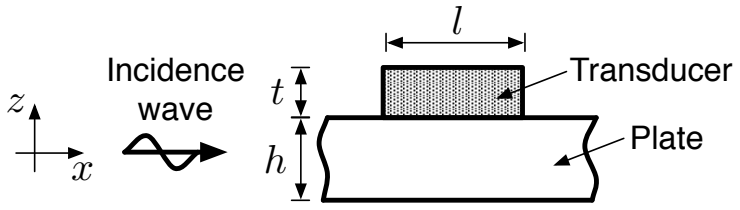

FIGURE 5.11: A transducer attached on the top surface of the plate.

a quasi non-dispersive region at low frequencies. The transducer length and thickness are $l = 0.8$mm and $t = 0.1$mm, respectively. Three transducer configurations are used:

(a) The transducer has the same density as the plate, but with lower Young's modulus, $E_{\text{trans}} = 0.01E_{\text{plate}}$.

(b) The transducer has the same Young's modulus as the plate, but with lower density, $\rho_{\text{trans}} = 0.1\rho_{\text{plate}}$.

(c) The transducer has both, lower Young's modulus and lower density, $E_{\text{trans}} = 0.01E_{\text{plate}}$ and $\rho_{\text{trans}} = 0.1\rho_{\text{plate}}$.

These configurations are selected to see the effects of transducer mass and stiffness on the wave reflections and transmissions. The maximum frequency considered is 1.5MHz. The reflection and transmission coefficients for configurations (a), (b) and (c) are shown in Figure 5.12. It is shown, that transducers with a lower Young's modulus than the plate (config.(a)) cause some spikes in the reflection and transmission coefficients. On the other hand, when the transducer has a lower density than the plate (config.(b)), there are no reflections and mode changes. The same results are obtained for config.(c), when the transducers have both, a lower Young's modulus and a lower density, than the plate. Therefore, having transducers as light as possible is a better design decision in SHM, as the wave propagations are not interrupted in the lower frequency range. This results also suggest, that having lighter transducers is much more important than having less stiffer transducers.

Next, the effect of transducer thickness on the Lamb wave propagation is considered. Five transducer thicknesses t are chosen; 0.2mm, 0.4mm, 0.8mm, 1mm and 2mm. The width of the transducers are 0.8mm. These transducers are attached to a 1mm thick aluminum plate. The Young's modulus and the density of the transducer with a thickness of 0.2mm are set equal to the aluminum plate. The mass of the transducers with other thickness values are maintained by reducing the density correspondingly. The S_0 mode is used as the incident wave. The maximum frequency considered is 1.5MHz. There are only A_0

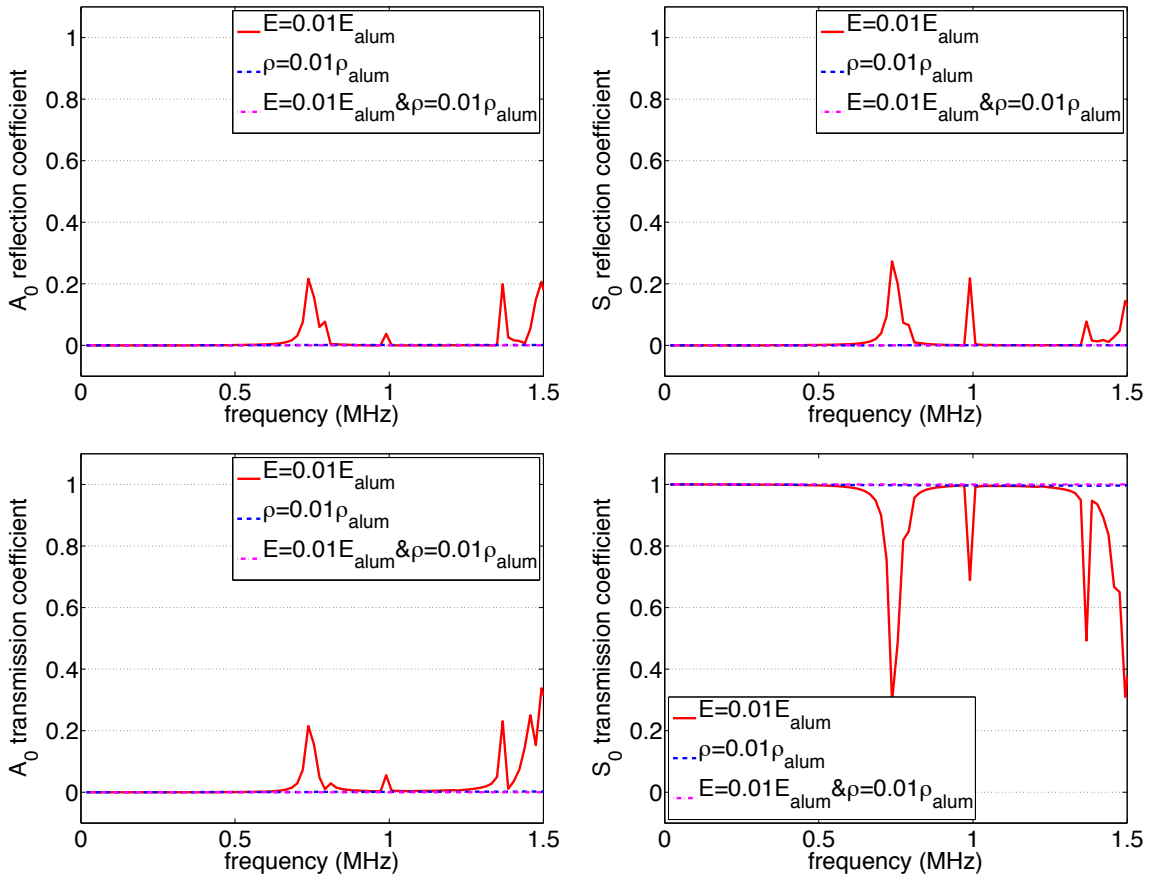

FIGURE 5.12: Mode reflections and transmissions for transducers with configurations (a)–, (b)- - and (c)-.- until the frequency of 1.5MHz.$h_{\text{trans}} = 0.1$mm and $l_{\text{trans}} = 0.8$mm.

and S_0 modes at this frequency range. Figure 5.13 shows the effects of the transducers height changes on the wave reflections and transmissions. By increasing the transducer thickness, the frequencies at the regions of high reflection and transmission of the A_0 mode are getting lower. This is undesirable. On the other hand, the effects on the S_0 mode reflection are less at a lower frequency range. We want less reflections and transmissions from the A_0 mode and also less reflections from S_0 mode at a lower frequency range. Thus, from this analysis, it follows that thinner transducers are a better design consideration as there are fewer reflections and transmissions of the A_0 mode at a lower frequency range.

The effect of the transducer width on the Lamb wave propagation is considered next. Five transducers with a width d are chosen; 1mm, 0.8mm, 0.6mm, 0.4mm and 0.2mm. The thickness of the transducers are 0.2mm. These transducers are attached to a 1mm thick aluminum plate. The Young's modulus and the density of the transducer with width 1mm are set equal to the aluminum plate. The mass of the transducers with other thickness values are maintained by increasing the density correspondingly. The S_0 mode is used as the incident wave. Figure 5.14 shows the effects of the transducers width changes on the wave reflections and transmissions. By reducing the transducer width, the regions with high reflection coefficient for the A_0 and the S_0 modes move toward lower frequencies.

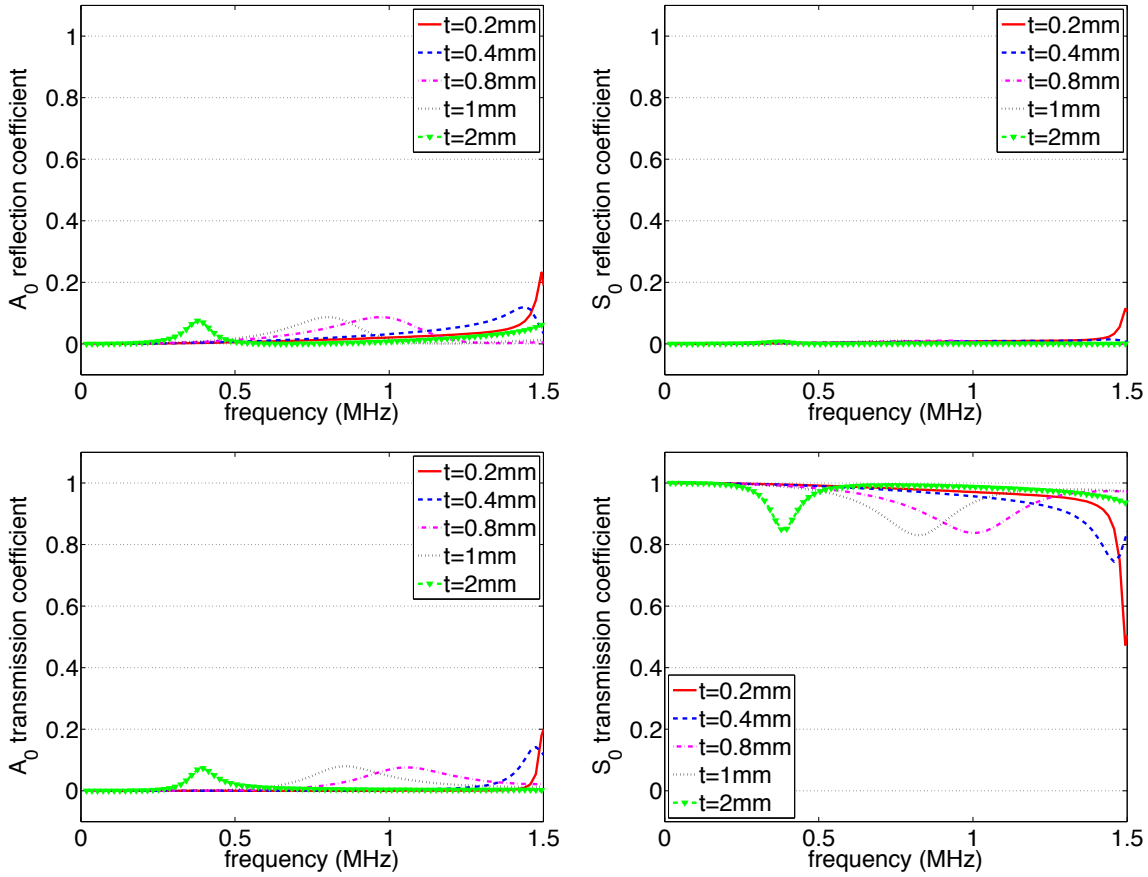

FIGURE 5.13: Mode reflections and transmissions for transducers with different thickness t until frequency 1.5MHz.

This is undesirable in SHM application. Thus, for the same masses, transducers with larger width are a better design consideration than transducers with smaller width.

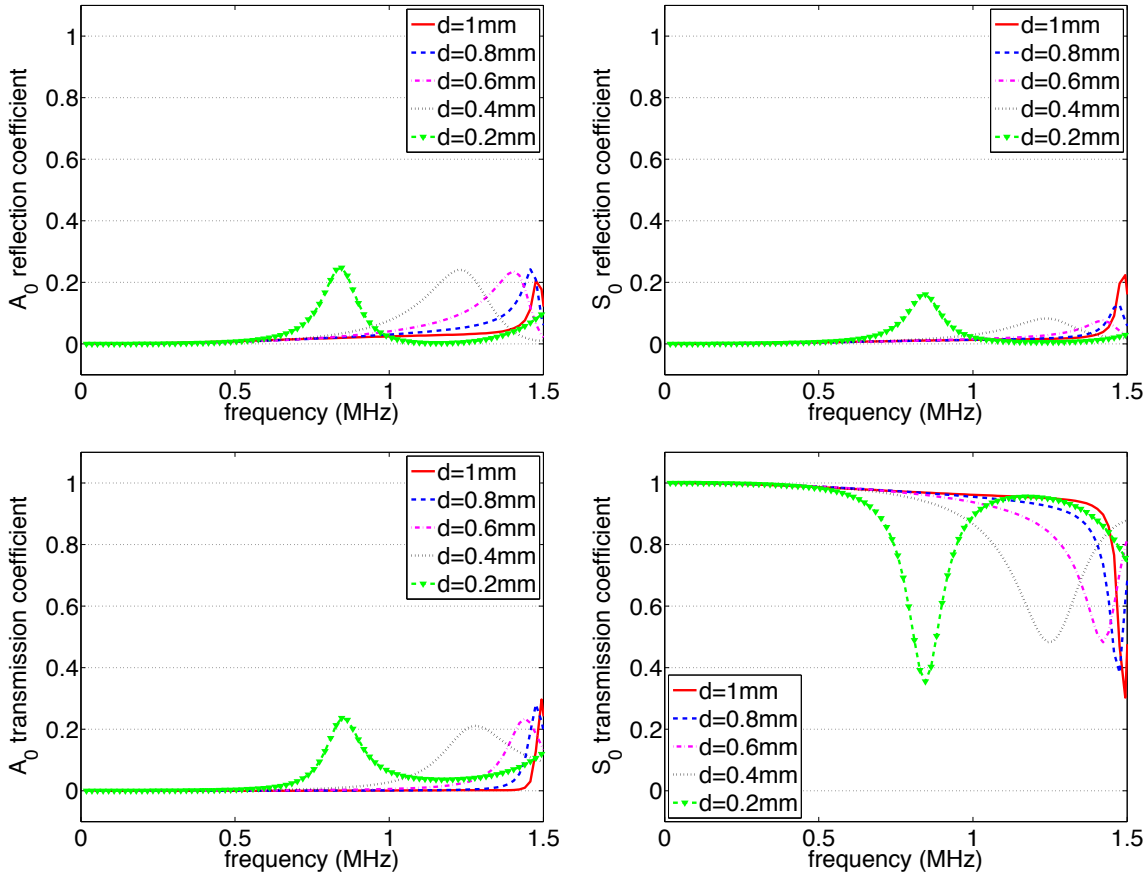

FIGURE 5.14: Mode reflections and transmissions for transducers with different width d until the frequency of 1.5MHz.

5.4.2.3 Stiffeners

Stiffeners are used to strengthen the plate structures without causing severe weight penalties. Thus, their usage are popular in the aircraft industries. Stiffeners are available in many shapes. Here, effects of the stiffener shapes on the Lamb wave reflections and transmissions in isotropic plates are studied. The mass of the different transducer shapes are keep constant to remove the influence of stiffener mass. These stiffeners are assumed to be not fully rigid, thus allowing the transmissions of Lamb waves. They are also assumed to be fully attached to the plate and the effects of attachment components (i.e rivets or bolts) are neglected. Five stiffener shapes are considered as shown in Figure 5.15. The stiffeners are attached to a 1mm thick aluminum plate. Each stiffener is 1mm thick and is made from aluminum. The S_0 mode is used as the incidence wave. The maximum frequency considered is 1MHz. The stiffeners and plates are modelled using square CPE4 elements in Abaqus with the element lengths of 0.2mm. The results of the reflection and the transmission coefficients of the stiffeners are given in Figure 5.16. The reflection and transmission behaviors are complex even at a low frequency range. However, the reflected and transmitted coefficients are larger for the S_0 mode which is the incidence wave. No clear indication of the different stiffener shapes can be seen on the reflection and transmission coefficients. However, as all stiffener have the same mass, the overall trend of

the reflection and transmission coefficients are about the same, even for different stiffener shapes.

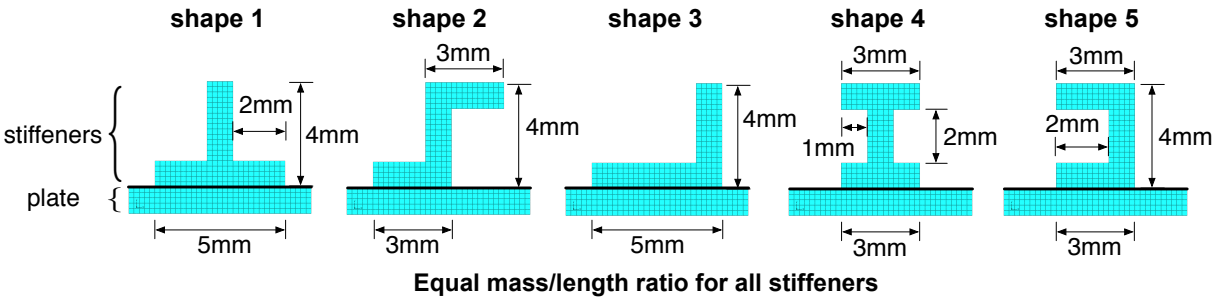

FIGURE 5.15: Five different stiffener shapes considered.

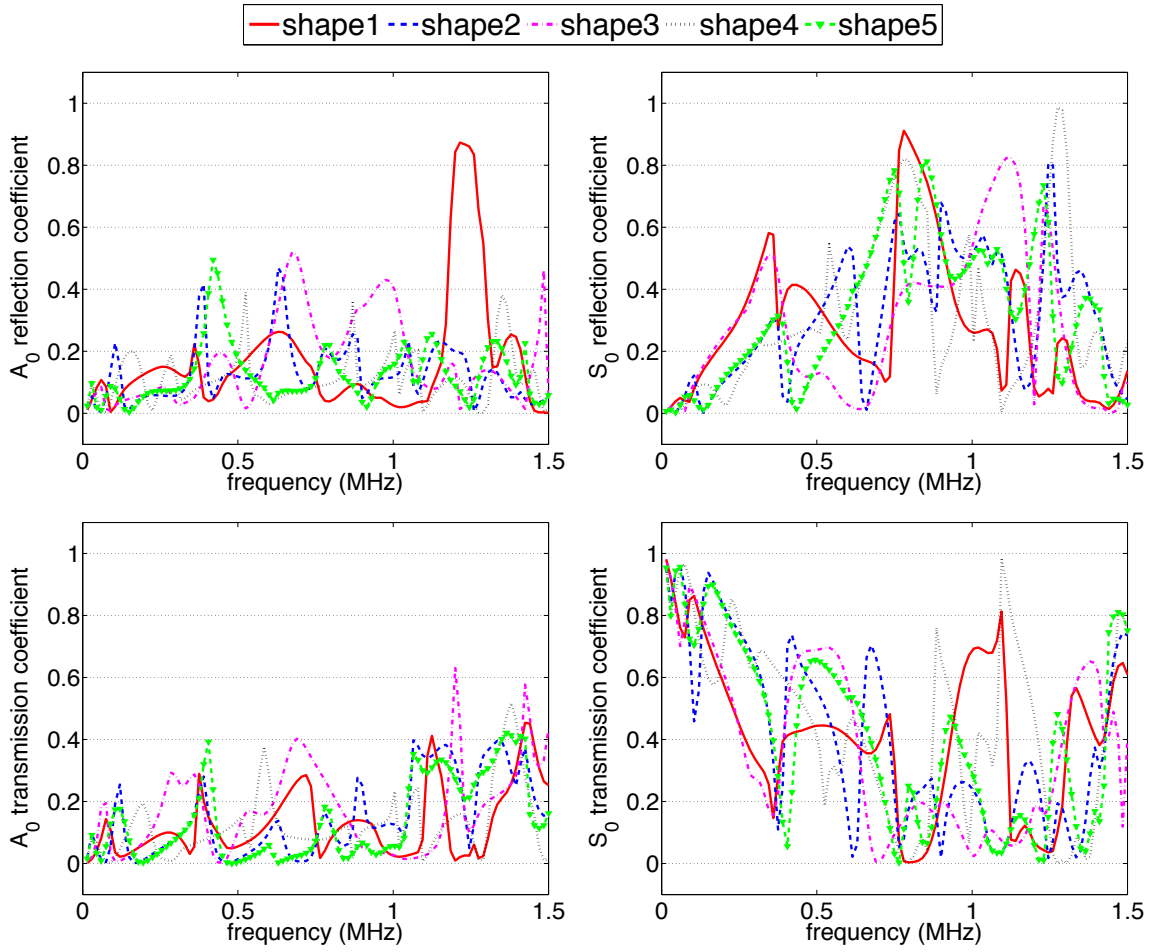

FIGURE 5.16: Mode reflections and transmissions for different stiffener shapes until the frequency of 1.5MHz.

The stiffener shape 1 and 3 have a larger base (5mm) than the other shapes (3mm). However, there is no clear trend in the reflection and transmission coefficients that separate the results of the larger base stiffeners than the lower base stiffeners. The reflections inside the stiffener plays a bigger role than the the coupling region between stiffeners and plate.

Chapter 6

Lamb wave actuation and sensing

6.1 Introduction

In the force response analysis, point forces are being considered as any forces can be decomposed into the point forces as applied in the FEM. This chapter starts with a two dimensional (2D) point force response analysis using the SAFE method. The point force response analysis is then extended to three dimensional (3D) by applying the 2D point force response analysis results and the stationary phase method. An approach to simulate the effect of plate edges is presented. Several application examples are then shown for the Lamb waves actuation and sensing simulations.

6.2 2D point force response

In the 2D point force response formulation, the approaches in [154, 155] are followed. We consider the case of a general 2D external force vector $\mathbf{f}^{(2D)}(t)$ acting on the plate as shown in Figure 6.1. The frequency component of this force can be obtained by applying Fourier transform as

$$\overline{\mathbf{f}}^{(2D)}(\omega) = \int_{-\infty}^{\infty} \mathbf{f}^{(2D)}(t) \exp(-i\omega t) \mathrm{d}t.$$

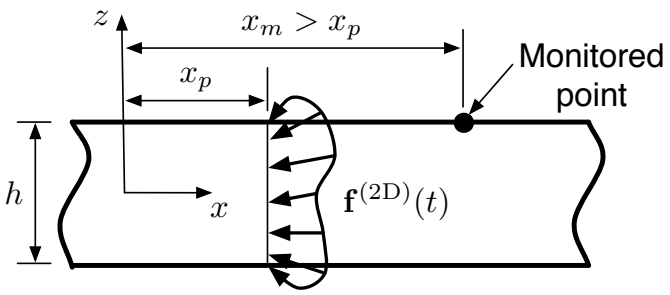

FIGURE 6.1: 2D system geometry

This transformation is done numerically using Fast Fourier Transform (FFT). The linear form of the SAFE equation, eq.(3.24), is written with the external force vector $\mathbf{F}$ for each circular frequency ω as follows

$$(\mathbf{A} - k\mathbf{B}(\omega))\mathbf{Q} = \mathbf{F}(\omega), \tag{6.1}$$

where $\mathbf{F}(\omega) = \begin{Bmatrix} \overline{\mathbf{f}}^{(2D)}(\omega) \\ \mathbf{0} \end{Bmatrix}$. Component of the force vector, $\overline{\mathbf{f}}_j^{(2D)}$, is non zero at the jth degrees of freedom where the force is being applied. The solution of equation (6.1) is written in terms of an eigenvector expansion [167] as

$$\mathbf{u}^{(2D)}(k,\omega) = \sum_{r=1}^{6N} \frac{1}{k_r - k} \cdot \mathbf{Q}_r \cdot \frac{\mathbf{Q}_r^T \mathbf{F}}{\mathbf{Q}_r^T \mathbf{B} \mathbf{Q}_r}. \tag{6.2}$$

The spatial Fourier transform and the inverse Fourier transform are defined in [154, 156], respectively as

$$\mathbf{u}(k,\omega) = \int_{-\infty}^{\infty} \mathbf{u}(x,\omega) e^{ikx} \mathrm{d}x,$$

$$\mathbf{u}(x,\omega) = \frac{1}{2\pi} \int_{-\infty}^{\infty} \mathbf{u}(k,\omega) e^{-ikx} \mathrm{d}k.$$

Thus, the solution in the x domain is obtained by applying the inverse Fourier transform to eq.(6.2) giving

$$\mathbf{u}^{(2D)}(x,\omega) = \frac{1}{2\pi} \sum_{r=1}^{6N} \int_{-\infty}^{+\infty} \frac{1}{k_r - k} \cdot \mathbf{Q}_r \cdot \frac{\mathbf{Q}_r^T \mathbf{F}}{\mathbf{Q}_r^T \mathbf{B} \mathbf{Q}_r} \exp\left(-ik_r x\right) \mathrm{d}k. \tag{6.3}$$

Equation (6.3) above is solved by using Cauchy's residual theorem to obtain the solution in the spatial domain. The solution depends on the location of the monitored point x_m with respect to the excitation point, x_p. For $x_m > x_p$ gives

$$\mathbf{u}^{(2D)}(x,\omega)\big|_{x_m > x_p} = -i \sum_{r=1}^{3N} \mathbf{Q}_r \cdot \frac{\mathbf{Q}_r^T \mathbf{F}}{\mathbf{Q}_r^T \mathbf{B} \mathbf{Q}_r} \exp\left(-ik_r x\right) \tag{6.4}$$

where $x = x_m - x_p$. The summation is made over the modes r which are the modes with real wavenumbers and non real wavenumbers with positive imiginary part. These wavenumbers are selected to ensure bounded displacements. The total number of these modes are $3N$ with N as the number of nodes. The integration contours for the Cauchy residual theorem and the obtained equations for $x_m > x_p$, $x_m < x_p$ and $x_m = x_p$ are shown in Table B.1 in Appendix B. The time domain response is then computed by using the inverse Fourier transform as

$$\mathbf{u}^{(2D)}(x,t) = \frac{1}{2\pi} \int_{-\infty}^{\infty} \mathbf{u}(x,\omega) \exp\left(i\omega t\right) \mathrm{d}\omega. \tag{6.5}$$

This integration is solved numerically by using the inverse FFT.

An alternative formulation is used to get the relationship between 2D and 3D force response analysis as shown later in section 6.3. In this alternative formulation the relationship between $\mathbf{u}^{(2D)}(x,\omega)$ and $\bar{\mathbf{f}}^{(2D)}(\omega)$ can be written as the convolution integral

$$\mathbf{u}^{(2D)}(x,\omega) = \int \mathbf{g}(x-\bar{x},\omega)\cdot\bar{\mathbf{f}}^{(2D)}(\bar{x},\omega)\mathrm{d}\bar{x}, \tag{6.6}$$

where $\mathbf{g}^{(2D)}(x-\bar{x},\omega)$ is the 2D Green's function [82]. $\mathbf{g}^{(2D)}$ can be written in terms of the one dimensional Fourier transform $\mathbf{G}^{(2D)}$ as

$$\mathbf{g}^{(2D)}(x,\omega) = \frac{1}{2\pi}\int_{-\infty}^{\infty}\mathbf{G}^{(2D)}(k,\omega)\exp\left(-ikx\right)\mathrm{d}k. \tag{6.7}$$

Applying the residue theorem, the integral in equation 6.7 can be solved as the sums of residuals for each mode r. For a monitored point located at $x_m > x_p$ as an example, it yields

$$\mathbf{g}^{(2D)}(x,\omega) = \sum_{r=1}^{3N}\mathbf{E}_r^{(2D)}(x,\omega)\exp\left(-ik_r x\right), \tag{6.8}$$

where

$$\mathbf{E}_r^{(2D)}(x,\omega) = -i\ \mathrm{res}\ \mathbf{G}^{(2D)}(k,z)\big|_{k=k_r}. \tag{6.9}$$

$\mathbf{E}_r^{(2D)}$ is defined as 2D modal excitability matrix. The same types of modes as before are selected. From the reciprocity approach, $\mathbf{E}_r^{(2D)}$ can be obtained as [168]

$$\mathbf{E}_r^{(2D)}(x,\omega) = -\frac{i\omega}{4P_r}\mathbf{U}_r\cdot\mathbf{U}_r^{*T}, \tag{6.10}$$

where superscript * denotes complex conjugate, the superscript T represents the matrix transpose and $\mathbf{U}_r$ is the eigenvector for the rth mode. P_r is the energy flux of the mode given by the equation 5.15.

6.3 3D point force response

In the 3D point force response analysis, the 2D point force response solution is used in combination with stationary phased method as shown in [82]. A multi-layered plate with Cartesian coordinates (x,y,z) is considered with the z axis normal to the surface. The source is modeled by a force distribution acting on the upper surface of the plate at $z=0$ as shown in Figure 6.2.

The frequency component of this force can be obtained by applying the Fourier transform as

$$\bar{\mathbf{f}}^{(3D)}(\omega) = \int_{-\infty}^{\infty}\mathbf{f}^{(3D)}(t)\exp\left(-i\omega t\right)\mathrm{d}t.$$

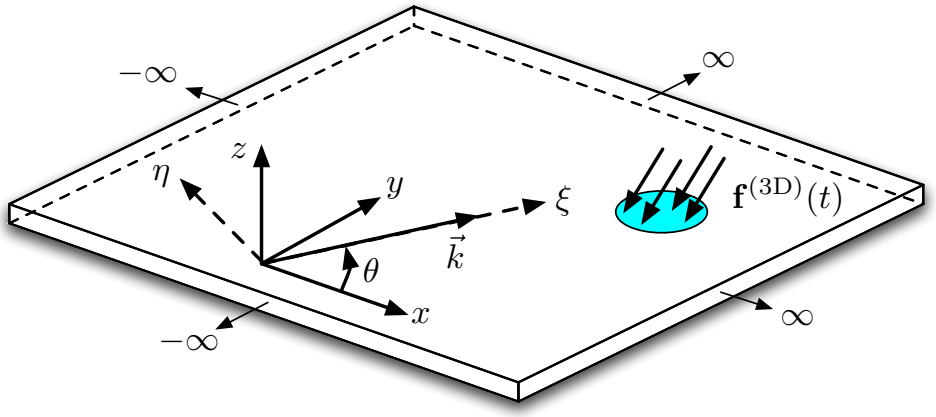

FIGURE 6.2: 3D system geometry

The relationship between $\mathbf{u}^{(3D)}(x, y, z, \omega)$ and $\overline{\mathbf{f}}^{(3D)}(\omega)$ can be written as the convolution integral

$$\mathbf{u}^{(3D)}(x, y, z, \omega) = \int\int \mathbf{g}^{(3D)}(x - \bar{x}, y - \bar{y}, z, \omega) \cdot \overline{\mathbf{f}}^{(3D)}(\bar{x}, \bar{y}, z, \omega) \mathrm{d}\bar{x}\mathrm{d}\bar{y}, \tag{6.11}$$

where $\mathbf{g}^{(3D)}(x - \bar{x}, y - \bar{y}, z, \omega)$ is the 3D Green's function of the system. This function can be expressed from its two dimensional spatial Fourier transform $\mathbf{G}^{(3D)}$ as

$$\mathbf{g}^{(3D)}(x, y, z, \omega) = \frac{1}{(2\pi)^2} \int\int \mathbf{G}^{(3D)}(k_x, k_y, z, \omega) e^{-i(k_x x + k_y y)} \mathrm{d}k_x \mathrm{d}k_y, \tag{6.12}$$

where $\mathbf{G}^{(3D)}(k_x, k_y, z, \omega)$ stands for the Green's function for plane waves propagating in the direction given by the wave vector $\mathbf{k}(k_x = k\cos\theta, k_y = k\sin\theta, 0)$, where θ is the angle between the direction of the phase velocity and the axis x as shown in Figure 6.3.

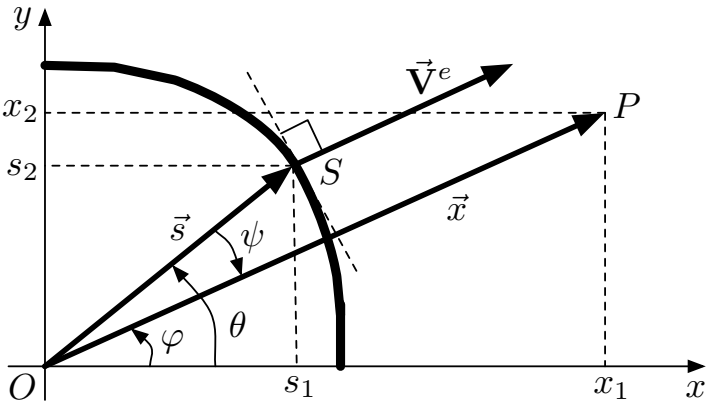

FIGURE 6.3: At the stationary phase point S, the energy velocity $\mathbf{V}^e$ is normal to the slowness curve $s(\theta)$, the slowness curve is an inverse of the phase velocity curve.

For a given source/receiver configuration defined by the distance $r = |\vec{OP}|$ and the angle φ with $x_1 = r\cos\varphi, x_2 = r\sin\varphi$, the Green's function can be written as

$$\mathbf{g}^{(3D)}(r,\varphi,z,\omega) = \frac{1}{(2\pi)^2}\int_{\varphi-\pi/2}^{\varphi+3\pi/2}\int_{\Gamma}\mathbf{G}^{(3D)}(k\cos\theta, k\sin\theta, z, \omega)\times e^{-ikr\cos\psi}k\mathrm{d}k\mathrm{d}\theta, \quad (6.13)$$

where Γ is the domain of real positive half axis and $\psi = \varphi - \theta$. The integral with respect to θ is divided into two parts (i) from $\varphi - \pi/2$ to $\varphi + \pi/2$, and (ii) from $\varphi + \pi/2$ to $\varphi + 3\pi/2$, where in the second part, θ is changed to $(\theta + \pi)$ and k to $-k$. Thus, the Green's function can be rewritten as

$$\mathbf{g}^{(3D)}(r,\varphi,z,\omega) = \frac{1}{(2\pi)^2}\int_{\varphi-\pi/2}^{\varphi+\pi/2}\int_{\Gamma\cup-\Gamma}\mathbf{G}^{(3D)}(k\cos\theta, k\sin\theta, z, \omega)\times e^{-ikr\cos\psi}k\mathrm{d}k\mathrm{d}\theta. \quad (6.14)$$

Only real values of wavenumber k are being considered. In the far field, the contributions of complex wavenumbers can be neglected as the corresponding modes have a larger order of decay [158]. Using the residue theorem, the Green's function for the propagative modes M is given by

$$\mathbf{g}^{(3D)}(r,\varphi,z,\omega) = \frac{1}{2\pi}\sum_{M}\int_{\varphi-\pi/2}^{\varphi+\pi/2}\mathbf{G}_M^{(3D)}(\theta,z,\omega)|k_M(\theta)|e^{-ik_M r\cos\psi_M}\mathrm{d}\theta, \quad (6.15)$$

where

$$\mathbf{G}_M^{(3D)}(\theta,z,\omega) = -i\,\mathrm{res}\left[\mathbf{G}^{(3D)}(k\cos\varphi, k\sin\varphi, z, \omega)\right]_{k=k_M(\theta)}. \quad (6.16)$$

For each Lamb mode and for a given direction of observation φ, the integral with respect to θ can be evaluated by the stationary phase method. Only the contribution of the angle θ for which the phase $\Phi_M(\theta) = k_M r\cos\psi$ varies slowly is considered. The first derivative of the phase Φ_M with respect to θ is given by

$$\frac{\mathrm{d}\Phi_M}{\mathrm{d}\theta} = \frac{\mathrm{d}k_M}{\mathrm{d}\theta}r\cos\psi_M + k_M r\sin\psi_M = 0, \quad (6.17)$$

and it vanishes for a value of θ_M such that

$$\frac{\mathrm{d}k_M}{\mathrm{d}\theta} = -k_M\tan\psi_M \qquad \text{with} \qquad \psi = \varphi - \theta. \quad (6.18)$$

Thus, the relationship between φ and θ can be obtained as

$$\varphi = \theta + \arctan\left[\frac{c_p'}{c_p}\right], \quad (6.19)$$

where $c_p' = \frac{\mathrm{d}c_p}{\mathrm{d}\theta}$.

It is assumed that there will only be one stationary phase point S (valid for isotropic and quasi-isotropic plates [158]). In this case, the slowness curve is convex for all θ, and equation (6.18) defines a one-to-one relation between angles φ and θ.

From equation (6.17) and for a given angle φ, the second order derivative of the phase is given by

$$\frac{\mathrm{d}^2\Phi_M}{\mathrm{d}\theta^2} = \left(\frac{\mathrm{d}^2 k_M}{\mathrm{d}\theta^2} + 2\frac{\mathrm{d}k_M}{\mathrm{d}\theta}\tan\psi_M - k_M\right) r\cos\psi_M. \tag{6.20}$$

Substituting the second order derivative of k_M, deduced from equation (6.18),

$$\frac{\mathrm{d}^2 k_M}{\mathrm{d}\theta^2} = -\frac{\mathrm{d}k_M}{\mathrm{d}\theta}\tan\psi_M - \frac{k_M}{\cos^2\psi_M}\left(\frac{\mathrm{d}\varphi}{\mathrm{d}\theta} - 1\right), \tag{6.21}$$

into equation (6.18) leads to

$$\frac{\mathrm{d}^2\Phi_M}{\mathrm{d}\theta^2} = \left(\frac{\mathrm{d}k_M}{\mathrm{d}\theta}\tan\psi_M + k_M\tan^2\psi_M - \frac{k_M}{\cos^2\psi_M}\frac{\mathrm{d}\varphi}{\mathrm{d}\theta}\right) \times r\cos\psi_M. \tag{6.22}$$

Since, from equation (6.17), the first two terms in brackets are opposite, the second order derivative of the phase Φ_M reduces to

$$\Phi_M'' = \left(\frac{\mathrm{d}^2\Phi_M}{\mathrm{d}\theta^2}\right)_{\varphi} = -\frac{-k_M r}{\cos\psi_M}\frac{\mathrm{d}\varphi}{\mathrm{d}\theta}, \tag{6.23}$$

which can be alternatively written as [82]

$$\Phi_M'' = -\frac{\omega}{c_p\sqrt{c_p^2 + (c_p')^2}}(c_p'' + c_p)\bigg|_{\theta=\theta_M}. \tag{6.24}$$

Substituting in equation (6.16), $\Phi_M(\theta)$ by its second order Taylor expansion yields

$$\mathbf{g}^{(3\mathrm{D})}(r,\varphi,x_3,\omega) = \frac{1}{2\pi}\sum_M \mathbf{G}_M^{(3\mathrm{D})}(\theta_M,x_3,\omega) \times |k_M| e^{-i\Phi_M} \int_{\varphi-\pi/2}^{\varphi+\pi/2} \mathbf{e}^{-i(\Phi_M''/2)(\theta-\theta_M)^2}\mathrm{d}\theta, \tag{6.25}$$

and finally

$$\mathbf{g}^{(3\mathrm{D})}(r,\varphi,x_3,\omega) = \frac{1}{\sqrt{r}}\sum_M \mathbf{B}_M \mathbf{G}_M^{(3\mathrm{D})}(\theta_M,z,\omega) e^{-ir\Phi_M}, \tag{6.26}$$

where $\mathbf{B}_M$ is defined as

$$\mathbf{B}_M = \frac{|k_M|}{\sqrt{2\pi|\Phi_M''|}} e^{-i(\mathrm{sign}(\Phi_M'')\pi/4)}. \tag{6.27}$$

The 3D Green's function $\mathbf{G}_M^{(3\mathrm{D})}$ is related to the 2D Green's function as shown in [82]. Consider the additional coordinate system $\xi-\eta-z$ which is obtained by rotating $x-y-z$ with angle θ along the z axis as shown in Figure 6.2. A special case of loading $\mathbf{f}^{(3\mathrm{D})}$ is defined as $\mathbf{f}^{(2\mathrm{D})}(\xi)$ which is invariant with the θ direction. For the 2D case, equation (6.28) becomes

$$\mathbf{u}(\theta,\xi,z,\omega) = \int\int \mathbf{g}^{(2\mathrm{D})}(\theta,x-\bar{x},z,\omega) \times \bar{\mathbf{f}}^{(2\mathrm{D})}(\bar{x})\mathrm{d}\bar{x}, \tag{6.28}$$

where $\mathbf{g}^{(2D)}(x-\bar{x}, z, \omega)$ is the 2D Green's function of the system. This 2D Green's function needs to be related with the 3D Green's function. The transformation between the $x-y-z$ coordinate system to $\xi-\eta-z$ coordinate system is given by

$$\begin{Bmatrix} \xi \\ \eta \\ z \end{Bmatrix} = \mathbf{T}(\theta) \begin{Bmatrix} x \\ y \\ z \end{Bmatrix}, \quad \text{with} \quad \mathbf{T}(\theta) = \begin{bmatrix} \cos\theta & sin\theta & 0 \\ -\sin\theta & cos\theta & 0 \\ 0 & 0 & 1 \end{bmatrix}. \tag{6.29}$$

The wavenumbers are related by

$$k_x = k_\xi \cos\theta - k_\eta \sin\theta \quad \text{and} \quad k_y = k_\xi \sin\theta + k_\eta \cos\theta. \tag{6.30}$$

Therefore, the 3D Green's function $\mathbf{G}_M^{(3D)}(k_x, k_y, z, \omega)$ is transformed into

$$\mathbf{G}_{M_\theta}^{(3D)}(k_\xi, k_\eta, z, \omega) = \mathbf{T}(\theta)\mathbf{G}_M^{(3D)}(k_\xi \cos\theta - k_\eta \sin\theta, k_\xi \sin\theta + k_\eta \cos\theta, z, \omega)\mathbf{T}^{-1}(\theta). \tag{6.31}$$

The Green's function $\mathbf{G}_{M_\theta}^{(3D)}(k_\xi, k_\eta, z, \omega)$ represent straight crested waves with propagation direction $(k_\xi, k_\eta, 0)$. For the 2D case, we have straight crested wave with propagation direction $(k_\xi = k, k_\eta = 0, 0)$ and corresponding 2D Green's function $\mathbf{G}_M^{(2D)}(\theta, k_\xi, z, \omega)$. This yields

$$\mathbf{G}_M^{(2D)}(\theta, k_\xi, z, \omega) = \mathbf{G}_{M_\theta}^{(3D)}(k, 0, z, \omega). \tag{6.32}$$

Thus, the 2D Green's function is related to 3D Green's function as

$$\mathbf{G}_M^{(2D)}(\theta, k_\xi, z, \omega) = \mathbf{T}(\theta)\mathbf{G}_M^{(3D)}(k\cos\theta, k\sin\theta, z, \omega)\mathbf{T}^{-1}(\theta). \tag{6.33}$$

6.4 Consideration for edge reflections

The 2D and 3D point force response analysis given in sections 6.2 and 6.3 are based on the infinite plates. In order to simulate the finite plates with edge reflections, the reflected waves are obtained by adding additional infinite plate solutions to the initial infinite plate solution Sol_{init} as shown in Figure 6.4. The additional infinite plate solutions are acting to the opposite of the incidence wave on the plate edges.

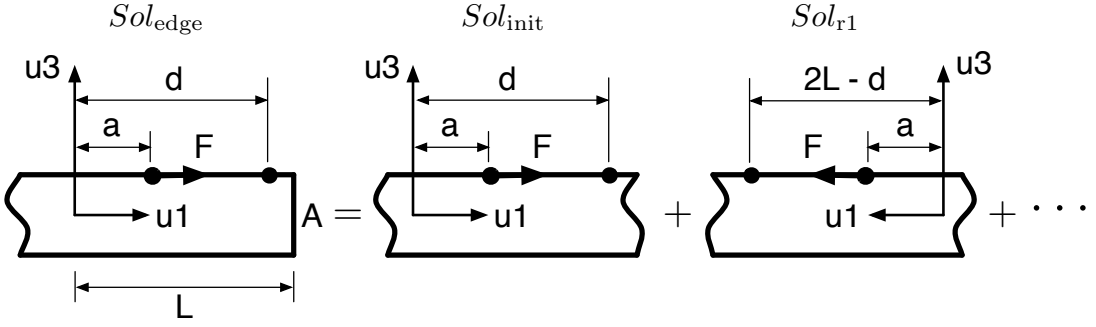

FIGURE 6.4: Plate edge reflections using additional infinite plate solutions. First reflection at edge A is represented by infinite plate solution Sol_{r1}.

The number of the additional infinite plate solutions required depends on the number of reflections considered. The wave reflection behaviors at the plate edges are obtained using the method outlined in Chapter 5. Depending on the plate edges, the types and amplitudes of the reflected modes are frequency dependent. Instead of using an opposite sign for the x-axis in the additional infinite plate solutions i.e in Sol_{r1} (see Figure 6.4), the additional infinite plate solutions can be calculated using the same x-axis direction as the initial infinite plate solution Sol_{init}. However, the signs and the amplitudes of the additional infinite plate solutions corresponding to the reflected waves are changed according to Table 6.1. These sign corrections are independent on the edge types (symmetrical or unsymmetrical plate edges) but dependent on the boundary conditions of the edges (free or fixed plate edges). In the fixed plate edges, the sign corrections for the reflected S modes and the reflected A modes are different. On the other hand, in the free plate edges, the sign corrections are the same for both modes. The numerical examples used to verify the sign corrections are given in section B.2, in Appendix B. In these examples, better agreements are obtained for the fixed edges compared to the free edges as the SAFE method can not take into account the dynamic motions of the plate edges.

TABLE 6.1: Amplitude sign corrections for different edge types, edge boundary conditions (BCs) and reflected Lamb modes.

Edges	Free BC						Fixed BC					
	S modes			A modes			S modes			A modes		
	u_x	u_y	u_z	u_x	u_y	u_z	u_x	u_y	u_z	u_x	u_y	u_z
Symmetrical	$+1$	-1	-1	$+1$	-1	-1	-1	$+1$	$+1$	$+1$	-1	-1
Unsymmetrical	$+1$	-1	-1	$+1$	-1	-1	-1	$+1$	$+1$	$+1$	-1	-1

6.5 Application examples

6.5.1 Mode tuning

The Lamb wave phased array actuation/sensing concept has been applied to the isotropic plates actuated by piezoceramic actuator in [6, 69, 73]. This actuation concept has been extended to the composite plates by using a quasi-isotropic mode which has an almost circular group velocity, in a modified phased array algorithm [74, 75]. The main problem of this approach is that, this certain mode needs to be excited without exciting other modes as well. In the examples given in [74], an A_2 mode has been used and excited using an air-coupled ultrasonic transducer in an unidirectional composite plate. However, the use of such air-coupled ultrasonic transducers is not practical for the in-situ SHM system in comparison to the piezoceramic actuators.

The key in the application of phased array concept for Lamb waves is to obtain a single mode with one value of group velocity. The SAFE method can be used to calculate the frequency where only the S_0 mode is excited in the plate from a thin fully coupled piezoelectric strip transducers. This frequency, where the A_0 mode is zero, is denoted

as the tuning frequency [39]. From the previous section, the response in the plate is obtained form the contribution of each Lamb mode involved at a certain circular frequency ω. The normalized displacement amplitude and the normalized strain amplitude for each mode can be derived from the same equation. Then, the tuning frequency points are obtained from the normalized strain curves. From equation (6.4), the vector of displacement amplitude of a particular mode r at the frequency ω for $x > x_p$ is given by

$$\mathbf{u}^r(x,\omega) = -i\frac{\mathbf{Q}_r^T\mathbf{F}}{\mathbf{Q}_r^T\mathbf{B}\mathbf{Q}_r}\exp\left(-ik_r x\right). \tag{6.34}$$

The strain amplitude along the x axis due to the excited point force is obtained by differentiating (6.34) with respect to the x axis as

$$\boldsymbol{\varepsilon}_{xx}^r(x,\omega) = -k_r\frac{\mathbf{Q}_r^T\mathbf{F}}{\mathbf{Q}_r^T\mathbf{B}\mathbf{Q}_r}\exp\left(-ik_r x\right). \tag{6.35}$$

Perfect bonding condition is assumed between the piezoelectric actuator strip and the infinite plate as shown in Figure 6.5. The forces from the thin actuator with a length of $2a$ can be simplified as two point forces acting at the end of the actuator at points $-a$ and a respectively, as shown in [39]. The shear lag effect from the adhesive layer is neglected for the thin actuator considered. The harmonic shear stress distribution on top of the plate is then given by

$$\tau(x) = a\tau_0\left[\delta(x-a) - \delta(x+a)\right] \tag{6.36}$$

where τ_0 is the shear stress amplitude. The Fourier transform of eq.(6.36) is

$$\bar{\tau}(x) = a\tau_0[-2i\sin k_r a]. \tag{6.37}$$

By applying the equation (6.37) in the $\bar{\mathbf{f}}$ term at the corresponding degrees of freedom in the equations (6.34) and (6.35) yield the displacement and strain amplitude for each mode r. The curves showing the variation of the strain amplitude with respect to ω can be plotted for both fundamental symmetric S_0 and antisymmetric A_0 modes. From this curves, the tuning frequency in the plate is obtained. A comparison is made with the approach in [6] for a 7mm length thin piezoelectric actuator fully attached to a 1.6mm thick aluminum plate. Good agreements are obtained as shown in Figure 6.6. This approach can be extended easily to the composite plates and require no analytical displacement and strain terms. Therefore, it is not limited to the isotropic plates only as the approach shown in [39].

The tuning frequency is also calculated for a 1mm thick $[45°/-45°/0°/90°]_s$ composite

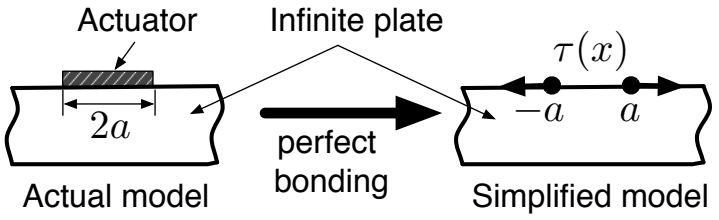

FIGURE 6.5: Simplified model for a perfectly bonded actuator.

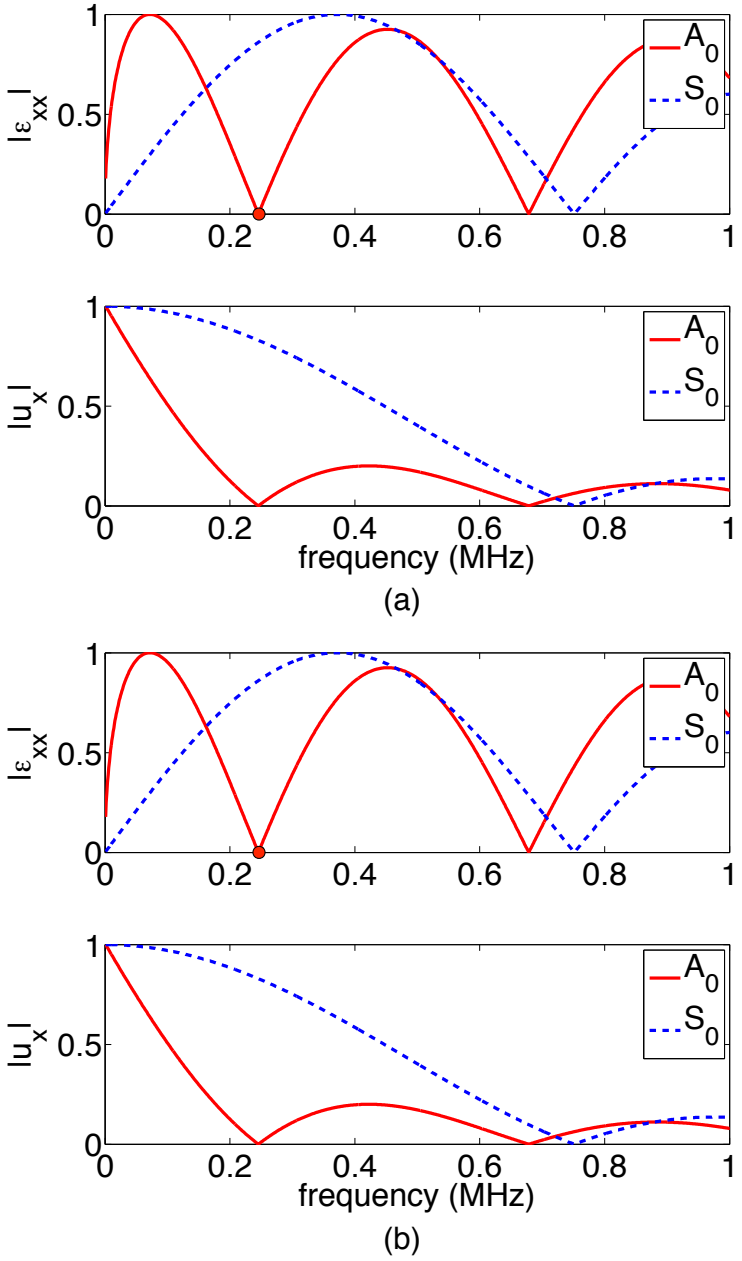

FIGURE 6.6: Normalized strain and displacement curves (a) approach by Giurgiutiu[6], (b) proposed approach using SAFE. The tuning frequencies are marked with dots.

TABLE 6.2: Homogenized elastic properties for the T300/914 laminate at 0^0degree [8] (elastic constants in GPa).

C_{11}	C_{12}	C_{13}	C_{22}	C_{23}	C_{33}	C_{44}	C_{55}	C_{66}	ρ (kg/m^3)
143.8	6.2	6.2	13.3	6.5	13.3	3.6	5.7	5.7	1560

plate. The material properties of the plate are given in Table 6.2. Due to the material anisotropy, there are at least three modes in the low frequency range, as shown in Figure 6.7(a). The normalized strain amplitude curves are shown in Figure 6.7(b). The tuning

frequency obtained is at 175kHz (denoted by a dot). At this frequency, the normalized strain amplitude curves for the SH_0 and A_0 modes are at minimum. Thus, only the S_0 mode is exited. Figures 6.7(c) and 6.7(d) show the variation of the phase velocity curves with the wave propagation angles for the S_0, A_0 and SH_0 modes, respectively, at the tuning frequency (175kHz). From these figures, the A_0 mode is highly dependent on the wave propagation angle. However, both, the S_0 and SH_0 modes, have no dependence on the wave propagation angle at this frequency. The variation of the tuning frequency with the wave propagation angle is shown in Figure 6.7(e). This curve is similar with the phase velocity curve for the A_0 mode (6.7(d)).

Thus, it can be concluded for this composite plate, the tuning frequency is only dependent on the A_0 mode. For verification, simulations are made using Abaqus for different excitation center frequencies as shown in Figure 6.8. At 175kHz the amplitude of the A_0 mode becomes minimum which corresponds correctly with the tuning frequency obtained from Figure 6.7(b). In these FE simulations, a five cycles tone burst Hann window is used as the point force and plain strain CPE4 elements (with 16 elements per 1mm) are applied to model the plate.

In the phased array actuation, the delay and sum beam forming method is used for the wave beam steering. The basic idea of this method is to apply an appropriate phase delay on each element of the phased array so that the output, which is the summation of the output from each element, is reinforced in the desired direction. In the following, an element E_n in a linear phased array as shown in Figure 6.9 is considered.

The beamformer output signal in direction $\vec{\xi}$ is given as

$$z(t) = \sum_{n=0}^{N-1} w_n y_n(t - \Delta_n), \tag{6.38}$$

where $y_n(t)$ is the output of each element, Δ_n is the phase delay, w_n is the amplitude weighting factor, and $z(t)$ is the output of the array. The values of Δ_n depend on the beamforming direction and the positions of the array elements. Under a far field assumption, the phase delay for steering the wave beam into a certain direction can be calculated as

$$\Delta_n = -\frac{\vec{\xi} \cdot \vec{s}_n}{c}, \tag{6.39}$$

where $\vec{\xi}$ is the unit vector for the steering direction, $\vec{s}_n$ is the position vector of the actual array element position and c is the wave phase velocity.

The main challenge in applying a phased array actuation concept for Lamb waves is the selection of the value c. Lamb waves are multi-modal, thus more than one value of the wave phase velocity are available. This problem can be solved by using the tuning frequency obtained in section 6.5.1. At this frequency, only one mode is highly excited while the other modes are being suppressed. Thus, in isotropic plates, by exciting at the tuning frequency, a single value of c can be obtained and used to direct Lamb waves to certain direction.

For example, a simulation in Abaqus has been made for a 1mm thick aluminum plate. To reduce the computational time, the plate is modelled using shell elements (S4R). A linear phase array with nine actuating elements is used. Each actuating element is a circular piezoelectric actuator with a diameter of 7mm. The actuator is modelled using solid elements (C3D8R). The piezoelectric effects and delays for each phased array actuating element are done using the VUMAT subroutine. The excitation frequency is set to be equal to the tuning frequency at 176kHz. The time delay is chosen to direct the wave at 45° angle from x-axis. The obtained displacements on the plate are given in Figure 6.10 showing the waves being directed at 45° angle.

However, for general composite plates, the value of the tuning frequency is dependent on the wave propagation angle. Thus, different tuning frequencies are needed for different wave propagation angles. Figure 6.11 shows the phased array actuation example for a 1mm thick $[45°/-45°/0°/90°]_s$ composite plate. The same type of phased array and FEM modelling technique are used. The time delay is chosen to direct the wave at 45° angle. Thus, the tuning frequency at 45° angle is required, which is 141kHz.

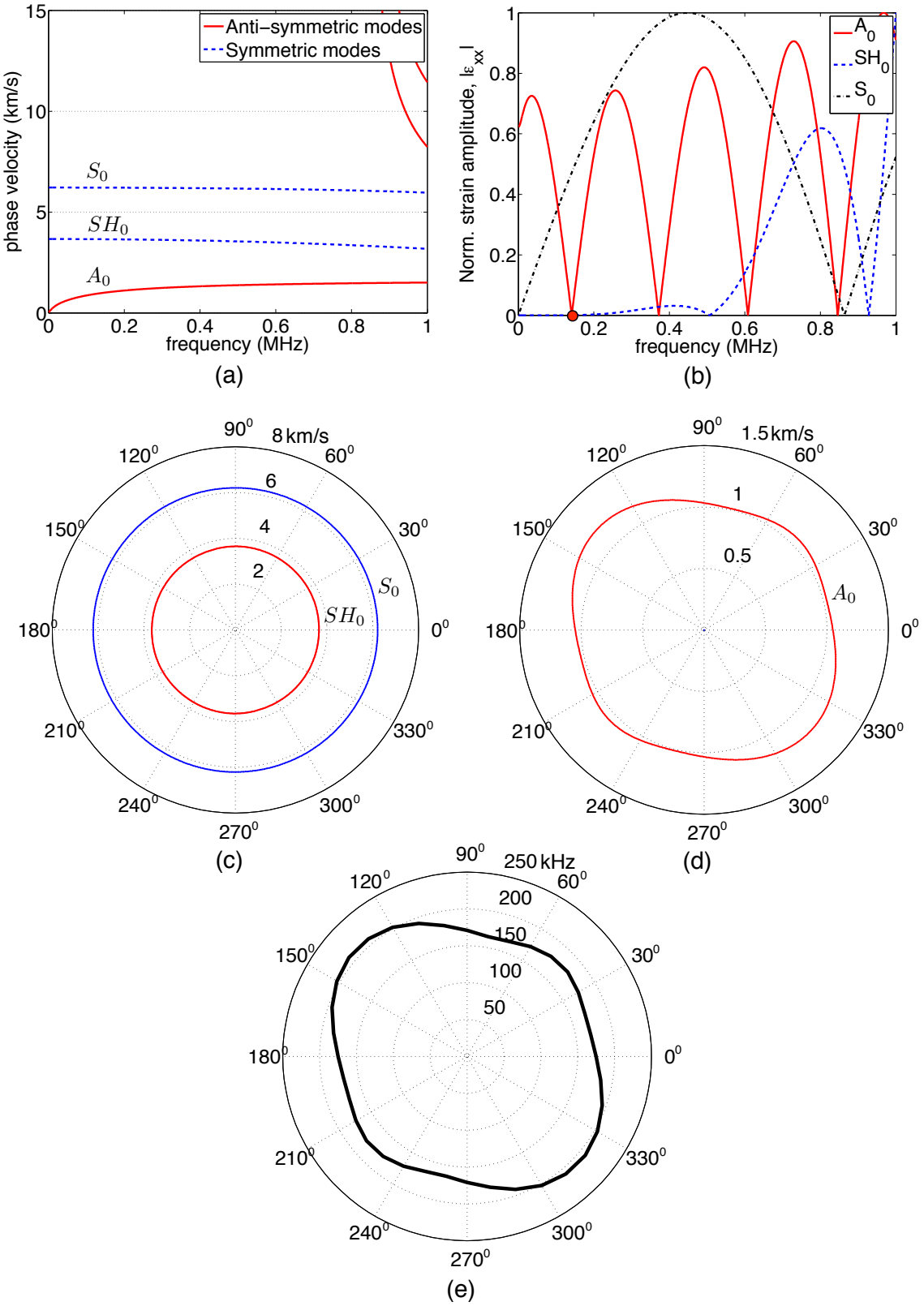

FIGURE 6.7: (a) Phase velocity curves at 0^0degree, (b) Normalized strain curves at 0^0degree (dot at tuning frequency = 175kHz), (c) S_0 and SH_0 modes phase velocity curves at 175kHz, (d) A_0 modes phase velocity curve at 175kHz, and (e) Variation of tuning frequency with wave propagation angle.

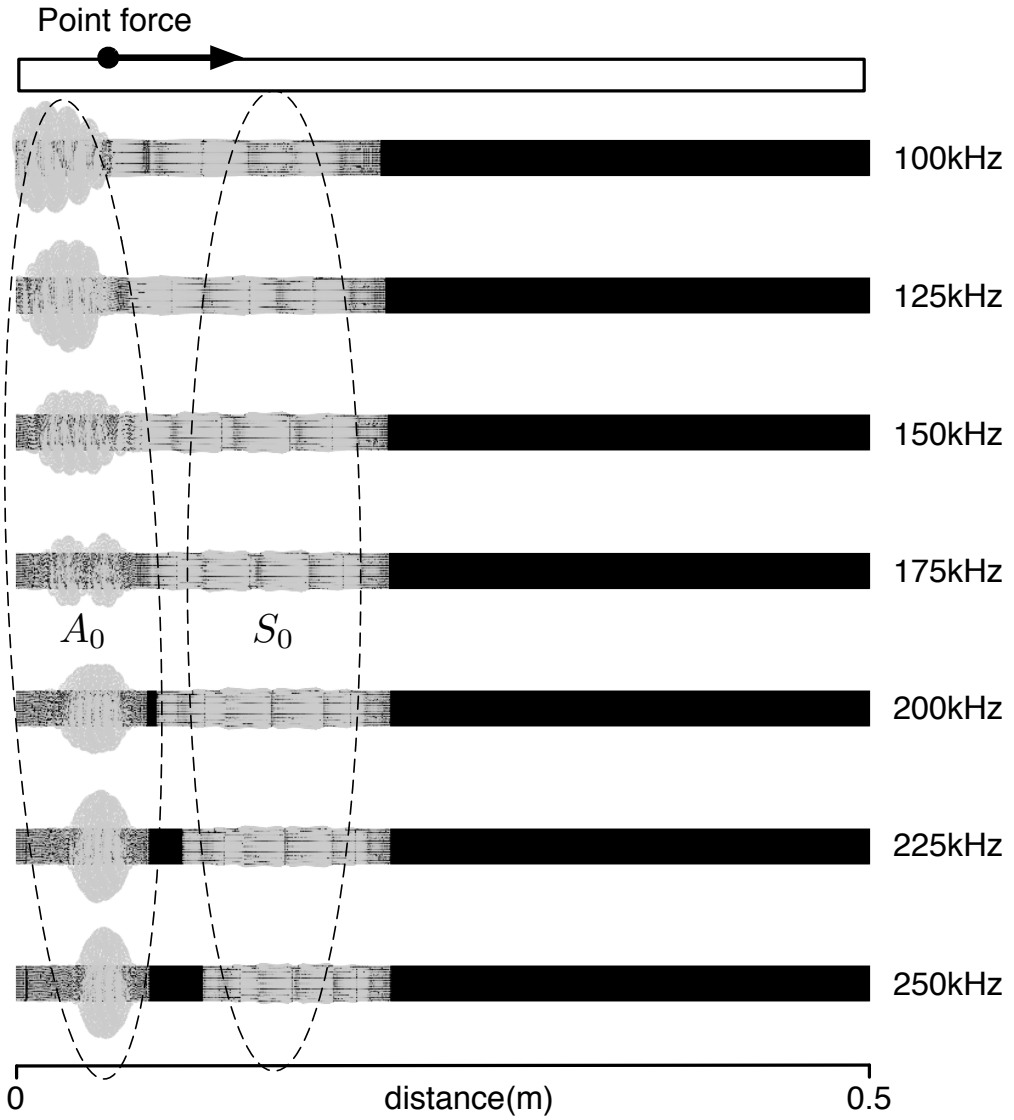

FIGURE 6.8: Emission of A_0 and S_0 waves using a point force source at $t = 40\mu s$ and propagation angle 0°. The propagation velocity of the A_0 mode increases with frequency and the emitted amplitude reaches a minimum at 175kHz. Shown are the displacement vectors.

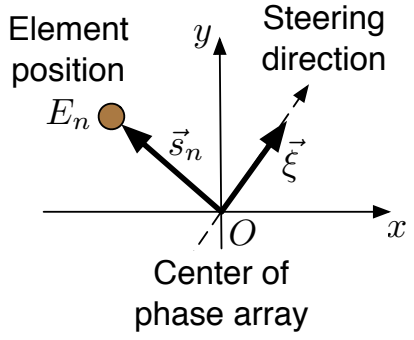

FIGURE 6.9: Phased array model.

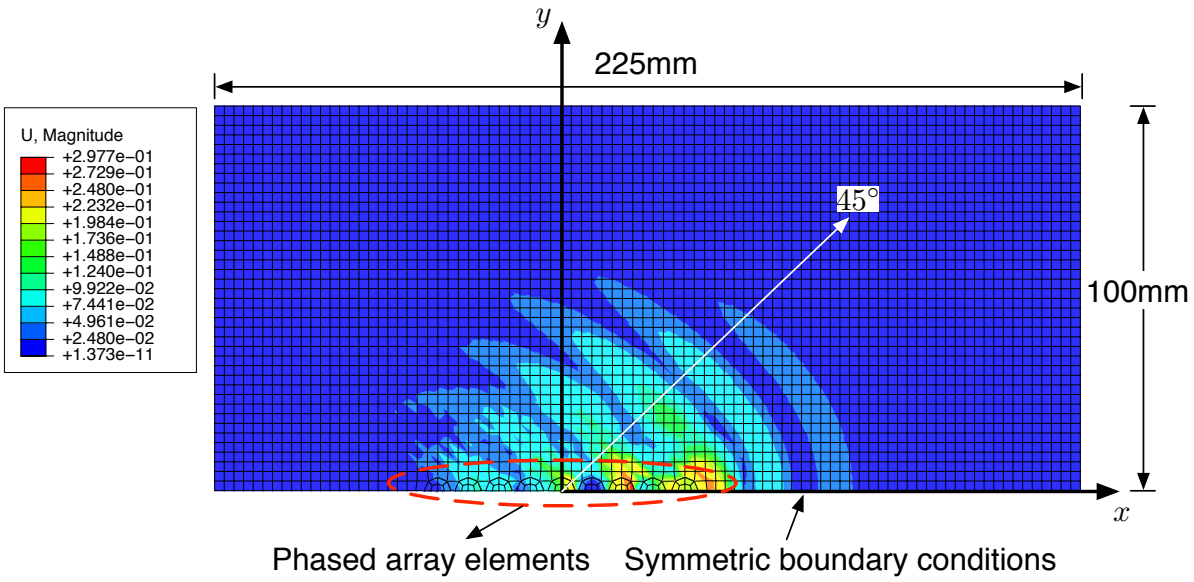

FIGURE 6.10: Abaqus simulation showing 45° beam steering in a 1mm thick aluminum plate using 9 element linear phased array at $t = 17\mu s$. Excitation (tuning) frequency is 176kHz.

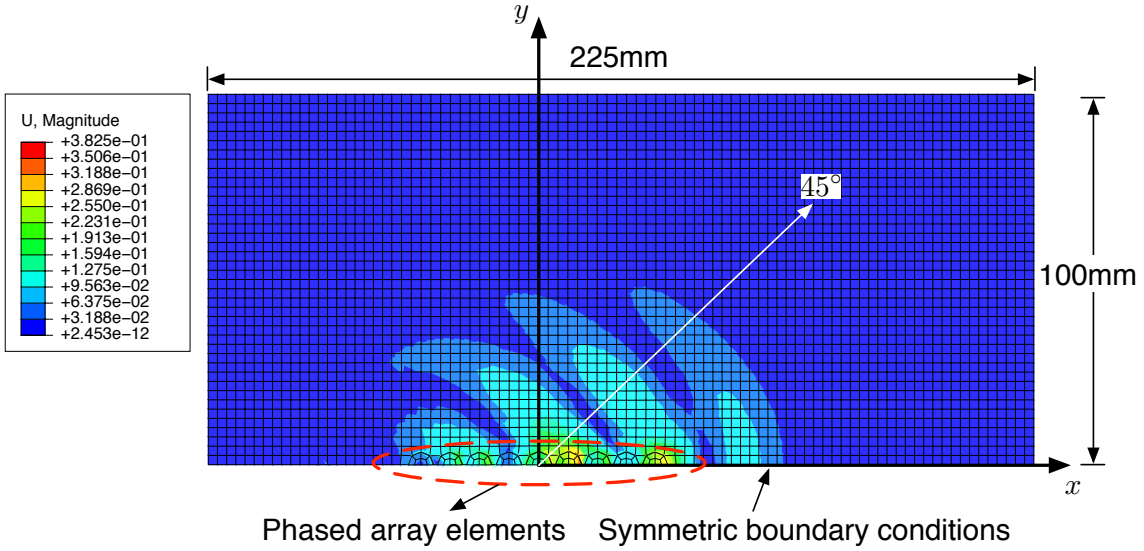

FIGURE 6.11: Abaqus simulation showing 45° beam steering in a 1mm thick $[45°/-45°/0°/90°]_s$ composite plate using 9 element linear phased array at $t = 15\mu s$. Excitation (tuning) frequency is 141kHz.

6.5.2 2D force response simulation

The simplification for perfectly bonded thin actuators are assumed here. Therefore, the actuator is modelled as two point force acting at opposite direction at the end of the actuator edges. Time response simulations are made for a 1mm thick aluminum plate with a 6mm length actuator attached on the top surface, as shown in Figure 6.12(a).

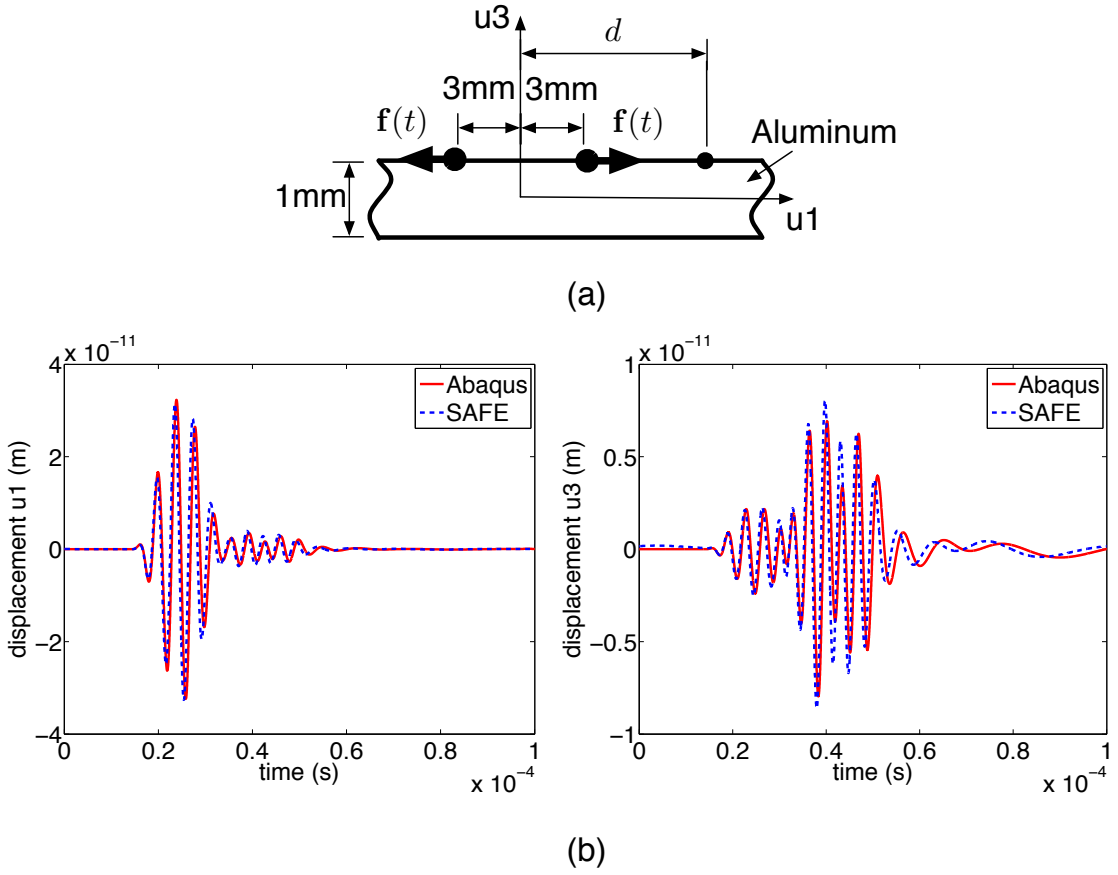

FIGURE 6.12: (a) 2D force response model for perfectly bonded actuator, and (b) Displacement at location $d = 80$mm.

Five cycles tone burst with Hann window at center frequency 250kHz is used as the excitation force. At this excitation frequency, only the S_0 and the A_0 modes are exited in the plate. The displacement results at a point located at a distance of $d = 80$mm is compared with Abaqus in Figure 6.12(b). A good agreement has been obtained.

The same model is extended for plate edge reflection examples as shown in Figure 6.13(a). Two vertical plate edges, edge A and edge B are located at both ends of the plate length. The same excitation force as in the case of the infinite plate example has been used. Thus, at this excitation frequency, only the S_0 and the A_0 modes need to be considered as the incidence Lamb modes.

The reflection behavior at the vertical plate edge for both modes are given in Figure 6.13(b). As the vertical plate edge is symmetric, the type of reflected modes are always

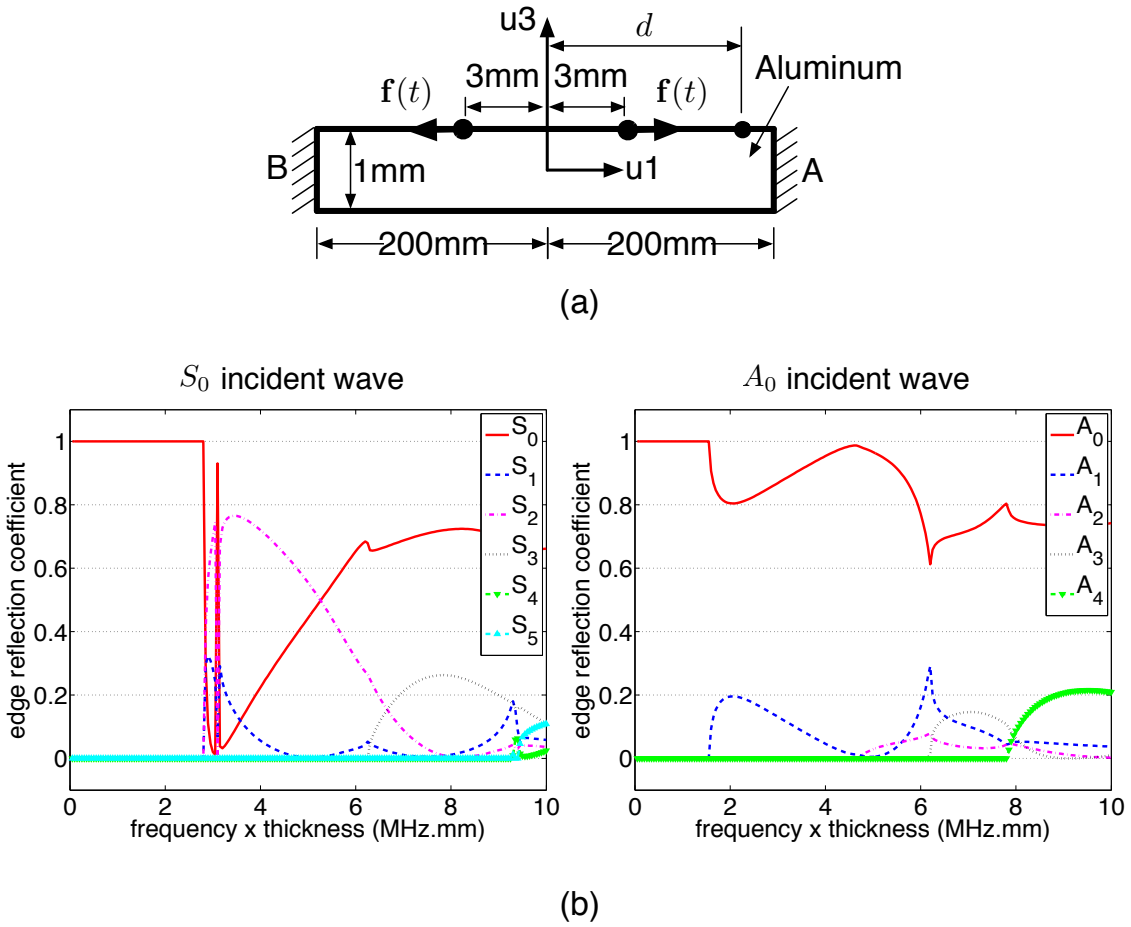

FIGURE 6.13: (a) 2D force response model for perfectly bonded acstuator with vertical plate edges A and B, and (b) Vertical edge reflection coefficient for aluminum plate with S_0 and A_0 as incidence waves.

the same as the incidence mode. The displacement results at a point located at a distance of $d = 20$mm and $d = 170$mm are compared with Abaqus as shown in Figure 6.14. The number of edge reflections depend on the simulation time considered. The longer the simulation time, the more reflections occur in the plate. For the point located at $d = 170$mm, which is near to the vertical edge A, only the reflection from vertical edge A need to be considered. Reflection from the vertical edge B has not reach this point within the simulation time duration. However, for the point located at $d = 20$mm, both reflections from vertical edges A and B, need to be considered within the simulation time duration.

The force response analysis can also be verified by calculating the dispersion curves from the obtained displacement results. Here, a typical procedure in calculating dispersion curves from experimental procedure is simulated. A set of out of plane displacements for several points along a straight line on the plate surface is calculated. Out of plane plate displacement is a typical measurement using laser vibrometer equipment. The same model as shown in Figure 6.14 is used. However, the center frequency of the loads is 100kHz. Displacements are calculated for points located at position $d = 150$mm to

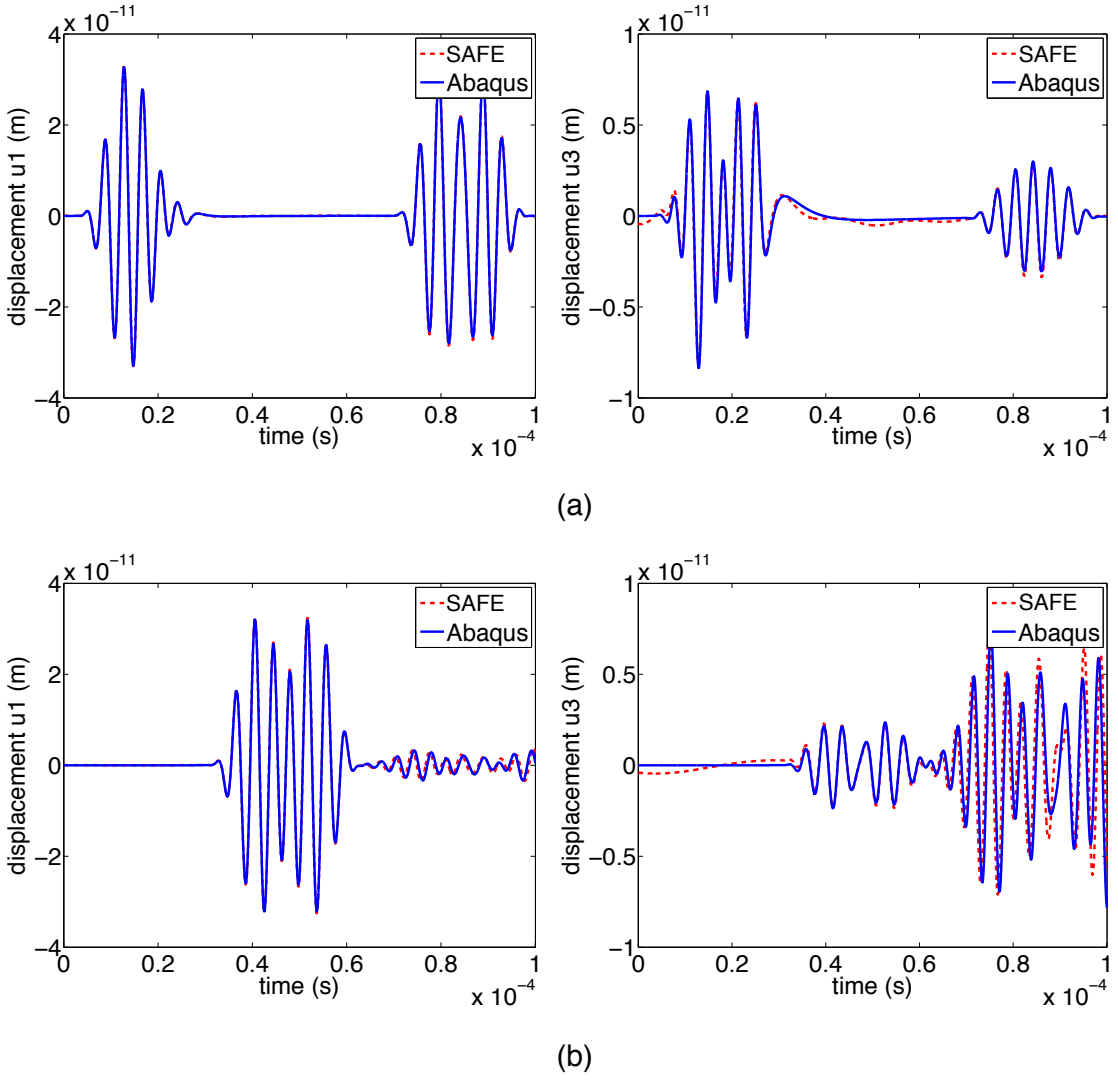

FIGURE 6.14: Displacement of points located at a distance (a) $d = 20$mm, and (b) $d = 170$mm.

$d = 250$mm with interval of 2mm between each point (a total of 51 points). Using 2D Fourier transformation [113], the dispersion relationship between wavenumber and frequency is obtained as shown in Figure 6.15. In obtaining these dispersion curves, the distance between the first and the last point considered is more important than the total number of points involved (compare Figure 6.16(a) and 6.16(b)). A larger distance in the space domain means higher resolution in the wavenumber domain (compare Figure 6.16(b) and 6.16(c)). This is analogous to the longer simulation time in the time domain that gives higher resolution in the frequency domain. With higher resolutions, the peaks of the 2D Fourier transformation coefficients corresponding to the dispersion curve lines can be seen more clearly.

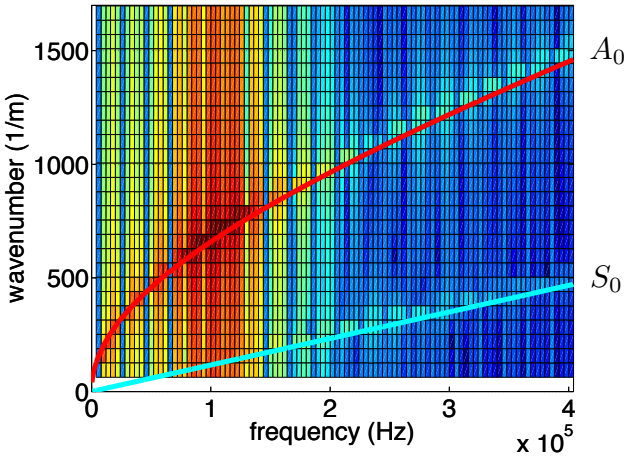

FIGURE 6.15: The Fourier coefficients of a measured wave in a wavenumber-frequency plane. This plot is logarithmically colored. Straight lines represent the actual dispersion curves calculated using SAFE.

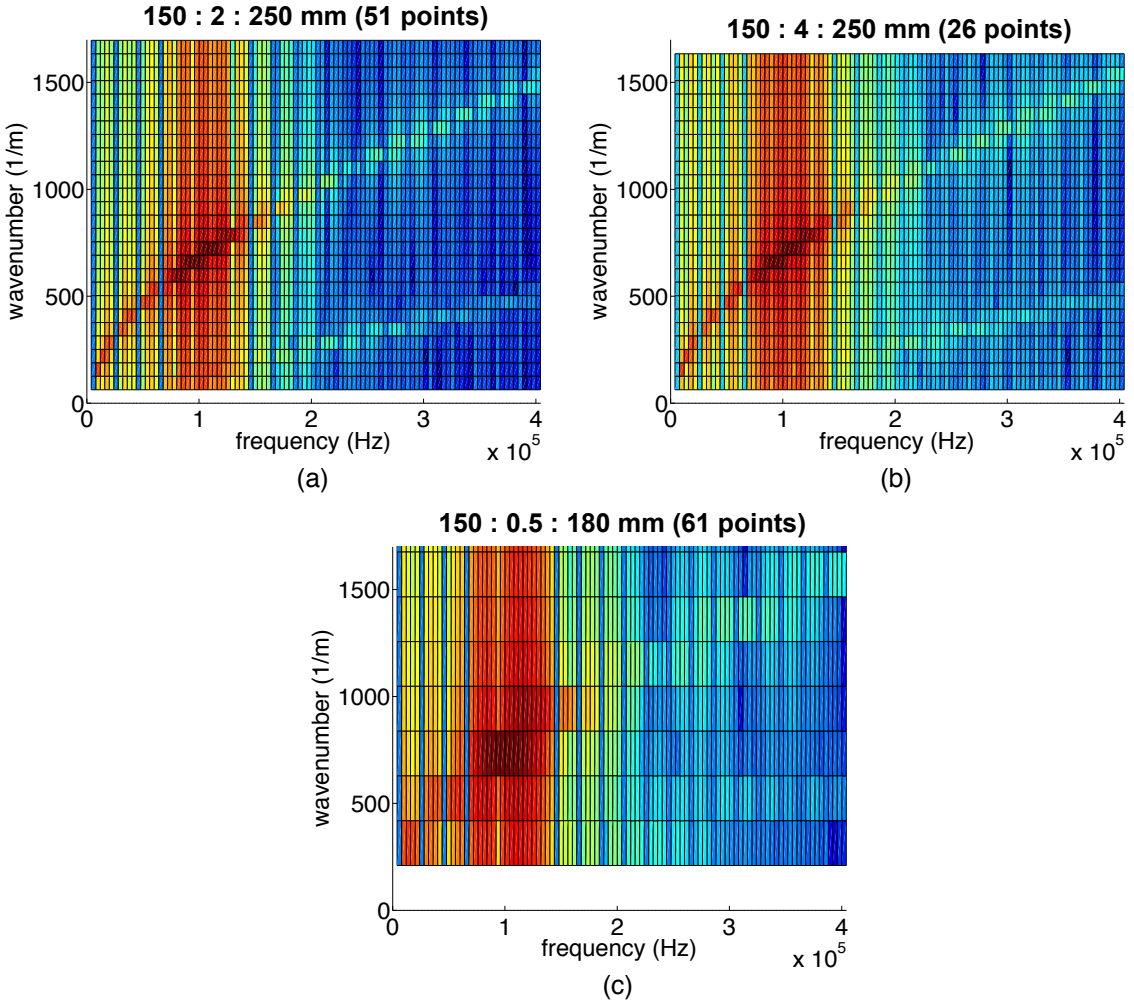

FIGURE 6.16: The effects of distance and number of points on the Fourier coefficients in a wavenumber-frequency plane. (a) 51 points considered from $d = 150$mm to $d = 250$mm with interval of 2mm, (b) 26 points considered from $d = 150$mm to $d = 250$mm with interval of 4mm, and (c) 61 points considered from $d = 150$mm to $d = 180$mm with interval of 0.5mm.

6.5.3 3D force response simulation

In the available literatures [75, 82, 158], 3D force response analysis have been made by coupling the SAFE method and the stationary phase method. However in their simulations, the applied point force is only at the origin of the plate coordinate as shown in Figure 6.17. In the following, an approach by considering additional phases in the solutions is developed to enable the point force locations to be shifted from the origin of the plate coordinate.

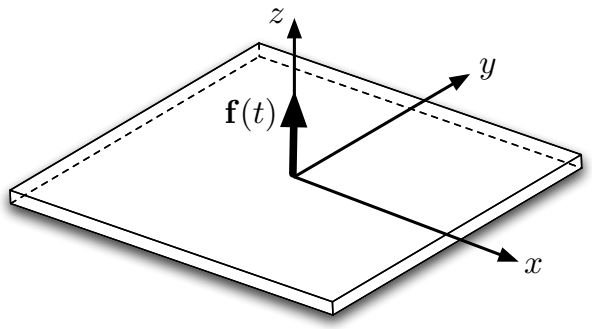

FIGURE 6.17: Point force applied at the origin of the plate coordinate

In order to understand why additional phases are considered, consider the case when the point force is applied at the origin of the plate coordinate in an infinite isotropic plate. The problem can be reduced to an axisymmetric problem where the point force is applied at the axisymmetric axis as shown in Figure 6.18. Displacements are calculated at a point located at a distance d from the origin. This point is located to the right of the origin (positive u1 axis). Displacements are obtained as a summation of contributions from right going waves and left going waves. Actually both wave directions are outward going waves. Here we denoted them as right going waves and left going waves depending on the sign of u1 axis for convenience.

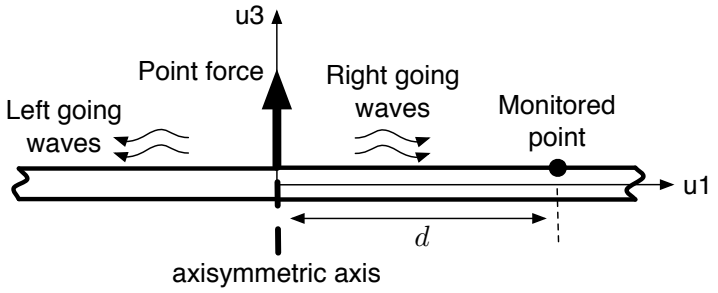

FIGURE 6.18: Axisymmetric model of point force applied at the origin of the plate coordinate

In the positive u1 axis direction left going waves will have the same phase as right going waves. Therefore, to calculate the displacements, contributions of both wave directions can be added together without considering the phase. The same conclusion can also be made if the measured point is located to the left of the origin (negative u1 axis). However, when the point force is not applied at the origin as shown in Figure 6.19, the phase difference between right going waves and left going waves (which contributes to the

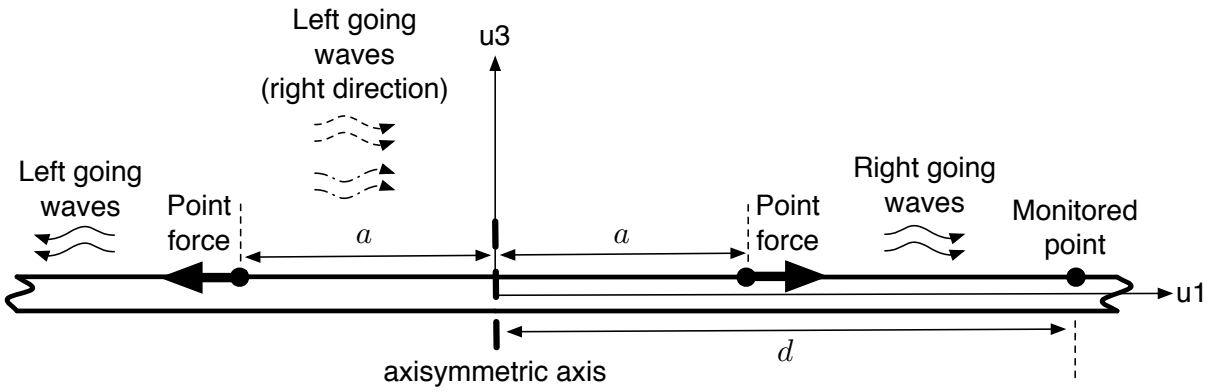

FIGURE 6.19: Axisymmetric model of point force applied at shifted position from the origin of the plate coordinate

right direction) need to be considered in calculating the displacements as shown in the next section. This additional phase term ϕ_{add} is added to $\mathbf{B}_M$ term in the equation (6.27) giving

$$\mathbf{B}_M = \frac{|k_M|}{\sqrt{2\pi|\Phi''_M|}} e^{-i(\text{sign}(\Phi''_M)\pi/4+\phi_{\text{add}})}. \tag{6.40}$$

For simplification, consider an infinite isotropic plate made from aluminum with a thickness of 1mm, a Young's modulus of 70GPa, a density of 2700kg/m^3 and a Poisson ratio of 0.33. Due to the material isotropy, the 3D force response problem can be reduced to an axisymmetric problem in the FEM. Thus, less computational resources are required for the calculation of our comparison results using Abaqus. In all excitation cases, the point force is equal to 1N, and taken as a five cycle Hann windowed tone burst with a center frequency of 250kHz. The displacements are calculated at a point on the top plate surface with the distance from origin of $d = 80$mm.

Figure 6.20 shows the comparison of the displacement results calculated using the SAFE method applying the stationary phase method and Abaqus. As the point force is located at the origin of the plate coordinate, no additional phase is required. For the symmetric Lamb modes excitation, the comparison of displacement results is shown in Figure 6.21. In this case, a phase shift of $\phi_{\text{add}} = \pi$ is added to the solution of the left going waves. The comparisons of the anti-symmetric Lamb mode excitation is shown in Figure 6.22. In this case, additional phase shifts are needed for both right going wave and left going wave. Additional phases of $\phi_{\text{add}} = \pi/2$ and $\phi_{\text{add}} = \pi$ are added to the right going wave and left going wave, respectively.

For some excitations that involve both symmetric and anti-symmetric Lamb modes, for example, the excitation in Figure 6.23, the excitation can be decomposed into symmetric and anti-symmetric Lamb mode excitations as shown in Figures 6.21 and 6.22, respectively. By adding the contributions from both symmetric and anti-symmetric modes, the total displacements can be obtained as given in Figure 6.23. However, the excitation as in Figure 6.24 can not be decomposed into symmetric and anti-symmetric modes. Based

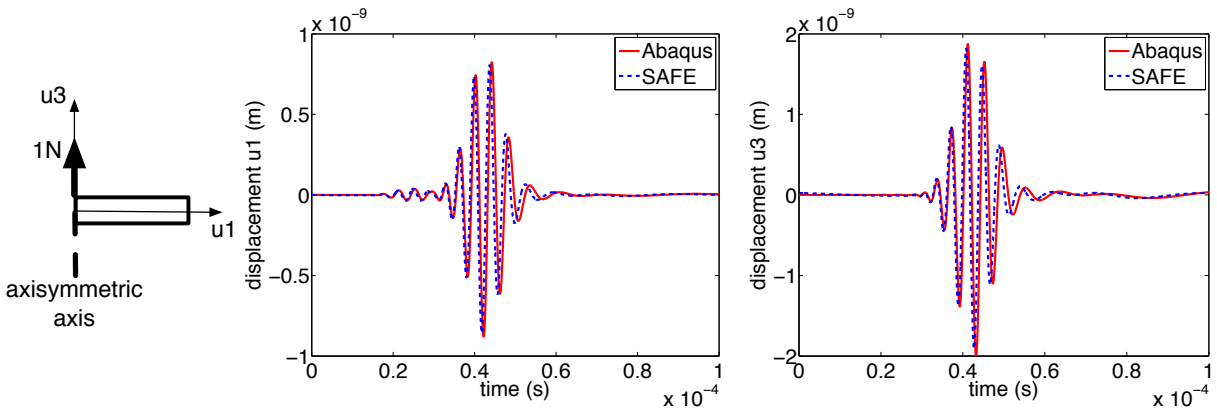

FIGURE 6.20: Result comparisons between the Abaqus and the SAFE method: point force at the origin of the plate coordinate.

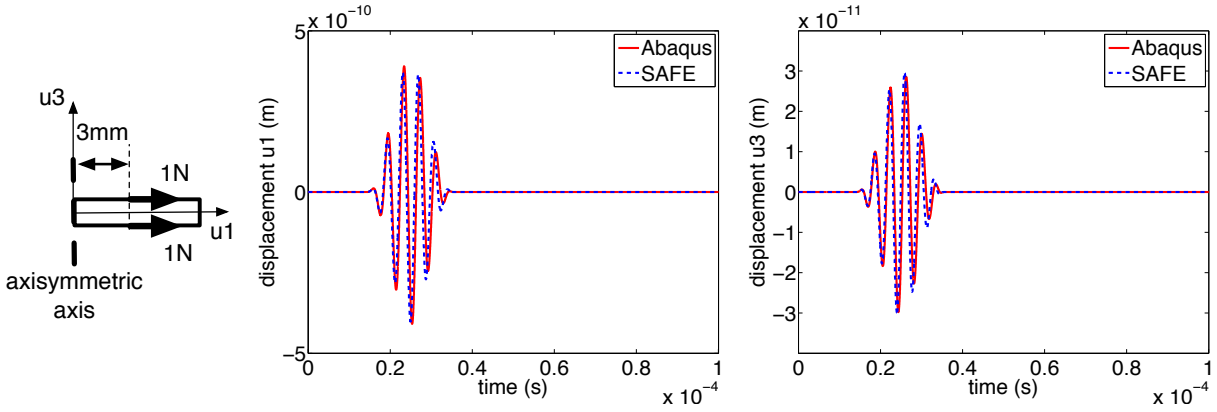

FIGURE 6.21: Result comparisons between the Abaqus and the SAFE method: symmetric Lamb modes excitation.

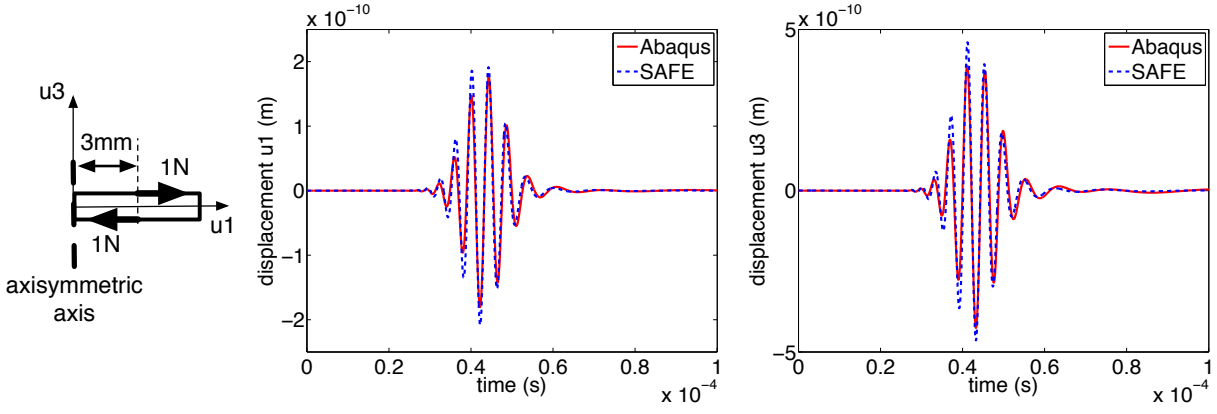

FIGURE 6.22: Result comparisons between the Abaqus and the SAFE method: anti-symmetric Lamb modes excitation.

on the trials made, the additional phase obtained specifically for this loading case is $\phi_{\text{add}} = -\pi/2$.

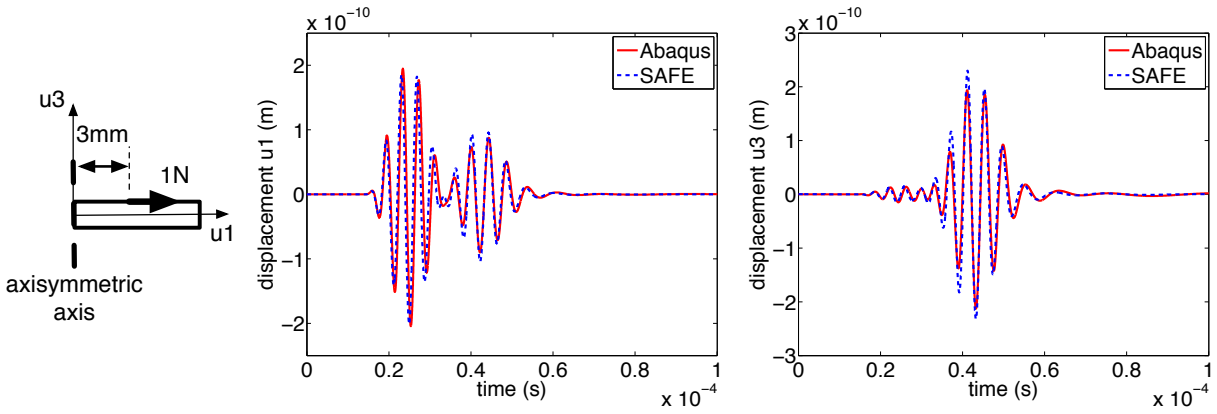

FIGURE 6.23: Result comparisons between the Abaqus and the SAFE method: horizontal point force located 3mm from the origin of the plate coordinate.

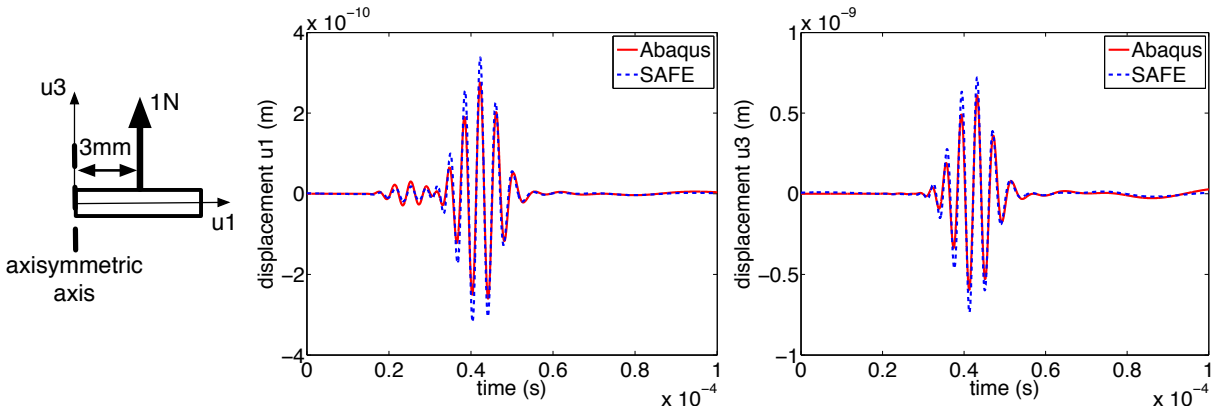

FIGURE 6.24: Result comparisons between the Abaqus and the SAFE method: vertical point force located 3mm from the origin of the plate coordinate.

Plate edge reflections can also be considered in the 3D case by applying the approach outlined in section B.2 as shown in Figure 6.25. The same plate and excitation force as mention before are used. The half plate length (or radius) is 150mm. The displacements are calculated at a point located at a distance of 75mm from the origin. Good agreements are obtained between the SAFE method and reference results in Abaqus.

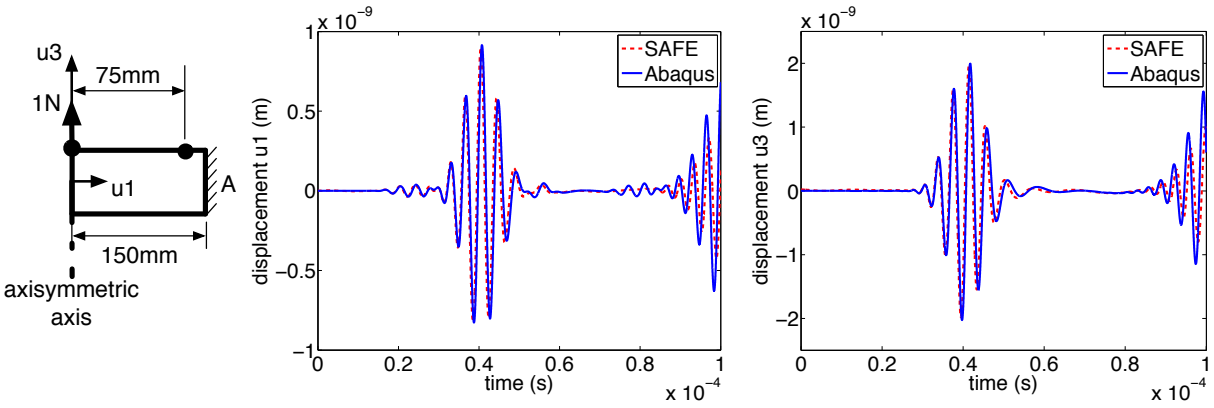

FIGURE 6.25: Result comparisons between Abaqus and SAFE: vertical point force located at the origin of the plate coordinate. Plate edge A is fixed.

6.5.4 Voltage response by rectangular strain sensors

Strain sensors are considered as it is more suitable for portable Lamb wave based SHM systems. Examples of the strain sensors are the piezoelectric (PZT) sensors and the micro-fiber composite (MFC) sensors. An approach to obtain the response of the rectangular piezoelectric and MFC sensors for isotropic plates is given in [7, 76, 77]. Within these reference papers, the analytical strain term for isotropic material [79] is applied in the sensors response equation. However, in general, such analytical strain terms are unavailable for composite plates. Thus, to extend the approach for composite plates, the SAFE method is used to calculate these strain terms, as given by equation (6.35). In composite plates, the sensor responses will depend not only on the rectangular sensor dimensions but also on the anisotropic material properties. However, for comparison purpose, only the rectangular PZT sensors on isotropic plates are being considered for the examples given in this section. The same approach can be extended to MFC actuators applying the formulation in [77].

6.5.4.1 Harmonic voltage response generated by rectangular piezoelectric sensor

Consider a plane wave propagating at an angle θ to a rectangular sensor as shown in Figure 6.26 with thickness $\hat{h}$, length l and width b, respectively. The PZT sensor is assumed to be transversal isotropic with the plane of isotropy in the 1-2 plane and poling along the thickness in the 3 direction.

The direct piezoelectric effect, eq.(6.41), and the converse piezoelectric effect, eq.(6.42), are given by

$$\mathbf{D} = \mathbf{e}^{(\sigma)}\mathbf{E} + \mathbf{d}\boldsymbol{\sigma}, \tag{6.41}$$

$$\boldsymbol{\sigma} = -(\mathbf{d}\mathbf{C}^{(E)})^T\mathbf{E} + \mathbf{C}^{(E)}\boldsymbol{\varepsilon}, \tag{6.42}$$

where $\mathbf{D}$ is the charge density vector $\mathbf{e}^{(\sigma)}$ is the dielectric permittivity at zero stress, $\mathbf{E}$ is the electric field, $\mathbf{d}$ is the piezoelectric coefficient, $\boldsymbol{\sigma}$ is the stress, $\mathbf{C}^{(E)}$ is the elastic

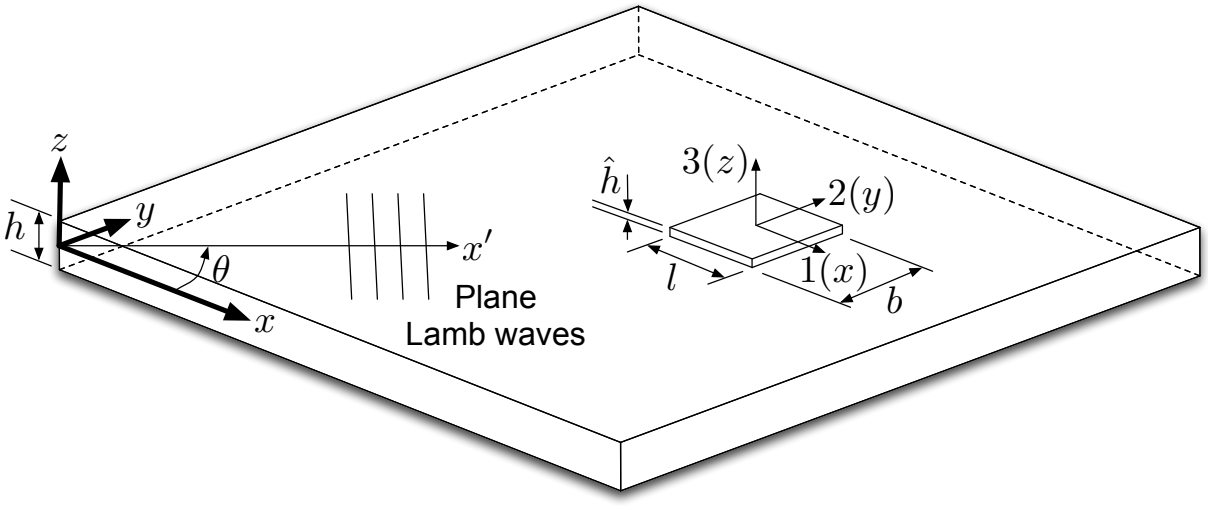

FIGURE 6.26: Plane Lamb wave in a general oblique incidence to a rectangular strain sensor.

stiffness matrix at a zero electric field, $\boldsymbol{\varepsilon}$ is the strain and the superscript T denotes transposed matrix, respectively. Applying plane stress conditions ($\sigma_{33} = \sigma_{23} = \sigma_{13} = 0$) and by substituting eq.(6.42) into eq.(6.41), the direct piezoelectric effect is obtained as

$$\mathbf{D} = \mathbf{d}\mathbf{C}^{(E)}\boldsymbol{\varepsilon} - \mathbf{d}(\mathbf{C}^{(E)})^T\mathbf{d}^T\mathbf{E} + \mathbf{e}^{(\sigma)}\mathbf{E}, \tag{6.43}$$

$$\therefore D_3 = [d_{31} \quad d_{32} \quad 0] \begin{bmatrix} C_{11}^{(E)} & C_{12}^{(E)} & 0 \\ C_{12}^{(E)} & C_{11}^{(E)} & 0 \\ 0 & 0 & C_{66}^{(E)} \end{bmatrix} \left(\begin{bmatrix} \varepsilon_{11} \\ \varepsilon_{22} \\ \gamma_{12} \end{bmatrix} - E_3 \begin{bmatrix} d_{31} \\ d_{32} \\ 0 \end{bmatrix} \right) + e_{33}^{(\sigma)} E_3, \tag{6.44}$$

where d_{31} and d_{32} are the piezoelectric constants and ε_{11}, ε_{22} and γ_{12} are the strain components of the sensor. In monolith pizoelectric sensor $d_{31} = d_{32}$. The components of stiffness matrix $\mathbf{C}^{(E)}$ are given as

$$C_{11}^{(E)} = \frac{Y^{(E)}}{1-\nu^2}, \tag{6.45}$$

$$C_{12}^{(E)} = \frac{\nu Y^{(E)}}{1-\nu^2}, \tag{6.46}$$

$$C_{66}^{(E)} = \frac{Y^{(E)}}{2(1+\nu)}, \tag{6.47}$$

where $Y^{(E)}$ and ν are the Young's modulus and the Poissons ratio of the piezoelectric sensor in the 1-2 plane of isotropy. Thus, eq.(6.44) becomes

$$D_3 = d_{31}(C_{11}^{(E)} + C_{12}^{(E)})(\varepsilon_{11} + \varepsilon_{22}) - [2d_{31}^2(C_{11}^{(E)} + C_{12}^{(E)}) - e_{33}^{(\sigma)}]E_3. \tag{6.48}$$

According to [7, 169] for an open circuit piezoelectric patch the total charge over the electrode area is zero, $\iint D_3 \mathrm{d}x\mathrm{d}y = 0$. Thus, the transducer voltage can be obtained

from

$$V = -\frac{\iiint E_3 \mathrm{d}x\mathrm{d}y\mathrm{d}z}{lb}. \tag{6.49}$$

By substituting eq.(6.48) into eq.(6.49) yields

$$V = \frac{d_{31}(C_{11}^{(E)} + C_{12}^{(E)})\hat{h} \iint (\varepsilon_{11} + \varepsilon_{22})\mathrm{d}x\mathrm{d}y}{lb[e_{33}^{(\sigma)} - 2d_{31}^2(C_{11}^{(E)} + C_{12}^{(E)})]}, \tag{6.50}$$

where the in-plane normal strains are assummed to be constant through the transducer thickness. Substituting the stiffness matrix components from equations (6.45),(6.46) and (6.47), the voltage generated by a rectangular piezoelectric sensor as a function of the in-plane strains is

$$V = \frac{d_{31}Y^{(E)}\hat{h} \iint (\varepsilon_{11} + \varepsilon_{22})\mathrm{d}x\mathrm{d}y}{lb[e_{33}^{(\sigma)}(1-\nu) - 2d_{31}^2 Y^{(E)}]}. \tag{6.51}$$

It is assumed, that the presence of the sensor has no significant effect on the strain field of the incident wave. The plane wave propagates along direction x' inclined at an angle θ from the sensor's lengthwise direction x as shown in Figure 6.26. The surface strain components along the wave propagation axes (x', y') must be rotated to the sensor geometrical axes (x, y). For plane waves $(\varepsilon_{y'y'} = 0)$, the following strain invariant can be written as

$$\varepsilon_{xx} + \varepsilon_{yy} = \varepsilon_{x'x'} + \varepsilon_{y'y'} = \varepsilon_{x'x'}. \tag{6.52}$$

Thus, eq.(6.51) becomes

$$V = \frac{d_{31}Y^{(E)}\hat{h} \iint (\varepsilon_{x'x'})\mathrm{d}x\mathrm{d}y}{lb[e_{33}^{(\sigma)}(1-\nu) - 2d_{31}^2 Y^{(E)}]}. \tag{6.53}$$

The strain term $\varepsilon_{x'x'}$ can be written in terms of modal strain amplitude A_ε as

$$\varepsilon_{x'x'} = A_\varepsilon \cdot e^{i\omega t - ikx'}, \tag{6.54}$$

where k, ω and t are the wavenumber, the circular frequency and the time, respectively. The voltage response to harmonic Lamb waves can be written in terms of the voltage response amplitude $\bar{V}$ as

$$V = \bar{V}e^{i\omega t}. \tag{6.55}$$

Thus, by solving eq.(6.53) and applying eq.(6.54), the amplitude of the voltage response to a particular Lamb mode r for the rectangular PZT sensors becomes

$$\bar{V}_{\mathrm{PZT}}^{(r)} = \mathbf{S}_{\mathrm{PZT}} \cdot \mathbf{I}_{\mathrm{PZT}}^{(r)} \cdot A_\varepsilon^{(r)}, \tag{6.56}$$

where

$$\mathbf{S}_{\mathrm{PZT}} = \frac{d_{31}Y^{(E)}\hat{h}}{\left[e_{33}^{(\sigma)}(1-\nu) - 2Y^{(E)}d_{31}^2\right]}, \tag{6.57}$$

$$\mathbf{I}_{\mathrm{PZT}}^{(r)} = \frac{4}{lbk_r^2 \sin\theta\cos\theta} \cdot \sin\left(\frac{k_r b \sin\theta}{2}\right) \sin\left(\frac{k_r l \cos\theta}{2}\right). \tag{6.58}$$

Applying the relationship $\lim_{a\to 0}\left(\frac{\sin(a)}{a}\right) = 1$, the amplitude of the voltage response for PZT sensors in the case of parallel incident waves ($\theta = 0$) becomes

$$\begin{aligned}\bar{V}^{(r)}_{\text{PZT}} &= \mathbf{S}_{\text{PZT}} \cdot A^{(r)}_{\varepsilon} \cdot \frac{2}{k_r l} \sin\left(\frac{k_r l}{2}\right), \\ &= \mathbf{S}_{\text{PZT}} \cdot A^{(r)}_{\varepsilon} \cdot \frac{\lambda_r}{\pi l} \sin\left(\frac{\pi l}{\lambda_r}\right),\end{aligned} \tag{6.59}$$

where λ_r is the wavelength of mode r. The equation (6.59) reduces further, when a point sensor is considered ($l, b \to 0$) giving

$$\bar{V}^{(r)}_{\text{PZT}} = \mathbf{S}_{\text{PZT}} \cdot A^{(r)}_{\varepsilon}. \tag{6.60}$$

An alternative formulation for the equation (6.51) is given in [135, 170], by treating the piezoelectric sensor as a parallel plate capacitor. This formulation gives a more conservative voltage response and change only the $\mathbf{S}_{\text{PZT}}$ term as

$$\mathbf{S}_{\text{PZT}} = \frac{d_{31} Y^{(E)} \hat{h}}{e^{(\sigma)}_{33}(1-\nu)}. \tag{6.61}$$

The effect of shear lag due to the bonding layer between the plates and the PZT sensors is neglected in our calculation, but it can be included following the approaches in [135, 170].

For comparison purposes, the harmonic voltage response amplitude is calculated for a rectangular PZT sensor subjected to parallel incident Lamb wave ($\theta = 0$) on a 2.38mm thick aluminum plate given in [7]. Four different sensor lengths l are considered, which are 12.7mm, 6.35mm, 3.17mm and 0mm (theoritical point sensor). The results comparing the approach in [7] and the SAFE method are given in Figure 6.27 and Figure 6.28 for the A_0 and the S_0 Lamb modes, respectively. In the calculation using the SAFE method, the A_ε term is obtained from equation (6.35).

The harmonic voltage responses are normalized to an average power flow P_m, which can be calculated using equation (5.15). Good agreements are obtained. A slight discrepancy can be seen in Figure 6.27 for a point sensor response of the A_0 mode. A good match is obtained for all sensor length, for the S_0 mode as shown in Figure 6.28. It is worth noting that in reference [7], an analytical strain expression is used [79]. This may lead to differences in the results as the SAFE method gives approximate solutions. However, the analytical expression is available only for isotropic plates.

6.5.4.2 Voltage response to arbitrary excitation

In the frequency domain, a linear system response subjected to an arbitrary excitation is obtained as the product of the system response to a harmonic excitation and the Fourier transform of the excitation. Thus, the voltage amplitude due to an arbitrary excitation $\bar{U} = \bar{U}(\omega)$ is calculated from the voltage amplitude due to a harmonic excitation $\bar{V} = \bar{V}(\omega)$

(a)

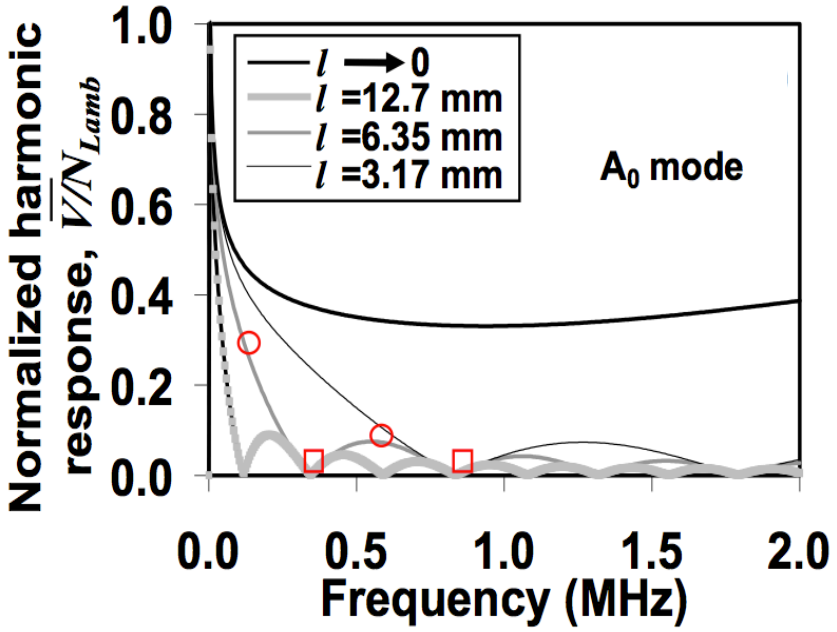

(b)

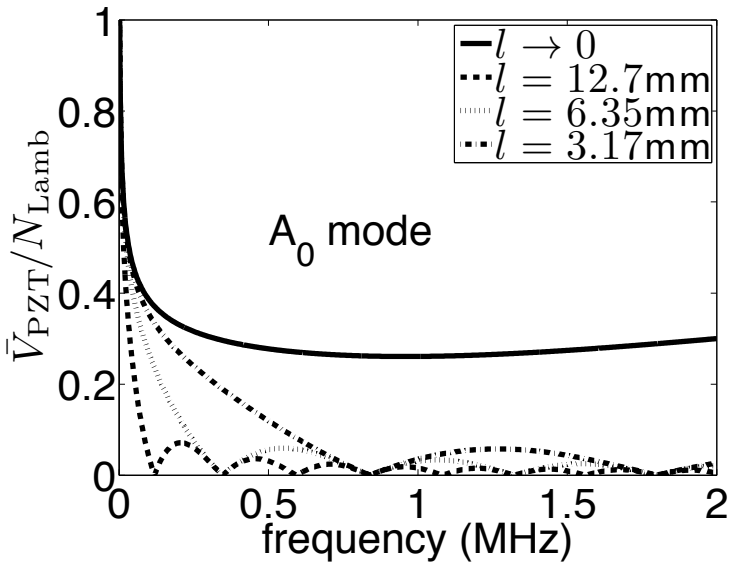

FIGURE 6.27: Normalized harmonic voltage response of a sensor subjected to parallel incident A_0 Lamb waves with varying sensor length l from (a) Reference [7], (b) SAFE.

and the amplitude of the Fourier transform of the excitation $\bar{P} = \bar{P}(\omega)$, as

$$\bar{U} = \bar{V} \times \bar{P} \tag{6.62}$$

For thin sensors, the surface strain at the sensors is assumed to be concentrated at the sensor edges. Thus, the sensor excitation is expressed in terms of the amplitude spectrum of the surface strain induced by an arbitrary source at the point of entry into the sensor, $\varepsilon^{(a)}_{x'x'} \mid_{z=h/2} (\omega)$ as [7]

$$\bar{P} = \frac{\varepsilon^{(a)}_{x'x'} \mid_{z=h/2} (\omega)}{\varepsilon_{x'x'} \mid_{z=h/2} (\omega)}, \tag{6.63}$$

(a)

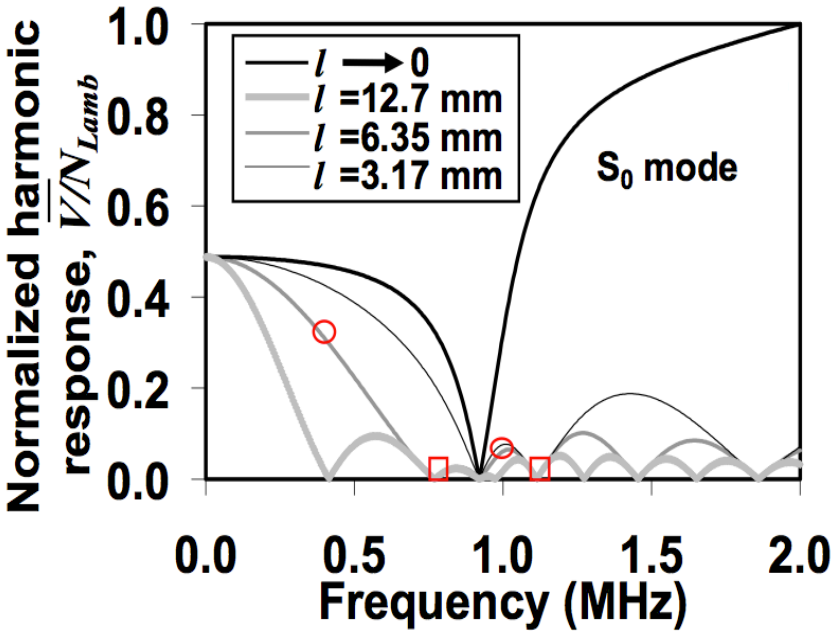

(b)

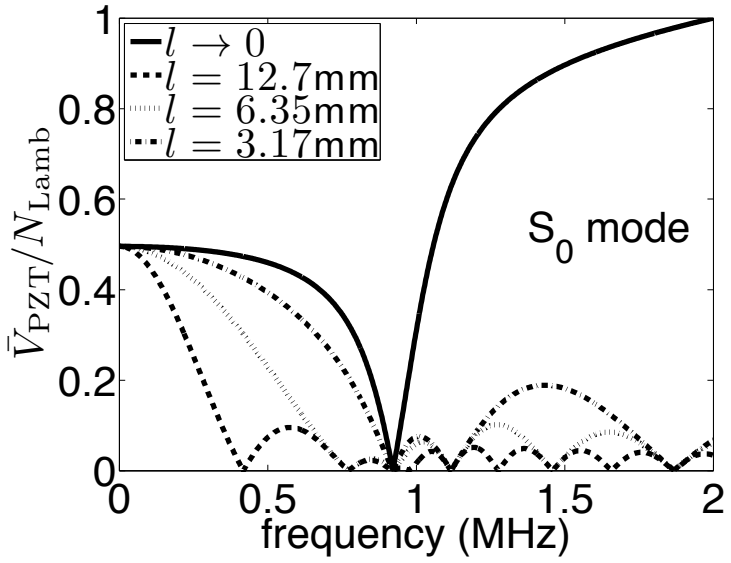

FIGURE 6.28: Normalized harmonic voltage response of sensor subjected to parallel incident S_0 Lamb wave with varying sensor length, l from (a) Reference [7], (b) SAFE.

where $\varepsilon_{x'x'}\ |_{z=h/2}\ (\omega)$ is the amplitude spectrum of the surface strain induced under harmonic conditions. The harmonic surface strain field at a point is equivalent to the sensor response to a harmonic excitation, when the sensor length l and width b are taken to be zero (point sensor). Thus, in general, the sensor response to arbitrary excitation becomes

$$\bar{U} = \bar{V} \times \frac{\varepsilon^{(a)}_{x'x'}\ |_{z=h/2}\ (\omega)}{\varepsilon_{x'x'}\ |_{z=h/2}\ (\omega)} = \bar{V} \times \frac{\varepsilon^{(a)}_{x'x'}\ |_{z=h/2}\ (\omega)}{\lim\limits_{l,b\rightarrow 0} \bar{V}/\mathbf{S}}. \tag{6.64}$$

As an example, for PZT sensors, the term $\varepsilon_{x'x'}\,|_{z=h/2}\,(\omega)$ for mode r is obtained from equation (6.60) as

$$\varepsilon_{x'x'}\,|_{z=h/2}\,(\omega) = \lim_{l,b\to 0} \bar{V}^{(r)}_{\mathrm{PZT}}/\mathbf{S}_{\mathrm{PZT}} = A^{(r)}_{\varepsilon}. \tag{6.65}$$

In order to find the strain term at the point of entry into the sensor $\varepsilon^{(a)}_{x'x'}\,|_{z=h/2}\,(\omega)$, the FEM can be applied as outlined in [7]. However, it is difficult to excite a single mode and also to differentiate the contribution of the available modes within the frequency range considered. The application of an appropriate continuous wavelet transform and a time gate may help to separate some of these modes, but can not solve the problem entirely [7]. However, by using the SAFE method, the term $\varepsilon^{(a)}_{x'x'}\,|_{z=h/2}\,(\omega)$ can be calculated easily for the single mode required. Furthermore, there is also no problem of plate edge reflection as in the FEM, due to the fact that the plate is considered infinite in the SAFE method.

For comparison, the same excitation function as in [7] is applied for the rectangular PZT sensor. The sensor is attached on a 2.38mm thick aluminum plate. Only parallel incidence waves ($\theta = 0$) are considered. The unmodulated tone burst is given in the time domain as

$$f(t) = \begin{cases} D\sin\omega_0 t & \text{for } |t| < T \\ 0 & \text{for } |t| > T \end{cases}, \tag{6.66}$$

where ω_0, $2T$, and D is the central frequency, the time duration of the wave and the amplitude factor, respectively. The Fourier transform of this tone burst is given by

$$\bar{F} = D\left[\frac{\sin n\pi\left(\dfrac{\omega}{\omega_0}+1\right)}{(\omega+\omega_0)} - \frac{\sin n\pi\left(\dfrac{\omega}{\omega_0}-1\right)}{(\omega-\omega_0)}\right], \tag{6.67}$$

where n is the number of cycles within the time window. By assuming that this quantity corresponds directly to the surface strain $\varepsilon^{(a)}_{x'x'}\,|_{z=h/2}\,(\omega)$, the excitation amplitude spectrum of the PZT sensors for mode r can be calculated from equation (6.63) as

$$\bar{P} = \frac{\varepsilon^{(a)}_{x'x'}\,|_{z=h/2}\,(\omega)}{\varepsilon_{x'x'}\,|_{z=h/2}\,(\omega)} = \frac{\bar{F}}{\lim\limits_{l,b\to 0}\bar{V}/\mathbf{S}} = \frac{\bar{F}}{A^{(r)}_{\varepsilon}}. \tag{6.68}$$

Substituting back equation (6.67), (6.68) and (6.59) into equation (6.62) gives the PZT sensor response amplitude for mode r as

$$\hat{U} = D\left[\frac{\sin n\pi\left(\dfrac{\omega}{\omega_0}+1\right)}{(\omega+\omega_0)} - \frac{\sin n\pi\left(\dfrac{\omega}{\omega_0}-1\right)}{(\omega-\omega_0)}\right]\cdot \mathbf{S}_{\mathrm{PZT}}\cdot\frac{\lambda_r}{\pi l}\sin\left(\frac{\pi l}{\lambda_r}\right). \tag{6.69}$$

The narrowband sensor response is plotted for the A_0 mode as shown in Figure 6.29 comparing the results from [7] and the SAFE method. Three different center frequencies for the tone burst are taken which corresponds to a large value (f_{max} at $\lambda = 2l$), an intermediate value (f_{int}) and the first zero value (f_{min} at $\lambda = l$) of the sensor response to the harmonic A_0 mode. These frequencies are $f_{max} = 0.35$MHz, $f_{int} = 0.55$MHz

and $f_{min} = 0.84$MHz, respectively. Comparing the results between reference [7] and the SAFE method for the tone burst excitation, there are some amplitude differences due to the factor D, the factor $\mathbf{S}_{\mathrm{PZT}}$ and the number of cycles n. These values were not given in the reference [7]. Therefore, the values of $n = 5$, $\mathbf{S}_{\mathrm{PZT}} = 1$ and $D = 1$ have been used in the calculations using the SAFE method. However, good agreements are observed for the peak locations.

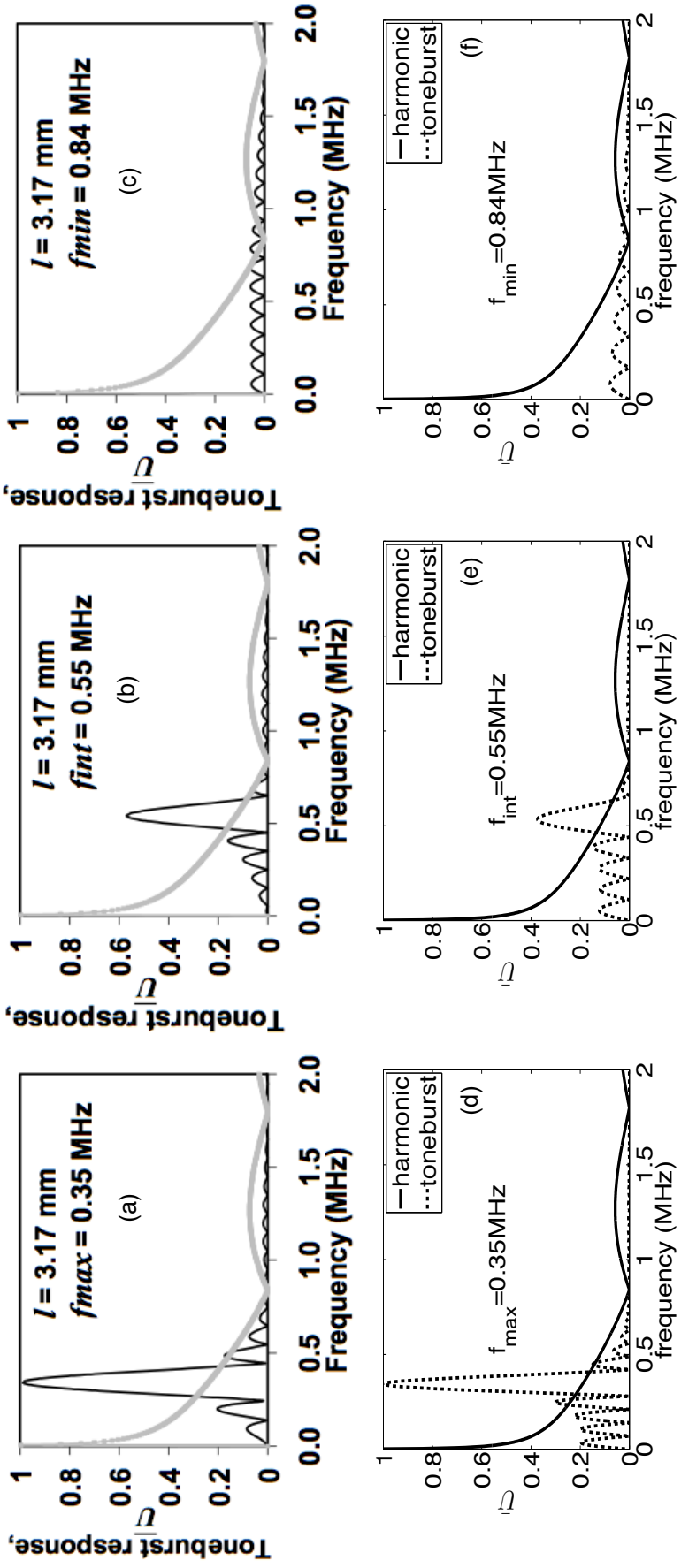

FIGURE 6.29: Frequency response of sensor subjected to parallel incident A_0 Lamb mode for harmonic and tone burst excitation using approaches in [7] [figure (a),(b) and (c)], and using the SAFE method [figure (d),(e) and (f)]. Grey line in figure (a),(b) and (c) represents the harmonic excitation while the black line represents the tone burst excitation.

6.5.5 Actuator/sensor coupled system simulation

The SAFE method has been coupled with the FEM in [156] to simulate thick actuators. By applying the same approach here, the couple SAFE-FE method is used to simulate both actuator and sensor. The actuator and sensor are represented in the FEM using the piezoelectric elements. This approach is useful when the shear lag effects can not be neglected especially in thick actuators and sensors. Consider a piezoelectric actuator strip with a length of $2a$ attached on the plate as shown in Figure 6.30.

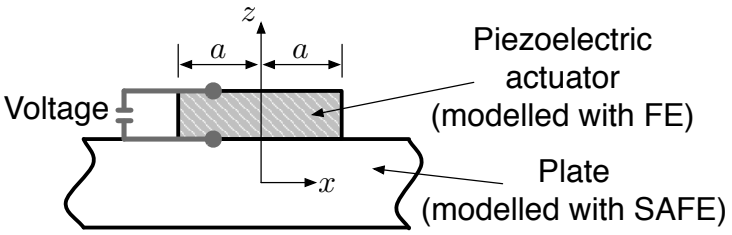

FIGURE 6.30: Piezoelectric actuator attached on an infinite plate.

The response of the plate to forces at each degree of freedom (dof) in contact with the piezoelectric actuator is computed from eq.(6.4). The plate receptance r_{ij} is defined as the response at dof i due to a unit force applied at dof j, i.e. $\mathbf{u}_i = r_{ij}\mathbf{f}_j$. Thus, the displacements at the interface dof ($\mathbf{U}_{\text{int}}$) due to the forces at the interface dof can be related by the receptance matrix R as

$$\mathbf{U}_{\text{int}} = R\mathbf{F}_{\text{int}}. \tag{6.70}$$

For example, if the actuator and the plate are connected at node number 1 and 2, then in a 2D force response analysis, equation 6.70 can be written as

$$\begin{Bmatrix} u_{x1} \\ u_{z1} \\ u_{x2} \\ u_{z2} \end{Bmatrix} = \begin{bmatrix} r_{x1x1} & r_{x1z1} & . & . \\ r_{z1x1} & r_{z1z1} & . & . \\ . & . & r_{x2x2} & r_{x2z2} \\ . & . & r_{z2x2} & r_{z2z2} \end{bmatrix} \begin{Bmatrix} f_{x1} \\ f_{z1} \\ f_{x2} \\ f_{z2} \end{Bmatrix}. \tag{6.71}$$

The coupling between the displacements and the loads for different nodes at the interface is already included in the piezoelectric element formulation in the FEM. Thus, the displacements and the forces are related only at the same node in equation 6.71.

The response of the plate is computed for a particular frequency of harmonic excitation. Therefore, the inverse of R gives matrix $\mathbf{D}^{\text{plate}}$, which is the dynamic stiffness matrix of the plate at these interface nodes. Thus

$$\mathbf{D}^{\text{plate}}\mathbf{U}_{\text{int}} = \mathbf{F}_{\text{int}}. \tag{6.72}$$

The matrix $\mathbf{D}^{\text{plate}}$ is symmetric and fully populated [156]. Dynamic stiffness matrix of the piezoelectric actuator $\mathbf{D}^{\text{piezo}}$ is computed at a particular circular frequency ω as

$$\mathbf{D}^{\text{piezo}} = \mathbf{K}^{\text{piezo}} - \omega^2\mathbf{M}^{\text{piezo}}. \tag{6.73}$$

For piezoelectric elements, there are additional degrees of freedom at the nodes corresponding to the nodal electrical potential. The matrix $\mathbf{D}^{\text{piezo}}$ can be partitioned into the degrees of freedom in contact with the plate, $\mathbf{U}_{\text{int}}$ and the degrees of freedom not in contact with the plate, $\mathbf{U}_{\text{non}}$. Thus, the two dynamic stiffness matrices from the plate and the actuator are combined to represent the piezoelectric actuator attached to the plate as

$$\begin{bmatrix} \mathbf{D}^{\text{piezo}}_{\text{non-non}} & \mathbf{D}^{\text{piezo}}_{\text{non-int}} \\ \mathbf{D}^{\text{piezo}}_{\text{int-non}} & \mathbf{D}^{\text{piezo}}_{\text{int-int}} + \mathbf{D}^{\text{plate}} \end{bmatrix} \begin{Bmatrix} \mathbf{U}_{\text{non}} \\ \mathbf{U}_{\text{int}} \end{Bmatrix} = \begin{Bmatrix} \mathbf{F}_{\text{non}} \\ \mathbf{F}_{\text{int}} \end{Bmatrix}. \tag{6.74}$$

The piezoelectric actuator are subjected to an electrical potential at the top surface and zero electrical potential at the bottom surface. By applying these boundary conditions with zero forces on the actuator, equation 6.74 is solved to get the actuator displacements. The displacements $\mathbf{U}_{\text{int}}$ at the interface nodes are substituted into equation 6.72 to obtain the forces $\mathbf{F}_{\text{int}}$ acting on the plate at the interface nodes. $\mathbf{F}_{\text{int}}$ is then used in equation (6.4) to obtain the plate displacements at any x distances. This approach allows the computation of the forced harmonic response of the piezoelectric transducers attached to the plates.

For comparison purpose, a piezoelectric actuator with a thickness of 0.2mm and a length of $2a$ = 6mm, attached on a 1mm thick aluminum plate is simulated. The material properties of the piezoelectric actuator are given in Table 6.3. The aluminum plate has a Young's modulus of 70GPa, a Poisson's ratio of 0.33 and a density of 2700kg/m^{-3}. The electrical potentials at the top and bottom actuator surfaces are 5 and 0 volts, respectively. These electrical potential are Hann windowed with a center frequency of 250kHz and 5 number of cycles. The actuator is modelled in Abaqus using square CPE4E piezoelectric plain strain elements with the element length of 0.1mm. The plate is modelled using the SAFE method with 5 quadratic 1D elements in the plate thickness. Displacements for a point located at a distance of 80mm from the center of the actuator are calculated. Results are compared with a fully FEM simulation in Abaqus as shown in Figure 6.31. A good agreement has been obtained. Two modes can be seen, S_0 mode followed by A_0 mode. The values of the displacement results obtained using the SAFE-FE method are slightly higher than the Abaqus results especially for the A_0 mode.

TABLE 6.3: Piezoelectrical material with a transversal isotropic material properties. The electric constant is $e_0 = 8.8542 \times 10^{-12}$As/(Vm). The poling is in the 3rd direction. Plane $1-2$ is the plane of isotropy.

Parameters	Values	Parameters	Values
$C_{11}^{(E)}$	1.0772×10^{11}N/m^2	d_{31}	-2.14×10^{-10}m/V
$C_{33}^{(E)}$	1.0052×10^{11}N/m^2	d_{33}	4.23×10^{-10}m/V
$C_{55}^{(E)}$	0.1962×10^{11}N/m^2	d_{15}	6.10×10^{-10}m/V
$C_{12}^{(E)}$	0.6326×10^{11}N/m^2	$e_{11}^{(\sigma)}/e_0$	1936
$C_{13}^{(E)}$	0.6398×10^{11}N/m^2	$e_{33}^{(\sigma)}/e_0$	2109
$C_{44}^{(E)}$	0.1962×10^{11}N/m^2	ρ	7760 kg/m^3
$C_{66}^{(E)}$	0.2224×10^{11}N/m^2		

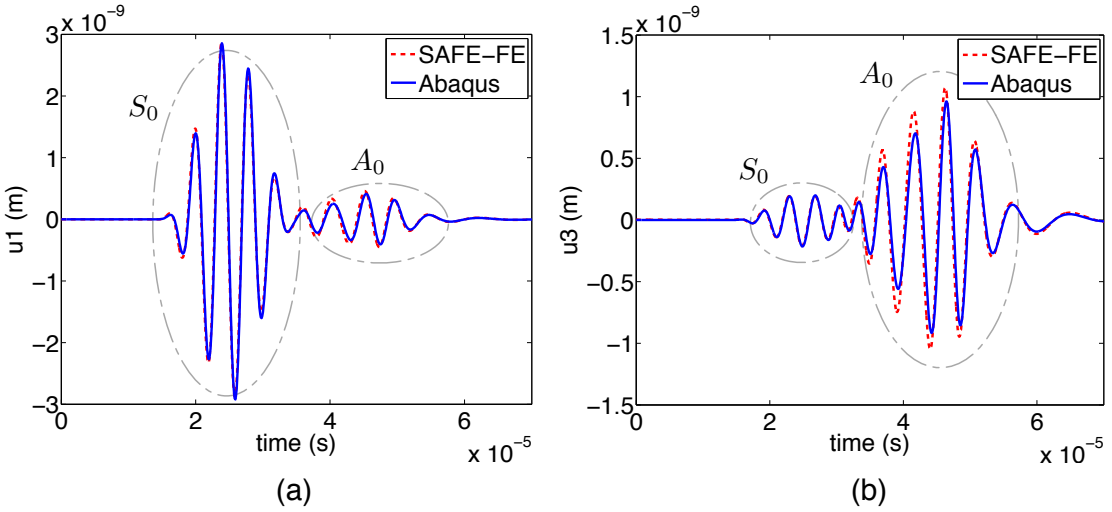

FIGURE 6.31: Displacement results for a point located at a distance of 80mm from the actuator; (a) Displacements along x axis, and (b) Displacements along z axis.

The same SAFE-FE modelling approach can be used to obtain the electrical potentials in sensors due to the Lamb wave propagations. For the sensors, it is assumed that the sensor bottom surface has a zero electrical potential. By applying this electrical potential and the displacements of the bottom surface nodes (interface nodes) $\mathbf{U}_{\text{int}}$ in the equation 6.74, the nodal electrical potentials at the sensor top surface are calculated. The nodal electrical potentials are averaged by summing the electrical potentials from every nodes on the sensor top surface and then dividing it with the total number of nodes considered. This yields the value of the average electrical potential on the sensor top surface.

As an example, the previous numerical example is extended by adding a sensor located at a distance of 80mm from the actuator. The sensor material properties, dimensions and FE model are equal to the actuator. The induced plate displacements by the actuator are converted into electrical potentials in the sensor . The average electrical potential on the sensor top surface is calculated using the SAFE-FE method and compared to the FEM result calculated using Abaqus. A good agreement has been obtained as shown in Figure 6.32.

The effect of an obstacle on the Lamb wave propagation can be simulated using the reflection and transmission coefficients obtained from the method outlined in Chapter 5. By multiplying the transmission coefficients on the amplitude of each Lamb mode considered, the sensor response with the presence of the obstacle can be calculated. As an example, a lap joint is considered as an obstacle in a 1mm thick aluminum plate. The geometry of the lap joint and the reflection and the transmission coefficients of the lap joint are shown in the Figures 6.33 and 6.34, respectively. In the SAFE-FE method, the actuator, the lap joint and the sensor are simulated using FEM while the infinite plate regions are simulated using the SAFE method. The same material, elements and boundary conditions as in the previous examples are applied to the actuator and the sensor. The plate is modelled using 5 quadratic 1D elements in the SAFE method. The lap joint is modelled using square plain strain elements (CPE4) in Abaqus with the element length of 0.1mm. A comparison with a FEM simulation in Abaqus is shown in Figure 6.35. There

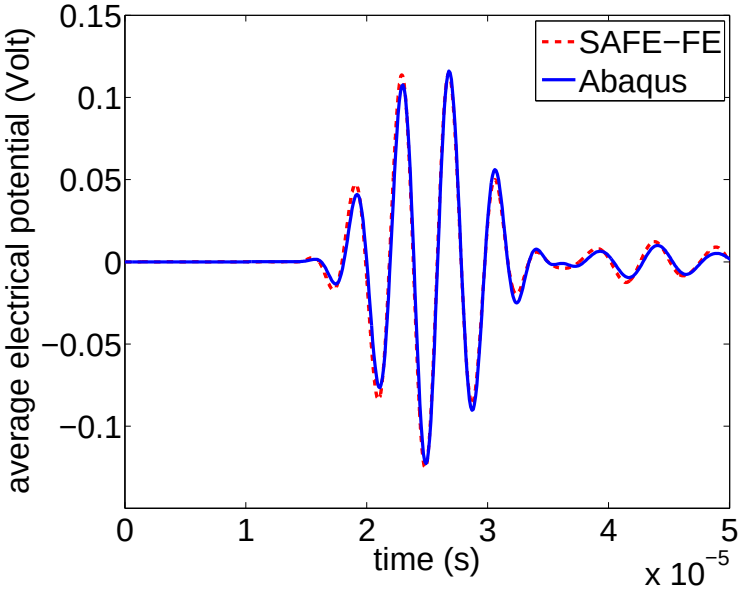

FIGURE 6.32: Average electrical potential on the top surface of a sensor located at a distance of 80mm from the actuator.

is a slight amplitude disagreement in the average electrical potential on the sensor top surface. This is caused by the dynamic motions of the lap joint which are not taken into considerations in the SAFE-FE method.

From the Figure 6.35, at the simulation time below 0.7×10^{-3}s, the reflections from the actuator and the sensor does not need to be considered. This is due to the fact that the lap joint is located at the middle between the actuator and the sensor with d1 = d2 = 114.5mm. However, when the lap joint location is changed to other locations as given in Table 6.4, there are reflections from the nearest transducer (either actuator or sensor, whichever is nearer), as shown in Figure 6.36. All the Abaqus solutions for different lap joint locations coincide at the first part, which corresponds to the effects of the lap joint. From these Abaqus results, we can conclude that the differences in the lap joint locations does not require different treatment in the SAFE-FE method as long as the total distances between actuator and sensor remain the same. Only the additional reflections from the actuator and sensor are required to be added to the solutions. However, only the lap joint effects are being considered in the SAFE-FE method; the results are shown in the Figure 6.36. Thus the effects from the actuator/sensor are not available.

TABLE 6.4: Locations of the lap joint with respect to the actuator and the sensor

Location	d1(mm)	d2(mm)
a	65	164
b	105	124
c	114.5	114.5
d	164	65

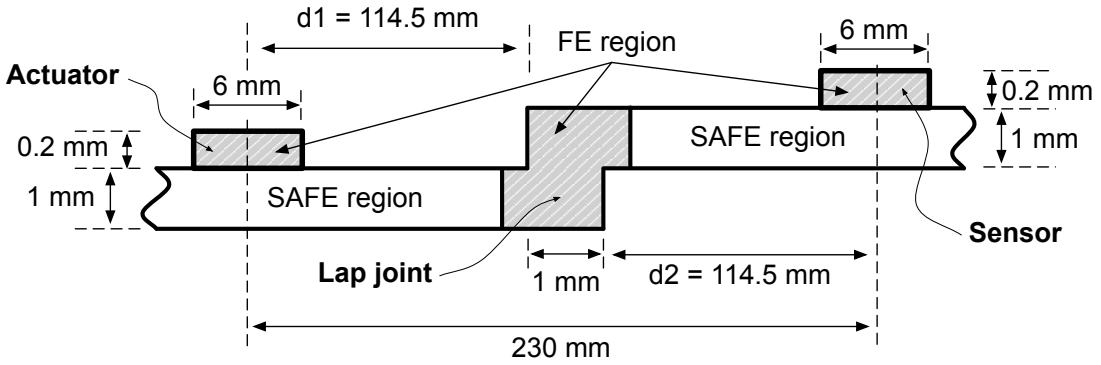

FIGURE 6.33: A lap joint located between an actuator and a sensor in a 1mm thick infinite aluminum plate.

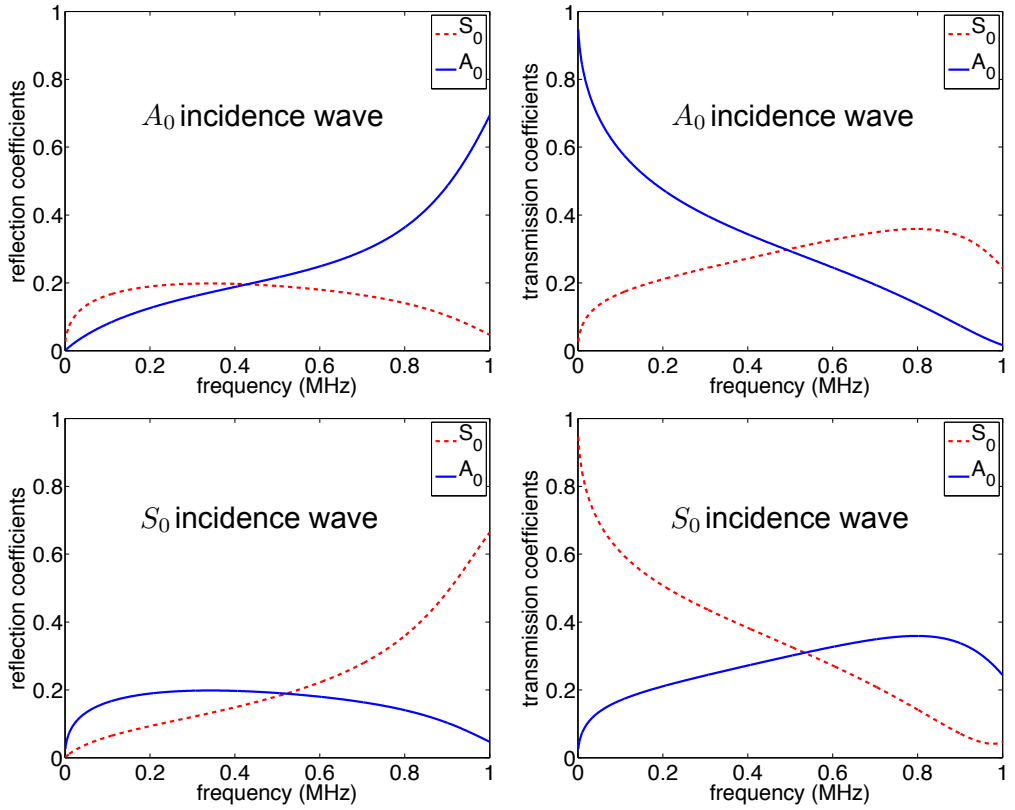

FIGURE 6.34: The reflection and the transmission coefficients of the lap joint due to the A_0 and the S_0 incidence Lamb waves.

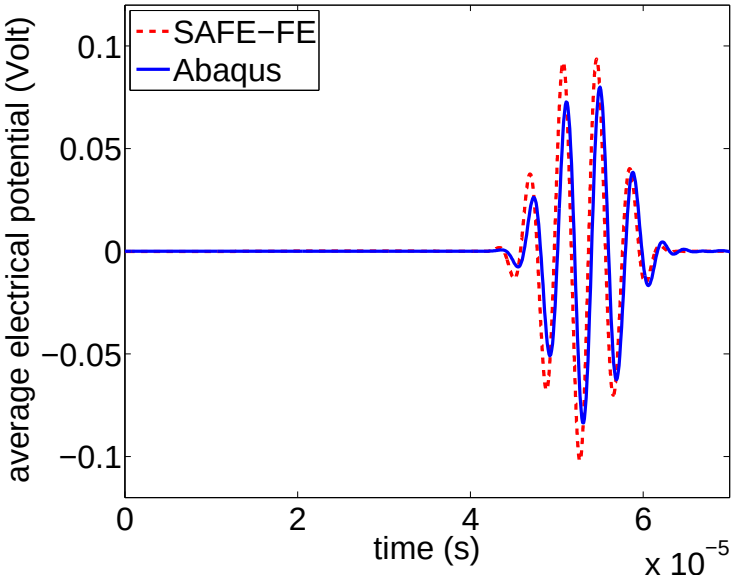

FIGURE 6.35: Average electrical potential on the top surface of the sensor.

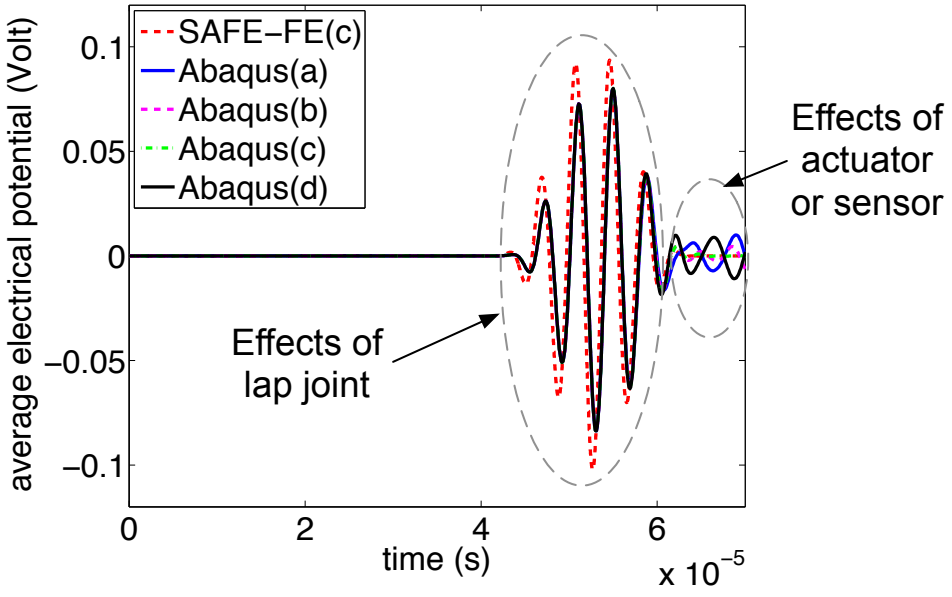

FIGURE 6.36: Average electrical potential on the top surface of the sensor for different lap joint locations (locations a to d).

Chapter 7

Conclusions and Future research

7.1 Conclusions

The three main capabilities of the SAFE method in the Lamb wave simulations have been explored in this thesis; (a) the calculation of the dispersion curves, (b) the reflection and transmission analysis due to obstacles, and (c) the force response analysis.

In the dispersion curves calculations, the SAFE method has been shown to be applicable for both isotropic and composite plates. The effects of symmetrical and unsymmetrical material properties with respect to the plate center plane is presented. The effects of the in-plane loading on the dispersion curves in isotropic plates are given which are limited to very frequency ranges. The example on the skew angle calculations illustrate the differences between the Lamb wave propagation directions and the group velocity (wave energy) directions commonly found in composite plates.

In the reflection and transmission analysis, the effects of symmetrical and unsymmetrical obstacles on the plane Lamb wave propagations are shown. Complex obstacles have been considered. Symmetrical obstacles reflect and transmit the same type of modes as the incidence Lamb modes. On the other hand, unsymmetrical obstacles always reflect and transmit both types of Lamb modes. The same analysis is extended to transducers and stiffeners on the plates. It is shown that a lighter transducer has lesser effect on Lamb wave propagations. In the case of the stiffener analysis, the reflections inside the stiffener cause a complex behavior in the Lamb wave reflections and transmissions. The stiffener base length is found to have insignificant effects on the Lamb wave reflection and transmission behavior.

In the force response analysis, the application of the SAFE method for 2D and 3D force response analysis are shown. An approach is introduced to consider the plate edges reflections as a superposition of infinite plate solutions. Additional phases are considered to allow the simulation of point forces which are not located at the origin. The application of the coupled SAFE-FE method for modelling actuator-obstacle-sensor coupled system is also presented.

The following conclusions are made about the observed advantages and disadvantages/limitations of the the SAFE method compared to the FEM.

Advantages of SAFE:

- The SAFE method is suitable for the dispersion curves calculations for both isotropic and composite plates. In contrast, dispersion curves are more difficult to obtain using other methods [4]. However, in the SAFE method, homogenized material properties need to be used for each layer. Each different material layer in the plate needs to be represented by at least one element.

- The different types of modes are already separated in the SAFE method. This is a huge advantage when particular modes are of interest. As the modes are separated, the influence on the reflections, the transmissions and the force responses can be obtained separately for each mode. The total solution is then obtained as a summation of the solutions from each participating mode. On the other hand in the FEM, the solutions obtained include all the modes involved and can not be separated easily according to each mode.

- The SAFE method is based on infinite plates (or waveguides). Thus, it is suitable for the analysis if the plate boundaries are irrelevant. This is normally the case for actuator and sensor simulations. Furthermore, this feature is useful for a comparison with experimental investigations as the effects of the boundaries are normally excluded by using clay at the plate edges to avoid any edge reflections. However in the FEM simulations, special types of the infinite elements need to be used to simulate infinite boundaries. Infinite boundaries are also achieved in the FEM by coupling the FEM with the boundary element method (BEM) as it is normally applied in acoustic simulations.

- The SAFE method is tuned for wave propagation problems. In this method, the wave propagation direction is represented by exponential functions. Thus, in order to represent the wavelength, the SAFE method is not affected by small element requirements as in the FEM. Only the discretizations in the thickness of the plates are affected by this requirements.

- By applying the Fourier transform method in the force response analysis, the SAFE method is efficient in obtaining the displacement solutions of particular points as a function of time. The distances between these points and the excitation sources does not affect the computational time. In contrast, the FEM requires more elements if the measured displacement points are located further away from the loading source. However, the FEM solves the displacements for all points in the model at each time increment. Iterations are made to consider all the time increment until the simulation time ended. On the other hand in the SAFE method, iterations are made at each point in the model where solutions are required. Thus, the SAFE method is more suitable than the FEM if only solutions at small regions are required.

Disadvantages/limitations of SAFE:

- Due to the fact that the SAFE method is tuned to the wave propagation problems, it is not as robust as the FEM, which can be applied to a wide range of problems.
- The SAFE method needs to be coupled with other methods i.e FEM and BEM in order to handle complex geometries. Thus, the application of the SAFE method is limited to infinite regions of waveguides only.
- In the force response analysis, the SAFE method is affected by typical problems in the numerical computations of the Fourier transform using the Fast Fourier transform (FFT). Due to periodicity assumption in the FFT, solutions at the end of simulation time should be equal to solutions at the beginning of simulation time (wrap-around effects). Thus, the solutions at the beginning are polluted (non zero) if the solutions at the end of simulation time are not zero.
- The SAFE method is based on infinite waveguides. Therefore, an additional approach is required to apply this method to finite plates, and to consider the reflections from the plate edges in the force response simulations.
- The SAFE method can not consider all effects at once as in the FEM. Each effect in the wave propagation behavior needs to be included separately and then added up together. The solutions are also obtained separately for each mode. Thus, the total responses of the whole plate are obtained as a summation of the mode responses.
- The SAFE method allows the material property variations only in the plate thickness direction. Thus, the SAFE method is no longer applicable when the material properties are varied along the wave propagation directions. Other methods such as the WFE method, have to be used in this case. An introduction to this method is given in Appendix C. However, in comparison to the WFE method, the SAFE method is still an easier and faster method to obtain the dispersion curves, if the plate material properties vary only in the thickness direction, i.e in laminated composite plates.

These advantages and disadvantages/limitations of the SAFE method for the Lamb wave simulations are summarized in Tables 7.1 and 7.2, respectively. The novelties of the presented work are in the studies of

- the effects of the symmetrical and the unsymmetrical material arrangements on the plate dispersion curves,
- the effects of the complex symmetrical and the unsymmetrical obstacles on the Lamb wave propagation behaviors,
- the calculation of the mode tuning curves for composite plates,
- the approach for modelling the point forces in the 3D force response analysis, and
- the approach for modelling the plate edges in the transient response analysis using the SAFE method.

TABLE 7.1: Advantages of the SAFE method.

Suitable for dispersion curves calculation
Mode readily differentiated
Tuned to the wave propagation problems (no severe element size requirements)
Suitable for infinite plates/waveguides
Faster than the FEM for small solutions
Each effects/interactions in the wave propagations are separated

TABLE 7.2: Disadvantages/Limitations of the SAFE method.

Not robust/applicable for many problems
Affected by numerical problem from FFT (wrap-around effects)
Require other method to handle complex geometry
Require additional approaches for finite plates
Plate material variation is limited along thickness direction
Each effects/interactions in the wave propagations need to be included separately

7.2 Future research

The examples given for the applications of the SAFE method are not exhaustive. This method has the potentials to be extended for solving other suitable problems. Some of the interesting problems are as follows:

- The Lamb wave reflection and transmission behavior in structures with branches. In this case, the number of boundaries between the SAFE and the FE regions are more than two and depend on the number of branches considered.
- The simulations of 3D obstacles with the considerations for non-plane waves.
- The implementation of the SAFE software into standard commercial FEM software, such as Abaqus.
- The simulation of complex actuator and sensor shapes.
- The inclusion of damping in the reflections and the force response analysis.
- The consideration of more than one stationary point in the stationary phased method for the simulation of general composite plates.
- The consideration of in-plane loads in composite plates. In composite plates, these in-plane loads may be directionally dependent.
- The application of the SAFE method to optimization procedures for determining the plate material properties.

Another point worth noting is that by using the SAFE method, only two main results are obtained; (i) the wavenumbers (from the eigenvalues), and (ii) the plate mode shapes (from the eigenvectors). By manipulating these two results and by applying other methods such as the FEM and the stationary phased method, the SAFE method has been used to study the effects of obstacles and also the force response analysis. Theoretically, the approaches presented in this work can be extended also to other numerical methods which produce wavenumbers and mode shapes of plates, i.e the WFE method.

Appendix A

Appendix for Chapter 5

A.1 Vertical plate edge reflection

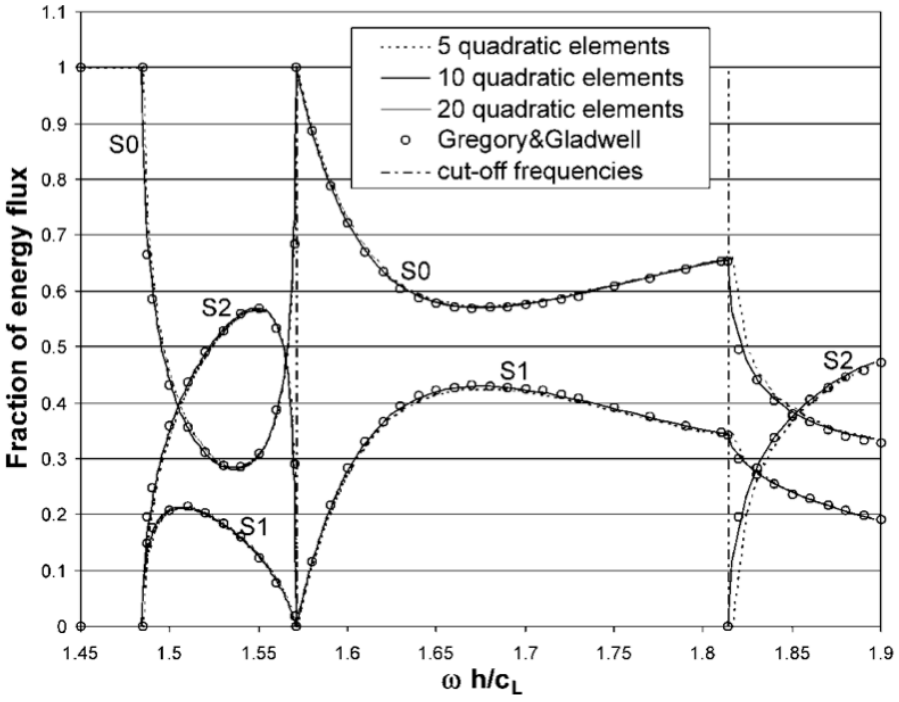

(a)

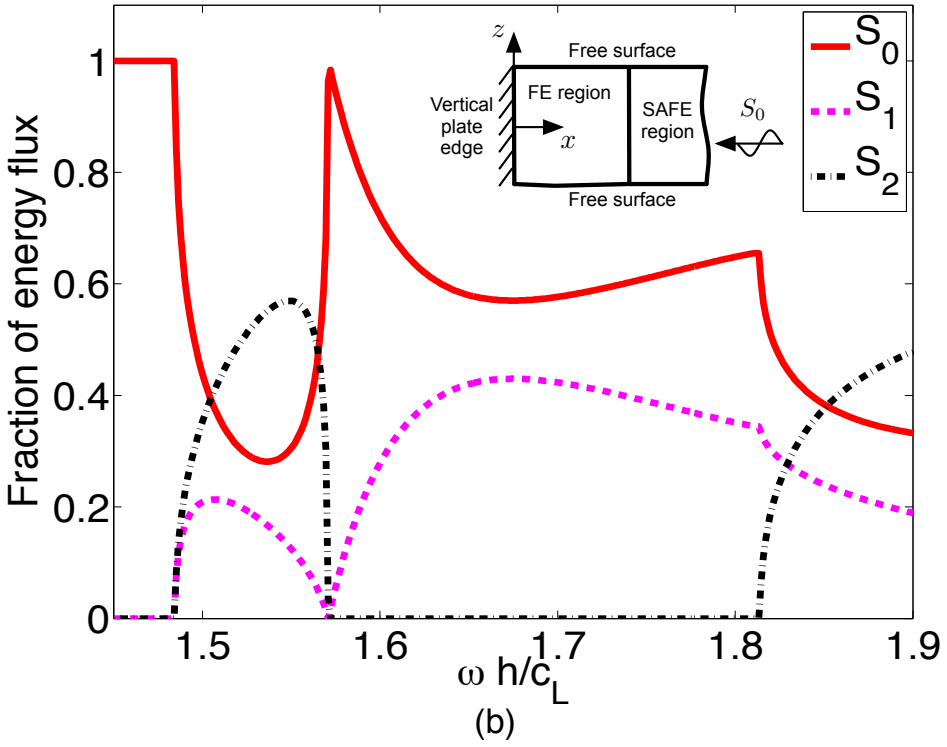

FIGURE A.1: Vertical plate edge reflection; (a) from Reference [5], (b) SAFE-FE implementation here. Isotropic plate data: $\nu = 0.25$, $h = 2$mm, $c_L = 1$km/s and $c_T = 1/\sqrt{3}$km/s.

A.2 Unsymmetric plate edge reflection

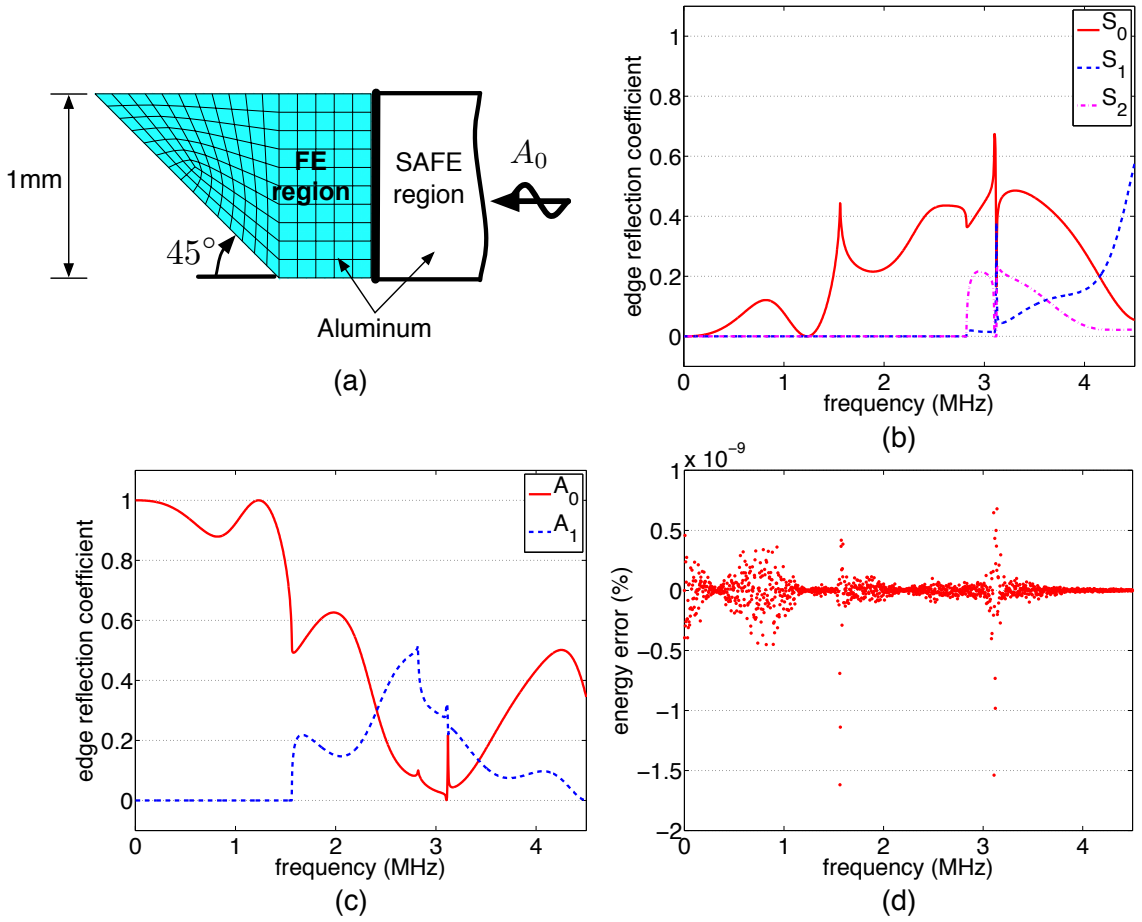

FIGURE A.2: A_0 mode reflection by an inclined free edge (45°); (a) SAFE-FE model, (b) Symmetric modes reflection, (c) Anti-symmetric modes reflection, (d) Percentage of energy error.

A.3 SAFE-FE middle plate reflection

A.3.1 Without damages

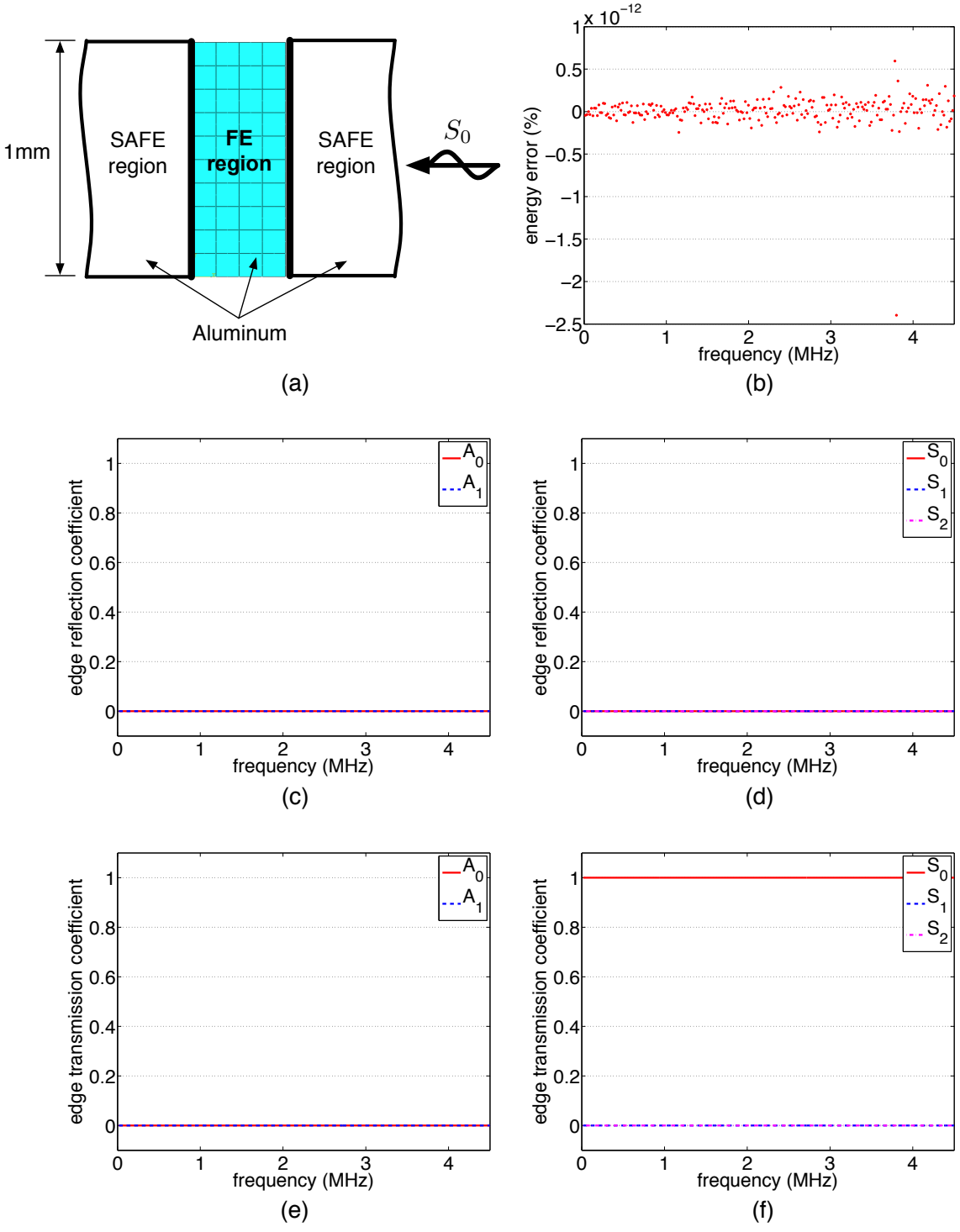

FIGURE A.3: SAFE-FE coupling at the middle of the plate (without damages) with S_0 incident wave; (a) SAFE-FE model, (b) Percentage of energy error, (c) Anti-symmetric modes reflection, (d) Symmetric modes reflection, (e) Anti-symmetric modes transmission, (f) Symmetric modes transmission.

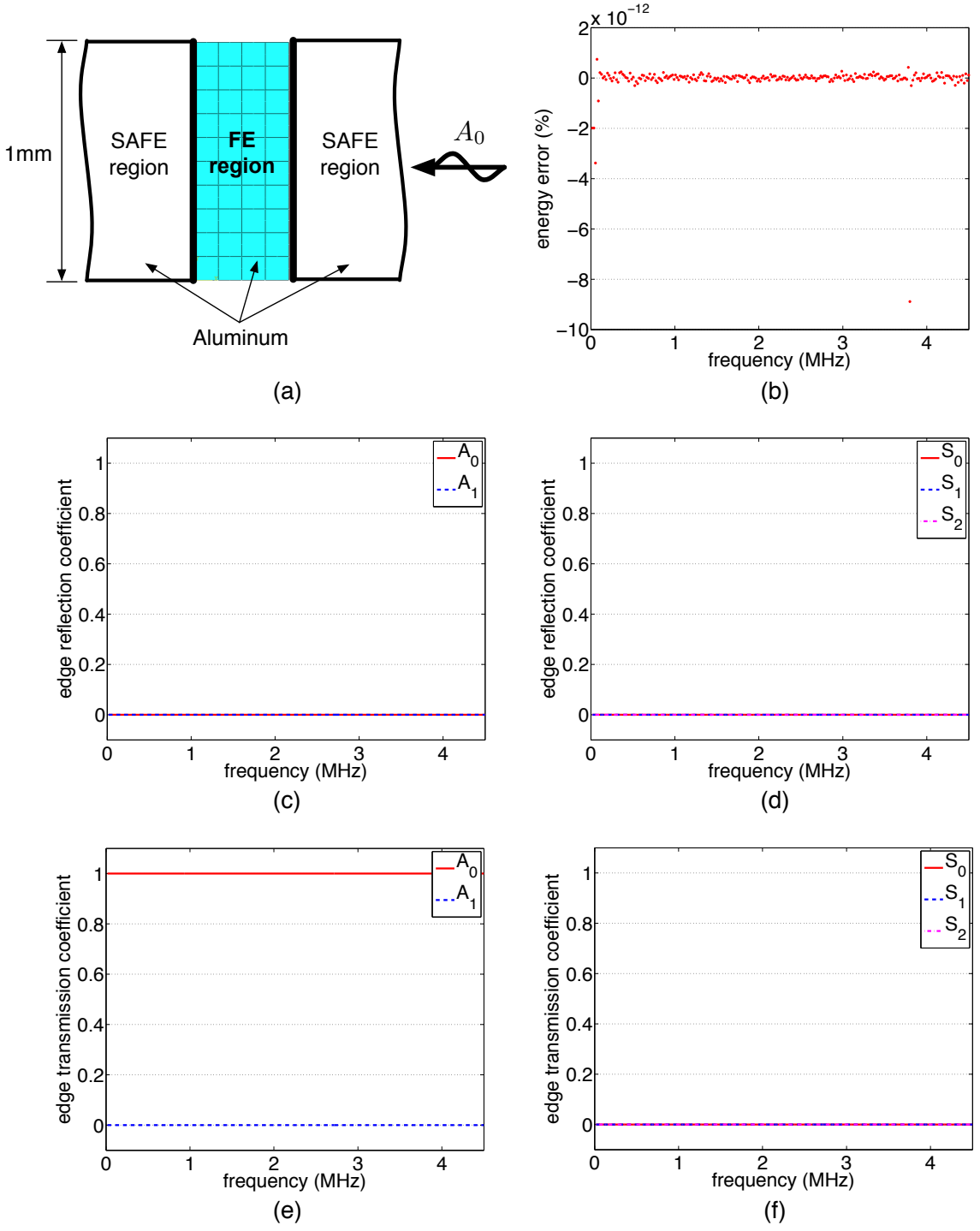

FIGURE A.4: SAFE-FE coupling at the middle of the plate (without damages) with A_0 incident wave; (a) SAFE-FE model, (b) Percentage of energy error, (c) Anti-symmetric modes reflection, (d) Symmetric modes reflection, (e) Anti-symmetric modes transmission, (f) Symmetric modes transmission.

A.3.2 Complex symmetric obstacle

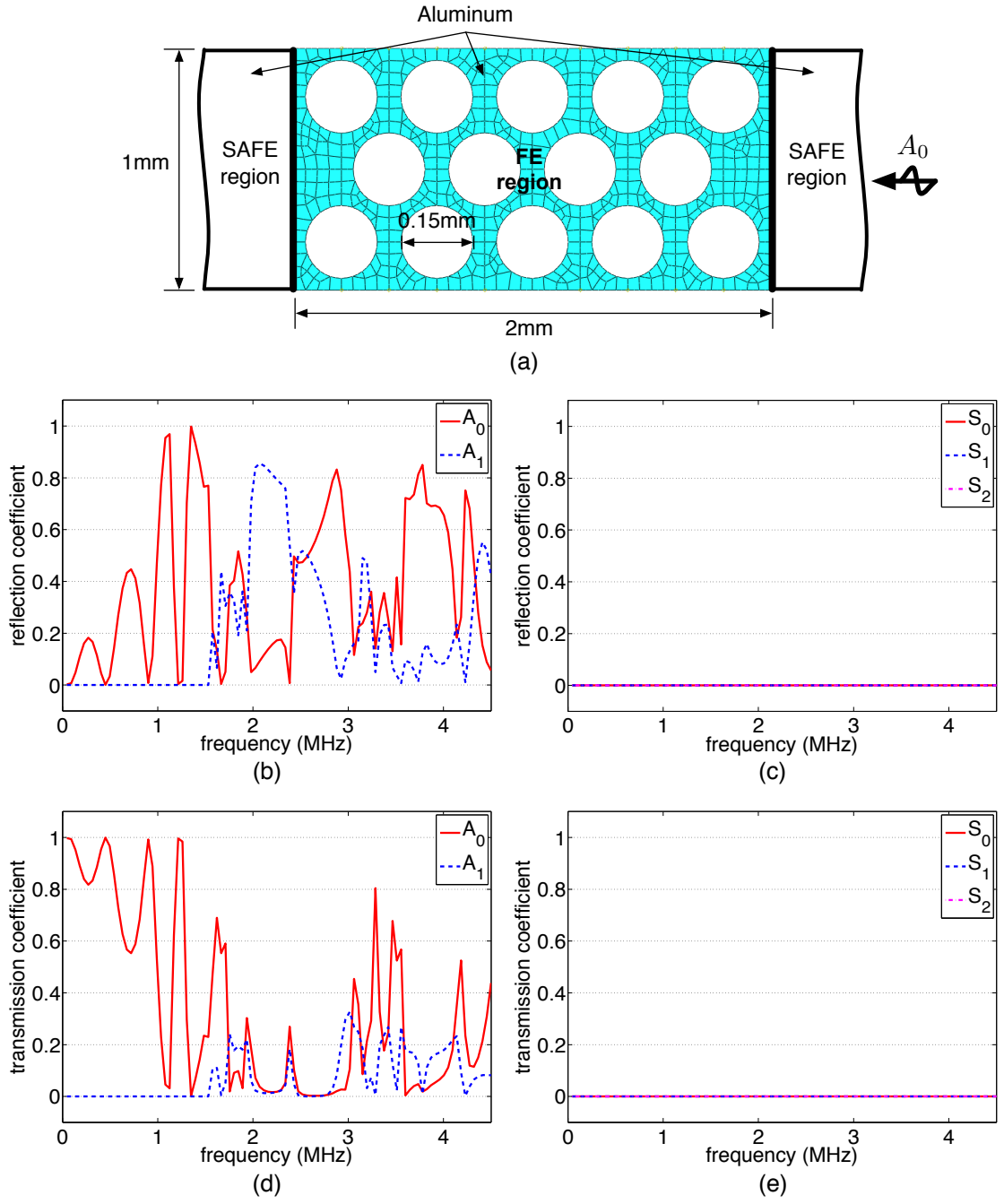

FIGURE A.5: SAFE-FE coupling at the middle of the plate (complex obstacle) with A_0 incident wave; (a) SAFE-FE model, (b) Anti-symmetric modes reflection, (c) Symmetric modes reflection, (d) Anti-symmetric modes transmission, (e) Symmetric modes transmission. Maximum absolute value for percentage of energy error is 3^{-10}.

A.3.3 Different materials

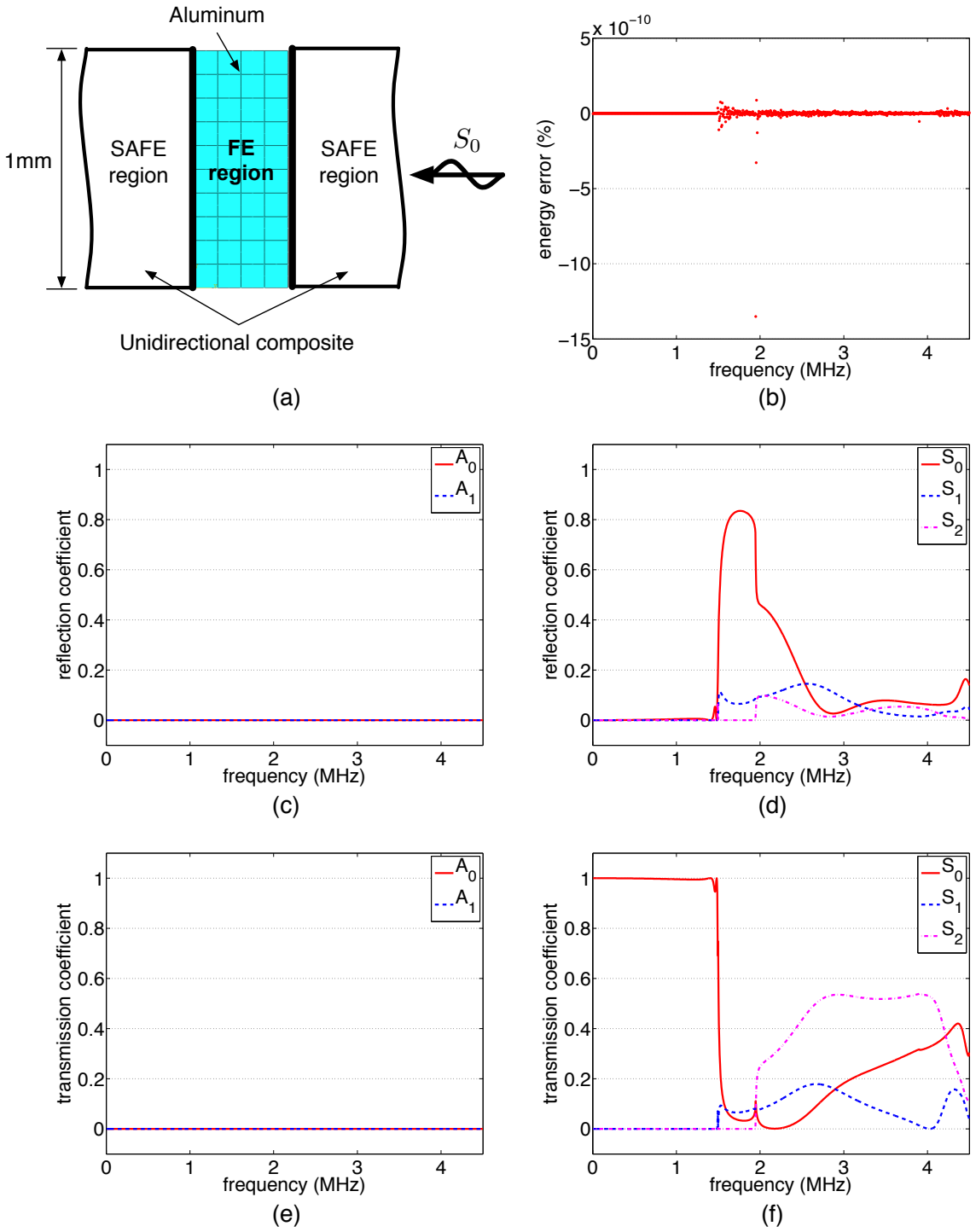

FIGURE A.6: SAFE-FE coupling at the middle of the plate (different materials) with S_0 incident wave; (a) SAFE-FE model, (b) Percentage of energy error, (c) Anti-symmetric modes reflection, (d) Symmetric modes reflection, (e) Anti-symmetric modes transmission, (f) Symmetric modes transmission. Material properties for unidirectional composite is given in Table 4.1.

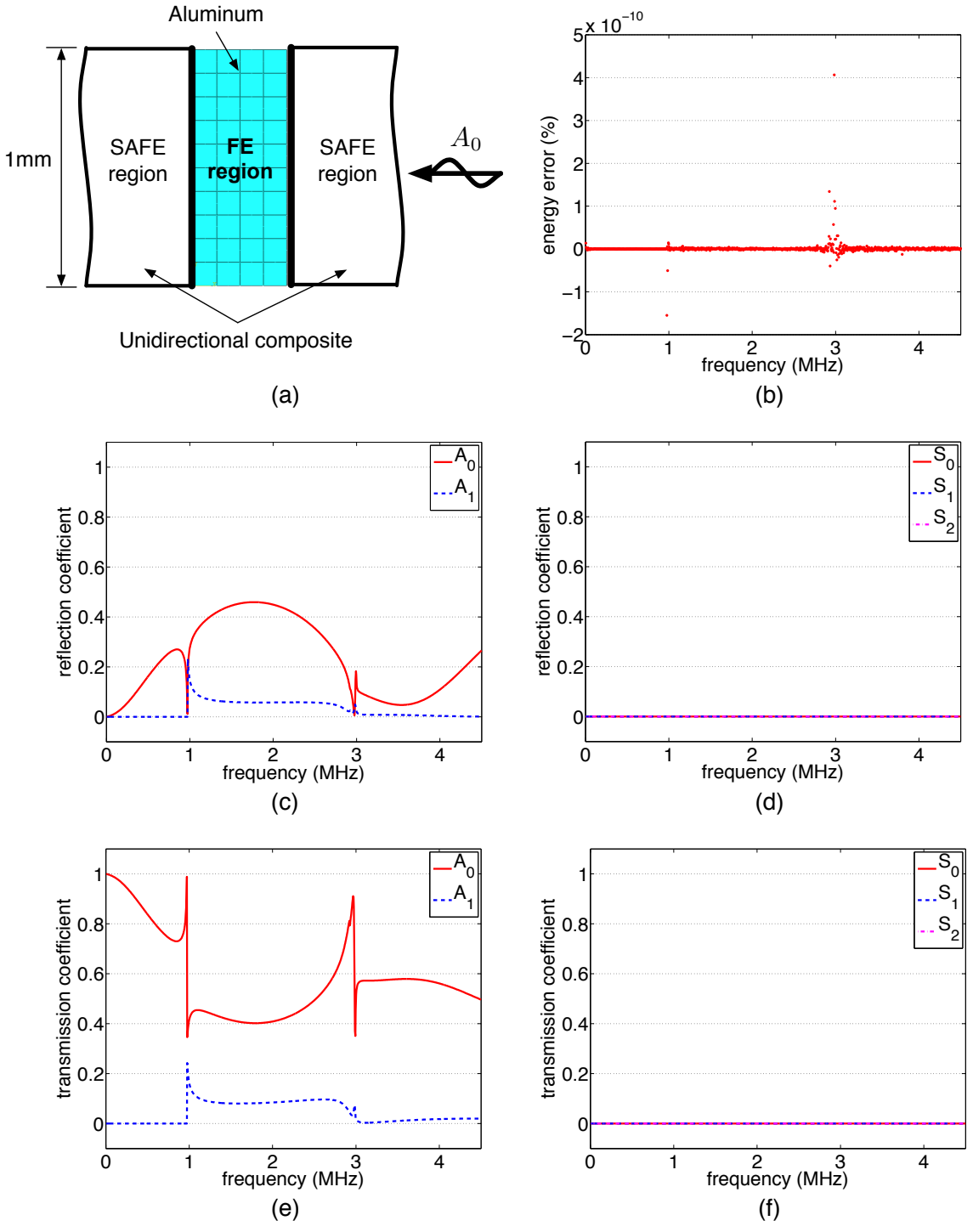

FIGURE A.7: SAFE-FE coupling at the middle of the plate (different materials) with A_0 incident wave; (a) SAFE-FE model, (b) Percentage of energy error, (c) Anti-symmetric modes reflection, (d) Symmetric modes reflection, (e) Anti-symmetric modes transmission, (f) Symmetric modes transmission. Material properties for unidirectional composite is given in Table 4.1.

Appendix B

Appendix for Chapter 6

B.1 Chauchy's integration contour for point force response

Location of x_m	Integration contour	Displacement
$x_m > x_p$	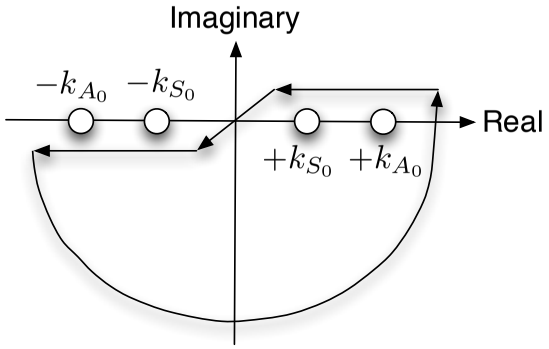	$\mathbf{u}(x,\omega)\big\|_{x_m>x_p} = -i\sum_{r=1}^{3N}\mathbf{Q}_r \cdot \frac{\mathbf{Q}_r^T\mathbf{F}}{\mathbf{Q}_r^T\mathbf{B}\mathbf{Q}_r}e^{-ik_r x}$
$x_m < x_p$	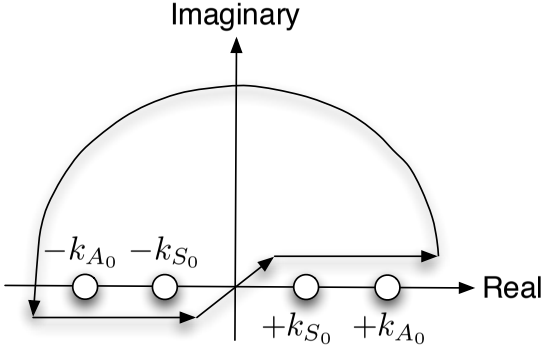	$\mathbf{u}(x,\omega)\big\|_{x_m<x_p} = i\sum_{r=1}^{3N}\mathbf{Q}_r \cdot \frac{\mathbf{Q}_r^T\mathbf{F}}{\mathbf{Q}_r^T\mathbf{B}\mathbf{Q}_r}e^{-ik_r x}$
$x_m = x_p$		$\mathbf{u}(x,\omega)\big\|_{x_m=x_p} = \frac{1}{2}\left(\mathbf{u}(x,\omega)\big\|_{x_m>x_p} + \mathbf{u}(x,\omega)\big\|_{x_m<x_p}\right)$

TABLE B.1: Integration contours for the Cauchy residue theorem. Distance $x = x_m - x_p$.

B.2 Verifications for edge reflections

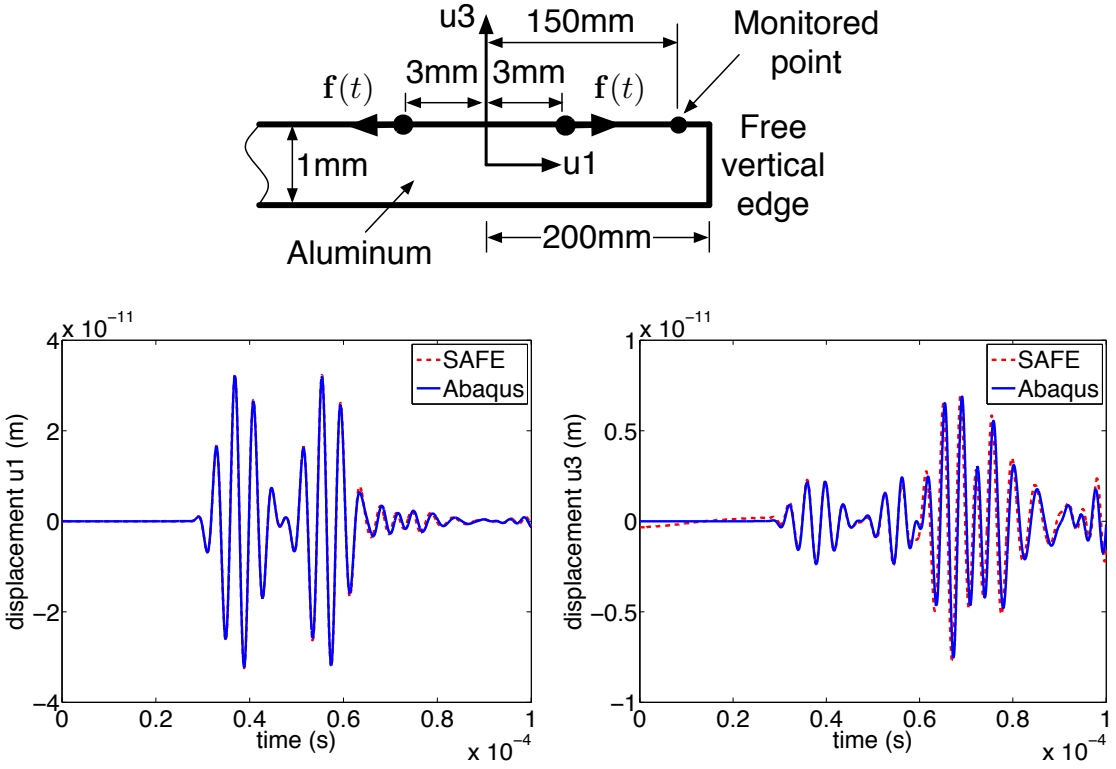

$\mathbf{f}(t)$ is a unit toneburst with Hann window at center frequency 250kHz

FIGURE B.1: Plate edge reflections using additional infinite plate solutions for free symmetrical plate edge. Displacements u1 and u3 calculated at monitored point.

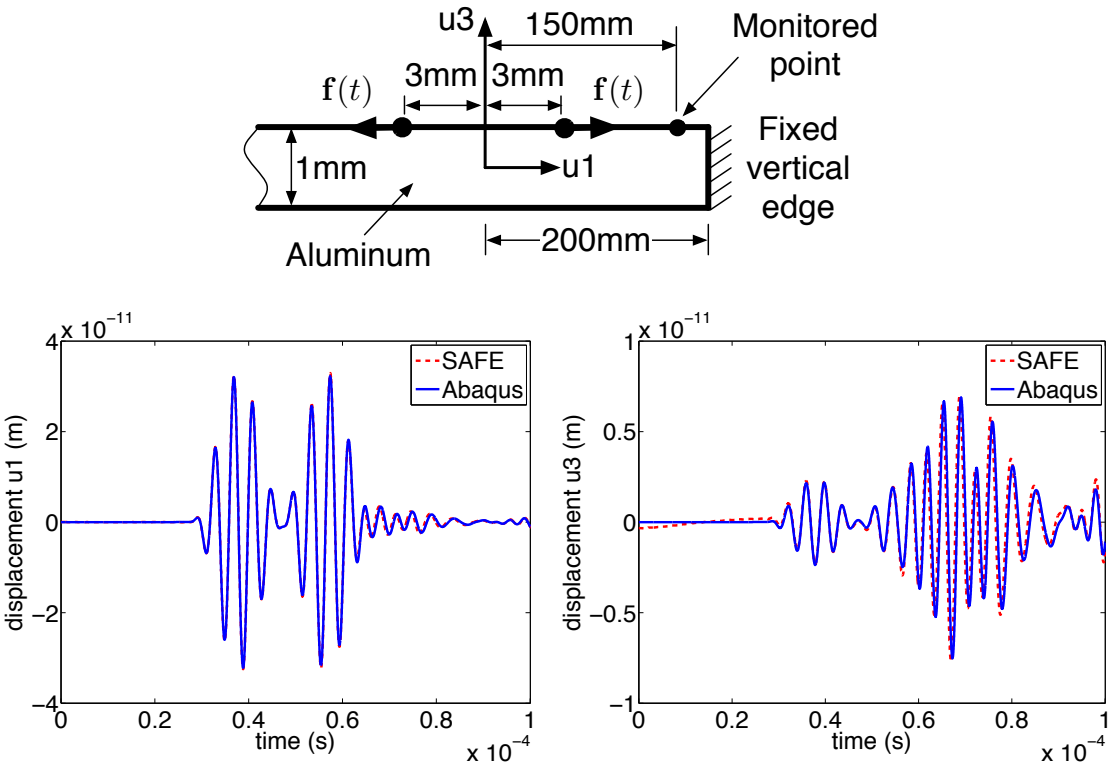

$\mathbf{f}(t)$ is a unit toneburst with Hann window at center frequency 250kHz

FIGURE B.2: Plate edge reflections using additional infinite plate solutions for fixed symmetrical plate edge. Displacements u1 and u3 calculated at monitored point.

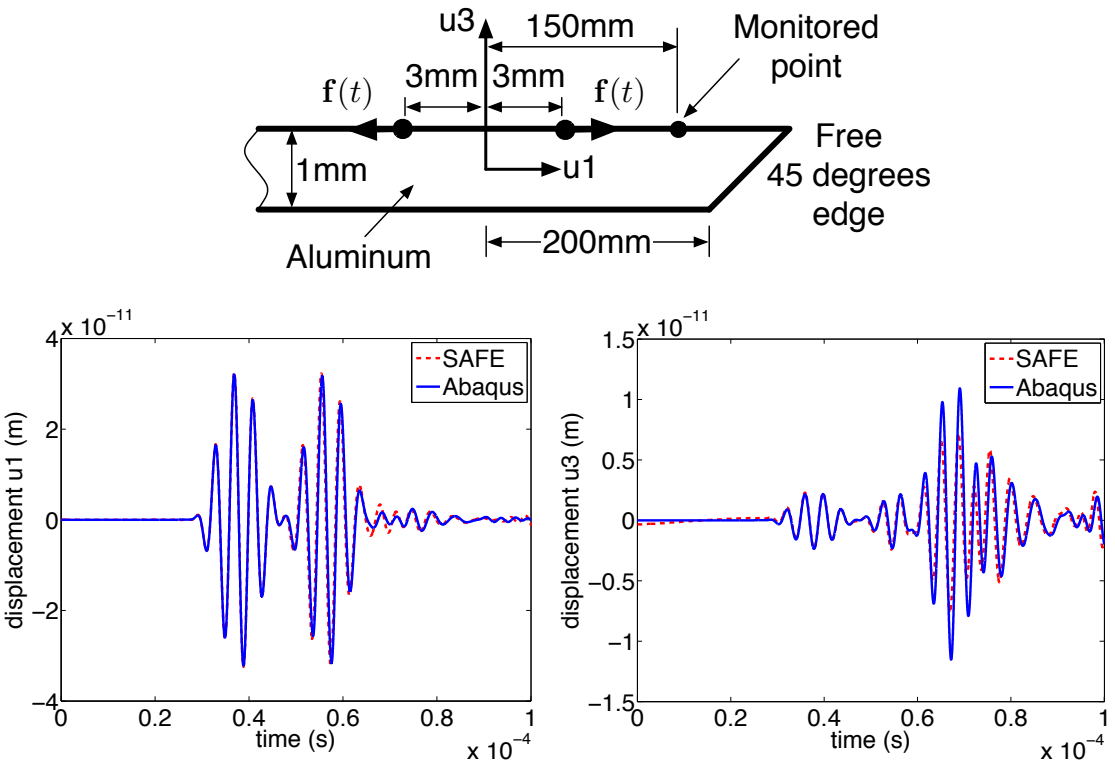

$\mathbf{f}(t)$ is a unit toneburst with Hann window at center frequency 250kHz

FIGURE B.3: Plate edge reflections using additional infinite plate solutions for free symmetrical plate edge. Displacements u1 and u3 calculated at monitored point.

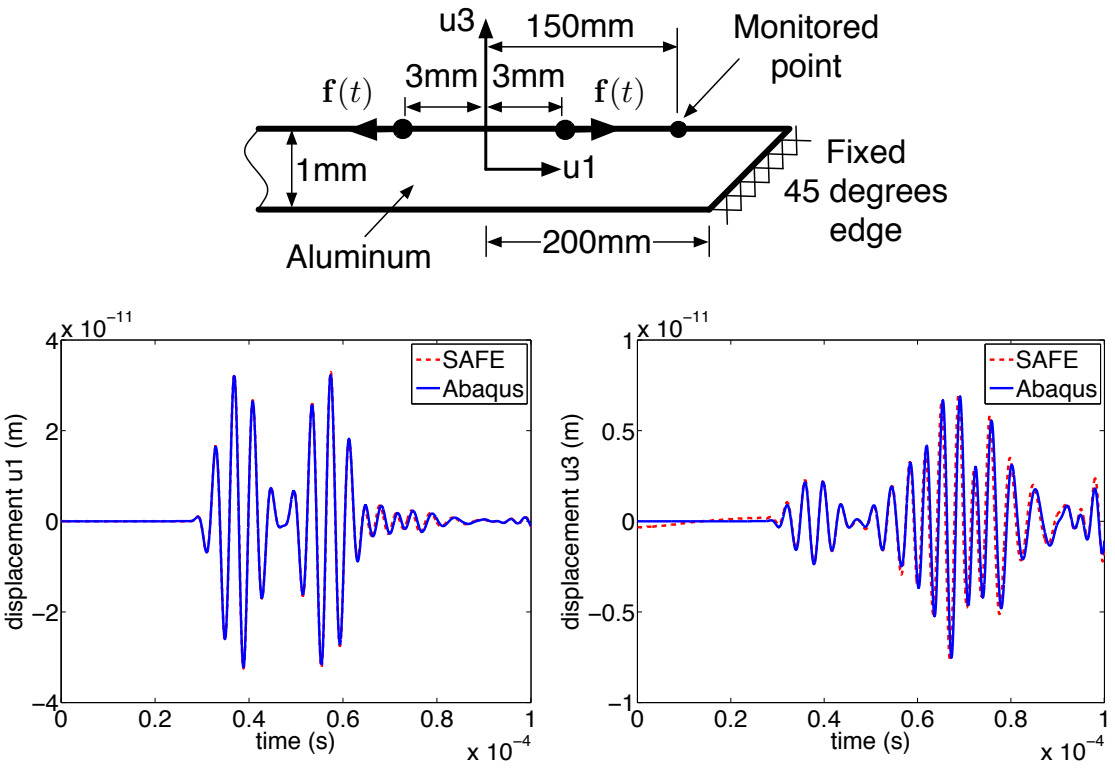

FIGURE B.4: Plate edge reflections using additional infinite plate solutions for free symmetrical plate edge. Displacements u1 and u3 calculated at monitored point.

Appendix C

Wave Finite Element method

The main principle of this method is to find a transfer function for a periodic section of the plates. Consider a periodic section n as shown in Figure C.1. This periodic section is modelled using the FEM. Nodes at the periodic boundaries and inside the finite element meshes are denoted by r, l and i respectively. From the FEM model, global matrices for

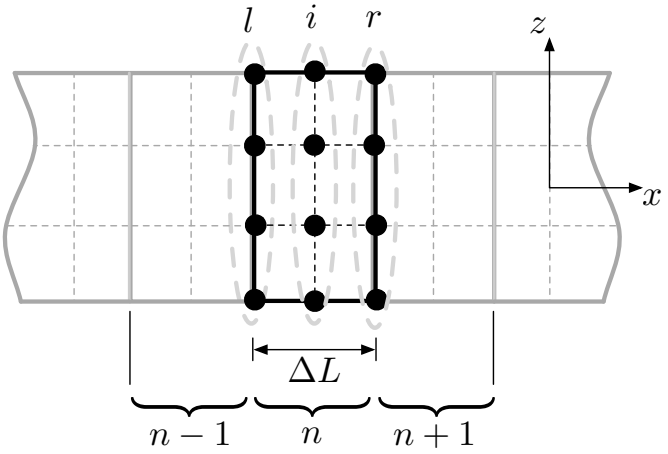

FIGURE C.1: A periodic section n in the infinite plates with periodic boundaries r and l. Width of the periodic section is denoted by ΔL.

stiffness $\mathbf{K}$, mass $\mathbf{M}$ and damping $\mathbf{C}$ are obtained. Thus, dynamic stiffness matrix for the periodic section at each circular frequency ω is obtained as

$$\mathbf{D}(\omega) = \mathbf{K} - i\omega\mathbf{C} - \omega^2\mathbf{M}. \tag{C.1}$$

The dynamic stiffness matrix is related to displacements $\mathbf{u}$ and forces $\mathbf{f}$ at the periodic section as

$$\mathbf{D}\mathbf{u} = \mathbf{f}. \tag{C.2}$$

Refering to Figure C.1, the displacements, the forces and the dynamic stiffness matrix can be partition into nodes at the boundaries r and l and inside the FE meshes. This

yields

$$\begin{bmatrix} \mathbf{D}_{ii} & \mathbf{D}_{ir} & \mathbf{D}_{il} \\ \mathbf{D}_{ri} & \mathbf{D}_{rr} & \mathbf{D}_{rl} \\ \mathbf{D}_{li} & \mathbf{D}_{lr} & \mathbf{D}_{ll} \end{bmatrix} \begin{Bmatrix} \mathbf{u}_i \\ \mathbf{u}_r \\ \mathbf{u}_l \end{Bmatrix} = \begin{Bmatrix} \mathbf{f}_i \\ \mathbf{f}_r \\ \mathbf{f}_l \end{Bmatrix}. \tag{C.3}$$

Taking the force at the inside nodes as zero, the equation above can be reduce to

$$\begin{bmatrix} \mathbf{S}_{rr} & \mathbf{S}_{rl} \\ \mathbf{S}_{lr} & \mathbf{S}_{ll} \end{bmatrix} \begin{Bmatrix} \mathbf{u}_r \\ \mathbf{u}_l \end{Bmatrix} = \begin{Bmatrix} \mathbf{f}_r \\ \mathbf{f}_l \end{Bmatrix} \tag{C.4}$$

where

$$\mathbf{S}_{rr} = \mathbf{D}_{rr} - \mathbf{D}_{ri}\mathbf{D}_{ii}^{-1}\mathbf{D}_{ir}, \tag{C.5}$$

$$\mathbf{S}_{rl} = \mathbf{D}_{rl} - \mathbf{D}_{ri}\mathbf{D}_{ii}^{-1}\mathbf{D}_{il}, \tag{C.6}$$

$$\mathbf{S}_{lr} = \mathbf{D}_{lr} - \mathbf{D}_{li}\mathbf{D}_{ii}^{-1}\mathbf{D}_{ir}, \tag{C.7}$$

$$\mathbf{S}_{ll} = \mathbf{D}_{ll} - \mathbf{D}_{li}\mathbf{D}_{ii}^{-1}\mathbf{D}_{il}. \tag{C.8}$$

Due to the plate periodicity, the displacements and the forces at the right side of one periodic section n must be the same as the displacements and the forces at the left right side of next periodic element $n+1$. Thus the displacements and the forces at the periodic boundaries can be written as

$$\mathbf{u}_r^{(n)} = \mathbf{u}_l^{(n+1)}, \tag{C.9}$$

$$\mathbf{f}_r^{(n)} = \mathbf{f}_l^{(n+1)}. \tag{C.10}$$

Rearranging matrix $\mathbf{D}$ give a frequency dependent transfer matrix relating the displacements and the forces at nodes on boundary n to $n+1$ as

$$\begin{bmatrix} \mathbf{u}_l^{(n+1)} \\ \mathbf{f}_l^{(n+1)} \end{bmatrix} = \mathbf{T}(\omega) \begin{bmatrix} \mathbf{u}_l^{(n)} \\ \mathbf{f}_l^{(n)} \end{bmatrix} \tag{C.11}$$

with

$$\mathbf{T}(\omega) = \begin{bmatrix} -\mathbf{S}_{lr}^{-1}\mathbf{S}_{ll} & \mathbf{S}_{lr}^{-1} \\ -\mathbf{S}_{rl} + \mathbf{S}_{rr}\mathbf{S}_{lr}^{-1}\mathbf{S}_{ll} & -\mathbf{S}_{rr}\mathbf{S}_{lr}^{-1} \end{bmatrix}. \tag{C.12}$$

Assuming a harmonic wave propagation in x direction along periodic section length ΔL and a complex wavenumber k, the displacements and the forces can be written as

$$\mathbf{u}_r = \exp(k\Delta L) \cdot \mathbf{u}_l, \tag{C.13}$$

$$\mathbf{f}_r = \exp(k\Delta L) \cdot \mathbf{f}_l. \tag{C.14}$$

These leads to an eigenvalue problem of

$$\mathbf{T}(\omega) \begin{bmatrix} \mathbf{u}_l^{(n)}(\omega) \\ \mathbf{f}_l^{(n)}(\omega) \end{bmatrix} = \lambda \begin{bmatrix} \mathbf{u}_l^{(n)}(\omega) \\ \mathbf{f}_l^{(n)}(\omega) \end{bmatrix} = \exp(k\Delta L) \begin{bmatrix} \mathbf{u}_l^{(n)}(\omega) \\ \mathbf{f}_l^{(n)}(\omega) \end{bmatrix}. \tag{C.15}$$

This eigenvalue problem has $2N$ solutions with N as total degrees of freedom at one of the periodic boundaries. From the obtained eigenvalue λ, the complex wavenumber is

given by

$$k = \frac{\ln(\lambda)}{\Delta L}. \tag{C.16}$$

By plotting the relationships between k and frequency, dispersion curves of the periodic plate are obtained. In Figure C.2, a comparison is made for the dispersion curves of a 1mm thick aluminum plate calculated using the analytical and the WFE method. Good agreements are obtained. However, the WFE method can be applied to obtain dispersion curves for periodic plates as shown in Figure C.3. In this example, the plate has a periodic layer of aluminum and steel material in the x direction (wave propagation direction). In the calculations for both examples, dynamic stiffness matrices are obtained from Abaqus. The periodic sections are modelled using CPE4 element with 10 elements per 1mm. The aluminum has a Young's modulus of 70GPa, a Poisson's ratio of 0.33 and a density of 2700kg/m^{-3} while the steel has a Young's modulus of 210GPa, a Poisson's ratio of 0.27 and a density of 7800kg/m^{-3}.

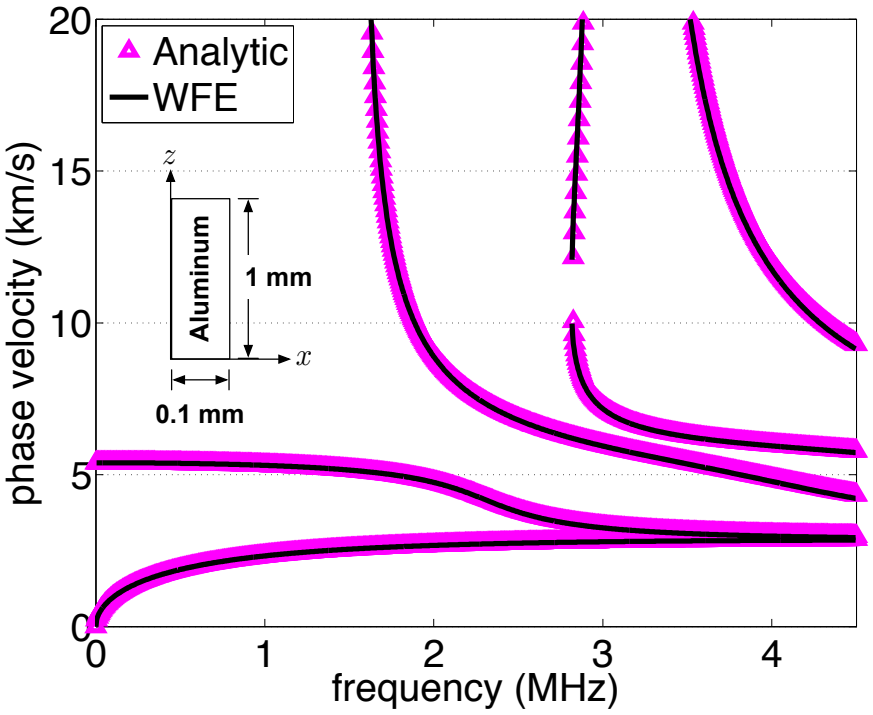

FIGURE C.2: Phase velocity curves comparison between the analytical and the WFE method for a 1mm thick aluminum plate. The periodic section of the aluminum plate is shown next to the dispersion curves.

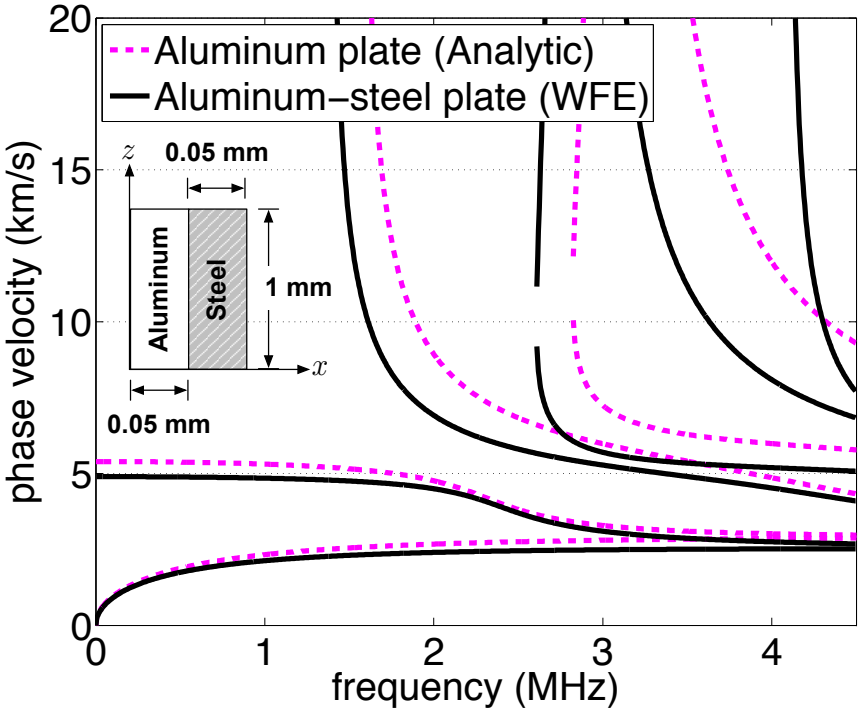

FIGURE C.3: Phase velocity curves for a 1mm thick periodic aluminum-steel plate using the WFE method. The periodic section of the aluminum-steel plate is shown next to the dispersion curves.

Bibliography

[1] H. Gao. *Ultrasonic guided wave mechanics for composite material structural health monitoring*. PhD thesis, The Pennsylvania State University, 2007.

[2] J. Pohl, A. Szewieczek, W. Hillger, G. Mook, and D. Schmidt. Determination of lamb wave dispersion data for shm. *5th European Workshop on Structural Health Monitoring*, 2010.

[3] D. Schmidt. Dokumentation - cfk-testplatten. Technical report, Deutsches Zentrum für Luft- und Raumfahrt, 2010.

[4] F. Chen and P. D. Wilcox. The effect of load on guided wave propagation. *Ultrasonics*, 47:111–122, 2007.

[5] J.M. Galan and R. Abascal. Numerical simulation of lamb wave scattering in semi-infinite plates. *Int. J. Numer. Meth. Engng*, 53:1145–1173, 2002.

[6] V. Giurgiutiu, L. Yu, G.B. Santoni, and B. Xu. Lamb wave tuning for piezoelectric wafer active sensor applications in in-situ structural health monitoring. *Review of Quantitative Nondestructive Evaluation*, 27:896–903, 2008.

[7] F.L. Scalea, H. Matt, and I. Bartoli. The response of rectangular piezoelectric sensors to rayleigh and lamb ultrasonic waves. *Journal of Acoustical Society of America*, 121(1):175–187, 2007.

[8] I. Bartoli, A. Marzani, F.L. di Scalea, and E. Viola. Modeling wave propagation in damped waveguides of arbitary cross-section. *Journal of Sound and Vibration*, 295: 685–707, 2006.

[9] C.R. Farrar and K. Worden. An introduction to structural health monitoring. *Phil. Trans. R. Soc. A*, 365:303–315, 2007.

[10] K. Diamanti and C. Soutis. Structural health monitoring techniques for aircraft composite structures. *Progress in Aerospace Sciences*, 46:342–352, 2010.

[11] C. Boller. Ways and options for aircraft structural health management. *Smart Materials and Structures*, 10:432–440, 2001.

[12] V. Giurgiutiu, J.M. Redmond, D.P. Roach, and K. Rackow. Active sensors for health monitoring of aging aerospace structures. *Proc. of SPIE*, 3985:294–305, 2000.

[13] Z. Su, L. Ye, and Y. Lu. Guided lamb waves for identification of damage in composite structures: A review. *Journal of Sound and Vibration*, 295:753–780, 2006.

[14] C. Potel, S. Baly, J.F. de Belleval, M. Lowe, and P. Gatignol. Deviation of a monochromatic lamb wave beam in anisotropic multilayered media: Asymptotic analysis, numerical and experimental results. *IEEE Transactions On Ultrasonics, Ferroelectrics, And Frequency Control*, 52(6):987–1001, 2005.

[15] J.L. Rose. A baseline and vision of ultrasonic guided wave inspection potential. *Journal of Pressure Vessel Technology*, 124:273–282, 2002.

[16] L. Rayleigh. On waves propagating along the plane surface of an elastic solid. *Proceedings of the London Mathematical Society*, 17, 1885.

[17] H. Lamb. On waves in an elastic plate. *Proceedings of the Royal Society, A. Mathematical, Physical and Engineering Sciences*, 93:114–128, 1917.

[18] A. E. H. Love. *Some Problems of Geodynamics*. Cambridge University Press, 1911.

[19] R. Stoneley. Elastic waves at the surface of separation of two solids. *Proceedings of Royal Society*, 106:416–428, 1924.

[20] J. G. Scholte. The range and existence of rayleigh and stoneley waves. *Mon. Not. Roy. Astron. Soc. Geophys. Suppl.*, 5:120–126, 1947.

[21] W. L. Pilant. Complex roots of the stoneley wave equation. *Bull. Seism. Soc. Am.*, 62:285–299, 1972.

[22] B.A. Auld. *Acoustic fields and waves in solids*. Robert E. Krieger Publishing Company, 1990.

[23] S.W. Kercel, M.B. Klein, and B. Pouet. Bayesian separation of lamb wave signatures. *4th International Workshop on Advances in Signal Processing for Non Destructive Evaluation of Material*, 2001.

[24] N. Hu, T. Shimomukai, C. Yan, and H. Fukunaga. Identification of delamination position in cross-ply laminated composite beams using s0 lamb mode. *Composites Science and Technology*, 68:1548–1554, 2008.

[25] S. Grondel, C. Paget, C. Delebarre, J. Assaad, and K. Levin. Design of optimal configuration for generating a0 lamb mode in a composite plate using piezoceramic transducers. *Journal of Acoustical Society of America*, 112(1):84–90, 2002.

[26] Z. Su, C. Yang, N. Pan, L. Ye, and L.M. Zhou. Assessment of delamination in composite beams using shear horizontal (sh) wave mode. *Composites Science and Technology*, 67:244–251, 2007.

[27] J.S. Lee, Y.Y. Kim, and S.H. Cho. Beam-focused shear-horizontal wave generation in a plate by a circular magnetostrictive patch transducer employing a planar solenoid array. *Smart Materials and Structures*, 18:1–9, 2009.

[28] Z. Su and L. Ye. *Identification of damage using lamb waves: from fundamentals to applications*. Springer-Verlag Berlin Heidelberg, 2009.

[29] T. Kundu, K. Maslov, P. Karpur, T.E. Matikas, and P.D. Nicolaou. A lamb wave scanning approach for the mapping of defects in [0/90] titanium matrix composites. *Ultrasonics*, 34:43–49, 1996.

[30] J.J. Ditri and K. Rajana. An experimental study of the angular dependence of lamb wave excitation amplitudes. *Journal of Sound and Vibration*, 204(5):755–768, 1997.

[31] R. Murayama and K. Mizutani. Conventional electromagnetic acoustic transducer development for optimum lamb wave modes. *Ultrasonics*, 40:491–495, 2002.

[32] N. Toyama and J. Takatsubo. Lamb wave method for quick inspection of impact-induced delamination in composite laminates. *Composites Science and Technology*, 64:1293–1300, 2004.

[33] K. Heller, L.J. Jacobs, and J. Qu. Characterization of adhesive bond properties using lamb waves. *NDT&E International*, 33:555–563, 2000.

[34] V. Giurgiutiu, J. Bao, and W. Zhao. Active sensor wave propagation health monitoring of beam and plate structures. *Proc. of SPIE*, 4327:234–245, 2001.

[35] M.J. Schulz, P.F. Pai, and D.J. Inman. Health monitoring and active control of composite structures using piezoceramic patches. *Composites: Part B*, 30:713–725, 1999.

[36] M.S. Azzouz, C. Mei, J.S. Bevan, and J.J. Ro. Finite element modeling of mfc / afc actuators and performance of mfc. *Journal of Intelligent Material Systems and Structures*, 12:601–612, 2001.

[37] R.B. Williams, G. Park, D.J. Inman, and W.K. Wilkie. An overview of composite actuators with piezoceramic fibers. *Proc. of SPIE*, 4753, 2002.

[38] E.K. Akdogan, M. Allahverdi, and A. Safari. Piezoelectric composites for sensor and actuator applications. *IEEE Transactions On Ultrasonics, Ferroelectrics, And Frequency Control*, 52(5):746–775, 2005.

[39] V. Giurgiutiu. Lamb wave generation with piezoelectric wafer active sensors for structural health monitoring. In *SPIE's 10th Annual International Symposium on Smart Structures and Materials and 8th Annual International Symposium on NDE for Health Monitoring and Diagnostics*, 2002.

[40] X. Wang, Y. Lu, and J. Tang. Damage detection using piezoelectric transducers and the lamb wave approach: I. system analysis. *Smart Matererials and Structures*, 17:1–15, 2008.

[41] J.L. Rose, S.P. Pelts, and M.J. Quarry. A comb transducer model for guided wave nde. *Ultrasonics*, 36:163–169, 1998.

[42] F. Bellan, A. Bulletti, L. Capineri, L. Masotti, G.G. Yaralioglu, F.L. Degertekin, B.T. Khuri-Yakub, F. Guasti, and E. Rosi. A new design and manufacturing process for embedded lamb waves interdigital transducers based on piezopolymer film. *Sensors and Actuators A*, 123-124:379–387, 2005.

[43] R. Paradies and B. Schlaepfer. Finite element modeling of piezoelectric elements with complex electrode configuration. *Smart Materials and Structures*, 18:1–13, 2009.

[44] Ken I. Salas. *Directional transduction for guided wave structural health monitoring.* PhD thesis, The University of Michigan, 2009.

[45] D. Schmidt, C. Heinze, W. Hillger, A. Szewieczek, M. Sinapius, and P. Wierach. Design of mode selective actuators for lamb wave excitation in composite plates. *Proc. of SPIE*, 7984:798409, 2011.

[46] H. Gu and M.L. Wang. A monolithic interdigitated pvdf transducer for lamb wave inspection. *Structural Health Monitoring*, 8:137–148, 2009.

[47] R. Lammering. Observation of piezoelectrically induced lamb wave propagation in thin plates by use of speckle interferometry. *Experimental Mechanics*, 50:377–387, 2010.

[48] S.S. Kessler, S.M. Spearing, and C. Soutis. Damage detection in composite materials using lamb wave methods. *Smart Materials and Structures*, 11:269–278, 2002.

[49] Y.L. Koh, W.K. Chiu, and N. Rajic. Effects of local stiffness changes and delamination on lamb wave transmission using surface-mounted piezoelectric transducers. *Composite Structures*, 57:437–443, 2002.

[50] Y.H. Kim, D.H. Kim, J.H. Han, and C.G. Kim. Damage assessment in layered composites using spectral analysis and lamb wave. *Composites: Part B*, 38:800–809, 2007.

[51] Z. Su, L. Ye, and X. Bu. A damage identification technique for cf/ep composite laminates using distributed piezoelectric transducers. *Composite Structures*, 57: 465–471, 2002.

[52] C.A. Paget, S. Grondel, K. Levin, and C. Delebarre. Damage assessment in composites by lamb waves and wavelet coefficients. *Smart Materials and Structures*, 12: 393–402, 2003.

[53] Y. Lu, X. Wang, J. Tang, and Y. Ding. Damage detection using piezoelectric transducers and the lamb wave approach: Ii. robust and quantitative decision making. *Smart Matererials and Structures*, 17:1–13, 2008.

[54] Z. Su, X. Wang, Z. Chen, L. Ye, and D. Wang. A built-in active sensor network for health monitoring of composite structures. *Smart Materials and Structures*, 15: 1939–1949, 2006.

[55] X. Zhao, G. Zhang H. Gao and, B. Ayhan, F. Yan, C. Kwan, and J.L. Rose. Active health monitoring of an aircraft wing with embedded piezoelectric sensor/actuator network: I. defect detection, localization and growth monitoring. *Smart Matererials and Structures*, 16:1208–1217, 2007.

[56] J. Hou, K.R. Leonard, and M.K. Hinders. Automatic multi-mode lamb wave arrival time extraction for improved tomographic reconstruction. *Inverse Problems*, 20: 1873–1888, 2004.

[57] T.R. Hay, R.L. Royer, H. Gao, X. Zhao, and J.L. Rose. A comparison of embedded sensor lamb wave ultrasonic tomography approaches for material loss detection. *Smart Materials and Structures*, 15:946–951, 2006.

[58] B.V. Soma Sekhar, K. Balasubramaniam, C.V. Krishnamurthy, and B. Maxfield. Algorithm for health monitoring of anisotropic plates using flexible ultrasonic patches. *Review of Quantitative Nondestructive Evaluation*, 26:1501–1508, 2007.

[59] A.H. Rohde, M. Veidt, L.R.F. Rose, and J. Homer. A computer simulation study of imaging flexural inhomogeneities using plate-wave diffraction tomography. *Ultrasonics*, 48:6–15, 2008.

[60] C.T. Ng and M. Veidt. A lamb-wave-based technique for damage detection in composite laminates. *Smart Materials and Structures*, 18:1–12, 2009.

[61] C.H. Wang, J.T. Rose, and F.K. Chang. A computerized time-reversal method for structural health monitoring. *Proc. of SPIE*, 5046:48–58, 2003.

[62] G. Butėnas and R. Kažys. Application of time reversal approach for focusing of lamb waves. *Ultragarsas (ultrasound)*, 62(2):38–43, 2007.

[63] Z. Su and L. Ye. A fast damage locating approach using digital damage fingerprints extracted from lamb wave signals. *Smart Materials and Structures*, 14:1047–1054, 2005.

[64] N. Pan, Z. Su, L. Ye, L.M. Zhou, and Y. Lu. A quantitative identification approach for delamination in laminated composite beams using digital damage fingerprints (ddfs). *Composite Structures*, 75:559–570, 2006.

[65] L. Wang and F.G. Yuan. Active damage localization technique based on energy propagation of lamb waves. *Smart Structures and Systems*, 3(2):201–217, 2007.

[66] A.S. Purekar, D.J. Pines, S. Sundararaman, and D.E. Adams. Directional piezoelectric phased array filters for detecting damage in isotropic plates. *Smart Materials and Structures*, 13:838–850, 2004.

[67] J. Rajagopalan, K. Balasubramaniam, and C.V. Krishnamurthy. A phase reconstruction algorithm for lamb wave based structural health monitoring of anisotropic multilayered composite plates. *Journal of Acoustical Society of America*, 119(2): 872–878, 2006.

[68] J. Rajagopalan, K. Balasubramaniam, and C.V. Krishnamurthy. A single transmitter multi-receiver (stmr) pzt array for guided ultrasonic wave based structural health monitoring of large isotropic plate structures. *Smart Materials and Structures*, 15: 1190–1196, 2006.

[69] V. Giurgiutiu and J. Bao. Embedded-ultrasonics structural radar for in situ structural health monitoring of thin-wall structures. *Structural Health Monitoring*, 121(3):121–140, 2004.

[70] S. Sundararaman, D.E. Adams, and E.J. Rigas. Biologically inspired structural diagnostics through beamforming with phased transducer arrays. *International Journal of Engineering Science*, 43:756–778, 2005.

[71] L. Yu and V. Giurgiutiu. Advanced signal processing for enhanced damage detection with piezoelectric wafer active sensors. *Smart Structures and Systems*, 1(2):185–215, 2005.

[72] P.Malinowski, T.Wandowski, I. Trendafilova, and W. Ostachowicz. A phased array-based method for damage detection and localization in thin plates. *Structural Health Monitoring*, 0(0):1–11, 2008.

[73] Lingyu Yu. *In-situ structural health monitoring with piezoelectic wafer active sensor guided-wave phased arrays*. PhD thesis, University of South Carolina, 2006.

[74] F. Yan and J.L. Rose. Guided wave phased array beam steering in composite plates. *Proc. of SPIE*, 6532:65320G–1, 2007.

[75] F. Yan, C.J. Lissenden, and J.L. Rose. Directivity profiles of guided wave phased arrays for multilayer composite plates. *Proc. of SPIE*, 7295:729514, 2009.

[76] H. M. Matt. *Structural Diagnostics of CFRP Composite Aircraft Components by Ultrasonic Guided Waves and Built-In Piezoelectric Transducers*. PhD thesis, University of California San Diego, 2006.

[77] H. Matt and F.L. Scalea. Macro-fiber composite piezoelectric rosettes for acoustic source location in complex structures. *Proc. of SPIE*, 6529:65290Q–1, 2007.

[78] S. Salamone, I. Bartoli, J. Rhymer, F.L. di Scalea, and H. Kim. Validation of the piezoelectric rosette technique for locating impacts in complex aerospace panels. *Proc. of SPIE*, 7984:79841, 2011.

[79] I.A. Viktorov. *Rayleigh and Lamb Waves*. Plenum Press, 1967.

[80] Ural (computer). Internet, 2011. URL http://en.wikipedia.org/wiki/Ural_(computer).

[81] D. Alleyne and P. Cawley. A two-dimensional fourier transform method for the measurement of propagating multimode signals. *Journal of Acoustical Society of America*, 89:1159–1168, 1991.

[82] A. Velichko and P.D. Wilcox. Modeling the excitation of guided waves in generally anisotropic multilayered media. *Journal of Acoustical Society of America*, 121(1): 60–69, 2007.

[83] G.R. Liu and S.S. Quek Jerry. A non-reflecting boundary for analyzing wave propagation using the finite element method. *Finite Elements in Analysis and Design*, 39:403–417, 2003.

[84] R. Balasubramanyam, D. Quinney, R.E. Challis, and C.P.D. Todd. A finite-difference simulation of ultrasonic lamb waves in metal sheets with experimental verification. *Journal of Physics D: Applied Physics*, 29:147–155, 1996.

[85] B.C. Lee and W.J. Staszewski. Modelling of lamb waves for damage detection in metallic structures: Part i. wave propagation. *Smart Materials and Structures*, 12: 804–814, 2003.

[86] B.C Lee and W.J. Staszewski. Modelling of lamb waves for damage detection in metallic structures: Part ii. wave interactions with damage. *Smart Materials and Structures*, 12:815–824, 2003.

[87] V.B. Yadav, T. Pramila, V. Raghuram, and N.N. Kishore. A finite-difference simulation of multi-mode lamb waves in aluminium sheet with experimental verification using laser based ultrasonic generation. In *5th. Asia-Pacific Conference on NDT*, 2006.

[88] X. Zhang and S. Yuan. Lamb wave propagation modeling for structure health monitoring. *Front. Mech. End. China*, 4(3):326–331, 2009.

[89] D.R. Mahapatra and S. Gopalakrishnan. A spectral finite element model for analysis of axialflexuralshear coupled wave propagation in laminated composite beams. *Composite Structures*, 59:67–88, 2003.

[90] A. Chakraborty and S. Gopalakrishnan. A spectrally formulated finite element for wave propagation analysis in layered composite media. *International Journal of Solids and Structures*, 41:5155–5183, 2004.

[91] P. Kudela, W. Ostachowicz, and A. Żak. Damage detection in composite plates with embedded pzt transducers. *Mechanical Systems and Signal Processing*, 2007. doi: doi:10.1016/j.ymssp.2007.07.008.

[92] Y. Cho and J.L. Rose. A boundary element solution for a mode conversion study on the edge reflection of lamb waves. *Journal of Acoustical Society of America*, 99 (4):2097–2109, 1996.

[93] Y. Cho and J.L. Rose. An elastodynamic hybrid boundary element study for elastic guided wave interactions with a surface breaking defect. *International Journal of Solids and Structures*, 37:4103–4124, 2000.

[94] T. Hayashi and S. Endoh. Calculation and visualization of lamb wave motion. *Ultrasonics*, 38:770–773, 2000.

[95] X.G. Zhao and J.L. Rose. Boundary element modeling for defect characterization potential in a wave guide. *International Journal of Solids and Structures*, 40:2645–2658, 2003.

[96] J. Koreck. Computational characterization of adhesive bond properties using guided waves in bonded plates. Master's thesis, Georgia Institute of Technology, 2006.

[97] B.R. Mace and E. Manconi. Modelling wave propagation in two-dimensional structures using finite element analysis. *Journal of Sound and Vibration*, 318:884–902, 2008.

[98] Elisabetta Manconi. *Modelling Wave Propagation In Two-dimensional Structures Using A Wave/finite Element Technique*. PhD thesis, University of Parma, 2008.

[99] M.N. Ichchou, J.-M. Mencik, and W. Zhou. Wave finite elements for low and mid-frequency description of coupled structures with damage. *Comput. Methods Appl. Mech. Engrg.*, 198:1311–1326, 2009.

[100] T. Kohrs and B. A.T. Petersson. Wave beaming and wave propagation in light weight plates with truss-like cores. *Journal of Sound and Vibration*, 321:137–165, 2009.

[101] S. Sorohan, N. Constantin, M. Gavăn, and V. Anghel. Extraction of dispersion curves for waves propagating in free complex waveguides by standard finite element codes. *Ultrasonics*, 51:503–515, 2011.

[102] A. Béchet, Y.H. Berthelot, and C.S. Lynch. A stress gradient-enhanced piezoelectric actuator composite (gepac) with integrated ultrasonic nde capability for continuous health monitoring. *Journal Of Intelligent Material Systems And Structures*, 16: 85–93, 2005.

[103] M. Predoi, Ş. Sorohan, M. Găvan N. Constantin, and D.M. Constantinescu. Analysis of lamb wave propagation in a steel plate. *22nd DANUBIA-ADRIA Symposium on Experimental Methods in Solid Mechanics*, 2005.

[104] R. Kažys, L. Mažeika, R. Barauskas, R. Raišutis, V. Cicėnas, and A. Demčenko. 3d analysis of interaction of lamb waves with defects in loaded steel plates. *Ultrasonics*, 44:e1127–e1130, 2006.

[105] C.K.W. Wong, W.K. Chiu, N. Rajic, and S.C. Galea. Can stress waves be used for monitoring sub-surface defects in repaired structures? *Composite Structures*, 76: 199–208, 2006.

[106] M. Ratassepp and A. Klauson. Curvature effects on wave propagation in an infinite pipe. *ULTRAGARSAS*, 59(2):19–25, 2006.

[107] A. Chakraborty. *Encyclopedia of Structural Health Monitoring*, chapter Chapter 49: Modeling of Lamb waves in composite structures, pages 923–939. John Wiley & Sons, 2009.

[108] A. Nayfeh and D. Chimenti. Free wave propagation in plates of general anisotropic media. *Journal of Applied Mechanics*, 56(4):881–886, 1989.

[109] M.J.S. Lowe. Matrix techniques for modeling ultrasonic waves in multilayered media. *IEEE Transactions on Ultrasonics, Ferroelectrics and Frequency Control*, 42(4): 525–542, 1995.

[110] A.H. Nayfeh. *Wave propagation in layered anisotropic media with applications to composites*. Elsevier Science B.V., 1995.

[111] M.J.S. Lowe, P. Cawley, and B.N. Pavlakovic. *Surface Waves in Anisotropic and Laminated Bodies and Defects Detection*, chapter A general purpose computer model for calculating elastic waveguide properties, with application to non-destructive testing, pages 241–256. Kluwer Academic Publishers, 2004.

[112] A. Karmazin, E. Kirillova, W. Seemann, and P. Syromyatnikov. Investigation of lamb elastic waves in anisotropic multilayered composites applying the greens matrix. *Ultrasonics 51*, 51:17–28, 2011.

[113] D.N. Alleyne and P. Cawley. A 2-dimensional fourier transform method for the quantitative measurement of lamb modes. *Proc. of IEEE Ultrasonics Symposium*, 2:1143–1146, 1990.

[114] G. Hayward and J. Hyslop. Determination of lamb wave dispersion data in lossy anisotropic plates using time domain finite element analysis. part i: Theory and experimental verification. *IEEE Transactions On Ultrasonics, Ferroelectrics, And Frequency Control*, 53(2):443–448, 2006.

[115] H. Jeong. Analysis of plate wave propagation in anisotropic laminates using a wavelet transform. *NDT&E International*, 34:185–190, 2001.

[116] S. Hurlebaus, M. Niethammer, and L.J. Jacobs. Automated methodology to locate notches with lamb waves. *Acoustics Research Letters Online, Acoustical Society of America*, 2(4):97–102, 2001.

[117] G. Waas. Earth vibration effects and abatement for military facilities (s-71-14) - analysis report for footing vibrations through layered media. Technical report, US Army Engineer Waterways Experiment Station, 1972.

[118] E. Kausel. An explicit solution for the green functions for dynamic loads in layered media. Technical report, Massachusetts Institute of Technology, 1981.

[119] J. Park. *Wave motion in finite and infinite media using the thin layer method*. PhD thesis, Massachusetts Institute of Technology, 2002.

[120] R.B. Nelson and S.B. Dong. High frequency vibrations and waves in laminated orthotropic plates. *Journal of Sound and Vibration*, 30(1):33–44, 1973.

[121] P.E. Lagasse. Higher-order finite-element analysis of topographic guides supporting elastic surface waves. *Journal of Acoustical Society of America*, 53(4):1116–1122, 1973.

[122] W. Karunasena, A.H. Shah, and S.K. Datta. Wave propagation in a multilayered laminated cross-ply composite plate. *Transactions of the ASME*, 58:1028–1032, 1991.

[123] L. Gavric. Computation of propagative waves in free rail using a finite element technique. *Journal of Sound and Vibration*, 185 (3):531–543, 1995.

[124] T. Hayashi, K. Kawashima, Z. Sun, and J. L. Rose. Analysis of flexural mode focusing by a semianalytical finite element method. *Journal of Acoustical Society of America*, 113(3):1241–1248, 2003.

[125] S. Finnveden. Evaluation of modal density and group velocity by a finite element method. *Journal of Sound and Vibration*, 273:51–75, 2004.

[126] A. Marzani, E. Viola, I. Bartoli, F.L. di Scalea, and P. Rizzo. A semi-analytical finite element formulation for modeling stress wave propagation in axisymmetric damped waveguides. *Journal of Sound and Vibration*, 318:488–505, 2008.

[127] C.M. Lee, J.L. Rose, and Y. Cho. A guided wave approach to defect detection under shelling in rail. *NDT&E International*, 42:174–180, 2009.

[128] J. Ryue, D.J. Thompson, P.R. White, and D.R. Thompson. Decay rates of propagating waves in railway tracks at high frequencies. *Journal of Sound and Vibration*, 320:955–976, 2009.

[129] M.R. Chitnis, Y.M. Desai, and T. Kant. Edge vibrations in composite laminated sandwich plates by using a higher order displacement based theory. *Journal of Sound and Vibration*, 238(5):791–807, 2000.

[130] G.R. Liu and Z.C. Xi. *Elastic waves in anisotropic laminates*. CRC Press, 2002.

[131] E. Barbieri, A. Cammarano, S. De Rosa, and F. Franco. Waveguides of a composite plate by using the spectral finite element approach. *Journal of Vibration and Control*, 15(3):347–367, 2009.

[132] X. Lin and F.G. Yuan. Diagnostic lamb waves in an integrated piezoelectric sensor/actuator plate:analytical and experimental studies. *Smart Materials and Structures*, 10:907–913, 2001.

[133] S. Banerjee, A.K. Mal, and W.H. Prosser. Analysis of transient lamb waves generated by dynamic surface sources in thin composite plates. *Journal of Acoustical Society of America*, 115 (5):1905–1911, 2004.

[134] L. Wang and F.G. Yuan. Lamb wave propagation in composite laminates using a higher-order plate theory. *Proc. of SPIE*, 6531:653101, 2007.

[135] M. Calomfirescu. *Lamb Waves for Structural Health Monitoring in Viscoelastic Composite Materials*. PhD thesis, Universitt Bremen, 2007.

[136] T. Pialucha, CCH. Guyott, and P. Cawley. An amplitude spectrum method for the measurement of phase velocity. *Ultrasonics*, 27:270–279, 1989.

[137] W. Sachse and YH Pao. On the determination of phase and group velocities of dispersive waves in solids. *Journal of Applied Physics*, 48(9):4320–4327, 1978.

[138] SH Díaz Valdéz and C. Soutis. Real-time nondestructive evaluation of fibre composite laminates using low frequency lamb waves. *The Journal of the Acoustical Society of America*, 11(5):2026–2033, 2002.

[139] C. Soutis. *Encyclopedia of Structural Health Monitoring*, chapter Chapter 17: Lamb wave-based SHM for laminated composite structures, pages 353–364. John Wiley & Sons, 2009.

[140] F. Jenot, M. Ouaftouh, M. Duquennoy, and M. Ourak. Corrosion thickness gauging in plates using lamb wave group velocity measurements. *Measurement Science And Technology*, 12:1287–1293, 2001.

[141] Y.H. Kim, S.J. Song, S.D. Kwon, Y.M. Cheong, and H.K. Jung. Determination of ultrasonic wave velocities and phase velocity dispersion curves of an inconel 600 plate using resonant ultrasound spectroscopy and leaky lamb waves. *Ultrasonics*, 42:551–555, 2004.

[142] B. Khler. Dispersion relations in plate structures studied with a scanning laser vibrometer. *European Conference on Non Destructive Testing*, pages 1–11, 2006.

[143] D. Ta, Z. Liu, and X. Liu. Combined spectral estimator for phase velocities of multimode lamb waves in multilayer plates. *Ultrasonics*, 44:e1145–e1150, 2006.

[144] J. Yang and J.C. Cheng. A new inverse method of elastic constants for a fibre-reinforced composite plate from laser-based ultrasonic lamb waves. *Chinese Physical Letter*, 18(12):1620–1623, 2001.

[145] N. Terrien, D. Osmont, D. Royer, F. Lepoutre, and A. Déom. A combined finite element and modal decomposition method to study the interaction of lamb modes with micro-defects. *Ultrasonics*, 46:74–88, 2007.

[146] W. Karunasena, K. M. Liew, and S. Kitipornchai. Reflection of plate waves at the fixed edge of a composite plate. *Journal of Acoustical Society of America*, 98(1): 644–651, 1995.

[147] W.M. Karunasena, K.M. Liew, and S. Kitipornchai. Hybrid analysis of lamb wave reflection by a crack at the fixed edge of a composite plate. *Comput. Methods Appl. Mech. Engrg.*, 125:221–233, 1995.

[148] W. Karunasena. Elastodynamic reciprocity relations for wave scattering by flaws in fiber-reinforced composite plates. *Journal of Mechanics of Materials and Structures*, 3(10):1831–1846, 2008.

[149] G. R. Liu. A combined finite element/strip element method for analyzing elastic wave scattering by cracks and inclusions in laminates. *Computational Mechanics*, 28:76–81, 2002.

[150] J. Tian, U. Gabbert, H. Berger, and X. Su. Lamb wave interaction with delaminations in cfrp laminates. *Computer, Materials and Continua*, 1(4):327–336, 2004.

[151] S. Banerjee, W. Prosser, and A. Mal. Calculation of the response of a composite plate to localized dynamic surface loads using a new wave number integral method. *Transactions of the ASME*, 72:18–24, 2005.

[152] A. Raghavan and C.E.S. Cesnik. Finite-dimensional piezoelectric transducer modeling for guided wave based structural health monitoring. *Smart Materials and Structures*, 14:1448–1461, 2005.

[153] A. Raghavan and C.E.S. Cesnik. 3-d elasticity-based modeling of anisotropic piezocomposite transducers for guided wave structural health monitoring. *Journal of Vibration and Acoustics*, 129:739–751, 2007.

[154] V. Damljanovic and R.L. Weaver. Forced response of a cylindrical waveguide with simulation of the wavenumber extraction problem. *Journal of Acoustical Society of America*, 115(4):1582–1591, 2004.

[155] P.W. Loveday and C.S. Long. Time domain simulation of piezoelectric excitation of guided waves in rails using waveguide finite elements. *Proc. of SPIE*, 6529:65290V–1, 2007.

[156] P.W. Loveday. Analysis of piezoelectric ultrasonic transducers attached to waveguides using waveguide finite elements. *IEEE Transactions on Ultrasonics, Ferroelectrics and Frequency Control*, 54(10):2045–2051, 2007.

[157] Juan Miguel Vivar-Perez, Zair Asrar Bin Ahmad, and Ulrich Gabbert. Spectral analysis and semi-analytical finite element method for lamb wave simulation. In *5th European Workshop on Structural Health Monitoring*, number ISBN 978-1-605-95024-2. DEStech, 2010.

[158] B. Chapuis, N. Terrien, and D. Royer. Excitation and focusing of lamb waves in a multilayered anisotropic plate. *Journal of Acoustical Society of America*, 127(1): 198–203, 2010.

[159] P.W. Loveday. Numerical comparison of patch and sandwich piezoelectric transducers for transmitting ultrasonic waves. *Proc. of SPIE*, 6166:616612, 2006.

[160] R.D. Cook. *Concepts and applications of finite element analysis.* John Wiley & Sons, 2001.

[161] M.R. Chitnis, Y.M. Desai, A.H. Shah, and T. Kant. Comparisons of displacement-based theories for waves and vibrations in laminated and sandwich composite plates. *Journal of Sound and Vibration*, 263:617–642, 2003.

[162] F. Yan and J.L. Rose. Composite plate inspection using a novel guided wave skew effect method. *Review of Quantitative Nondestructive Evaluation*, 28:1049–1056, 2009.

[163] P. W. Loveday. Semi-analytical finite element analysis of elastic waveguides subjected to axial loads. *Ultrasonics*, 49:298–300, 2009.

[164] V. Giurgiutiu. *Structural health monitoring with piezoelectic wafer active sensors.* Academic Press/Elsavier, 2008.

[165] E. G. Thompson. *An introduction to the finite element method - theory, programming and applications*. John Wiley & Sons, 2005.

[166] R. Basri and W.K. Chiu. Numerical analysis on the interaction of guided lamb waves with a local elastic stiffness reduction in quasi-isotropic composite plate structures. *Composite Structures*, 66:87–99, 2004.

[167] A. Piersol and T. Paez. *Harris's shock and vibration handbook, 6th edition*. McGraw-Hill Professional, 2009.

[168] I. Núñez, R.K. Ing, C. Negreira, and M. Fink. Transfer and green functions based on modal analysis for lamb waves generation. *Journal of Acoustical Society of America*, 107 (5):2370–2378, 2000.

[169] H.S. Tzou. *Piezoelectric shells: distributed sensing and control of continua*, volume 19 of *Solid Mechanics and its Applications*. Kluwer Academic Publisher, 1993.

[170] J. Sirohi and I. Chopra. Fundamental understanding of piezoelectric strain sensors. *Journal of Intelligent Material Systems and Structures*, 11:246–257, 2000.